

# A multi scale consolidation model for press moulding of hybrid textiles into complex geometries

Présentée le 17 novembre 2023

Faculté des sciences et techniques de l'ingénieur  
Laboratoire de mise en oeuvre de composites à haute performance  
Programme doctoral en manufacturing

pour l'obtention du grade de Docteur ès Sciences

par

## Vincent WERLEN

Acceptée sur proposition du jury

Prof. Y. Bellouard, président du jury  
Prof. V. Michaud, Dr C. Rytka, directeurs de thèse  
Prof. R. Akkerman, rapporteur  
Dr N. Bernet, rapporteur  
Prof. J.-F. Molinari, rapporteur



*"No lifetime is long enough for those who wish to create, Raul. Or for those who simply wish to understand themselves and their lives. It is, perhaps, the curse of being human, but also a blessing."*

- Dan Simmons, *The Rise of Endymion*

*"The scientists of today think deeply instead of clearly. One must be sane to think clearly, but one can think deeply and be quite insane."*

- Nikola Tesla

*"If you 're going through hell, keep going."*

- Winston Churchill



## Acknowledgements

The past four years of research were for me humbling as I realized how little is known in the grand scheme of things, and even in what we know there are often uncertainties. The contribution of this thesis is nothing but a tiny step on the path of our quest of understanding the universe, which does not prevent me from feeling very happy and proud about placing it. I could for sure never have done it alone and would like here to express gratitude to the many people who have been by my side and supported me during the long inward journey that was my PhD.

I would like to express my profound gratitude to those directly involved with the supervision of my work: Professor Véronique Michaud, for her seemingly unlimited availability and readiness to equally give valuable advice, insights and feedback. Professor Christian Rytka, for fully investing himself in order to create for me the best possible working conditions. Professor Clemens Dransfeld, for his availability, interesting inputs and the friendly discussions despite his remote location. Professor Christian Brauner, for his advice and sharing different toolings that allowed me to gain precious insights for my research. I am convinced that my supervisors had the biggest influence in making my PhD a positive experience, providing my guidance, sharing knowledge and experience but also giving me the freedom to pursue my own path and ideas.

Many people at work contributed to make my life easier or more pleasant, and for that I am very grateful: Dennis, who was always ready to help or give support. Dani, who burned his fingers many time while helping me but always remained very calm about it. Halime, who was very patient with me putting her carefully designed tools at very elevated temperatures, in the vacuum, and sometimes even making them explode. Sabine, who spent quite some time dealing with the complicated administrative paperwork. Igor, for the support with Comsol, the exciting exchanges and his friendship. The whole LPAC team, which was always readily helped me with my experiments at EPFL. Many more people helped me in different ways, and I would like to warmly thank all of them. My PhD was definitely made better thanks to the positive and friendly atmosphere at work, the nice exchanges during the (lucrative) coffee breaks or lunches, but also the time spent together outside work. These interactions with people having such a diverse background definitely enriched me on a daily basis. On some days I would have insightful exchanges which helped me to grow as a person, and on some other days 🍷omas would tell me about gold-plated nuclear bombs.

I would like to thank my incredible family for always standing by my side and for all the love. I am very grateful to my parents for always encouraging me to follow my own path, to my dad for always having been an example for me and to my mom for the unconditional love and support. I would like to thank Alison for patiently looking with mild interest at my fitting graphs and not killing me over it. Special thoughts to my brother, who unfortunately left us. Hopefully you will enjoy life in Canada. I am very happy to have Ziemniaku by my side, messing with me on a daily basis, and going with me on adventures whenever possible. A big shout-out to all my friends, without whom life would not be as colourful and fun, and to "the last of us" without which it would not be as based. Special thanks to Lino for the many years of shared friendship, and whomst showed me that the autistic side of the force is a pathways to many abilities some might consider... unnatural.



# Abstract

Side-by-side hybrid textiles are an intermediate step for the production of fibre-reinforced thermoplastic composites. Press moulding these materials combining reinforcing fibre textiles and thermoplastic matrix textiles or flexible layers is a promising method to produce high-end fibre-reinforced thermoplastic composites parts with complex geometry at relatively short cycle times and lower costs. Since most of the established manufacturing methods for fibre-reinforced thermoplastic composites can only produce parts with limited complexity, press moulding of hybrid textiles could broaden the manufacturing capabilities and offer a whole new set of possibilities. However, the current lack of three-dimensional consolidation model prevents the establishment of this technology, as appropriate design and process parameters cannot be determined and defect formation cannot be predicted.

This thesis presents the development of a three-dimensional consolidation model for press moulding of hybrid textiles. First, a literature review is presented to identify the limits of models addressing effects relevant for consolidation. A model for the stress response of textile stacks, which is an effect taking place during consolidation, is validated and a numerical approach to characterize the model parameters is presented. Then, a novel consolidation model for hybrid textiles including air entrapment, dissolution and diffusion is developed and validated experimentally using glass reinforcements and polypropylene or polyethylene matrices. Direct measurement validates the model of Gebart for permeability, a key model parameter, at very high fibre volume fractions and it is shown that entrapped air significantly influences impregnation. Finally, the model is extended in three-dimensions with some restrictions by considering a free-form plate with non-uniform thickness. By adopting a unit-cell approach with three-phase flow, it is possible to take into account the volume change resulting from matrix flow and impregnation, and by adopting a homogenization method the computational challenges of a full-scale simulation can be bypassed. This novel consolidation model provides insights to explain the fiber movement in non-uniform thickness plates, enables part and process optimization, and paves the way for high-quality composite part production.





# Zusammenfassung

Side-by-Side-Hybridtextilien sind Zwischenprodukte auf dem Weg zur Herstellung von faserverstärkten thermoplastischen Verbundwerkstoffen. Das Pressformen dieser Materialien, bei dem verstärkende Fasertextilien und thermoplastische Matrixtextilien oder flexible Schichten kombiniert werden, ist eine vielversprechende Methode, um hochwertige faserverstärkte thermoplastische Verbundwerkstoffteile mit komplexer Geometrie mit relativ kurzen Zykluszeiten und geringeren Kosten herzustellen. Mit etablierten Fertigungsverfahren für faserverstärkte thermoplastische Verbundwerkstoffe lassen sich nur Teile mit begrenzter Komplexität herstellen. Aus diesem Grund könnte das Pressformen von Hybridtextilien die Fertigungsmöglichkeiten erweitern und eine ganze Reihe neuer Möglichkeiten bieten. Jedoch fehlt derzeit ein dreidimensionales Konsolidierungsmodell, was die Etablierung dieser Technologie verhindert, da geeignete Design- und Prozessparameter nicht bestimmt und die Fehlerbildung nicht vorhergesagt werden können.

In dieser Arbeit wird die Entwicklung eines dreidimensionalen Konsolidierungsmodells für das Pressformen von Hybridtextilien vorgestellt. Zunächst wird eine Literaturübersicht präsentiert, um die Grenzen von Modellen zu ermitteln, die für die Konsolidierung relevante Effekte berücksichtigen. Da das Spannungsverhalten von Textilien die Konsolidierung beeinflusst, wird ein dafür geeignetes Modell validiert und ein numerischer Ansatz zur Charakterisierung der Modellparameter wird vorgestellt. Anschließend wird ein neuartiges Konsolidierungsmodell für Hybridtextilien entwickelt und experimentell mit Glasfasern und Polypropylen oder Polyethylen validiert. Dieses Modell berücksichtigt Lufteinschlüsse, Diffusion und Löslichkeit der Luft im Matrixmaterial. Dabei validieren direkte Messungen das Modell von Gebart für die Permeabilität, einem Schlüsselparameter, bei sehr hohen Faservolumenanteilen, und es wird gezeigt, dass eingeschlossene Luft die Imprägnierung erheblich beeinflusst. Schliesslich wird das Modell mit einigen Einschränkungen auf drei Dimensionen erweitert, indem eine Freiformplatte mit ungleichmässiger Dicke berücksichtigt wird. Durch die Anwendung eines Einheitszellenansatzes mit Dreiphasenströmung ist es möglich, die aus der Matrixströmung und der Imprägnierung resultierende Volumenänderung zu berücksichtigen, und durch die Anwendung einer Homogenisierungsmethode können die Herausforderungen einer rechnerischen massstabgetreuen Simulation umgangen werden. Dieses neuartige Konsolidierungsmodell liefert Erkenntnisse, um Faserverschiebung in Platten mit variabler Dicke zu erklären, ermöglicht eine Bauteil- und Prozessoptimierung und ebnet den Weg für die Herstellung hochwertiger Verbundwerkstoffteile.



# Contents

<b>Acknowledgements</b>	<b>i</b>
<b>Abstract</b>	<b>iii</b>
<b>Zusammenfassung</b>	<b>v</b>
<b>1 Introduction</b>	<b>3</b>
1.1 Objectives . . . . .	9
1.2 Approach . . . . .	10
1.3 Dissertation outline . . . . .	11
<b>2 State-of-the-Art</b>	<b>13</b>
2.1 Impregnation . . . . .	13
2.2 Viscosity . . . . .	15
2.3 Permeability . . . . .	16
2.4 Air evacuation, entrapment and dissolution . . . . .	23
2.5 Fibre disorientation . . . . .	24
2.6 Textile stress response . . . . .	26
2.7 Impregnation & consolidation models . . . . .	29
<b>3 Materials and material characterization</b>	<b>33</b>
3.0.1 Thermoplastics . . . . .	33
3.0.2 Reinforcing fibres . . . . .	36
<b>4 Textile stress response</b>	<b>41</b>
4.1 Materials and methods . . . . .	43
4.1.1 Materials . . . . .	43
4.1.2 Experimental test setup . . . . .	43
4.1.3 Experimental testing procedure . . . . .	44
4.1.4 Model approach . . . . .	45
4.1.5 Model accuracy . . . . .	49
4.2 Results . . . . .	50
4.2.1 Materials . . . . .	50
4.2.2 Definition of model parameters . . . . .	50
4.2.3 Influence of strain deviations . . . . .	59
4.3 Summary . . . . .	62

<b>5</b>	<b>Consolidation model</b>	<b>65</b>
5.1	Model approach . . . . .	68
5.1.1	Process description . . . . .	68
5.1.2	Initial conditions . . . . .	68
5.1.3	Impregnation . . . . .	69
5.1.4	Gas Diffusion and dissolution . . . . .	71
5.2	Materials and material characterization . . . . .	72
5.2.1	Tow permeability . . . . .	74
5.3	Methods . . . . .	76
5.3.1	Experimental test setup . . . . .	76
5.3.2	Analysis . . . . .	77
5.4	Results . . . . .	77
5.5	Discussion . . . . .	81
5.6	Summary . . . . .	85
<b>6</b>	<b>Three-dimensional extension</b>	<b>87</b>
6.1	Approach . . . . .	90
6.2	Constitutive equations . . . . .	91
6.2.1	Medium descriptors . . . . .	91
6.2.2	Constitutive equations . . . . .	92
6.2.3	Consolidation model . . . . .	92
6.2.4	Boundary conditions . . . . .	94
6.2.5	Initial conditions . . . . .	95
6.3	Materials and material characterization . . . . .	96
6.4	Case study . . . . .	97
6.5	Experimental verification . . . . .	99
6.6	Discussion . . . . .	102
6.7	Summary . . . . .	104
<b>7</b>	<b>Summary and outlook</b>	<b>105</b>
<b>Appendix</b>		<b>109</b>
A	Initial amount of entrapped air . . . . .	109
B	Fibre volume fraction . . . . .	110
C	Derivation of fibre volume fractions . . . . .	111
D	Matrix volume change . . . . .	112
E	Derivative of impregnation degree . . . . .	114
F	Derivative of thickness . . . . .	114
G	Initial conditions . . . . .	115
H	Additional Pictures . . . . .	115
<b>List of symbols</b>		<b>138</b>
<b>Publications</b>		<b>143</b>

**Curriculum Vitae**

**145**



# Chapter 1: Introduction

The unending pursuit of product enhancement drives mechanical engineers and scientists around the world to achieve unprecedented levels of lightness, strength, and rigidity. Similarly, constant efforts to refine manufacturing processes lead to heightened efficiency, reliability, and reduced production costs. Product and process optimization are sought by the industry and larger public alike, as they are undeniably linked to superior and more affordable products. Design optimization is one of the methods available for product optimization, it traditionally consists in choosing the right materials and optimally distributing it in space with regard to a given objective, in accordance with a given objective [1]. For instance, the objective may entail reducing the weight of a product while preserving its structural integrity, or maximizing its stiffness without adding weight. Figure 1.1 showcases a stunning example of optimization, wherein the weight of a jet engine bracket is minimized without compromising its structural capacity.



Figure 1.1: Showcasing of the comprehensive optimization process of a jet engine bracket, spanning from the top left to the bottom right. The first image depicts the original design utilized in commercial aircraft, while the final image displays the weight-optimized component, attaining significant weight reduction [2].

Structural optimization of fibre-reinforced composites is drastically more complex because of their pronounced anisotropy, which denotes that their mechanical properties are direction-dependent [3]. Therefore, in addition to efficient material distribution in space, internal design optimization is required to ideally choose fibre orientation in each layer of the composite. Furthermore, other parameters such as fibre volume content, signifying the volumetric percentage of fibres within the composite, or weaving architectures (in the case of woven reinforcements) also profoundly impact mechanical properties and necessitate optimization. Figure 1.2 illustrates the internal morphology of a composite and its internal parameters that undergo modification during internal design optimization.

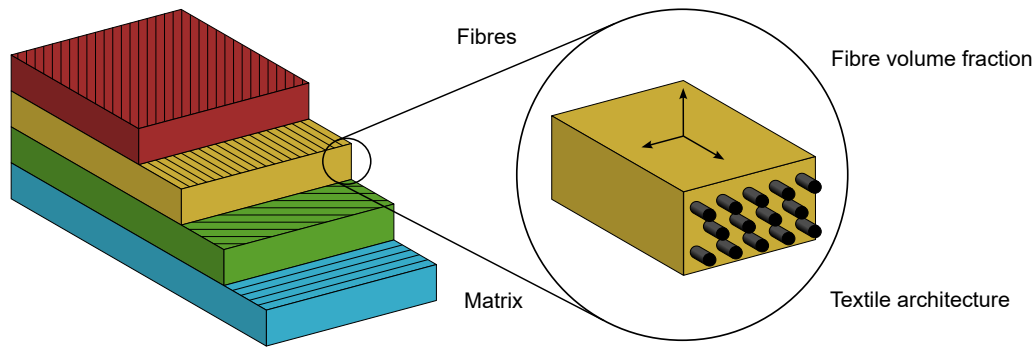


Figure 1.2: The composite material comprises numerous stacked layers, illustrated schematically on the left-hand side, with each layer possessing a predetermined fiber orientation, fiber volume fraction, and textile architecture, as portrayed in the close-up on the right. During internal optimization, each of these parameters is subject to modification, with the ultimate goal of enhancing the material’s mechanical properties.

Even though challenging, methods have been developed to optimize, to a certain extent, both the geometry and the internal design of the part with regard to a given objective. A prime example of such an approach is demonstrated in Figure 1.3, which showcases the application of genetic algorithms to design lightweight wind turbine blades. In that work, genetic algorithms were first used to optimize the laminate shell skin, subsequently the topology of the shear webs were optimized and finally the optimal shape of the blade was found through inverse geometrical design.

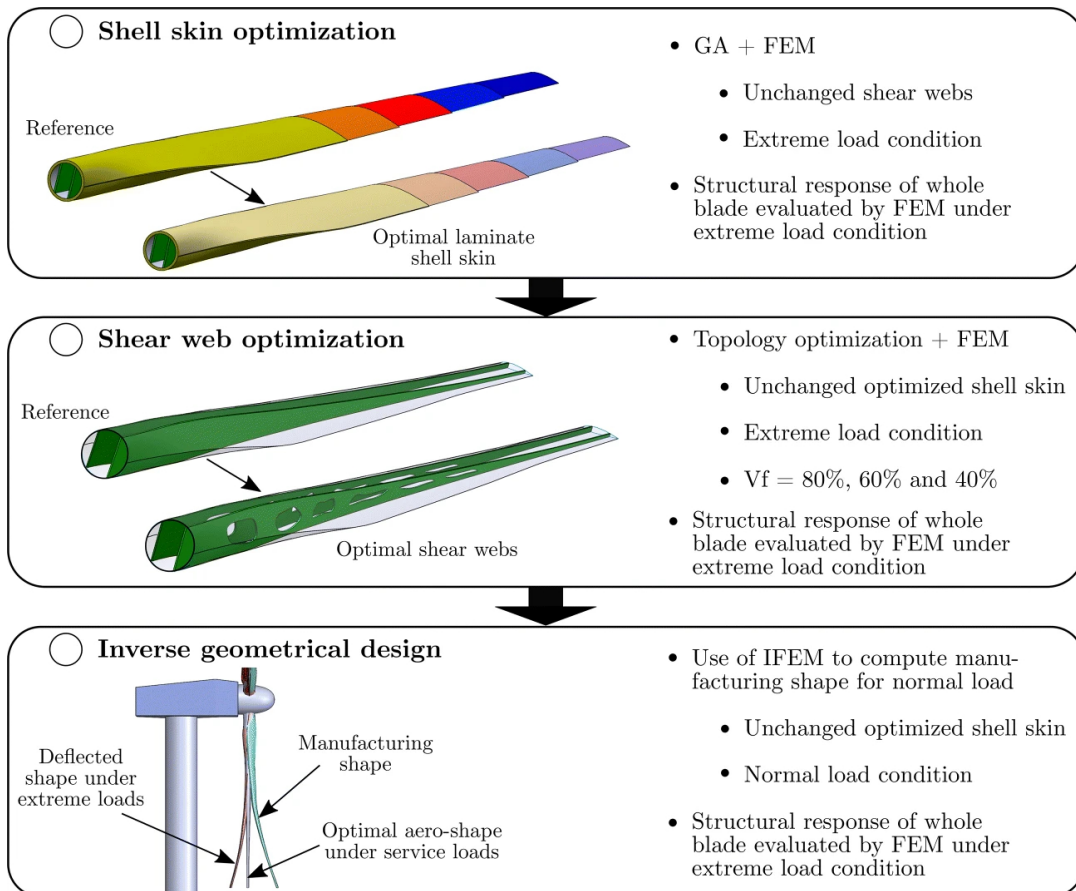


Figure 1.3: Methodology to design lightweight composite wind turbine blades as presented by Albanesi et al. [4].



Nevertheless, knowing the optimal design and producing it are two different matters, which is why structural optimization is bound by manufacturing capabilities. When it comes to fibre-reinforced composites, the geometrical complexity that can be achieved is inextricably linked to the production process. Consequently, for the creation of top-of-the-line, high-performance components, manufacturing techniques that permit complex shapes and sophisticated structural optimization are necessary.

Diverse manufacturing methods exist for the production of fibre-reinforced composites, which are commonly classified based on the matrix system used to hold the fibres together. In the case of thermosetting resins, a hardener causes polymer chains to cross-link during curing, which is an irreversible process [5]. Thermoplastic resins can undergo reversible phase changes between solid (glassy or semi-crystalline), rubbery and molten states [6]. As a result, fibre-reinforced thermoplastics (FRTP) can be welded and even recycled, albeit the recycling technologies are not mature yet [7]. Moreover, FRTP exhibit superior chemical resistance and potential for high-volume production compared to thermoset composites, which typically require several hours for curing. However, the production of FRTP poses challenges due to the high viscosity of thermoplastics, necessitating elevated temperatures and pressures, in processes such as compression moulding. Nevertheless, an increasing attention is given to FRTP due to their compelling advantages.

Although decades of research have been dedicated to fibre-reinforced composites, the production processes are not yet fully mastered, although significant breakthroughs occur on a regular basis. For instance, the successful manufacture of the first-ever large thermoplastic composite wind blade [9] and the production of a thermoplastic composite fuselage demonstrator as part of the European Clean Sky 2 project, depicted in Figure 1.5, are noteworthy achievements. Currently, the production of fibre-reinforced thermoplastics mostly relies on processes using pre-impregnated intermediate materials. For example, tapes are employed in automated tape laying and thermoforming is executed with organosheets. The methods mentioned above are plagued by the high costs of semi-finished products, their ability to produce parts with intricate geometries

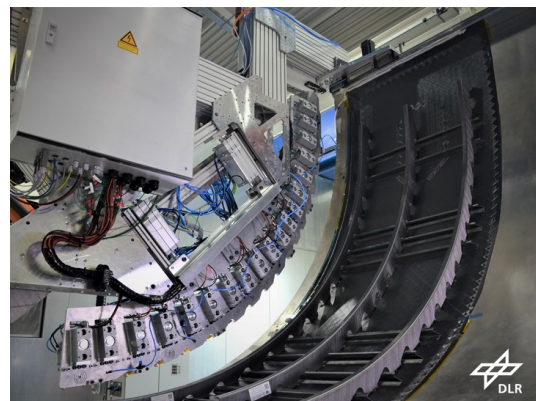


Figure 1.4: Picture of the automated tape laying process for the production of the upper shell fuselage skin section of an Airbus A350. A robotic arm continuously heats, places and consolidates layers of tapes to produce the desired geometry. While ATL is currently mostly used with thermoset composites, recent progress enables its application to thermoplastic composites as showcased in Figure 1.5.

Figure 1.5: Picture of the full-scale FRTP upper fuselage demonstrator produced within the Clean Sky 2 project along with the machinery for assembly. Continuous ultrasonic welding and resistance welding were leveraged to weld stringers and C-frames to the in-situ consolidated composite skin with integrated lightning strike protection [8].

is limited, and the restrained diversity of organosheets available on the market limit the internal design freedom. Automated tape laying for instance, illustrated in Figure 1.4, can only produce double-curved shells with very large curvature radii.

Other manufacturing routes for FRTP commonly rely on hybrid systems, meaning that the fibres and thermoplastic are blended at different scales, as represented in Figure 1.6. While in hybrid rovings the blending takes place at the microscopical scale, in hybrid textiles and side-by-side hybrid textiles it occurs at the mesoscopical scale. Generally speaking, a more intimate hybridization such as in commingled yarns reduces the consolidation time as the matrix flow lengths are reduced. However, the additional mingling step results in higher production costs, especially if an intimate mingling is sought. One of the drawbacks of hybrid textiles is that they can possibly lose their structural integrity during processing, since matrix rovings melt and no longer contribute to fabric stability. Hybrid side-by-side textiles do not suffer from this drawback, and offer a very elevated design freedom as most of the parameters can easily and locally be changed. In addition, using flexible thermoplastic plies such as veils increase drapeability and facilitates the production of semi-complex parts.

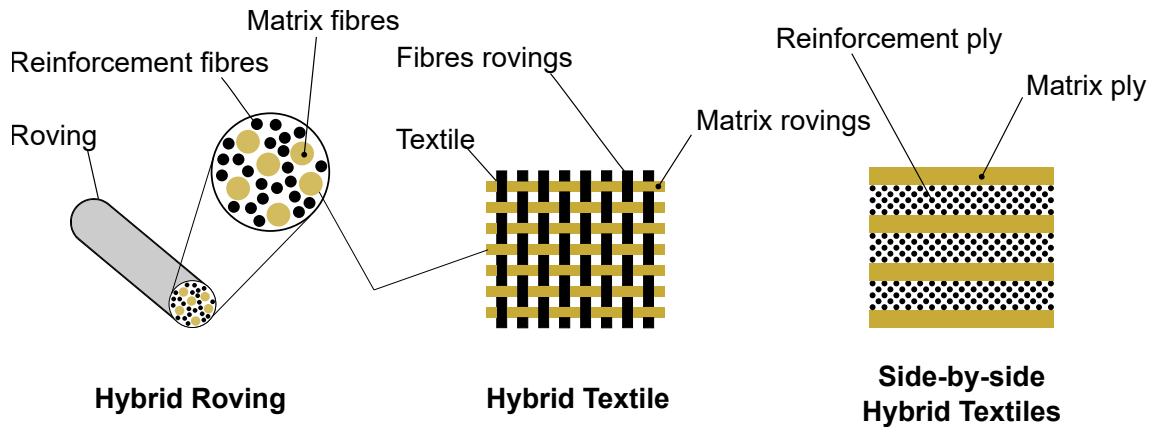


Figure 1.6: Classification of hybrid materials.

Recently, Reynolds et al. [10] investigated rapid isothermal stamp forming of multilayered textile and thermoplastic veils and proved that this process could produce structural parts within a cycle time of 330 s. During isothermal stamp forming, the fabric is preheated to soften the polymer, then transferred to the hot tool where it is draped and consolidated isothermally through the stamping process before being rapidly cooled down under pressure. A similar process suitable for the consolidation of hybrid textiles is press moulding, in which the composite placed into a mould is consolidated in a press. Compared to rapid isothermal stamp forming, press moulding can produce more complex geometries, however in such cases draping can not simply be done by closing the mould and might have to be done by hand. Variants of press moulding include two-stage press moulding, in which one hot stage is used for consolidation and one cold stage is used for cooling down under pressure. This enables faster cycle times, as the whole press does not need to be heated up and cooled down for each cycle. Another variant is rapid variothermal mould pressing, in which the part is consolidated in a press with rapid heating and cooling capabilities. In rapid variothermal mould pressing heating and cooling gradients are controlled, which could reduce defects related to inhomogeneous cooling such as warping.

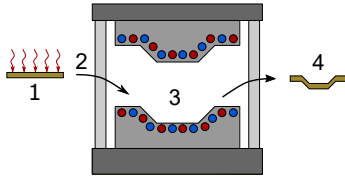


Figure 1.7: Schematic representation of the rapid isothermal stamp forming process: 1) heating of the fabric 2) transfer to the heated isothermal press 3) pre-forming and consolidation 4) cooling down and demoulding.

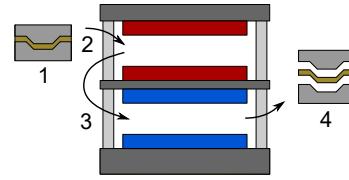


Figure 1.8: Schematic representation of the two-stage press moulding process: 1) draping 2) transfer to the hot stage and consolidation 3) displacement to the cold stage and cooling down 4) demoulding.

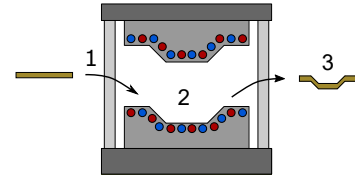


Figure 1.9: Schematic representation of the rapid variothermal mould forming process: 1) draping in the mould 2) heating up, consolidation and cooling down 3) demoulding.

Despite the increased geometrical complexity and potentially lower costs at relatively fast cycle times, press moulding of hybrid textiles is barely established in the industry due to the lack of appropriate consolidation models, especially three-dimensional ones. As a consequence, process parameters such as consolidation pressure and consolidation time must be found empirically. Worse, defects such as porosity or fibre disorientation cannot be predicted, especially for complex geometries. As a result, part and process design is exceedingly difficult and requires time-consuming and costly trial-and-error. Hence the risks, difficulties and effort represent a considerable burden, which prevents establishment of the technology in the industry.

What is exactly consolidation? Although quite intuitive to understand and widely used, surprisingly no rigorous definition of consolidation was formulated for composite processes, whereas its meaning is well defined in soil sciences. In this thesis and for press moulding, consolidation is loosely defined as the set of processes taking place when pressure is applied on the stack formed of the textile, the molten matrix and air. This implies that effects taking place before, for example air evacuation (if any), or after, for example warping, are not part of it. Consolidation can be understood as consisting of the accumulation and interplay of different physical processes arising both at the micro and macro scale. Perhaps the most important is matrix flow, which is referred to as impregnation if the matrix flows into previously dry areas. If air or gas is trapped into the composite, the applied pressure will trigger diffusion of the gas into the molten polymer, reduce the bubble size and eventually collapse it. If the pressure gradients at the meso scale become too large, matrix flow will begin to drag the fibres along with them, resulting in fibres disorientation. A schematic representation of consolidation is shown in Figure 1.10.

While the different phenomena constituting consolidation are mostly well known and understood, reliable three-dimensional consolidation models are still lacking. This is unfortunate, as such a model is necessary for a proper implementation of the press moulding of thermoplastic composites at an industrial scale. Combining press moulding with hybrid textiles could facilitate the production of high-end semi-complex thermoplastic composites, reduce costs, and overall enable new possibilities and applications.

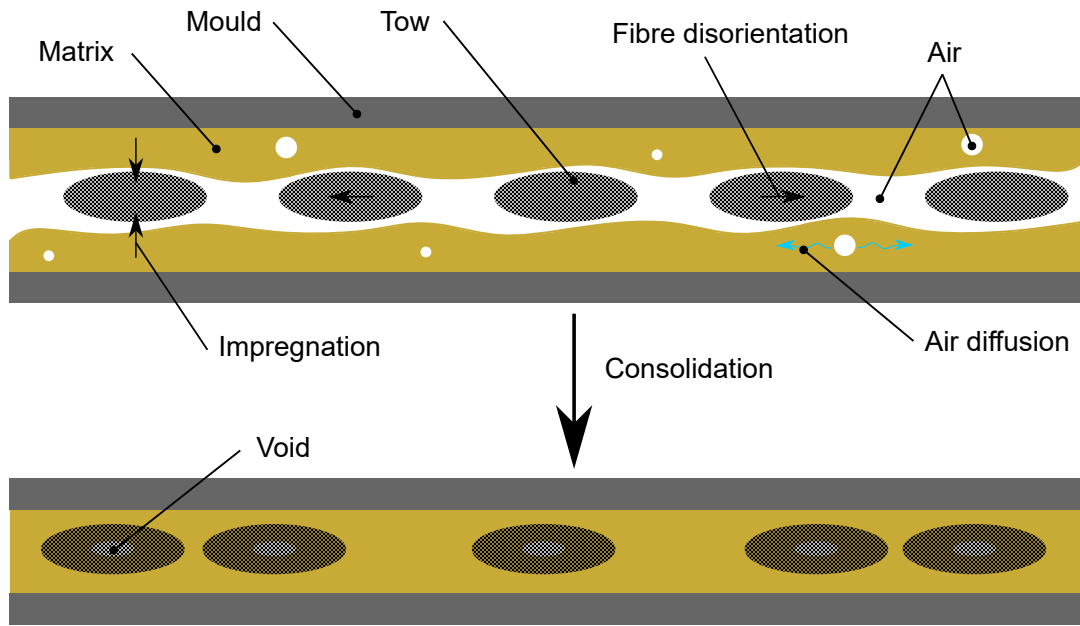


Figure 1.10: Schematic representation of consolidation.

## 1.1 Objectives

The objective of this work is to develop a three-dimensional consolidation model for press moulding of hybrid textiles, which is suitable for finite-element analysis (FEA). This model intends to enable first time right design and process parameters setting for the press moulding of hybrid textiles for complex parts, which could thus become attractive for the industry.

The current state-of-the-art consolidation of hybrid textiles is represented in Figure 1.11a, where a stack with given shape and internal geometry is subjected to a standard consolidation cycle. For complex shapes, defects such as depicted on the right might happen, which the consolidation model developed within this work intends to predict. Ultimately, optimizing both design and process would allow the production of defect-free parts as pictures in Figure 1.11b. Taking advantage of the vast design freedom of hybrid textiles, this would enable the production of extremely optimized, high end parts. While process and design optimization of press moulding of hybrid textiles for high-end applications are not part of the objectives of this work, it is intended to pave the way towards it.

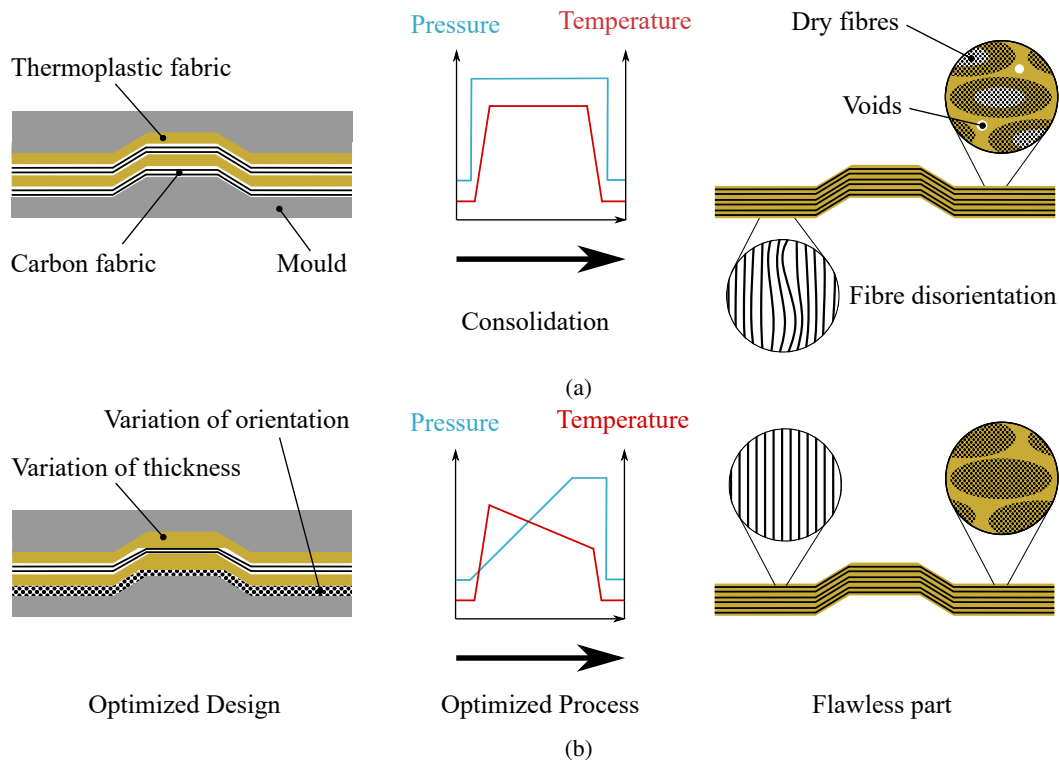


Figure 1.11: **1.11a:** Representation of state-of-the art consolidation of hybrid textiles. For complex shapes defects such as depicted on the right might happen. The simulations models developed in this thesis will enable the prediction of such defects. **1.11b:** Representation of an optimized consolidation process where appropriate selection of the design and process parameters prevents defect formation.

This work is part of the collaborative project "Consolidation of Thermoplastic hybrid yarn materials (ConThP)", together with the Faserinstitut Bremen in Germany. The project foresees the implementation of the three-dimensional consolidation model developed in this thesis for tailored fibre placement of high-end fibre-reinforced thermoplastics. This project was funded by the German Research Foundation [394279584] and the Swiss National Science Foundation [200021E/177210/1].

## 1.2 Approach

Developing a three-dimensional consolidation model is challenging, since different effects influence each other and the volume is not conserved as voids get filled during impregnation. Therefore, simply adding the models for the different phenomena taking place during consolidation is not possible. Developing a full-scale simulation is also difficult due to the multi-scale nature of the process, which represents a formidable computational challenge. Moreover, the complex interactions between textile, matrix and air at both the micro and macro level makes their description difficult. Wysocki et al. attempted to model consolidation with a two-phase continuum framework and entropy inequality [11]–[13], a similar approach was followed by Rouhi et al. [14]–[16]. In both cases, the difficulty to determine the values of variables related to the entropy inequality equation make their implementation challenging in practice.

In this work, a homogenization method based on a unit cell approach and a consolidation model is adopted to describe the three-dimensional consolidation of thermoplastic composites, which avoids the need for numerically expensive full-scale simulations at both the macro and micro level. Instead, finite element analysis is performed only on the homogenized medium at the macro level only. Despite this simplification, the state of the homogenized medium remains well described by a set of descriptors as shown in Figure 1.12. Furthermore, knowledge about the architecture of the textile allows to reconstruct, to some extent, the microstructure of the composite. By describing the temporal change of descriptors through established physical laws rather than entropy inequality equations, the difficulty to determine the values of the variables can be tackled. For this, a set of experiments were carried out with model thermoplastic polymers films such as polypropylene and polyethylene and a glass fibre textile, so as to calibrate and verify the modelling approach.



Figure 1.12: Schematical representation of the thermoplastic composite at the meso scale on the left, and the corresponding homogenized medium with descriptors on the right: the impregnation degree  $\xi$ , the fibre volume content  $\nu_f$ , the matrix volume content  $\nu_m$  and the void volume content  $\nu_v$ .

### 1.3 Dissertation outline

It is of prime importance to have a clear overview of the state-of-the-art about the different phenomena taking place during consolidation, since the consolidation model will be built upon it. The state-of-the-art is presented in Section 2, thereby an emphasis is placed on underlining the advantages and limitations of the different models. The materials used in this study and their characterization are presented in Section 3.

In Section 4 a suitable viscoelastic model for the dry textile stress response is validated in lubricated conditions, so that it can later be incorporated in the consolidation model. Then, a numerical approach to characterize the viscoelastic fibre bed stress response is presented. In this work, it is also shown that deviations from the prescribed strain have a significant effect on viscoelastic parameter extraction. This chapter is based on a publication [17].

Section 5, which is also based on a publication [18], presents a novel consolidation model for hybrid textiles, in which air entrapment, dissolution and diffusion in the molten polymer are considered. One of the key parameters of the model is tow permeability, which is described by the analytical model of Gebart and validated at very high fibre volume fractions by direct tow permeability measurement. The model offers new and comprehensive insights about the phenomena taking place during consolidation.

This consolidation model is then extended towards 3D in Section 6 by adopting a unit-cell approach and homogenizing the medium to bypass the multi-scale nature of the problem. Implementation in Finite-Element-Method (FEM) shows how in-plane matrix pressure gradients can arise in parts and cause fibre disorientation. An article based on this chapter was submitted and will be the object of a publication. Finally, a conclusion and an outlook are presented in Section 7.





# Chapter 2: State-of-the-Art

This chapter aims at giving an overview of the state-of-the-art and of the available models that describe effects relevant for the consolidation of hybrid textiles, to which the discussion is limited. Because the phenomena taking place during consolidation are not unique to hybrid textiles, many of the models presented here were originally developed for other processes. Therefore, for each of the underlying phenomena the most relevant models and pieces of work will be presented with an emphasis on the advantages and limitations of each.

In this chapter, first the state-of-the-art of impregnation will be addressed in section 2.1, then viscosity, permeability in sections 2.2 and 2.3 respectively, the aspects related to air evacuation, entrapment and dissolution in section 2.4, fibre disorientation and textile stress response in the sections 2.5 and 2.6 and finally an overview of the current models about impregnation and consolidation will be given in section 2.7.

## 2.1 Impregnation

Impregnation can be understood as the act of wetting the fibres, which requires matrix to flow to previously dry locations. It is common to distinguish between flow at the meso level, which is taking place in the fabric between the fibre bundles, and flow at the micro level, which is taking place in the fibre bundle themselves. For both Darcy's law, formulated in Equation 2.1.1 is used in the vast majority of the cases [19]. In this equation  $q$  is the volumetric flux of the fluid,  $K$  is the permeability,  $\eta$  the fluid viscosity and  $P$  the pressure. Relating the flux discharge with fluid velocity  $v$  through porosity  $\phi$  yields Equation 2.1.2:

$$q = -\frac{K}{\eta} \nabla P \quad (2.1.1)$$

$$v = -\frac{K}{\eta\phi} \nabla P \quad (2.1.2)$$

Darcy's law as written here is valid for incompressible and creeping saturated flows. For sharp flow fronts it is possible to apply Darcy's law only in the saturated region to describe analytically unsaturated flow, which is a common approach when this type of solutions are sought. Another method is to use Richard's equation, which extended Darcy's equation to unsaturated flows by introducing saturation  $S$  defined in Equation 2.1.3 and describing it as a function of pressure. Neglecting gravity and assuming that permeability  $K$  is independent of saturation the equation may be written as in Equation 2.1.4 [20], [21]:

$$S = \frac{V_l}{1 - V_f} \quad (2.1.3) \quad c(p) \frac{\partial P}{\partial t} - \nabla \cdot \left( \frac{K k_r}{\eta} (\nabla P) \right) = 0 \quad (2.1.4)$$

whereas  $V_l$  is the volume occupied by the liquid,  $V_f$  the volume occupied by the fibres and  $c(p)$  is the so-called moisture capacity. The left term of Equation 2.1.4 describes the temporal change of saturation and  $k_r$  is a factor between 0 and 1 relating the change of permeability in function of the saturation. In this approach the flow front is not sharp and its shape, meaning how the saturation evolves across the flow front as a function of pressure, depends on the  $c(p)$ . Authors such as van Genuchten [22] proposed models to describe this function, however it requires to determine four parameters beforehand. Authors such as Klunker [23] neglected the dependance of the permeability on saturation by setting the relative permeability  $k_r$  to 1 and proposed a simplified model for the moisture capacity requiring only one parameter  $\alpha$  by assuming the shape of the function. The advantage of this approach, besides its simplicity, is that by letting the parameter  $\alpha$  tend towards infinity the flow front becomes sharp as shown in Figure 2.1. In practice this cannot be done in FEM because a sharp flow front causes numerical instabilities, however by selecting appropriate  $\alpha$  values and element sizes good approximations of the sharp flow front case can be obtained.

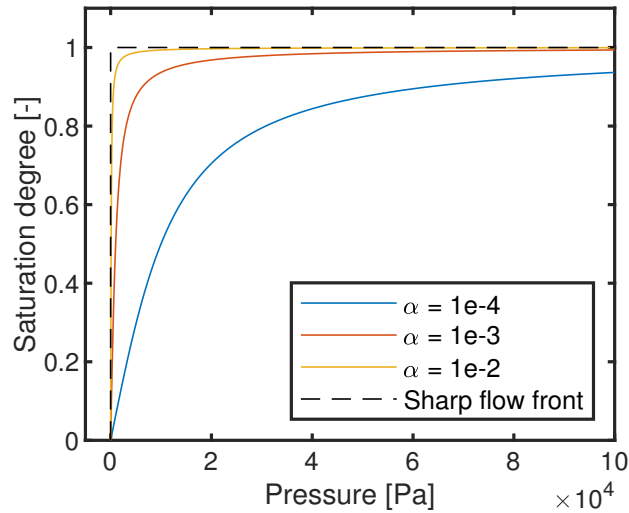


Figure 2.1: Saturation in function of the pressure according to the model of Klunker for different values of the  $\alpha$  parameter and for a sharp flow front.

Several models dealing with the infiltration of fibre bundles assume a sharp flow front, which is often referred to as the so-called slug flow assumption. A micrograph of the flow front in unidirectional carbon fibre tapes presented by Jespersen et al. [24] and in tows presented by Studer et al. [25] for instance both suggest validity of this assumption. However, for unsaturated flow in other media at the meso level such as textiles, a partially saturated flow front emerges and needs to be considered for a correct description of the flow behaviour. An extensive literature study was presented by Michaud in [26] for unsaturated flow in Liquid Composite Moulding (LCM). Two main strategies are reviewed, the first one is based on the multiphase flow equation as presented above, which bases on Richard's equation. The second one is an indirect approach with solutions based on saturated flows and the introduction of a sink term, such approaches were adopted for instance by Wolfrath et al. [27].

## 2.2 Viscosity

Description of impregnation requires knowledge about the viscosity, which is for polymers temperature and shear rate dependent. The viscosity  $\eta$  of molten thermoplastics in function of the shear rate  $\dot{\gamma}$  is usually characterized by a first Newtonian range at low shear rates followed by a shear thinning range. Within the first Newtonian range the viscosity takes a constant value  $\eta_0$  which is referred to as the zero-shear viscosity. At more elevated shear rates the molecules orient themselves to some extent in the flow direction, which results in some disentanglement lowering their flow resistance and causing the shear-thinning behaviour [28] [29]. To describe this behaviour the models of Cross [30] and Carreau [31] are commonly used, these are shown respectively in Equation 2.2.1 and 2.2.2.

$$\frac{\eta(\dot{\gamma})}{\eta_0} = \frac{1}{1 + (A_{\dagger} \cdot \dot{\gamma})^{B_{\dagger}}} \quad (2.2.1) \quad \frac{\eta(\dot{\gamma})}{\eta_0} = \frac{1}{(1 + (A_{\diamond} \cdot \dot{\gamma}^2))^{B_{\diamond}}} \quad (2.2.2)$$

whereas  $A_{\dagger}$ ,  $B_{\dagger}$ ,  $A_{\diamond}$  and  $B_{\diamond}$  are model parameters. The viscosity also depends on temperature as at more elevated temperatures the increased kinetic activity makes it easier for the molecules to overcome internal flow resistance caused by the friction of neighbouring molecules [29]. The viscosity of molten polymers in function of the temperature can be described by an Arrhenius type function [32] [33].

$$\eta(T) = A_{arrh} e^{-\frac{B_{arrh}}{T}} \quad (2.2.3)$$

whereas  $A_{arrh}$  and  $B_{arrh}$  are model parameters. Figure 2.2 schematically represents the viscosity behaviour of polymers. In Figure 2.2a the viscosity in function of the shear rate is displayed at different temperatures, one can see that towards lower shear rates the viscosity approaches a constant value -the zero-shear rate  $\eta_0$ - and that shear thinning mainly affects higher shear rates. Figure 2.2b then shows how the dependence of the zero-shear rate on temperature.

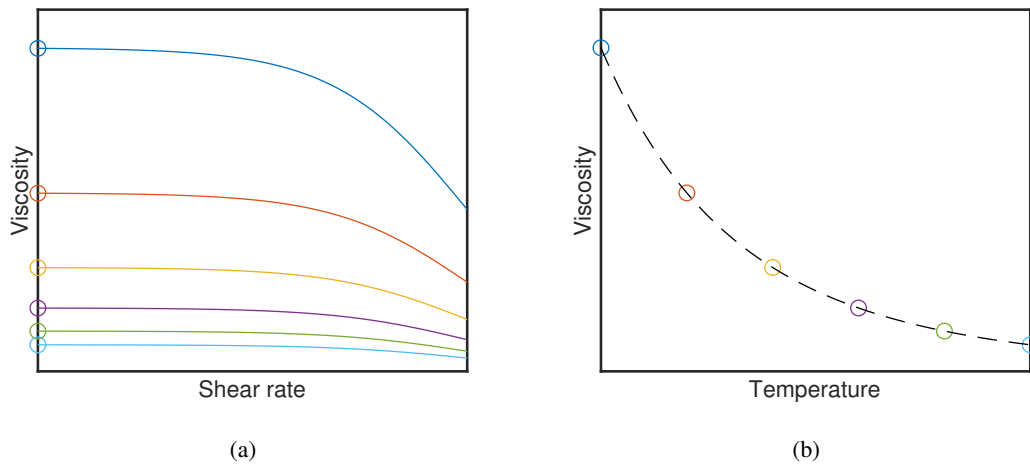


Figure 2.2: a) representation of how the viscosity evolves in function of the shear rate according to the model of Cross at different temperatures. The viscosity at low shear rates tends to the zero-shear viscosity, which is represented in function of the temperature in b) following an Arrhenius function. The zero-shear viscosity at different temperatures is represented in both Figures with circles.

During the manufacture of thermoplastic composites the elevated viscosity result in very slow flow speeds and shear rates. Bernet et al. [34] found that, for the consolidation of carbon fibres and PA12 commingled yarns, the shear rate was low enough to neglect shear thinning and assume the viscosity to be well described by the zero-shear viscosity. Seo et Lee [35] investigated the impregnation of carbon tows with polyetheretherketone (PEEK) and claim that shear thinning should be considered as it amounts to about 20% of differences in viscosity. In the literature however, most of the authors disregarded this effect and the zero-shear viscosity was mostly adopted without any further justification.

## 2.3 Permeability

Understanding the mechanisms ruling the permeability of textiles and correctly modelling them is a prerequisite for a good description of the impregnation behaviour, and has been the object of many researches for that reason. Broadly speaking two cases arise depending on whether the medium is homogeneous at a meso scale or not, these are schematically represented in Figure 2.3. Typically for woven fabrics the flow mainly takes place in the inter tow spaces but also through the tow themselves where the flow resistance is however much higher due to the smaller channel size, which results in a dual scale flow. This effect does not take place in fibrous reinforcement with more uniform pore distribution, such as nonwoven fabrics or inside the fibre tows. In any case the permeability of fibrous reinforcements strongly depends on their porosity, as changing the available space for the fluid to flow directly affects the flow resistance. Hence, most of the models predict the permeability as a function of the fibre volume fraction.

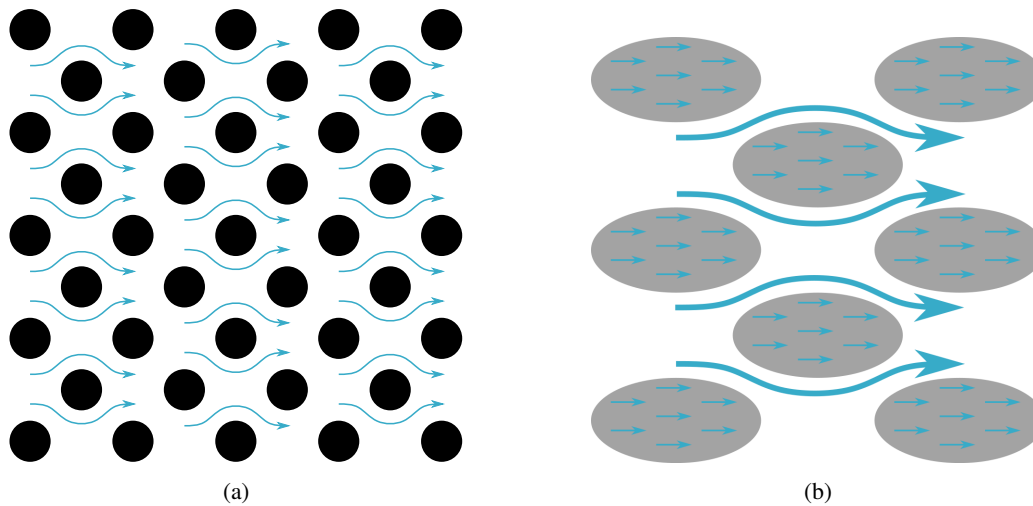


Figure 2.3: Figure 2.3a represents the case where the flow is homogeneous at the meso scale while Figure 2.3b depicts a dual scale flow.

A large body of work is found for modelling the permeability and a variety of systems and conditions has been described. The popular Kozeny-Carman model [36] for instance was originally developed for granular beds with isotropic distribution. Many models considered aligned cylinders, some were developed for dilute systems while others focussed on close packed geometries, some are based on a lubrication approach and others on drag, many predict transverse permeability only, a few are valid for non-newtonian fluids. Among these models one can cite

the modified Kozeny-Carman equation presented by Gutowski [37], the models of Happel [38], Drummond and Tahir [39], Sparrow and Loeffler [40], Kuwabara [41], Sangani and Acrivos [42], Gebart [43], Hasimoto [44], Yu and Soong [45], Spielman and Goren [46] or Brusckhe and Advani [47]. Further models were proposed for elliptical fibres [48] and for chopped fibre bundle beds [49].

These models cover a wide range of fibre volume fraction going from very low to very high and were found to all provide reasonably good agreement with experimental data in a comparative study of literature data done by Jackson and James [50] and shown in Figure 2.4. Experimental validation was performed for carbon fibres in the fibre direction up to 0.8 by Gutowski [37] and in the transverse direction up to fibre volume fractions of 0.59 by Gebart [43] and 0.72 by Gutowski [37]. For comparison, the maximal packing of aligned fibres in a hexagonal arrangement is 0.91 [43].

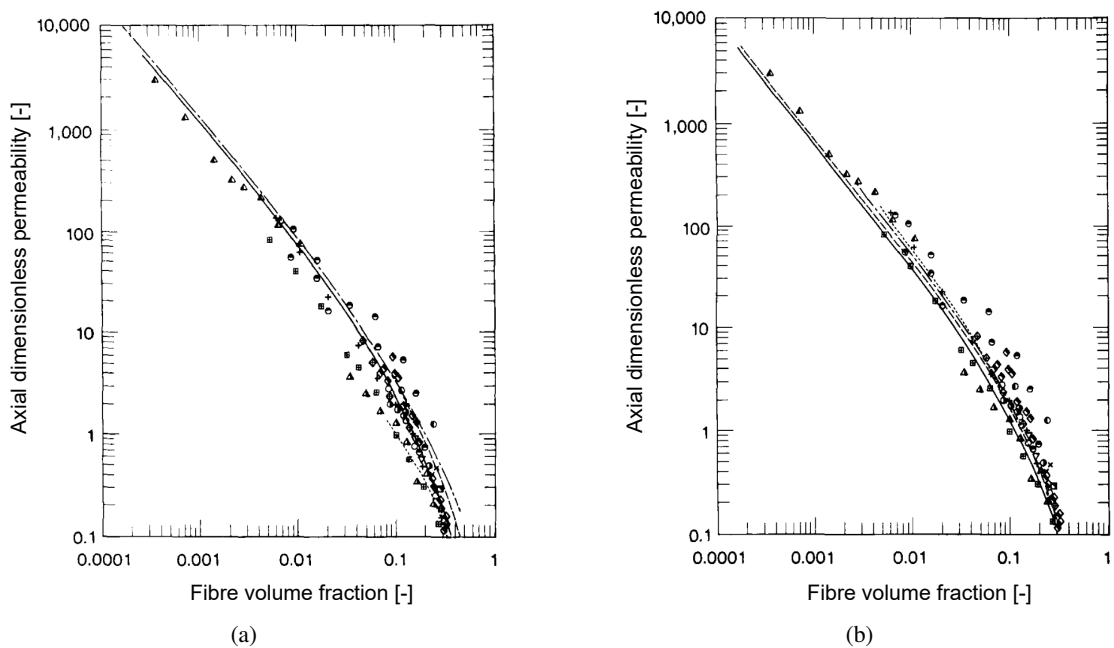


Figure 2.4: In Figure 2.4a: comparison of the axial dimensionless permeability  $\frac{K}{r^2}$  as predicted by Happel [38], Drummond & Tahir [39], Sparrow & Loeffler [40] in function of the fibre volume fraction and as measured experimentally. In Figure 2.4b: comparison of the transverse dimensionless permeability  $\frac{K}{r^2}$  as predicted by Happel [38], Kuwabara [41], Hasimoto [44], Sangani & Acrivos [42], Drummond & Tahir [39], Yu & Soong [45], Spielman & Goren [46] in function of the fibre volume fraction and as measured experimentally. Adapted from [50], to which the reader is redirected for a complete interpretation of the graphs.

To the best knowledge of the author, no permeability measurements at higher fibre volume fractions is reported in the literature. Interestingly enough, several authors reported tow fibre volume fraction  $\nu_{f,tow}$  around 0.75 for compacted textiles. Ali et al. measured  $\nu_{f,tow}$  ranging from 0.6 to 0.62 and from 0.58 to 0.78 for two different textile architectures depending on the compaction state [51], Endruweit et al. measured values ranging from 0.65 to 0.75 [52] and Bernet et al. between 0.74 and 0.77 [34] in similar studies. This implies that no model for transverse permeability was experimentally validated at the tow fibre volume fractions commonly occurring during manufacture.

Although originally developed for granular beds, the Carman-Kozeny equation [36] was found to be applicable to model the permeability of fibre bundles in the fibre direction but not in the transverse direction [37]. For this reason, Gutowski et al. later proposed the modified Carman-Kozeny equation which gives a good fit for the permeability, especially in fibre direction [37]. The modified Carman-Kozeny equation is derived considering that fibres are not straight but undulate and act as elastic bending beams. The geometry of the fibres is characterized by their diameter, the length between two contact points and the undulating height. As pressure is applied the beams deform and the undulating height decreases, which decreases the porosity and the area available for flow as shown in Figure 2.5. Based on these geometric characteristics and the elastic properties of the fibres Gutowski et al. then derived equations for the fibre bed stress response and permeability [37]. Because of the difficulty to determine the geometric characteristic values of the fibres such as the distance between two contact points the constants are regrouped in so-called Kozeny constants which are then determined experimentally. Despite being popular otherwise, the modified Carman-Kozeny equation is difficult to apply for tows because of the difficulty to directly measure their permeability and this consideration applies to many others semi-analytical models.

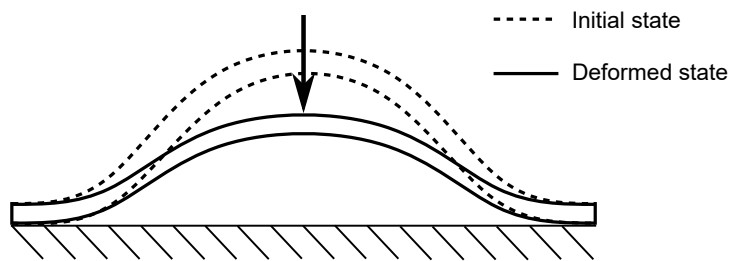


Figure 2.5: Schematic representation of the assumed fibre geometry at rest and deformed. One can see that the area available for fluid flow under the fibre diminishes as the fibre deforms.

As the packing density of the fibres increases the flow path width decreases, which in turn lowers the permeability. This process goes on until the maximum packing density of the fibres is reached, at which point the flow channels in transverse direction are completely closed and the fibrous medium becomes impermeable. At elevated fibre volume fractions directly measuring the transverse permeability therefore becomes challenging and only few attempted to measure the tow permeability itself. Gennaro et al. [53] proposed a method to measure both the macro and micro transversal permeability with compaction experiments, however the tow fibre volume fraction is not reported. Godbole et al. [54] directly measured the permeability of tows which had only a fibre volume fraction of 0.59, in addition no pressure was applied to the tows such that the influence of compaction pressure on both the tow fibre volume fraction and permeability is unknown. Phillips et al. [55] stopped consolidation experiments after different times and measured the impregnation degree to infer tow permeability. They found that the tow permeability remained constant with applied pressure in the range between 10 and 100 bars, but they did not state the fibre volume fraction neither.

Since semi-analytical models such as the modified Carman-Kozeny requires experimental measurements which are particularly arduous to perform, in the literature most of the researchers dealing with tow permeability used purely analytical models such as the one proposed by Gebart

[43], which addressed the permeability of tows with a simplified model considering tows perfectly aligned in a quadratic or hexagonal manner. His model predicts both the permeability in the fibre direction  $K_{//}$  and transverse to it  $K_{\perp}$  in equations respectively 2.3.2 and 2.3.1. The parameters in this equation change depending on the fibre arrangement to describe either the case of quadratic or hexagonal arrangement and are listed in Table 2.1.

$$K_{\perp} = A_{geb} r_f^2 \left( \sqrt{\frac{\nu_{f,max}}{V_f}} - 1 \right)^{\frac{5}{2}} \quad (2.3.1) \quad K_{//} = \frac{8r_f^2}{B_{geb}} \frac{1 - \nu_f^3}{\nu_f^2} \quad (2.3.2)$$

Fibre Arrangement	$A_{geb}$	$\nu_{f,max}$	$B_{geb}$
Quadratic	$\frac{16}{9\pi\sqrt{2}}$	$\frac{\pi}{4}$	57
Hexagonal	$\frac{16}{9\pi\sqrt{6}}$	$\frac{\pi}{2\sqrt{3}}$	53

Table 2.1: List of parameter values for Gebart's model

In these equations, // denotes a property in fibre direction and  $\perp$  transverse to it.  $A_{geb}$  and  $B_{geb}$  are constants,  $\nu_{f,max}$  is the maximum theoretical fibre packing for a given packing configurations and  $r_f$  is the radius of the fibres. The value of the normalized permeability  $\frac{K}{r_f^2}$  in function of the fibre volume fraction for the quadratic and hexagonal fibre arrangement are shown in Figure 2.6. As the fibre volume fraction approaches the maximal packing the transverse permeability tends toward zero since the flow paths becomes completely blocked.

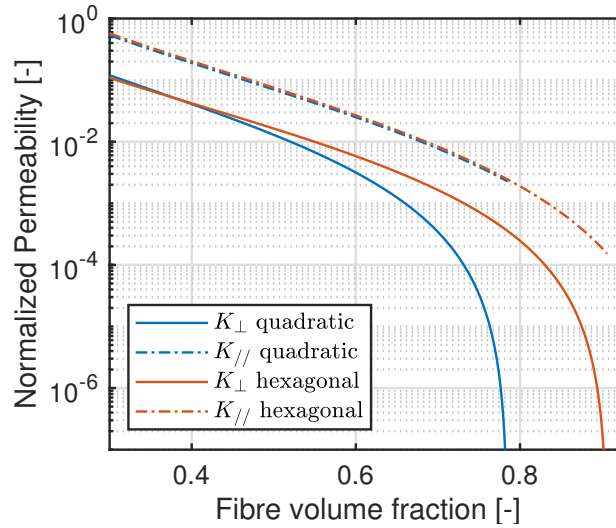


Figure 2.6: Normalized Permeability  $\frac{K}{r_f^2}$  in transverse and fibre direction according to the model of Gebart for quadratic and hexagonal fibre arrangement.

The limitations of this model lies in its assumptions, namely that the fibres tows can be considered as parallel cylinders with regular spacing and arrangement. A large number of studies however studied the microstructure of fibre bundles and report how it displays variability inside the tow, in direct contradiction with these assumptions. Godbole et al. [54] reported that the assumption of constant inter-tow distance does not hold and many authors measured local variation of the fibre volume content in the tow [52], [54], [56], [57]. The fibre architecture was found

not to have regular arrangement [52], [54], [57], Gommer et al. [58] reported that the initially random filament distribution tended to adopt more square and hexagonal packing with increasing load, however they stress that this is a tendency and that the filaments are not arranged in an ideal periodic pattern. Many authors characterized the variability of the fibre bundle distribution in tows either by looking at cross-sections [52], [57], [59] or at the tow itself by reconstructing the filament path [60].

These deviations from an ideal arrangement have a direct impact on the permeability, therefore affecting the predictive capacities of many analytical models having such assumptions. Bechtold and Ye [59] generated several fibre arrangements with different degree of regularity, which was characterized with the so-called Morishita index. The transverse permeability was then determined with two-dimensional flow simulation and it was found that a decreasing degree of regularity resulted in a lower permeability. Endruweit et al. [52] characterized the tow microstructure as a repartition between different fibre arrangements depending on the number of nearest neighbour and then described it as a function of the fibre volume fraction. Gebart's constants were derived for triangular and pentagonal arrangement, finally the average transverse permeability in function of the fibre volume fraction was calculated, which was also found to be lower than when assuming idealised fibre arrangement with square or hexagonal packing. Several other authors investigated the influence of deviations from ideal arrangement on the permeability and came to the same conclusion. It was found that transverse permeability was dominated by zones with locally reduced filament spacing [61]–[63]. Regarding the axial permeability, it was found that zones with low filament density becomes the main flow channel, resulting in a higher permeability when compared to a uniform distribution [61], [64], [65].

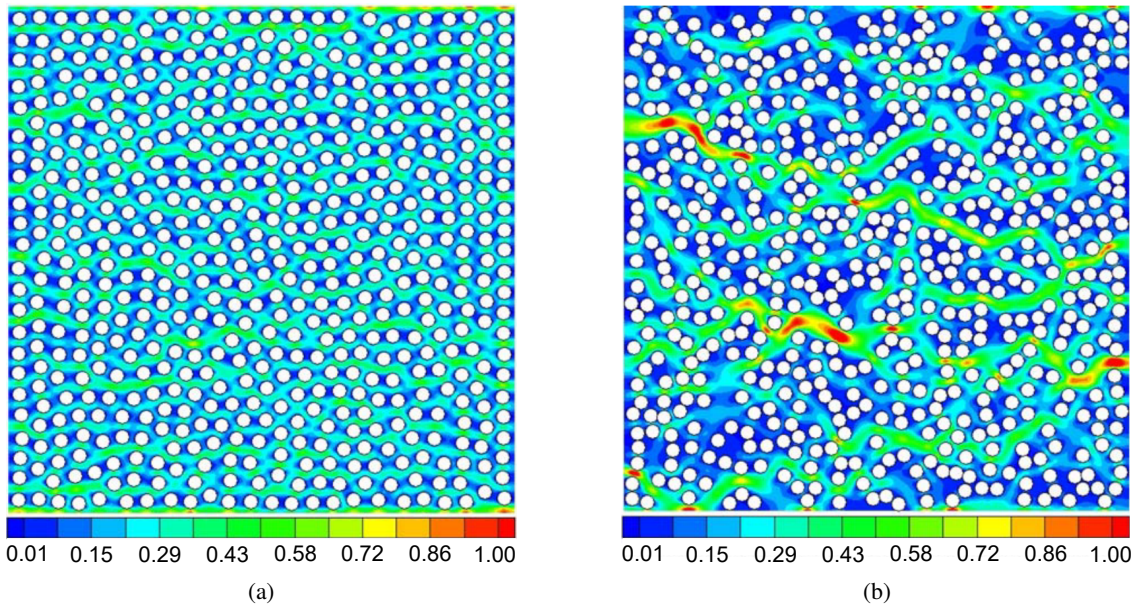


Figure 2.7: Contours of fluid speed for transverse flows across unidirectional random fibre arrays with different degree of disorder. One can see very different flow patterns: while in Figure 2.7a the fluids flow behaviour is homogeneous through the structure, Figure 2.7b shows that fibre arrays with high degree of disorder displays zones with very low permeability with some channels in between where the fluid can flow. Overall, the permeability decreases with increasing degree of disorder. Adapted from [63].



These studies based on flow simulations share in common the difficulty to analyse effects at high fibre volume fractions. To begin with, the generation of equivalent microstructure is challenging at elevated fibre volume fraction and methods viable for high fibre volume fractions were only presented relatively recently [58], [66]. The very narrow flow paths at elevated fibre volume fraction require locally very fine mesh, which result in important increases in computational costs and quickly become a limiting factor. In addition, in two-dimensional analyses the flow path can be completely or almost completely closed as shown in Figure 2.8, preventing flow simulations. It could be that the matrix is then forced to flow in the axial direction to reach a location where the inter-filament flow path is no-longer closed, which would result in a three-dimensional flow. Although methods to reconstruct tows or create equivalent structures were proposed [58], [66]–[68] the literature lacks three dimensional studies on the permeability of aligned fibres at since and was mainly focused on a two-dimensional approach.

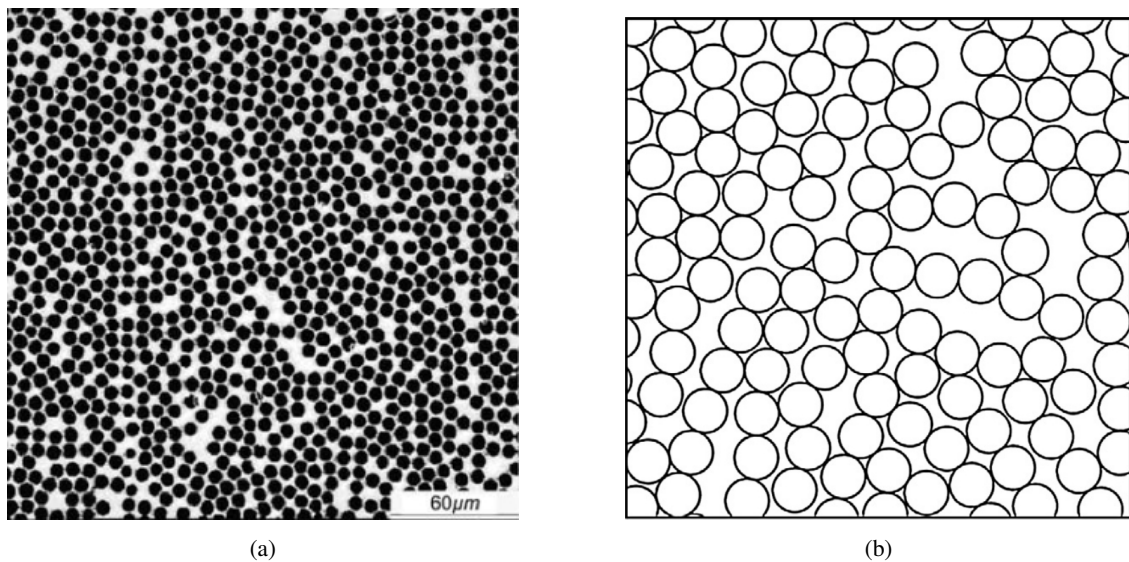


Figure 2.8: Two-dimensional tow structure, as computed for a unidirectional composite laminate by Vaughan and McCarthy [66] and as generated by Gommer et al. [58] for a fibre volume fraction of 0.7. In both cases, the flow paths appear to be completely closed.

For textiles that are inhomogeneous at the meso level the complexity and variety of textiles makes analytical approaches difficult, so that permeability is usually measured and fitted to a power law function. The characterization of the permeability of textiles is known to be prone to large scatter. In a first permeability round robin exercise, Arbter et al. let different participants measure the in-plane permeability of the same textile without specifications regarding the procedure and found a scatter in the measured permeability of more than one order of magnitude [69]. Therefore, an international benchmark exercise was performed to identify the sources of deviations with the aim to define standardized test procedures [70]. Besides measurement errors caused by the methodology and apparatus such as cavity deformation or inaccuracies in the determination of the fluid pressure they highlighted the impact of textile variation, which can originate from the textile manufacturing process.

Another source of error is related to the history of textile compaction and handling which directly affects its structure as shown in Figure 2.9, compaction behaviour and permeability as shown by Kabachi et al. [71]. Recently, Yun et al. [72] presented a method for the full characterization of permeability including skew terms, which are usually neglected.

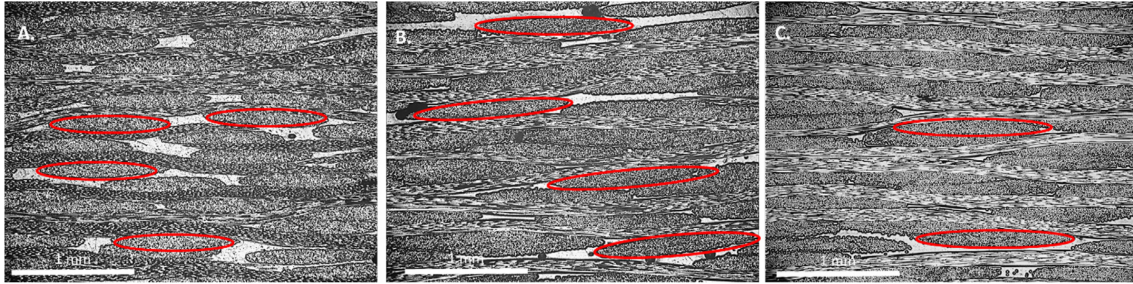


Figure 2.9: Cross-sections of a woven fabric compacted without cyclic compaction to a fibre volume fraction 49.92% in Figure A, to 56.86% in Figure B and C whereas the sample displayed in Figure B was subjected to cyclic compaction and not sample in Figure C. Figures B and C exhibits increased nesting due to the higher compaction. The yarns subjected to cyclic compaction are more elongated and are tilted when compared to the ones not subjected to cyclic compaction, as outlined in the Figures [71].

Besides measurements, an increasing interest is given to numerical simulations to predict the permeability of textiles, for which the acquisition of their internal architecture is required. Some researchers reconstructed it, such as Nordlund et al. [73] who investigated the effects of geometrical perturbations on the geometry and showed that the stitching had a large influence on the permeability of non-crimped stitched fabrics (NFC) or Chen & Ye [74] who proposed a model to predict woven fabric permeability and obtained satisfactory agreement with with experimental data. The difficulty of this approach is to describe the change of geometry after compaction, for this reason the simulation of the textile deformation with mechanical models is appealing and a group of researchers based their studies on the software WiseTex [75]–[79]. Another advantage of this approach is that it can also be used for micro-mechanical and structural analysis [80]. However, further improvements are required until such methods can reliably predict permeability as highlighted by Swery [81] who pointed out a factor 2 between predicted and measured permeability. Some other researchers such as Straumit et al. [82] or Ali et al. [51] obtained the geometry from micro-computed tomography (micro CT). Independently of the methods, a dual-scale approach is usually adopted where flow in the tows is considered, leading to a decrease of permeability when compared to single-tow approaches [83]. Overall, these methods commonly remain limited by computational power, especially for dual scale, three-dimensional flow.

## 2.4 Air evacuation, entrapment and dissolution

Void management is an important aspect in the production of fibre-reinforced polymers (FRP) as voids are well-known to decrease the mechanical performance of composites [84], which is why a maximum allowable porosity is usually defined in production, commonly 1%. Several mechanisms can cause porosity: incomplete impregnation, air entrapment or the emissions of volatiles during consolidation. During the production of thermoset-based composites voids can be caused by entrapped air or volatiles originating from moisture or by-products of the curing reaction [85]. For thermoplastic composites however, the origin of voids is usually limited to entrapped air, as no volatiles are produced since no curing reaction takes place and standard manufacturing guidelines recommends drying of thermoplastics susceptible of absorbing moisture.

One way to avoid air getting entrapped in the composite is to remove it prior to consolidation, which is commonly done in Vacuum-Assisted Resin Infusion (VARI), Out Of Autoclave (OOA) and Autoclave processing [86]. Arafath et al. [87] proposed a simplified model to predict the amount of air entrapped in function of time, which is especially relevant for very large parts such as windmill blades since the time required for air removal scales with the square of the length.

For the production of thermoplastic composites air removal prior to consolidation is uncommon and the literature documenting it is scarce and concerns a few specific techniques only. Oven Vacuum Bag (OVB) consolidation of thermoplastic composites was investigated by Zhang [88] for high-temperature thermoplastics, however it concerned pre-impregnated materials. Recently, Schneeberger et al. investigated OVB of hybrid bicomponent fibres for large structures [89] such as wind turbine blades. In press moulding of thermoplastic composites applying vacuum is challenging for several reasons, for instance because few seals withstand the elevated temperatures - especially for high-temperature thermoplastics - and because of the difficulty to prevent molten polymer from flowing in the vacuum vent. No documentation about successful application of vacuum in press moulding of fibre-reinforced thermoplastic composites was found in the literature.

The description of bubbles growth and collapse mechanisms is necessary for the correct prediction of porosity and was therefore the object of several studies. Wood and Bader [85] addressed the evolution of bubbles in pure resin and considered two main mechanisms: air absorption at the interface and the diffusion of diluted species in the resin. At the interface species will be absorbed or resorbed until the saturation concentration  $C_s$  at equilibrium is reached, which was described as a linear function of pressure by Henry [90] in equation 2.4.1, thereby  $H$  is Henry's constant. The diffusion of species then depends on the concentration  $C$  and the diffusion coefficient  $D$  as described by Fick's law [91] and the flux of species  $J$  is described by equation 2.4.2:

$$C_s = H \cdot P \quad (2.4.1)$$

$$J = D \nabla C \quad (2.4.2)$$

The diffusion was largely studied and various analytical solutions and approximations are given for different cases and boundary conditions. Epstein and Plesset [92] formulated an approximate solution for the growth and collapse of bubbles in liquids, approximate solutions for cylindrical symmetrical cases were proposed by Carlslaw and Jaeger [93] and more recently Phillips [94], analytical solutions for various cases were compiled by Crank [95].

Even though porosities can arise in the form of bubbles in a resin-rich area, during the manufacture of FRP other shapes can arise in other locations such as in bundles or between fibres [85]. It is for instance well known that, during resin transfer moulding (RTM), incorrect process parameters favours the entrapment of air in the bundles as a result of dual scale flow [96]. The diffusion in bundles is influenced by the fibres which can be considered as impermeable, however very few authors proposed models to describe this. Lundström investigated the dissolution of oblong shaped bubble during RTM and experimentally determined a reduction factor for the reduced diffusion due to fibres [97]. Leterrier and G'sell [98] highlighted gas dissolution as void reduction mechanisms during the processing of thermoplastic composites and Zhang et al. [99] investigated void reduction mechanisms in OVB, however neither proposed any model.

Several authors considered air entrapment during impregnation [34], [100] and demonstrated their impact on residual porosity. However, the dissolution of air was never addressed in the open literature and a void-free laminate cannot be attained in these models, which is in contradiction with experimental results. Rozant et al. [100] for instance predicted a constant residual porosity while a decay was measured. Therefore, models about air dissolution during the manufacture of thermoplastic composites are overall lacking.

## 2.5 Fibre disorientation

For the flow in fibrous media several regimes exist: if the fluid flows past a solid phase which remains fixed in space and does not undergo deformation then one speaks of percolation, if the viscous forces exerted by the fluid drag along the fibres one speaks of fibre-matrix flow. Fibre displacement and disorientation resulting from fibre-matrix flow can cause defects in the parts and significantly impact the mechanical properties. Fibre waviness for instance was found to lower the tensile, compressive and flexural strength, acts as a failure initiator and reduces the fatigue life [101], [102].

A number of researchers studied fibre-matrix flow of aligned fibres, which is also commonly referred to as squeeze flow. Early investigations by Balasubramanyam et al. [103] showed that in unidirectional fibre-reinforced polymers the fibres move together with the matrix in the transverse direction and behave microscopically as a viscous fluid. In the fibre direction however the fibres constrain the flow such that squeeze flow deformation is strictly perpendicular to fibre direction, as also claimed by Cogswell [104]. Balasubramanyam et al. [103] therefore proposed to model it as an incompressible anisotropic fluid and found reasonable agreement with experiments.

Still for aligned fibres in viscous fluids, Schuler and Advani [105] investigated the influence of fibre volume fraction on the transverse shear viscosity of squeeze flow and proposed a cell model to calculate this effect. Belnoue et al. [106] presented a modelling concept describing the compressibility of toughened uncured thermosets prepreps. They improved the approach of Schuler and Advani by considering the influence of the orientation of adjacent plies on transverse squeeze flow, which can also be adapted to thermoplastic materials, and validated their model with experimental results. Ghnatios et al. [107] and Sorba et al. [108] proposed, on the same basis, a 3D model taking the orientation of the stacked ply into account. Fibre displacement and waviness as a result of squeezed flow in stacked UD plies is shown in Figure 2.10.



Figure 2.10: Photograph of a  $[0/90]_6$  stack of UD layers after compression, where one can clearly see fibre displacement and waviness [108].

Fibre-matrix flow has also been investigated for short and long fibre reinforced composites. Servais et al. [109] experimentally tested squeeze flow of long fibre reinforced thermoplastics and adapted a model for predicting squeeze flow pressure of short fibre suspensions. Picher-Martel et al. [110] proposed a 2D model to predict the fibre-matrix flow behaviour of random oriented strands reinforced thermoplastics. They modelled the composite as Bingham fluid and found that the equivalent viscosity and yield strength increased with strand length. The model was found to fit the experimental data quite well.

When it comes to the fibre-matrix flow in composites where the reinforcement is a textile, the literature is much more scarce. Textiles have continuous fibre reinforcement in several directions, which should constrain squeeze flow in all direction according to the assumptions of the model of Schuler [105]. The composite therefore does not behave macroscopically as a fluid, however fibre matrix flow can take place and cause tows to slide past each other in a process called fibre washout. Hautefeuille et al. investigated fibre matrix flow in saturated fabrics by compacting fabric stacks and measuring the full field flow induced deformations [111], then identified and quantified the drag forces acting on the textile during fibre washout [112]. In their work, Hautefeuille et al. compacted stacks of fabrics impregnated with silicone oil of different viscosities with different compaction speeds. They observed that at low viscosity and compaction speed a percolation regime and no flow-induced deformation takes place and found an onset for flow-induced deformation with higher viscosity and compaction speeds as shown in Figure 2.11. They report that the onset for fibre washout starts when the product of the strain rate and the viscosity exceeds a certain value, which depends on the fabric architecture.

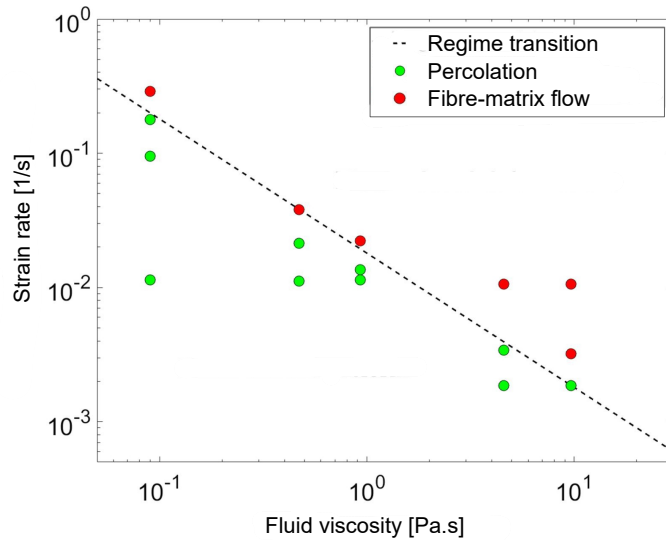


Figure 2.11: Reported flow regime at different strain rates and fluid viscosity along with the regime transition between percolation and fibre-matrix flow. Adapted from [111].

Bodaghi et al. investigated fibre washout during high pressure resin transfer moulding [113], [114] and also identified transfer of force from the matrix onto the fabric as cause of fibre washout. They then carried out an experimental parametric study to investigate the influence of different parameters and found out that the flow front position, the injection and compaction pressure significantly significantly influenced the onset of fibre washout. Furthermore, they recommend to gradually increase injection pressure at the beginning of the injection. Nevertheless, quantitative models to predict and model fibre matrix flow are still lacking when the composites are based on woven fibres.

## 2.6 Textile stress response

In a porous medium the mechanical equilibrium dictates the relationship between the applied stress  $\sigma_{app}$ , also called effective stress, the matrix pressure  $P_m$  and the stress in the porous medium, which is the reinforcing textile in the case of fibre-reinforced polymers. This relationship is also called Terzaghi's principle and was proposed by the eponymous researcher [115]. Although formulated three-dimensionally, most of the models only consider the through-thickness direction only and it then reads:

$$\sigma_{app} = P_m + \sigma_{tex} \quad (2.6.1)$$

where  $\sigma_{tex}$  is the through-thickness textile compaction response. For press moulding processes a few authors assumed homogeneous through-thickness properties and inferred the matrix pressure with known applied pressure and calculated textile stress response, which was then used in the impregnation model. This was done by Groupe & Akkerman for film stacking [116] and by Philips et al. for co-woven fabrics [55] for instance and could be used by extension for other hybrid textiles. In processes such as Compression Resin Transfer Moulding (CRTM), resin film infusion (RFI) or Thermoplastic Compression Resin Transfer Moulding (TP-CRTM) the textile is impregnated in the through-thickness direction. The out-of-plane flow induces a deformation of the textile, influencing its compaction, permeability (see Section 2.3) and stress response alto-

gether. Since the textile opposes a resistance to the flow there is a pressure transfer between the matrix and fabric, which follows Terzaghi's principle as shown in Figure 2.12. Several authors proposed models to describe these processes [25], [117]–[121], which all require material models describing the mechanical response of textiles in the through-thickness direction.

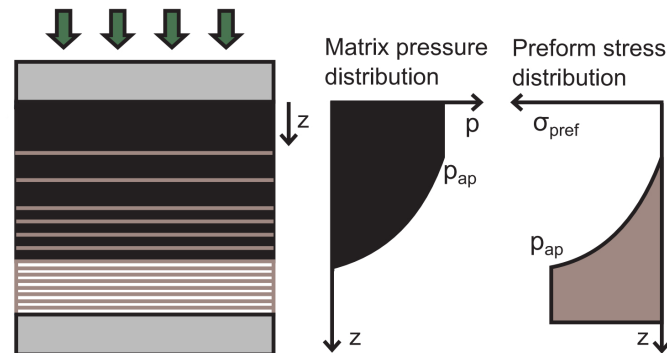


Figure 2.12: Schematical representation of through-thickness impregnation and the resulting compaction of the textile on the left and the corresponding pressure repartition between matrix and textile on the right. Adapted from [25].

The description of the mechanical behaviour of fibre textiles has been and is still an active research topic as witnessed by the rich literature dealing with this matter. During the compaction of a stack of textiles the fibres are pressed together and act as elastic bending beams. Fibres and tows slide past each other to rearrange themselves, causing friction forces. The resulting nesting of the fibres and fibre bundles is thereby influenced by the lubrication of the textile. These combined effects result in a complex viscoelastic behaviour [122].

Early models only considered the elastic response of the fibre beds. In 1946, Van Wyk modelled the compression behaviour of wool with bending beams [123]. Several authors subsequently proposed models based on the same assumption, such as Gutowski [37] or Toll [124] who considered different types of assembly following a micromechanical approach. Toll demonstrated that for aligned fibres and weave the elastic stress response exponentially depends on the fibre volume fraction, coming to the same conclusions as Robitaille & Gauvin [125] who based their work on experimental evidence. Note that the fibre volume fraction is commonly used to describe the compaction of textiles instead of strain, however both are directly related [17]. However, fibre beds display a pronounced viscoelastic behaviour as represented in Figure 2.13, which depicts the stress response of textile stacks at different strain rates. In this Figure, the quasi-static stress response refers to the remaining stress response after complete decay of the viscous effects, which would also take place at infinitely slow compaction speeds. The aforementioned models are only valid to describe the quasi-static stress response, as other effects are neglected. With increasing strain speeds the viscoelastic effects becomes increasingly important and the total stress response becomes larger.

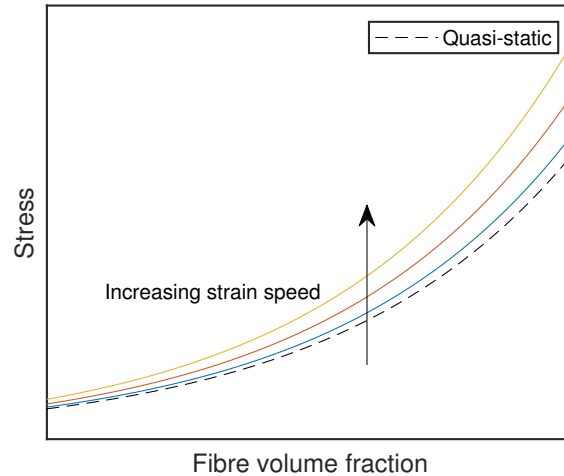


Figure 2.13: Schematical representation of the quasi-static compaction curve along with the compaction curves at different strain speeds.

Because of this behaviour, soon time-dependent models were proposed. This matter was commonly described with rheological models consisting of a combination of spring and dampers, usually a generalized Maxwell model. Also known as the Maxwell-Wiechert model, it consists of a spring placed in parallel with an arbitrary number of spring-dashpot elements called Maxwell elements as shown in Figure 2.14. Kim and McCarthy [126] were the first to describe the relaxation of fibre textiles with this model in 1991, using a linear model with five spring-dashpot elements.

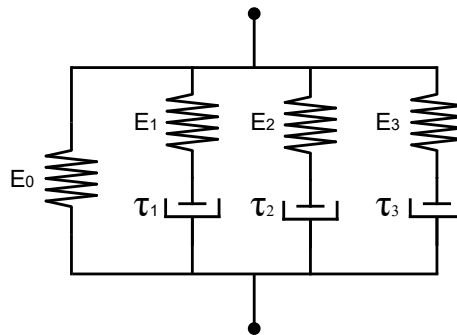


Figure 2.14: Schematical representation of the generalized Maxwell model with three branches [17].

In further studies several Maxwell models were proposed with a different number of branches and nonlinear springs to describe the quasi-static stress response of the textile [127] or strain-dependent parameters [128], following the findings of Bickerton et al. [122] who found that the time dependent response of fibre beds depends on the strain and compaction rate. More recently, Danzi et al. [129] proposed a three-branches Maxwell model with strain-dependent springs and strain-rate dependent dashpots, which was found to give good results over a wide range of strains and strain speeds. However, this model was only verified with one dry textile so that its performance with different textiles remains to be proven both in dry and wet conditions.



Some other models with different approaches not based on the Maxwell-Wiechert model were proposed, such as the one proposed by Kelly [130]. This model is only valid for textiles materials whose stress-time responses at different compaction velocities collapse onto a master-curve, which is not the case for all types of fibre reinforcements as shown by Danzi et al. [129]. The influence of cyclic compaction on the fibre bed response is usually not considered in these models, but was investigated by Kabachi et al. [71] and found to have measurable effects on the compaction curve, through-thickness permeability, time-dependant and quasi-static stress response.

## 2.7 Impregnation & consolidation models

As of today the large majority of models considering impregnation are based on the law of Darcy [19]. Analytical solutions are commonly sought to spare simulations or to integrate them into the frame of a wider analytical model. They are known in 1D for a constant and homogeneous permeability. Some authors such as Philips et al. [55] or Hou et al. [131] approximated fibre bundles in prepregs presenting a large aspect ratio as a layer with homogeneous thickness such as to model impregnation in unidirectional Cartesian coordinates. The same approach was used by Ye et al. [132], [133] and Klinkmüller et al. [134] for commingled yarn. Using the same methodology for several plies becomes less reliable because as relaxation takes place the permeability changes, which contradicts the assumption for that solution. The impregnation of cylinders can be solved unidirectionally in radial coordinates, an approach that was adopted by Bernet et al. [34] for commingled yarns based on the observation that unimpregnated areas tended to adopt that shape. For a cylinder with homogeneous permeability, matrix pressure  $P_m$  outside the cylinder and gas pressure  $P_g$ , capillary pressure  $P_c$  which is denoted as positive if enhancing the flow, cylinder radius  $R_{eqv}$  and radial distance to the flow front  $r$  as represented in Figure 2.15 the differential equation derived from Darcy's law reads [34]:

$$r \cdot \ln\left(\frac{r}{R_{eqv}}\right) \dot{r} = \frac{K \cdot P_{dp}}{\eta(1 - \nu_{f,tow})} \quad (2.7.1)$$

where  $P_{dp}$  is the driving pressure equals to  $P_m + P_c - P_g$ . Fibre bundles can be well described with ellipses, however for this geometry no analytical solution to Darcy's law are known. In his work dealing with the impregnation of commingled yarns, Van West et al. [135] proposed to solve the impregnation of equivalent cylinders with the same hydraulic radius instead, as represented in Figure 2.15. Numerical simulations indicated a good match between the time required for the full impregnation of ellipses of different aspect ratios and their equivalent cylindrical counterpart. The aspect ratio of an ellipse is defined as the ratio of the semi-major and minor axes  $l_h$  and  $l_w$  and the equivalent radius  $R_{eqv}$  reads:

$$R_{eqv} = \sqrt{2} \frac{l_w^2 \cdot l_h}{\sqrt{l_w^2 + l_h^2}} \quad (2.7.2)$$

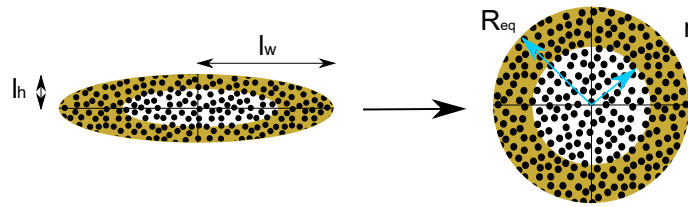


Figure 2.15: Illustration of an elliptical tow on the left and the equivalent circle proposed by Van West [135] on the right.

Grouve and Akkerman [116] adopted the same approach to model the impregnation of tows in film stacking and Kobayashi et al. [136] to micro-braided yarns. While for the impregnation of fibre tows their steep compaction curve makes up for a rather constant permeability [55], for other reinforcements such as weaves and nonwoven matrix flow influences the compaction. As the compaction state is linked to permeability which influences the matrix flux, the two phenomena are coupled and several authors therefore proposed models which considered both. Sommer and Mortensen considered the case where the fibrous reinforcement first gets compacted by the fluid applied by the pressure then relax upon impregnation following Terzaghi's law [137]. Neglecting viscoelastic effects they derived a set of equations which they solved with a Boltzmann transformation.

Several authors published studies based on their work: Michaud and Manson [118] extended the model by predicting the kinetics of impregnation and the evolution of the fiber volume fraction distribution during impregnation and considering two practical cases of thermoplastic polymer composite impregnation processes. In the first one the amount of resin is large and the preform relaxes completely while in the second one the preform reaches the mould wall before complete relaxation. They demonstrated that the time required for preform relaxation may be much larger than that for impregnation, then successfully applied this model to the impregnation of needled bundle glass fibre mats in [119]. Wolfrath et al. analysed the deconsolidation of glass mat reinforced composites in [138] and could predict the final void content in [139]. However, the kinetics of deconsolidation were found to be underestimated because the fibre bed is not completely saturated as assumed. Studer et al. [140] used a similar approach to model direct thermoplastic melt impregnation by injection moulding through-thickness impregnation, which is pictured in Figure 2.16. This model was used on fabrics with different textile architectures whose influence was studied in [25]. With textiles the relaxation has been found to be marginal so that the process is best suited for high final fibre volume fractions.

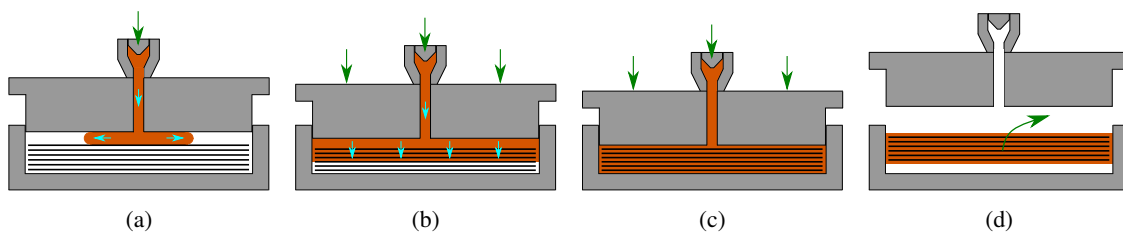


Figure 2.16: Schematic representation of the direct thermoplastic melt impregnation with variothermal injection moulding process. Figure 2.16a shows the thermoplastic melt injection followed by the textile impregnation in Figure 2.16b, then cooling down in Figure 2.16c and finally part ejection in Figure 2.16d. Adapted from [25].

While the overwhelming majority of the models assumed that the air is free to escape the composite and does not get entrapped, some authors considered air entrapment in their models and showed that it has an impact on the residual porosity. Bernet et al. [34] addressed impregnation and void formation in commingled yarns. Rozant et al. [100] adopted a similar approach for knitted fabrics and found similar results regarding residual porosity.

Even though the topics of air evacuation, entrapment and dissolution has been addressed in the literature, it mainly concerns thermoset composites. Kay for instance modelled gas transport and void formation in composite prepregs [141]. His work is focused on thermoset composites and considers some effects such as the release of volatiles during resin curing which are not relevant for thermoplastic composites. However, some other effects needs consideration and some aspects of his model could be adapted for thermoplastic composites. Very few studies on thermoplastics were performed, such as the one from Zhang [88], [99] addressing OVB consolidation of pre-impregnated thermoplastics.

So what about consolidation models? Impregnation, fibre bed stress, response, perhaps air entrapment and dissolution are all aspects that should be predicted by a consolidation model. Even if a large body of work is covering one or several of these aspect as widely discussed in this chapter, to this date no model is able to capture all these relevant effects at once. Moreover, many of these modelled have been proposed in 1D and an extension to a three-dimensional work frame still remains to be done. Wysocki et al. attempted to model consolidation with a two-phase continuum framework and entropy inequality [11]–[13], a similar approach was followed by Rouhi et al. [14]–[16]. Despite being an interesting approach successful at formulating a set of equations, in both cases the difficulty to determine the values of variables related to the entropy inequality equation make their implementation, let alone validation challenging in practice. Another aspect which arguably belongs to consolidation is fibre disorientation because of its relevance for the mechanical properties, yet for textiles a criterion for its onset let alone a knowledge-based quantitative description are completely lacking. However, the work of Hautefeuille [111], [112] forms a good starting point for further studies on the topic.

In summary, a reliable consolidation model taking into account all the relevant effects and in a three-dimensional manner is still lacking to this day. Even if most of the different phenomena are rather well understood, a framework to couple all of these together is still missing. Nevertheless, a reliable three-dimensional consolidation model would be of great interest, as it would facilitate the production of complex shaped thermoplastic parts and their optimization.



# Chapter 3: Materials and material characterization

In this thesis, a quasi-unidirectional (UD) glass weave is used for the reinforcing ply, while for the thermoplastic ply either polypropylene (PP) or high-density polyethylene (HDPE) in the form of foils were used. The glass fabric, shown in Figure 3.1a, has a Leno weave architecture and was provided by Tissa Glasweberei AG. According to the technical datasheet, the textile has an areal weight  $M_f^A$  of  $931 \frac{\text{g}}{\text{m}^2}$ . The main tows have 2400 tex and were woven with a density of  $3.5 \frac{\text{tows}}{\text{cm}}$ . The supporting weave consists of two twisted tows with each 68 tex with a density of  $3.5 \frac{\text{tows}}{\text{cm}}$  in the weave direction and 68 tex tows with a density of  $5 \frac{\text{tows}}{\text{cm}}$  in the weft direction. For the polymers, PP BJ100HP and HDPE Lupolen 5031L from respectively Borealis and Basell were obtained in granulate form. The technical datasheets specify a solid-state density  $\rho_m^s$  of  $906 \frac{\text{kg}}{\text{m}^3}$  for PP and  $952 \frac{\text{kg}}{\text{m}^3}$  for HDPE and a melting temperature  $T_m$  of  $165 \text{ }^\circ\text{C}$  for PP and  $131 \text{ }^\circ\text{C}$  for HDPE. The polymers were then processed into 0.15 mm foils with a Collin FT E20T-MP-IS extruder. Figure 3.1b illustrates the polymer in the form of granulates and processes foils.

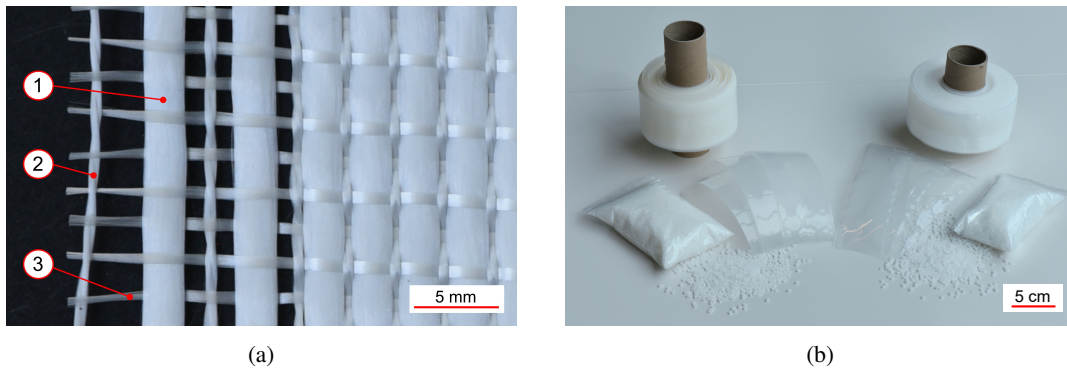


Figure 3.1: a) Picture of the quasi-UD glass fibre weave with a Leno textile architecture. The main tows are indicated by 1), the supporting weave is indicated by 2) and 3). b) Picture of the granulate, film rolls and single foils, whereas PP is on the left and HDPE on the right.

## 3.0.1 Thermoplastics

The polymers were analysed with differential scanning calorimetry (DSC) with a DSC25 from TA instruments to check their melting behaviour as shown in Figure 3.2. The samples were subjected, without previous drying, to two heating cycles with heating and cooling rates of  $10 \frac{^\circ\text{C}}{\text{min}}$ . The curves of the first and second heating are very similar for PP and HDPE, as one would expect for a commercial grade thermoplastic. The slight change of melting temperature and en-

thalpy is mainly due to the cooling rate, as this latter influences the degree of crystallinity for instance. As the manufacturing conditions of the polymer are usually unknown, its properties is usually measured at the second heating cycle because it is associated with known and controlled crystallization. Therefore, the melting temperatures  $T_m$  of PP and HDPE were determined to be respectively 165 and 131 °C, which is in line with the technical datasheets provided by the manufacturers.

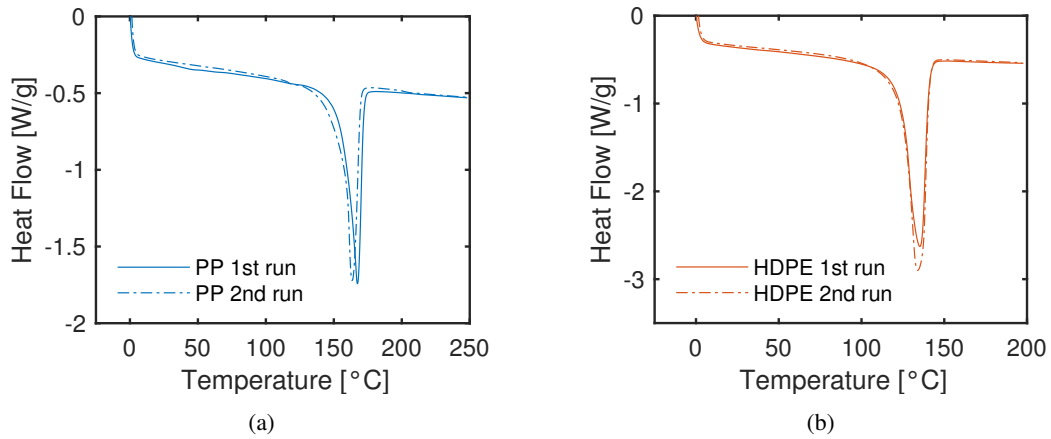


Figure 3.2: DSC results for PP in Figure 3.2a and HDPE in Figure 3.2b.

The viscosity of the thermoplastics were measured as a function of the shear rate at different temperatures with an Anton Paar Physica MCR 300 plate-plate rheometer. Figure 3.3 shows the results for PP in Figure 3.3a and HDPE in Figure 3.3b. One can see that, for both polymers, the dependence of the viscosity on the shear rate is limited between  $0.1$  and  $1 \frac{1}{s}$ , then decreases with higher shear rates. The zero-shear viscosity  $\eta_0$  as a function of the temperature  $T$  in Kelvin was measured by fitting the viscosity at  $0.1 \frac{1}{s}$  to the Arrhenius-type function shown in Equation 3.0.1 [29]. The measured zero-shear viscosities along with the fits for PP and HDPE are shown in Figure 3.4, and the values of the different parameters measured during parameter characterization are summarized in Table 3.1 at the end of this chapter.

$$\eta_0(T) = A_{arrh} e^{B_{arrh}/T} \quad (3.0.1)$$

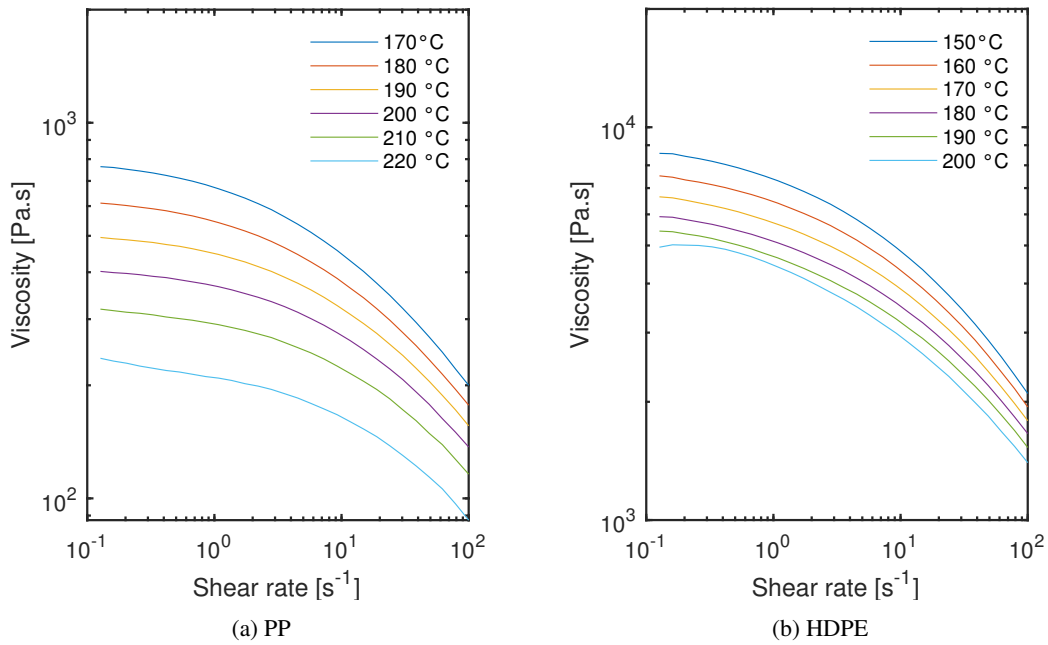


Figure 3.3: Viscosity as a function of the shear rate at different temperatures for the different polymers.

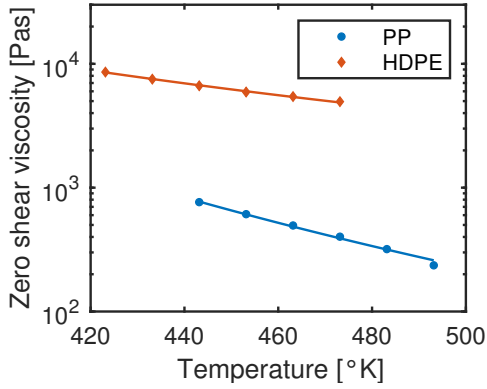


Figure 3.4: Measured zero shear viscosity as a function of the temperature and resulting fit.

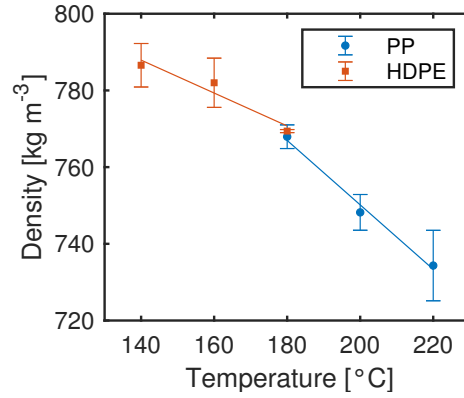


Figure 3.5: Measured molten density as a function of the temperature along with fit.

The molten densities  $\rho_m^m$  of PP and HDPE were measured at a range of temperatures with a MI-2 melt flow indexer, for each temperature three repeats were carried out. The density of the molten polymer displays a slight dependence on temperature, and was therefore fitted to the linear function  $A_\rho^m \cdot T + B_\rho^m$  with the temperature in Kelvin. The results are shown in Figure 3.5, for both thermoplastics the density decreases with more elevated temperatures, which is an expected behaviour. The solid-state densities of PP and HDPE are respectively  $906$  and  $952 \frac{\text{kg}}{\text{m}^3}$  according to the technical datasheets. Finally, the areal weight of the foils was measured to be  $0.144 \frac{\text{kg}}{\text{m}^2}$  for PP and  $0.152 \frac{\text{kg}}{\text{m}^2}$  for HDPE by cutting specimens with known dimensions with a CNC cutting machine and weighed with a precision scale.

### 3.0.2 Reinforcing fibres

The density of the fabric  $\rho_f$  was measured to be  $2524 \frac{\text{kg}}{\text{m}^3}$  with the buoyancy method using a precision scale with an immersion set-up and three samples, which is in line with typical glass fibre densities. The reinforcing textile stress response was measured with a Zwick Roell Z100 universal testing machine equipped with 135mm perforated steel. The plies were individually coated with the silicone oil Xiameter PMX 200 (Dow Europe GmbH) to obtain a similar lubricating effect as the molten polymer. The quasi-static textile stress response was fitted to the Equation 3.0.2 following suggestions by Robitaille et Gauvin [125], thereby  $\sigma$  is the textile stress response and  $\nu_f$  is the fibre volume fraction.

$$\sigma_{tex} = A_{tex} \cdot e^{B_{tex} \cdot \nu_f} \quad (3.0.2)$$

Figure 3.6 shows the fitted quasi-static stress response of a lubricated textile stack. Detailed information about the testing procedure and viscoelastic textile stress response in both dry and lubricated conditions are detailed in Section 4.

In order to accurately describe consolidation and define the proper assumptions during modelling, the first step is to investigate the microstructure of the composite. To that end, composite plates were manufactured with the quasi-UD glass textile and PEEK foils as a reference viscous matrix by press moulding under a pressure of 20 bars. The plates were then embedded in resin, polished and analysed with a Keyence VKX1100 confocal microscope as shown in Figure 3.7.



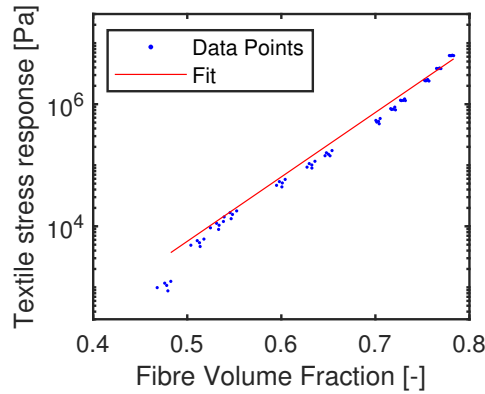


Figure 3.6: Measured quasi-static stress response points as a function of the fibre volume fraction for the textile in lubricated condition along with fit.

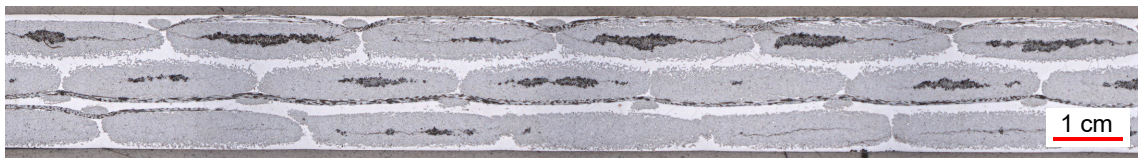


Figure 3.7: Micrograph of a plate pressed pressed with glass quasi-UD textile and PEEK foils.

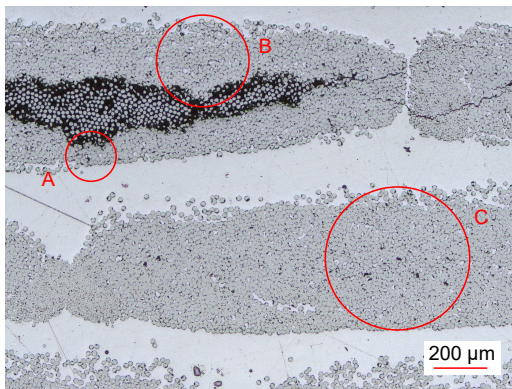


Figure 3.8: Close up of Figure 3.7 with 5x magnification, where the different zones "A", "B" and "C" are indicated.

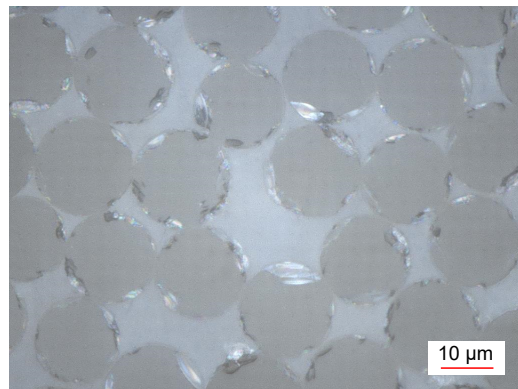


Figure 3.9: Close up of Figure 3.7 with 150x magnification.

This picture is representative of the state during consolidation as many tows are not completely impregnated and allows to make several observations. To begin with, the flow front is sharp and the tows are regularly spaced and are surrounded by polymer, in which few to no porosities are present. The tows of the quasi-UD glass fabric were found to be well described with ellipses with semi minor and major axes of respectively 0.33 and 1.1 mm. A close-up picture shown in Figure 3.8 shows local differences in flow length, which is the shortest in the zone labelled "A" and longest in the zone "B". This tends to indicate zones with respectively locally lower and higher permeability, since the matrix pressure in the inter-tow region should be homogeneous. Local changes in fibre volume fraction could very well explain changes in permeability, therefore it was measured locally. To that end, circles were manually fitted on the fibres of high-magnification pictures such as the one shown in Figure 3.9. The area of the fitted circles was then measured with the software ImageJ to infer the local fibre volume fraction, which is obtained by dividing the area

occupied by the fibres with the total area. The fibre volume fraction was respectively measured to be 0.79 and 0.76 in the zones "A" and "B" respectively, which is an expected result since higher volume fractions result in lower permeability.

A fibre volume fraction of 0.78 was measured in the zone "C", which is considered as a reference value since the microstructure is completely impregnated and thus at rest. Despite these slight local changes in fibre volume fraction and permeability, the overall impregnation profile is close to what would be expected if the tow had an homogeneous permeability, since the shape of unimpregnated zones can be well approximated as ellipses located at the center of the tows. Hence, this tends to indicate that the tow fibre volume fraction - and thus permeability - can be approximated as constant and homogeneous overall.

Another question that arises is to know how the microstructure changes with applied pressure. To investigate that effect, plates were manufactured under different applied pressures. Three layers of the quasi-UD glass fabrics were impregnated with a thermoset resin curing at room temperature with vacuum assisted resin injection (VARI). The plates were then placed in a press where pressure was applied overnight during curing. The edges of the plate were open the resin was free to bleed, which prevented pressure build-up in the resin and ensured that the whole applied pressure was transferred to the textile. Six plates were manufactured with different pressures of 1, 2.5, 5, 10, 20 and 50 bars. The plates were then cut, embedded in resin and analysed with a Keyence VKX1100 optical microscope. The results are shown in Figure 3.10, where microscope pictures of samples pressed at 1 and 50 bar are shown respectively in Figures 3.10a and 3.10b.

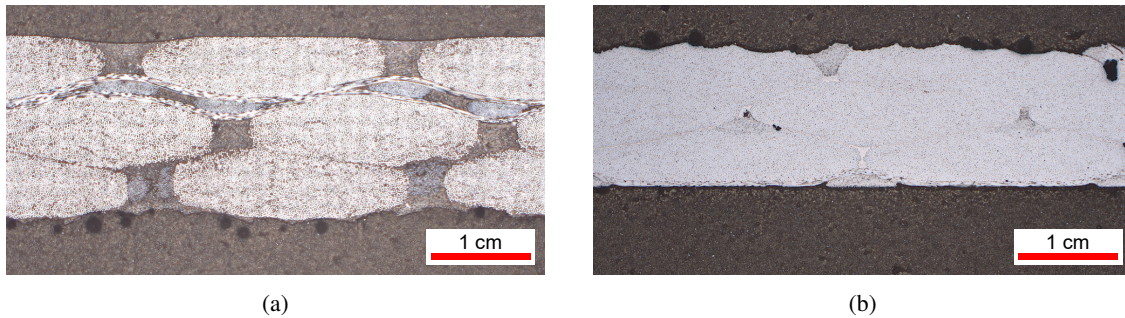


Figure 3.10: Microscope pictures of plates pressed under 1 bar of pressure in Figure 3.10a and 50 bar of pressure in Figure 3.10b.

The tows cross sections were found to still keep their elliptical geometry at elevated pressures. Manual fitting yielded semi-minor and major axes of 0.25 and 1.36 mm, indicating that the tows become slightly thinner as compared to the initial configuration in the through thickness direction and wider in the other one. These findings are in line with other studies in which tow deformation during compaction was also observed, such as Ali et al. [51]. More comprehensive measurements of the tow dimensions during consolidation are presented in Section 5, which also in line with these observations.

The fibre volume fraction of the different samples were measured with a Matlab script based on a circular Hough transform to detect the fibres. The tow fibre volume fraction as a function of the applied pressure was then fitted to a function of the form  $A_{tow}^{\nu f} \cdot \log(P_{app}) + B_{tow}^{\nu f}$  based on equation 3.0.2 by least square fitting of the error between the curve and the fit. The measured tow fibre volume fraction as a function of the pressure is shown in Figure 3.11 along with the

fit, thereby one measurement was done at each different pressure. The fibre volume fraction is found to slightly increase with increasing pressure but the dependence is weak, which is in line with previous findings. The packing of the fibres can be overall well described with a hexagonal arrangement and the fibre diameter was measured to be  $9.0 \mu\text{m}$ . All the parameters determined during the material characterization are summarized in Table 3.1.

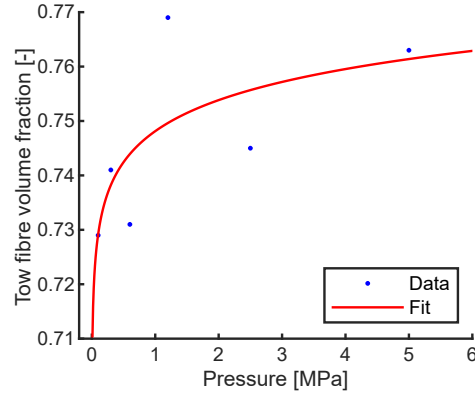


Figure 3.11: Measured and fitted tow fibre volume fraction as a function of pressure.

Table 3.1: List of the different material parameters measured during the material characterization along with their value.

Property	Variable	Material	Value	Unit
Melting temperature	$T_m$	PP	165	$^{\circ}\text{C}$
		HDPE	131	$^{\circ}\text{C}$
Zero-shear viscosity	$A_{arrh}$	PP	$1.63 \cdot 10^{-2}$	$\text{Pa}\cdot\text{s}$
		HDPE	43.4	$\text{Pa}\cdot\text{s}$
	$B_{arrh}$	PP	$4.77 \cdot 10^3$	K
		HDPE	$2.23 \cdot 10^3$	K
Density solid polymer	$\rho_m^s$	PP	906	$\text{kg}\cdot\text{m}^{-3}$
		HDPE	952	$\text{kg}\cdot\text{m}^{-3}$
Density molten polymer	$A_{\rho}^m$	PP	-0.84	$\text{kg}\cdot\text{m}^{-3}\cdot\text{K}^{-1}$
		HDPE	-0.43	$\text{kg}\cdot\text{m}^{-3}\cdot\text{K}^{-1}$
	$B_{\rho}^m$	PP	918	$\text{kg}\cdot\text{m}^{-3}$
		HDPE	848	$\text{kg}\cdot\text{m}^{-3}$
Areal weight	$A_w$	Glass textile	0.931	$\text{kg}\cdot\text{m}^{-2}$
		PP foil	0.144	$\text{kg}\cdot\text{m}^{-2}$
		HDPE foil	0.152	$\text{kg}\cdot\text{m}^{-2}$
Density of the textile	$\rho_f$	Glass textile	2524	$\text{kg}\cdot\text{m}^{-3}$
Quasi-static stress response	$A_{tex}$	Glass textile	0.03	Pa
		Glass textile	24.2	-
Tow semi-major axis	$l_w$	Glass textile	1.3	mm
Tow semi-minor axis	$l_h$	Glass textile	0.33	mm
Fibre radius	$r_f$	Glass textile	9	$\mu\text{m}$
Tow fibre volume fraction	$A_{tow}^{\nu f}$	Glass textile	$8.23 \cdot 10^{-3}$	-
		Glass textile	0.6244	-



# Chapter 4: Textile stress response

During the manufacturing of fibre-reinforced composites the fibrous reinforcement will usually be compacted to increase the fibre volume fraction and to improve the mechanical properties of the final part. In press moulding, textile compaction is intimately linked to consolidation since a part of the pressure applied on the mould is distributed on the textile. The development of a robust material model able to accurately describe textile stress response is highly desirable because it is essential for the simulation of many composite manufacturing processes, not only for press moulding but also several other manufacturing techniques such as Compression Resin Transfer Moulding (CRTM) [142], [143], Resin Film Infusion (RFI) [24], [120], [144] or direct thermoplastic melt impregnation [25], [140], [145].

The description of the mechanical behaviour of fibre textiles has been and is still an active research topic as witnessed by the rich literature dealing with this matter [71], [118], [119], [123], [124], [126]–[130], [138], [139], [146], [147], see Section 4. During the compaction of a stack of textiles the fibres are pressed together and act as elastic bending beams. Fibres and tows slide past each other to rearrange themselves, causing friction forces. The resulting nesting of the fibres and fibre bundles is thereby influenced by the lubrication of the textile. These combined effects result in a complex viscoelastic behaviour [122].

The characterization of fibre beds is no trivial task and significantly different results can be obtained with the same material depending on the testing equipment and methodology. The first international benchmark exercise on textile permeability and compressibility characterization highlighted that the main source of variation is uncertainty in the measurement of the cavity height [148], mainly due to machine compliance. To counteract this effect, methods such as that presented by Sousa and al. [149], which presented an indirect thickness measurement method, can be applied to identify and eliminate errors in cavity height measurement. During the characterization of fibre beds, several effects will cause a deviation between the prescribed and the measured strain. These different effects are listed below together with the terminology that is adopted in this work:

- **Machine compliance:** The compliance of the testing machine itself leads to errors in cavity height measurements. This is usually corrected on the basis of an empty compaction curve.
- **Machine deflection:** As the applied force decreases during relaxation, the machine deformation decreases as well, which induces a change in cavity height. This behaviour was reported by Sousa and al. [149] and could significantly impact the results but has been neglected by the analytical approach adopted by many authors.
- **Actuation error:** The deviation between the prescribed and measured cavity height caused by the controller inaccuracy. This effect especially takes place at the start and end of a compaction because the control of the machine needs to react to the measured force values.

In this chapter, the parameters of the material model are determined with a numerical approach that can overcome simplifications usually met with analytical approach and consider machine deflection and actuation error which are usually neglected. This methodology is applied to validate the three-branches Maxwell model recently proposed by Danzi [129]. Finally, the impact of neglecting machine deflection during parameter extraction on the quality of the results is investigated.

The model recently proposed by Danzi et al. [129] is distinguished by its ability to accurately model the textile stress response over a large range of strain and strain speeds. As during press moulding the compaction speed is usually not constant and because different applied pressures result in different strain speeds, this model seems all indicated. However, this model was only verified with one dry textile so that its performance with different textiles remains to be proven, both in dry and wet conditions.

In this work, the approach and methodology initially follows that proposed by Danzi et al. [129]. Therefore, a variant of the Maxwell model with three branches as shown in Figure 4.1 is considered: an elastic branch with strain dependent stiffness  $E_0(\epsilon)$ , three viscoelastic branches with strain dependent stiffnesses  $E_1(\epsilon)$ ,  $E_2(\epsilon)$ ,  $E_3(\epsilon)$  and strain-rate dependent relaxation times  $\tau_1(\dot{\epsilon})$ ,  $\tau_2(\dot{\epsilon})$  and  $\tau_3(\dot{\epsilon})$  where the subscript indicates to which branch the parameter belongs to. The branches are sorted with increasing order of relaxation time so that the first, second and third branches are responsible respectively for the short-, middle- and long-term response of the fibre bed.

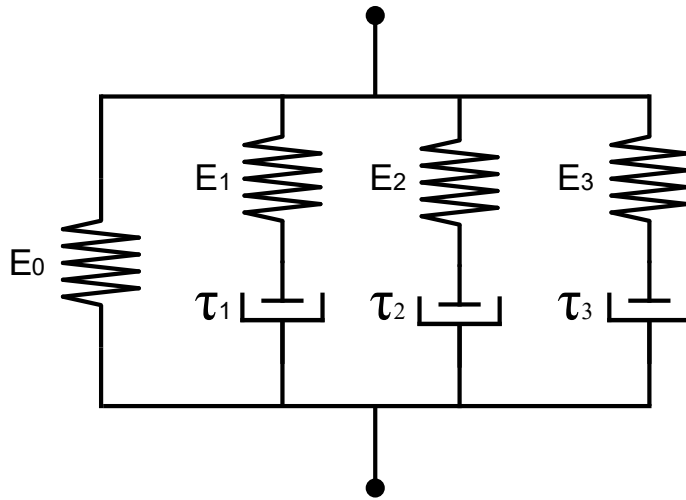


Figure 4.1: Schematic representation of a Maxwell model with three branches. The elastic branch is characterized by a single spring on the left while the viscoelastic branches consist of a spring and damper in series.

The different models presented in Section 4 generally rely on an analytical approach considering a linear generalized Maxwell model to derive nonlinear parameters. In this work, the use of a finite difference numerical approach is investigated in order to improve the data analysis and to quantify the impact of some simplifications usually taken in the analytical approach, such as the assumption of a perfectly constant strain during a relaxation experiment. For the parameter extraction small compaction steps are considered and the viscoelastic branches behaviour are ap-

proximated as linear but the elastic branch is considered non-linear. The compaction history of the textile is neglected and it is assumed that the superposition principle for multiple steps functions can be applied to derive model parameters.

## 4.1 Materials and methods

### 4.1.1 Materials

Different textile architectures based either on glass or carbon yarns have been considered to evaluate the performance of the model on a broad range of materials. Four different textiles were selected and tested in this study: a chopped glass fibres mat shown in Figure 4.2a, the quasi-unidirectional (UD) glass weave presented in Section 3 and shown in Figure 4.2b, a biaxial carbon non-crimp fabric with  $\pm 45^\circ$  fibre orientation shown in Figure 4.2c and a carbon plain weave shown in Figure 4.2d. For each of these fabrics the areal weight was measured with a scale while the density of the fabric was measured with the buoyancy method using a Kern precision scale with an immersion set-up, three samples were tested for both methods.

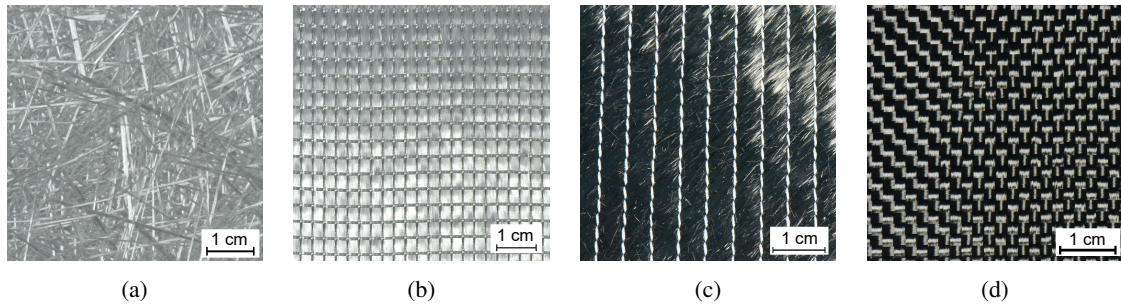


Figure 4.2: Pictures of the different textiles used for the experiments.

### 4.1.2 Experimental test setup

Single plies were cut to squares with a side length of 175 mm using a CNC cutting machine. The plies were then laid with an orientation of  $0^\circ$  to form a stack, whereby the number of plies is chosen for each material such that the total thickness is approximately 13 mm in uncompressed state. Each textile was tested in both dry and wet conditions with a Zwick Roell Z100 universal testing machine. The sample is placed between two steel plates with a diameter of 135mm as shown in Figure 4.3, whereas the bottom one is perforated and a groove allows the fluid to flow. The bottom plate contained  $\varnothing 2$  mm holes spaced with a regular distance of 4mm between each others. The grooves underneath are 2.2mm wide and regularly spaced at 3.7 mm distance. The plies were individually impregnated with the 200 cSt silicon oil Xiameter PMX 200 (Dow Europe GmbH) for wet experiments. The individual plies were then stacked and gently pressed with a roll such as to evacuate air between them.

The machine was calibrated to correct compliance prior to compression testing in order to enable a precise cavity height measurement. An empty compaction test was performed to check the quality of the compliance correction and to properly set the tool distance before each set of experiments.

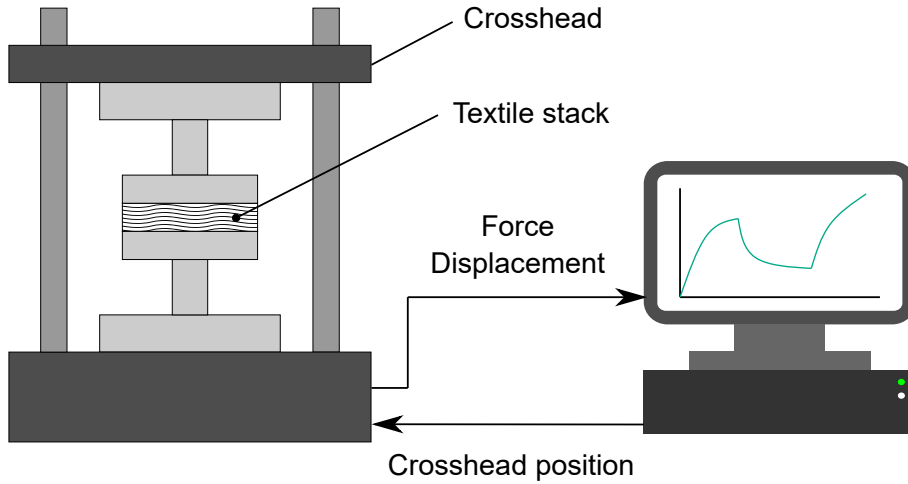


Figure 4.3: Setup of the compaction test.

### 4.1.3 Experimental testing procedure

The experimental testing procedure is based on multiple steps compaction with constant compaction velocity and variable holding times at a given position. The experiment was repeated with the following compaction velocities: 0.1, 0.5, 2.0, 6.0 and 12.0 mm/min, each time with a new textile sample. The compaction velocities were chosen such as to cover a broad range of strain speeds while taking the limits of the mechanical testing machine into account. The test is designed to gain information on the time dependent response of the fibre bed over a range of strains and strain speeds.

The testing procedure consists of twelve compaction steps covering the whole range of fibre volume fractions as summarized in Table 4.1. The compaction goes on until a defined force is reached before letting the fibre relax at constant strain for a given period of time. The stress is directly obtained by dividing the force with the compaction tool area. The stress differences at each compaction step are defined as large enough in order to guarantee a minimal tool displacement and a sufficient measurement quality but as small as possible in order to minimize changes in the viscoelastic fibre bed behaviour. This results in a greater relative stress increase at higher fibre volume fractions because of the non-linear fibre behaviour. The first, fourth, seventh and tenth compaction steps are larger steps used as transitions between different regions of fibre volume fractions and are not considered in the evaluation of the model parameters, but are used to verify that the model remains valid at larger strains. The holding time is reduced at lower fibre volume fractions to minimize the total experiment duration.

The fibre bed response is commonly described through its fibre volume fraction  $\nu_f$  rather than its strain. The fibre volume fraction is obtained with equation 4.1.1, where  $N$  is the number of layers,  $M_f^A$  the areal weight of the fabric,  $\rho$  the density of the fabric and  $h_{cav}$  the cavity height, which is measured as the cross-head displacement corrected with machine compliance. The strain is directly related to the cavity height with Equation 4.1.2 where the strain  $\epsilon$  is defined as positive with closing tool distance.

$$\nu_f = \frac{N \cdot M_f^A}{\rho \cdot h_{cav}} \quad (4.1.1)$$



$$\epsilon = \frac{h_{cav,0} - h_{cav}}{h_{cav,0}} \quad (4.1.2)$$

Thereby,  $h_{cav,0}$  is the initial tool separation distance corresponding to the stack thickness in uncompressed state. These two equations can be combined to relate fibre volume fraction and strain:

$$\nu_f = \frac{N \cdot M_f^A}{\rho \cdot h_{cav,0}(1 - \epsilon)} \quad (4.1.3)$$

Table 4.1: Overview of the multiple compaction step procedure. The 5N corresponds to the preload at the beginning of the test.

Step nr.	Maximum Force [kN]	Maximum Stress [Pa]	Holding time [s]
-	5e-3	349	0
0	20e-3	1397	30
1	0.1	$6.99 \cdot 10^3$	500
2	0.2	$1.40 \cdot 10^4$	500
3	0.3	$2.10 \cdot 10^4$	500
4	1	$6.99 \cdot 10^4$	500
5	2	$1.40 \cdot 10^5$	500
6	3	$2.10 \cdot 10^5$	500
7	10	$6.99 \cdot 10^5$	1000
8	15	$1.05 \cdot 10^6$	1000
9	20	$1.40 \cdot 10^6$	1000
10	40	$2.79 \cdot 10^6$	1000
11	60	$4.19 \cdot 10^6$	1000
12	95	$6.64 \cdot 10^6$	1000

#### 4.1.4 Model approach

A Finite Difference Method (FDM) is adopted to obtain the response of the Maxwell model, which can be assumed linear over sufficiently small intervals. The model response of a Maxwell model is the sum of the stresses of the individual branches. For the present case with three viscoelastic branches it reads:

$$\sigma = \sigma_0 + \sum_{i=1}^{i=3} \sigma_i \quad (4.1.4)$$

where  $\sigma$  is the stress, the superscript 0 denotes the elastic branch and the superscripts from 1 to 3 the viscoelastic branches. The stress response of the elastic branch is given by Equation 4.1.5. For the branches with a spring and a damper in series the viscoelastic behaviour is strain-rate dependent [150] and the stress response is described with the constitutive Equation 4.1.6.

$$\sigma_0 = E_0(\epsilon)\epsilon \quad (4.1.5)$$

$$\frac{\partial \epsilon}{\partial t} = \frac{1}{E_i} \frac{\partial \sigma_i}{\partial t} + \frac{\sigma_i}{\eta_i(\dot{\epsilon})} \quad (4.1.6)$$

$$\tau(\dot{\epsilon}) = \frac{\eta_i(\dot{\epsilon})}{E_i} \quad (4.1.7)$$

In these equations  $\epsilon$  is the overall strain and  $\sigma$  the stress. The superscript 0 denotes the elastic branch and the superscripts from 1 to 3 the viscoelastic branches.  $E(\epsilon)$  is the strain dependent Young's modulus,  $\eta_i(\dot{\epsilon})$  the strain-rate dependent viscosity of the dashpot elements and  $\tau_i(\dot{\epsilon})$  their corresponding relaxation time. With the FDM approach the derivatives are transformed into finite differences  $\delta$  and the viscoelastic branches are linearized. This implies that the parameters of these branches are constant over  $\delta t$  and the strain rate as well. Relating the dashpot viscosity with the relaxation time as expressed in Equation 4.1.7 into 4.1.6 yields:

$$\sigma_i(t + \delta t) = \sigma_i(t) + E_i \delta \epsilon_i - \frac{\sigma_i}{\tau_i(\dot{\epsilon})} \delta t \quad (4.1.8)$$

This equation can be solved if the initial conditions are known. It is assumed that the fibre bed is completely relaxed at the end of each step, contiguous to the start of the next compaction. The stress in each viscoelastic branch is therefore zero as initial conditions. Bringing together the Equations 4.1.4, 4.1.5 and 4.1.8 enables to numerically solve the Maxwell model with:

$$\sigma(t + \Delta t) = E_0(\epsilon) \epsilon + \sum_{i=1}^{i=3} \left[ \sigma_i(t) + E_i \Delta \epsilon_i - \frac{\sigma_i}{\tau_i(\dot{\epsilon})} \delta t \right] \quad (4.1.9)$$

This approach provides the stress response as a function of time if the model parameters are already known. However, there is no direct way to extract these parameters with known stress response. The measured stress response for a given strain input is therefore compared to the stress response obtained with the FDM method and a given set of parameters. The parameters are then optimized with a Simplex algorithm [151] such that the FDM model response corresponds to the measurements. The algorithm is implemented in a three dimensional manner, meaning that three parameters can be optimized at once while the others are fixed. At each iteration, the model response is calculated with the FDM method and the current set of parameters. The sum of the square differences (SSQ) between the FDM model response  $\sigma_{model}(t)$  and the measurements  $\sigma_{meas.}(t)$  is evaluated with equation 4.1.10. Based on that, the algorithm defines a new set of model parameters such as to minimize the SSQ. The iteration goes on until convergences is observed, at which point the parameters are returned as solution.

$$SSQ = \sum_{t_{start}}^{t_{end}} \left[ \left( \sigma_{tex}^{model}(t) - \sigma_{tex}^{meas.}(t) \right)^2 \right] \quad (4.1.10)$$

The sampling rate was set to make a measurement each 0.25s or if the tool displacement exceeded 10  $\mu\text{m}$ . As this time scale is one order of magnitude lower than the effects taking place in the branch with the fastest relaxation time (around 2s), the time interval is sufficiently small for the behaviour to be well approximated as linear. The approach to determine the parameters of the Maxwell model is very similar to that proposed by Danzi [129]. In the procedure that was defined, no more than three parameters are determined at once, meaning that the three dimensional optimization algorithm described above is sufficient. The properties found with the fitting algorithm at each of the compaction steps are associated with the fibre volume fraction at the beginning of the holding step.

The model parameters extraction can be separated in three stages. During the first step the strain dependent compression modulus of the elastic branch  $E_0(\nu_f)$  is extracted. Then, the Young's moduli  $E_i(\nu_f)$  of the viscoelastic branches are determined at the reference strain speed. Finally, the strain-rate dependent relaxation times  $\tau_i(\dot{\epsilon})$  are extracted. During this procedure the large compaction steps (N° 1,4,7 and 10, see Table 4.1) are not considered. Note that the Young's moduli are expressed as function of the fibre volume fraction in the following and can easily be transformed as a function of the strain using Equation 4.1.2.

**Stage 1:** Definition of the compression modulus.

The elastic branch of the Maxwell model is responsible for the quasi-static response of the fibre bed. The stress and strain values at the end of the different steps form the quasi-static compaction curve because it is assumed that the fibre-bed is completely relaxed at the end of each compaction step. This curve takes an exponential form as suggested by Robitaille and Gauvin [125] and is fitted to Equation 4.1.11. In this equation,  $A_{tex}$  and  $B_{tex}$  are fitting parameters while  $\nu_{f0}$  is the initial fibre volume fraction. The strain is calculated based on the cavity height  $h_{cav,0}$  which was measured at the preload of 5N, see Table 4.1. Fitting of the quasi-static datapoints to equation 4.1.11 allows to extract the Young's Modulus of the elastic branch  $E_0(\nu_f)$ . Due to measurements errors it can happen that a force is recorded at the measured  $\nu_{f0}$ , leading to a divide by zero in Equation 4.1.11, therefore  $\nu_{f0}$  is fitted as well rather than measured.

$$E_0(\nu_f) = \frac{A_{tex} \cdot e^{B_{tex} \cdot \nu_f}}{\left| \frac{\nu_{f0}}{\nu_f} - 1 \right|} \quad (4.1.11)$$

**Stage 2:** Definition of the Young's moduli of the viscoelastic branches.

The stiffness parameters  $E_i$  of the three viscoelastic branches are extracted with the optimization algorithm explained earlier at each compaction step of the reference speed, which is arbitrarily set to 2 mm/s. Thereby these stiffnesses are considered as constant over each compaction step. Meaningful guessed values are used for the relaxation times: 2, 20 and 200 seconds which were found to provide good fits. Using the model parameters derived in Stage 1 for the Young's modulus  $E_0(\nu_f)$  comes along with its fitting error. As a result, the measured stress might be incorrectly parted into elastic and viscoelastic stress, which will not tend towards zero for quasi-static states at the beginning and end of the compaction steps. Incorrect determination of the viscoelastic stress will perturb the optimization algorithm and cause improper parameter extraction. For this reason, a measured Young's modulus is defined for each compaction step by fitting the quasi-static values at the beginning and the end of the current step to Equation 4.1.11, where the fitted value of  $\nu_{f0}$  obtained in stage one is used. This stiffness is not constant but a function of the measured fibre volume fraction. Note that the measured Young's modulus is only used for parameter extraction and will not be part of the model.

Figure 4.4 represents the strain input imposed to the fibre bed and the corresponding measured stress response. The elastic stress response obtained with the Maxwell model on the basis of the measured and modelled Young's modulus are displayed as well. The measured stiffness yields a correct quasi-static stress response and allows a proper extraction of the measured elastic stress response. The optimization algorithm will fit the stiffness parameters to the viscoelastic response, which is the difference between the measured stress and the elastic response. The fitting procedure yields a set of stiffness parameters  $E_i$  for each compaction step. These display an exponential dependence on the fibre volume fraction and are fitted to a function of the form  $A_{tex} \cdot e^{B_{tex} \cdot \nu_f}$ . The parameter set for the second stage is summarized in Table 4.2.

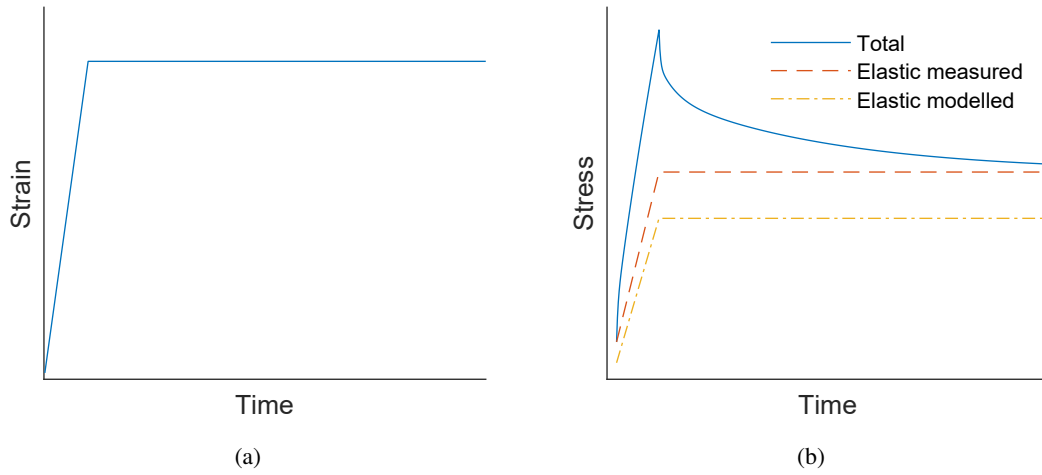


Figure 4.4: a) Representation of the strain curve imposed to the fibre bed. b) Representation of the corresponding measured stress response along with the elastic stress modelled with the FDM method based on different Young's moduli. The label "measured" indicates that the measured stiffness has been used while the label "modelled" is linked to the stiffness derived in stage one.

Table 4.2: Parameter set for the second stage.

$E_0(\nu_f)$	Approximated at each step
$E_1^i, E_2^i, E_3^i$	Fitting variable
$\tau_1=2, \tau_2=20, \tau_3=200$	Fixed parameters

### Stage 3: Definition of the relaxation times.

The third stage aims at describing the variation of the relaxation times as a function of the strain speed. The FDM model uses the same compaction modulus  $E_0$  for the same reasons, as well as the set of stiffness parameters  $E_i$  obtained in Stage 2 for the viscoelastic branches, still considered as constant over the individual compaction steps. During parameter extraction, the relaxation times are fitted to the measurements for each compaction step at the different compaction speeds with the optimization algorithm. The relaxation times are assumed constant within a compaction step. The fitted variables are then associated with the measured average strain speed at each step, which corresponds to the strain difference from the start of compaction to the start of relaxation over the elapsed time. The relaxation times with respect to the strain speed are finally fitted to a

function of the form  $A_\tau \cdot \dot{\epsilon}^{B_\tau}$ , which is found to provide a better fit than the function  $A_\tau \cdot e^{B_\tau \cdot \dot{\epsilon}}$  proposed by Danzi [129]. The parameter set for the third stage is summarized in Table 4.3.

Table 4.3: Parameter set for the third stage.

$E_0(\nu_f)$	Approximated at each step
$E_1^i, E_2^i, E_3^i$	Derived in Stage 2
$\tau_1, \tau_2, \tau_3$	Fitting variables

#### 4.1.5 Model accuracy

To quantify the accuracy of the model, the stress response of the fibre bed is calculated for each compaction step based on the measured strain with the resulting model and compared to the measured stress response. At the beginning and towards the end of a compaction step, the difference corresponds to the modelling error of the elastic branch since the viscoelastic response is negligible. However, at the peak stress the viscoelastic response is the highest and the modelling error is expected to overall reach its maximum at this point. For this reason, the model accuracy is measured at the peak stress.

The total model error is the sum of the errors emanating from the elastic and viscoelastic branches and they can add up but also subtract from each other. It is desirable to know the extent of their respective contribution to the total model error, which cannot yet be directly read from the measurements. For this reason, the measured stress response is parted into an elastic and viscoelastic part using the same method presented in the second stage based on the measured Young's modulus. At the peak measured stress, it reads:

$$\sigma_{meas.}^{max}(\epsilon, \dot{\epsilon}) = \sigma_{E,meas.}^{max}(\epsilon) + \sigma_{VE,meas.}^{max}(\dot{\epsilon}) \quad (4.1.12)$$

where the subscript meas. denotes the measured stress, max that the property is measured at the peak stress, E the elastic and VE the viscoelastic stress. The modelled peak stress obtained with the FDM method is easily parted into elastic and viscoelastic parts and it can be written as:

$$\sigma_{model}^{max}(\epsilon, \dot{\epsilon}) = \sigma_{E,model}^{max}(\epsilon) + \sigma_{VE,model}^{max}(\dot{\epsilon}) \quad (4.1.13)$$

The total relative modelling error is defined in Equation 4.1.14. The measured relative elastic error is defined in Equation 4.1.15 as the difference between the measured and modelled elastic stress at the peak stress divided by the measured peak stress. The measured relative viscoelastic error is defined in a similar way in Equation 4.1.16.

$$Error = \frac{|\sigma_{meas.}^{max}(\epsilon, \dot{\epsilon}) - \sigma_{model}^{max}(\epsilon, \dot{\epsilon})|}{\sigma_{meas.}^{max}(\epsilon, \dot{\epsilon})} \quad (4.1.14)$$

$$Error_E = \frac{|\sigma_{E,meas.}^{max}(\epsilon) - \sigma_{E,model}^{max}(\epsilon)|}{\sigma_{meas.}^{max}(\epsilon, \dot{\epsilon})} \quad (4.1.15)$$

$$Error_{VE} = \frac{|\sigma_{VE,meas.}^{max}(\dot{\epsilon}) - \sigma_{VE,model}^{max}(\dot{\epsilon})|}{\sigma_{meas.}^{max}(\epsilon, \dot{\epsilon})} \quad (4.1.16)$$

## 4.2 Results

### 4.2.1 Materials

The measured material properties are reported in Table 4.4. The densities of the fabrics are in the expected range for carbon and glass. The small deviations can arise due to different fibre types, sizing or experimental measurement errors. The textile architecture influences the fibre volume fraction and thus the number of layers required to reach a certain thickness in uncompressed state. The thickness of the glass mat is above the target value, but this is not expected to have any impact on the measured strain or outcome.

Table 4.4: Material properties of the different fabrics and measured initial sample height.

Fabric	Areal Weight [ $\frac{g}{m^2}$ ]	Density [ $\frac{kg}{m^3}$ ]	Number of layers	Sample height [mm]
Glass mat	571	2400	14	17.1
Glass quasi-UD	931	2524	16	13.8
Carbon plain weave	203	1754	45	13.3
Carbon biaxial	571	1711	14	13.9

### 4.2.2 Definition of model parameters

In the following, the analysis and illustrations describes the results obtained with the carbon plain weave in dry condition if not explicitly specified otherwise. These results are representative of the behaviour observed with the other textiles in both dry and wet conditions. Different or noticeable behaviour of the other fabrics are described when relevant for the analysis.

Figure 4.5 shows the tool distance and resulting stress value obtained for a multiple steps compaction test, which is the basis of the following analysis. Even though the initial sample thickness is similar for all the fabrics, varying final sample thicknesses are obtained because of the different textile behaviour. Still, the strain profile is comparable each time so that this is not expected to have any effect on the analysis.

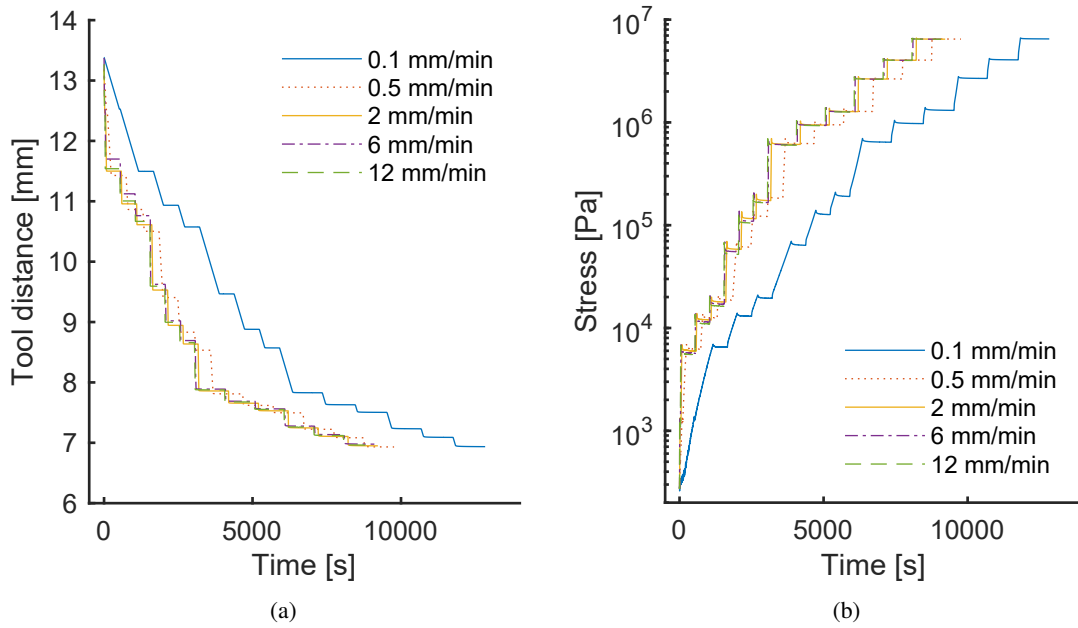


Figure 4.5: 4.5a: Tool distance as a function of time for the multiple compaction steps at different strain rates for the carbon plain weave in dry condition. 4.5b Corresponding measured stress as a function of time.

**Stage1:** Figure 4.6 shows the quasi-static stress response of the five multiple steps compaction experiments performed at different strain rates, and the resulting fitted curve. An overall good fit quality is obtained over the entire data set which spans over the whole range of fibre volume fractions. Note that the measured value typically spans over several order of magnitudes due to the exponential behaviour of the fibre beds and the measurements covering the whole range of fibre volume fractions. The fitting of the Young's moduli is performed in a logarithmic scale because it ranges over three order of magnitudes.

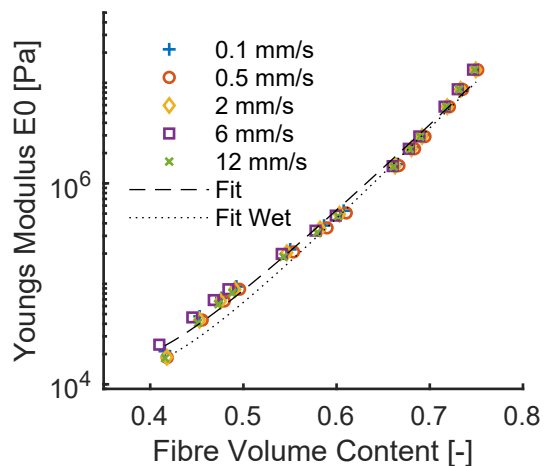


Figure 4.6: Quasi-static data points of the Young's modulus  $E_0$  in function of the fibre volume content obtained with different compaction speeds and resulting fitting curve for the carbon plain weave in dry condition. The fitting curve of the carbon plain weave obtained in wet conditions is displayed along for comparison.

The coefficients of determination  $R^2$  of the fits for the different experiments are listed in Table 4.5. An excellent fit quality, comparable for all the experiments, is obtained. Yet, a relatively elevated scatter of the measurements is also observed, which is acceptable because fibre beds are known to display such a behaviour. The fit quality is comparable in dry and wet conditions. The fibre beds display a lower stiffness in wet conditions, as observed by several authors [71]. Lubricated fibres can slide past each other and rearrange themselves more easily due to a reduced friction. Table 4.6 summarizes the fitted parameters of Equation 4.1.11 obtained for the different tests. The stiffening parameter  $B_{tex}$  is responsible for the shape of the exponential curve, the parameter  $A_{tex}$  is a simple multiplication factor and  $\nu_{f0}$  corresponds to the fibre volume fraction in uncompressed state. In the following, the subscript in the variables  $A_{tex,i}$  and  $B_{tex,i}$  refers to the branch whose property is being fitted.

Table 4.5: Resulting fit quality of the different experiments.

Material	State	$R^2$
Glass mat	Dry	0.992
Glass mat	Wet	0.996
Glass quasi-UD	Dry	0.988
Glass quasi-UD	Wet	0.991
Carbon biaxial	Dry	0.996
Carbon biaxial	Wet	0.994
Carbon plain weave	Dry	0.993
Carbon plain weave	Wet	0.992

Table 4.6: Resulting model parameters for the compression modulus  $E_0$ .

Material	State	$A_{tex,0}$	$B_{tex,0}$	$\nu_{f0}$
Glass mat	Dry	94.64	16.42	0.144
Glass mat	Wet	70.17	16.98	0.153
Glass quasi-UD	Dry	0.12	22.93	0.276
Glass quasi-UD	Wet	0.03	24.22	0.414
Carbon biaxial	Dry	1.14	19.91	0.279
Carbon biaxial	Wet	0.68	20.66	0.262
Carbon plain weave	Dry	0.71	21.23	0.333
Carbon plain weave	Wet	0.26	22.49	0.348

The stiffening parameter remains rather constant for a same material independently of its state. However, the multiplication factor decreases in wet state, indicating that the quasi-static stress response is smaller at equal fibre volume fraction. The fitted uncompressed fibre volume fractions in dry and wet states are very close to each other, except for the quasi-UD weave. The  $\nu_{f0}$  obtained are generally smaller than the fibre volume fraction measured at the preload of 5N, which is an expected behaviour considering the very low stiffness of fibre beds close to their uncompressed states. This trend is not observed for the quasi-UD glass weave in dry conditions and this behaviour is imputed to a poorer fit, also observable in Table 4.5. The values obtained at the first stage otherwise reflect an expected behaviour.

When comparing the different materials it is observed that the range of stiffnesses is rather similar and from  $10^4$  to  $10^7$  Pa in dry conditions. The carbon plain weave has a higher stiffness at low fibre volume fractions ( $2.2 \cdot 10^4$  Pa), probably because the weaving contributes to a higher initial number of contact points between bundles. The range of fibre volume fractions is changing depending on the material and degree of fibre alignment. The quasi-UD weave and the carbon bi-



axial fibres with straight fibres reach the highest fibre volume fraction at maximal load with 0.78, the carbon weave slightly less with 0.75, the glass dry fibres only 0.67 since the fibres are neither aligned nor organized. The fibre volume fraction at the preload is also significantly lower for the glass mat with a fibre volume fraction of 0.2 against 0.38 to 0.46 for the other materials.

**Stage 2:** Figure 4.7a shows an average result of the stiffness parameter extraction procedure, for which the modelled stress response is fitted to the measured one. An overall very good fit quality is observed, with higher deviation in the mid-term holding step. The long-term stress response error is rather low and corresponds to the remaining stress in the viscoelastic branches, validating the quasi-static assumption at the end of the compaction steps. It is also noted that the fit quality slightly decreases at very high fibre volume fraction, yet remains largely acceptable. The stress response of the individual viscoelastic branches of the Maxwell model for the fitted curve shown in Figure 4.7a is displayed in Figure 4.7b.

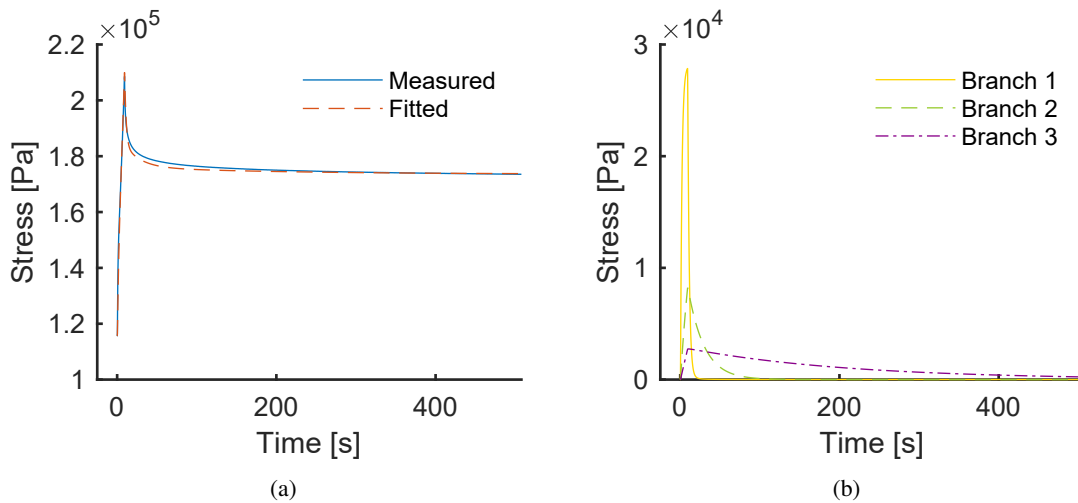


Figure 4.7: Figure 4.7a displays the measured fibre bed stress response in function of the time for the sixth compaction step at reference speed for the carbon plain weave in dry condition, along with the result of the fitting procedure. Figure 4.7b displays the stress response of the individual viscoelastic branches of the Maxwell model.

At the end of the stiffness parameter extraction, the set of relaxation times in function of the fibre volume fraction is fitted for each of the parameter  $E_1$ ,  $E_2$  and  $E_3$  as shown in Figure 4.8a on a logarithmic scale. The quality of the fit is very good for all the three branches, whose Young's moduli once again span over three order of magnitudes. For comparison, the same fit is displayed for the carbon plain weave in wet condition in Figure 4.8b. One can see that the two figures display a strikingly similar behaviour. The difference of values in dry of wet conditions are hardly noticeable because of the logarithmic scale. The stiffness is decreasing from the first to the third branch, however the amplitude of their response is comparable because of the increasing relaxation time as shown in Figure 4.7b.

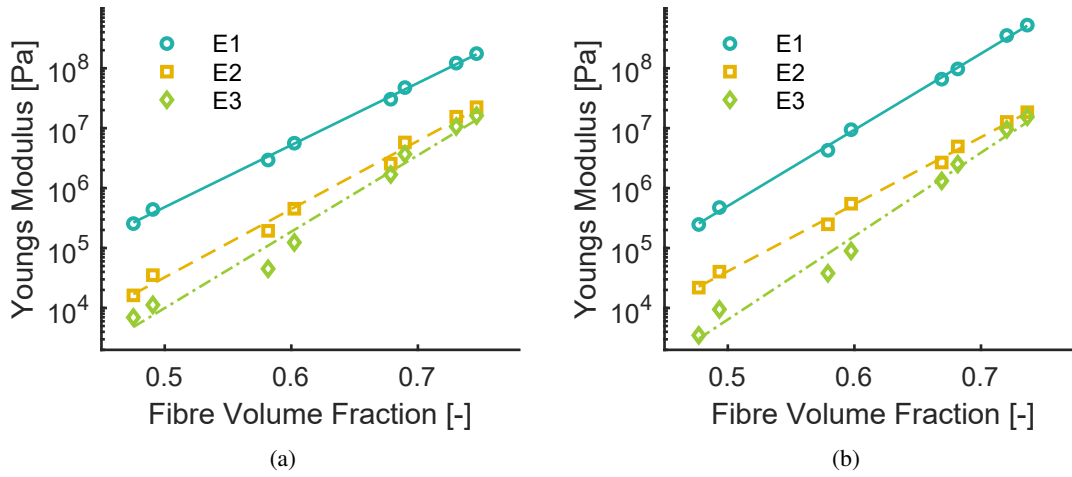


Figure 4.8: Stiffness value of the different viscoelastic branches as a function of the fibre volume fraction for the reference compaction speed of the carbon plain weave in dry condition in Figure 4.8a and in wet condition in Figure 4.8b.

Table 4.7 summarizes the result of the fitting procedure for all the samples, where similar fitting results are obtained. It is observed that the fit is usually better suited to the fibre beds in wet conditions. Such a behaviour might be explained by the fact that fibres gliding past each other can be modelled with a viscoelastic model, which is however less suited when the fibres are sliding because it is a friction-based mechanism.

Table 4.7: Resulting fit quality of the quasi-static compaction curve.

Sample	State	$R^2$ value		
		$E_1$	$E_2$	$E_3$
Glass mat	Dry	0.994	0.997	0.995
Glass mat	Wet	0.996	0.996	0.996
Glass quasi-UD	Dry	0.996	0.985	0.977
Glass quasi-UD	Wet	0.995	0.987	0.978
Carbon biaxial	Dry	0.990	0.995	0.992
Carbon biaxial	Wet	0.998	0.997	0.994
Carbon plain weave	Dry	0.999	0.992	0.977
Carbon plain weave	Wet	0.999	0.997	0.982

Table 4.8 displays the parameters resulting from the fitting of the individual viscoelastic branches for the different tests. It is observed that the stiffening factor  $B_{tex}$  is rather similar in dry and wet conditions as expected. The different materials exhibits similar viscoelastic branches stiffness behaviour over the range of measured fibre volume fraction. In uncompressed state, the dry glass mat has almost equivalent stiffnesses  $E_1$  and  $E_2$  whereas the first is about one order of magnitude larger than the latter in other textiles.

Table 4.8: Resulting model parameters for the Young's moduli  $E_i$ .

Material	State	Branch	$A_{tex,i}$	$B_{tex,i}$
Glass mat	Dry	$E_1$	99.1	23.9
		$E_2$	210	20.7
		$E_3$	17.1	24.0
	Wet	$E_1$	244	22.0
		$E_2$	271	20.1
		$E_3$	28.1	23.1
Glass quasi-UD	Dry	$E_1$	$6.01 \cdot 10^{-1}$	26.2
		$E_2$	$7.82 \cdot 10^{-3}$	29.7
		$E_3$	$3.65 \cdot 10^{-4}$	33.4
	Wet	$E_1$	$1.22 \cdot 10^{-1}$	28.1
		$E_2$	$1.36 \cdot 10^{-3}$	31.8
		$E_3$	$8.03 \cdot 10^{-5}$	35.2
Carbon biaxial	Dry	$E_1$	6.51	23.0
		$E_2$	1.57	23.2
		$E_3$	$6.53 \cdot 10^{-2}$	27.0
	Wet	$E_1$	48.7	20.5
		$E_2$	1.42	23.2
		$E_3$	$8.54 \cdot 10^{-2}$	26.4
Carbon plain weave	Dry	$E_1$	3.20	23.8
		$E_2$	$6.63 \cdot 10^{-2}$	26.2
		$E_3$	$4.20 \cdot 10^{-3}$	29.4
	Wet	$E_1$	$2.22 \cdot 10^{-1}$	29.3
		$E_2$	$1.04 \cdot 10^{-1}$	25.8
		$E_3$	$6.99 \cdot 10^{-4}$	32.1

**Stage 3:** Figure 4.9 shows a typical result of the relaxation time extraction procedure, for which the modelled stress response is fitted to the measured one. The quality of the fit is improved when compared to stage 2 since all of the parameters have been extracted. The fit quality at other compaction speeds is of comparable quality. Figure 4.9a and 4.9b compare the fit for the carbon plain weave in dry and wet conditions, one can see similar fit qualities. These two Figures also allows to observe the change of behaviour in the textile response when in wet condition, one can clearly see that the amplitude of the relaxation is more pronounced when wet.

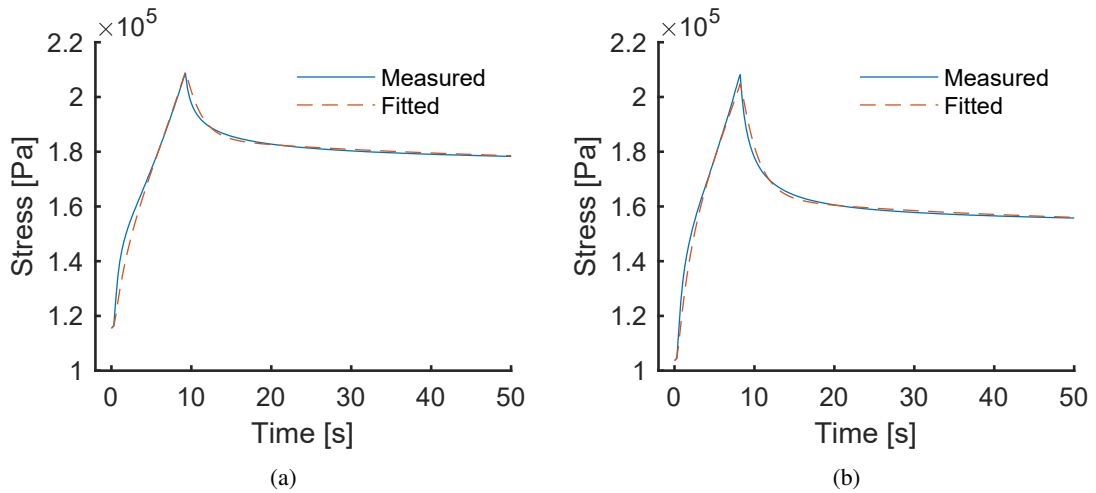


Figure 4.9: Measured fibre bed stress response as a function of the time for the sixth compaction step of the carbon plain weave in dry condition in Figure 4.9a and in wet condition in Figure 4.9b at reference speed, along with the result of the fitting procedure during the relaxation time parameters extraction.

The obtained relaxation times with corresponding measured compaction speeds have been fitted for the different viscoelastic branches as shown in Figure 4.10, which displays both the dry and the wet case. In the dry case, a fit quality which is decreasing from the first to the third branch is obtained. While for the first branch the fit is very good, it is fair for the second and poor for the third. In any cases, the mean relative error between the data points and the fit is 7.7 % so that the accuracy remains sufficient. The relaxation time for the third branch seems to depend linearly on the strain speed rather than exponentially. The reader will notice that although five different compaction velocities have been prescribed, the measured strain rates are rather dispersed. This is due to the actuation error of the machine, which tend to increase at more elevated compaction velocities. It is observed that the fit quality decreases in wet conditions, but overall the same considerations apply.

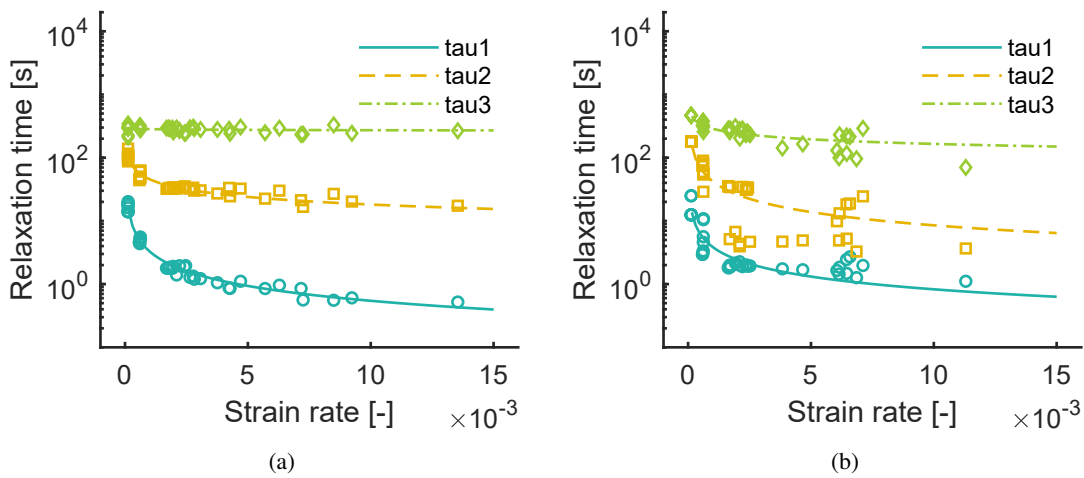


Figure 4.10: Relaxation times of the different viscoelastic branches in function of the compaction speed for the carbon plain weave in dry condition in Figure 4.10a and wet condition in Figure 4.10b.

Table 4.9 displays the  $R^2$  values of the three branches for the different experiments. Globally, the same trends and fit quality are observed in all the experiments. The carbon plain weave displays a noticeable behaviour in the fitting of  $E_3$  since the other fabrics have much better fit qualities. Table 4.10 displays the parameters resulting from the fitting of the relaxation times for the different tests. Once again, the subscript  $i$  in the fitting variable indicates to which branch does the parameter refers to. Similar trends and no particular differences between the relaxation times of the different materials are observed.

Table 4.9: Resulting fit quality of the quasi-static compaction curve.

Sample	State	$R^2$ value		
		$\tau_1$	$\tau_2$	$\tau_3$
Glass mat	Dry	0.831	0.706	0.420
Glass mat	Wet	0.860	0.803	0.766
Glass quasi-UD	Dry	0.914	0.608	0.466
Glass quasi-UD	Wet	0.905	0.582	0.355
Carbon biaxial	Dry	0.962	0.731	0.315
Carbon biaxial	Wet	0.905	0.750	0.304
Carbon plain weave	Dry	0.966	0.929	0.059
Carbon plain weave	Wet	0.775	0.963	0.854

Table 4.10: Resulting model parameters for the relaxation times  $\tau_i$ .

Material	State	Branch	$A_{\tau,i}$	$B_{\tau,i}$
Glass mat	Dry	$\tau_1$	$2.04 \cdot 10^{-2}$	0.73
		$\tau_2$	1.61	0.46
		$\tau_3$	178	$6.26 \cdot 10^{-2}$
	Wet	$\tau_1$	$6.79 \cdot 10^{-2}$	0.59
		$\tau_2$	1.37	0.50
		$\tau_3$	120	0.13
Glass quasi-UD	Dry	$\tau_1$	$1.46 \cdot 10^{-2}$	0.78
		$\tau_2$	5.34	0.30
		$\tau_3$	188	$5.81 \cdot 10^{-2}$
	Wet	$\tau_1$	$1.16 \cdot 10^{-2}$	0.81
		$\tau_2$	4.35	0.32
		$\tau_3$	173	$6.43 \cdot 10^{-2}$
Carbon biaxial	Dry	$\tau_1$	$1.73 \cdot 10^{-2}$	0.77
		$\tau_2$	3.18	0.38
		$\tau_3$	204	$4.72 \cdot 10^{-2}$
	Wet	$\tau_1$	$2.19 \cdot 10^{-2}$	0.71
		$\tau_2$	1.46	0.49
		$\tau_3$	149	$8.24 \cdot 10^{-2}$
Carbon plain weave	Dry	$\tau_1$	$1.49 \cdot 10^{-2}$	0.78
		$\tau_2$	2.88	0.40
		$\tau_3$	252	$1.71 \cdot 10^{-2}$
	Wet	$\tau_1$	$3.79 \cdot 10^{-2}$	0.67
		$\tau_2$	0.34	0.70
		$\tau_3$	54.7	0.24

**Modelling Error:** The quality of the model is appreciated by modelling the stress as a function of time for the different compaction steps based on the measured strains before weighting it against the measured stress curves. Figure 4.11 shows an example highlighting the difference between the modelled and measured stress, in this case for a large compaction step. Note that the difference between the curves towards the end of the compaction step is entirely due to fitting inaccuracies of  $E_0$ , which can be an important source of discrepancy between measurements and predictions.

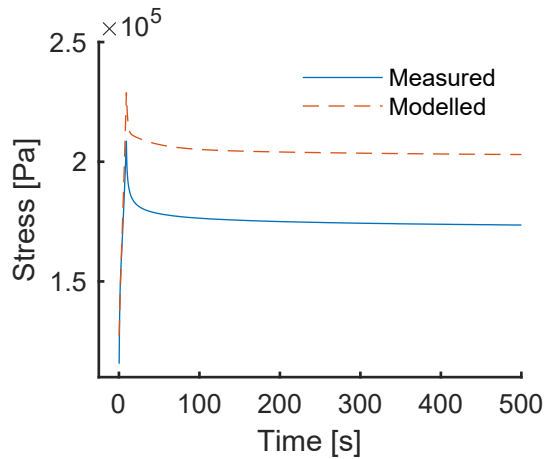


Figure 4.11: Measured and modelled stress in function of the time for the sixth compaction step at reference speed for the carbon plain weave in dry condition.

Figure 4.12 displays the modelling error averaged over the different compaction speeds in Figure 4.12a and the compaction steps in Figure 4.12b. Little variation of the model accuracy over the whole range of the compaction speeds is observed. As the viscoelastic response becomes larger at more elevated strain speeds, its contribution to the modelling error raise as well. When averaged over the different compaction steps, it is observed that the modelling error has important discrepancies. This behaviour can be explained on one hand by the different fit qualities which can change from location to location. On the other hand, the total error is the sum of the errors of the elastic and viscoelastic branches, which can either add up or cancel each other.

In Figure 4.12b the results for the large compaction steps - the first, fourth, seventh and tenth step - do not stand out, validating the model even at larger strains. Overall, the mean modelling error amounts to 12.98 %, which is very accurate considering that fibre beds displays large discrepancies in their behaviour.

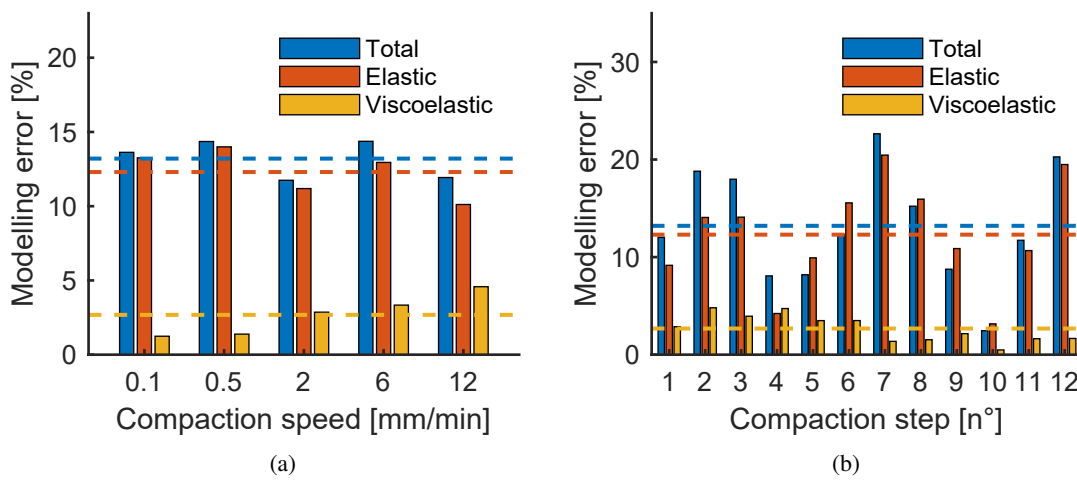


Figure 4.12: Figure 4.12a shows the mean modelling error over different compaction speeds for the carbon plain weave in dry condition and Figure 4.12b. The dashed line is the overall mean modelling error.

Analytical models as presented in [128] [129] [126] assume a perfectly constant strain during relaxation, and many present constitutive equations based on a generalized linear Maxwell model where the stiffness  $E_0$  is assumed constant over a small compaction step. As small variations in strain during relaxation are considered, assuming a constant elastic stiffness  $E_0$  is not reasonable because of its exponential behaviour. The numerical method presented thus considers the measured strain and introduces a variable stiffness  $E_0(\nu_f)$  to correctly model the elastic stress. This results in a better parameter extraction as the measured stress is more accurately parted into elastic and viscoelastic stress. The stiffnesses of the viscoelastic branches are yet still assumed constant during the parameter extraction and the compaction steps are kept as small as possible for this reason. The impact of this assumption is thought to be rather small but should still be quantified in future work.

Table 4.11 displays the mean modelling error of the different experiments. The accuracy of the viscoelastic model is globally lower when applied to wet fibre beds. Albeit this decreasing accuracy, the modelling errors are deemed to remain fully acceptable. It is supposed that the variations of the mean modelling errors between the different materials either in dry or wet conditions are mainly due to statistical effects. It is very interesting to note that while for some fabrics the

main source of modelling error comes from the elastic branch, for others it is the viscoelastic ones. One should also keep in mind that as the viscoelastic stress response becomes larger, the modelling error repartition will shift towards the viscoelastic part according to equations 4.1.15 and 4.1.16.

Table 4.11: Resulting modelling accuracy of the different samples.

Material	State	Mean Modelling Error [%]		
		Total	Elastic	Viscoelastic
Glass mat	Dry	16.38	8.57	11.58
Glass mat	Wet	13.32	6.64	11.52
Glass quasi-UD	Dry	18.38	13.13	5.79
Glass quasi-UD	Wet	13.82	11.37	5.40
Carbon biaxial	Dry	12.38	7.77	7.37
Carbon biaxial	Wet	20.19	8.94	14.12
Carbon plain weave	Dry	12.98	12.30	2.31
Carbon plain weave	Wet	18.68	10.51	14.10

### 4.2.3 Influence of strain deviations

Significant differences between the prescribed and the measured strains were noticed, especially at higher loads. This behaviour is thought to be primarily caused by a combination of machine deflection and actuation error. Machine deflection can be well observed in Figure 4.13, where one can see the measured strain significantly deviating from the prescribed strain during relaxation. Regarding the actuation error, it is observed that the measured average strain speed considerably differs from the prescribed one at elevated loads and strain speeds. This indicates that the testing machine is getting closer to its limits. An analytical approach is mostly adopted in the literature, in which the assumed ideal strain profile is based on the strain profile prescribed to the machine, yet high discrepancies between the prescribed and measured strain profiles are noted. Although analytical methods could be based on the measured average strain speed instead of the prescribed one, this is not a standard practice. It is also observed that the strain speed is not perfectly constant during compaction, which is another consequence of actuation error that is not considered in analytical methods.

To investigate the effects of strain deviations on the results, the model parameters at reference were extracted with the assumed strain as input to the FDM model at each step. The assumed strain profile consists of a compaction at constant strain rate until the strain value corresponding to the measured fibre volume fraction at the end of relaxation is reached. The strain rate is set at the measured strain rate. Then, a constant strain is assumed until the end of the relaxation step. An example of the assumed strain profile is shown in Figure 4.13, as compared to the prescribed strain and the measured strain. The stress response was modelled based on the measured strain and the extracted model parameters and compared to the measured stress. The modelling error was calculated with the same procedure as mentioned earlier. The elastic parameters are not affected by actuation error and thus only the viscoelastic modelling error are considered.

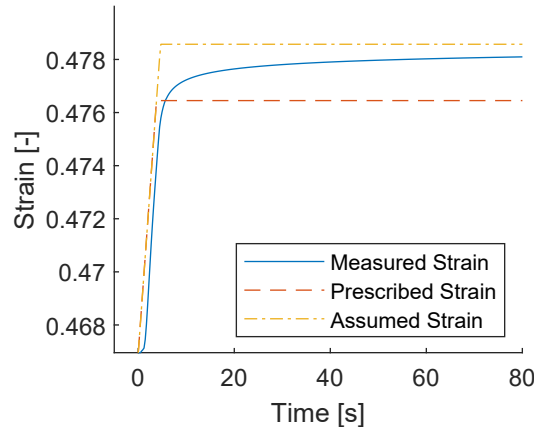


Figure 4.13: Strain as a function of time during a compaction step, as prescribed to the testing machine, as assumed for the analytical model and as measured for the twelfth compaction step at reference speed for the carbon plain weave in dry condition.

Figure 4.14 displays an example of measured viscoelastic stress along with two stress curves modelled based on the measured strain profile and parameters extracted either with the measured or assumed strain profile. As one can see, the difference between the two stress curves is consequent and the analytical method yields far less precise results. This highlights the necessity to consider the effects of strain deviations during parameter extraction to accurately describe the viscoelastic behaviour of textiles. Using an assumed ideal strain will otherwise result in erroneous model parameter definition and incorrect stress modelling of the fibre bed.

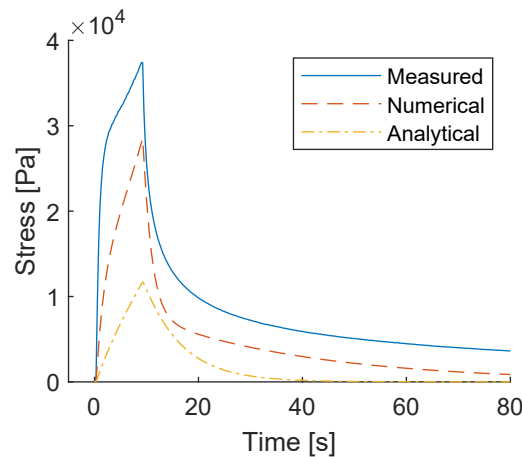


Figure 4.14: Measured viscoelastic stress along with the stress modelled based on the parameters extracted with the numerical and analytical methods for the sixth compaction step at reference speed for the carbon plain weave in dry condition.

In Figure 4.15 the viscoelastic modelling error obtained numerically (measured strain) and analytically (assumed strain) are compared. The viscoelastic error increases by a factor higher than three if the actuation error from the machine is not considered. A significantly greater modelling error is obtained with the numerical method even for the first compaction steps with low stress levels, which is unexpected. The difference between the numerical and analytical modelling error is rather constant over the range of applied loads and compaction speeds as one can see in Figure 4.15b. Another interesting observation is that the relaxation times are closer to a constant value



when extracted with the measured strain profile, as it should be according to the model assumptions. This behaviour is certainly based on the fact that the measured and assumed strain speed can significantly differ from each other. The same analysis was repeated for all the experiments and the results are reported in Table 4.12, where the same trends are observed for all experiments.

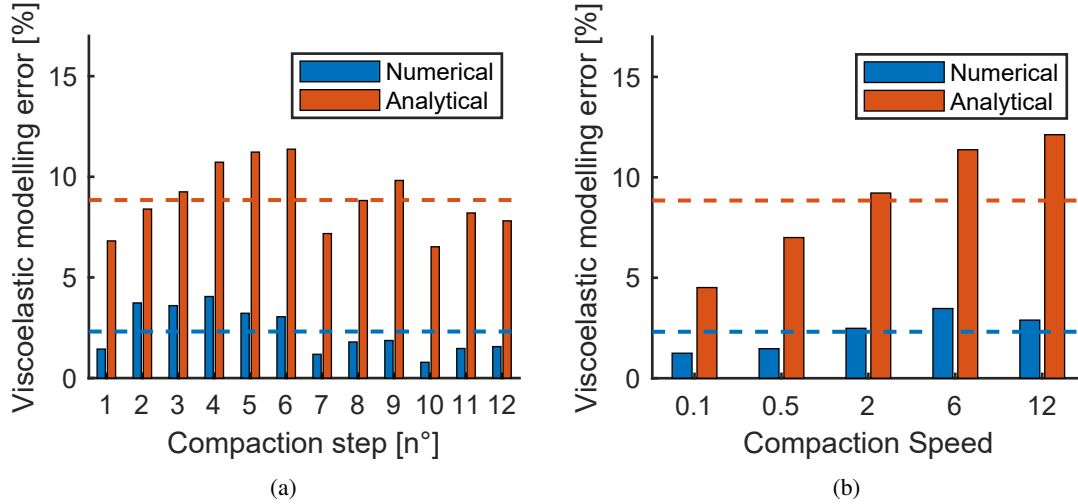


Figure 4.15: Viscoelastic modelling error with parameters extracted based on the measured (numerical) and assumed (analytical) strain for the carbon plain weave in dry condition. Figure 4.15a shows the viscoelastic modelling error over the compaction steps and Figure 4.15b over the compaction speed. The dashed line is the overall mean viscoelastic modelling error.

Table 4.12: Resulting modelling accuracy of the different samples.

Material	State	Mean Viscoelastic Modelling Error [%]	
		Numerical	Analytical
Glass mat	Dry	11.58	26.45
Glass mat	Wet	11.52	22.30
Glass quasi-UD	Dry	5.79	7.80
Glass quasi-UD	Wet	5.40	10.85
Carbon biaxial	Dry	7.37	16.40
Carbon biaxial	Wet	14.12	19.56
Carbon plain weave	Dry	2.31	8.85
Carbon plain weave	Wet	14.10	14.86

It is known that precise measurement of the tool distance is necessary for accurate compaction tests. The previous findings underly the importance of both correct strain and strain rate measurement. However, the extent of the effects of strain deviations is noteworthy. Hence, more accurate methods should be used in future works such as the one proposed by Sousa and al. [149], which measures both loading and unloading compliance. In addition, one should carefully consider the limits of the testing equipment as the imposed strain speed might not be constant during compaction or deviate from the prescriptions.

### 4.3 Summary

In this chapter, the use of a non-linear variant of the three-branches Maxwell-Wiechert model with strain dependent stiffnesses and strain-rate dependent relaxation times as proposed by Danzi et al. [129] in order to model the compressive behaviour of several textiles as a function of strain and strain rate was validated. A method to numerically solve the model by linearizing it over small time intervals was proposed, allowing to calculate the textile response for any strain profile. It was demonstrated that the model yields accurate results over a wide range of textile architectures and fibre volume fractions in both dry and wet conditions considering the large variability of fibre beds.

A numerical method for parameter extraction overcoming simplifications usually met in analytical models such as a constant Young's modulus  $E_0$  and an ideal strain profile is presented and validated. The parameter extraction is based on the measured strain profile rather than the prescribed one as both can differ due to machine deflection and actuation error. This method also enables model validation with any strain profile, which should be considered in future research. Because in the approach that is followed, presented by Danzi [129], only three parameters are optimized at once, the global minimum is not guaranteed to be found. In addition, it has not been established that the necessary and sufficient conditions for the simplex algorithm to find the global minimum are present. However, the quality of the fits that are presented in this work proves the validity of the approach and suggests that the improvement provided by finding the global minimum is rather small.

The model presented here does not take into account any effects related to cyclic compaction, which have a direct influence on the textile compaction response [71], and therefore only applies to textiles which have not been subjected to multiple compaction/ decompaction cycles. The model is rather intended for processes where the textile will be subjected to a single compaction such as encountered in press moulding, CRTM or RFI. Processes with a wide range of strain, strain speeds and strain profiles can be modelled. Regarding that, the influence of the compaction history on the results should be quantified in future work to evaluate its effect, which may probably very much depend on the textile architecture. It remains to be verified if the developed model remains valid for relaxation, which would enable other applications such as direct thermoplastic melt infusion.

It is observed that the measured strain profile differs from the prescribed one in terms of total strain and strain rate, moreover the strain rate is not perfectly constant during compaction. It is shown that strain deviations resulting from machine compliance and actuation error have an important impact that can skew the viscoelastic parameter extraction if not considered, resulting in incorrect modelling of fibre beds stress response. This is detrimental for the manufacturing techniques which require knowledge about the fibre bed stress response such as press moulding, CRTM [142], [143], RFI [24], [120], [144] or direct thermoplastic melt impregnation [25], [140]. It is found that the viscoelastic modelling error drastically decreases when considering strain deviations, and therefore advocate for the necessity of doing so. Another consequence of these results is that strain deviations in the tool should be considered during manufacturing.

Because the measurements are so sensitive on the tool distance and strain, LVDT or more accurate methods such as proposed by Sousa and al. should be used. Further improvements on the model include for instance the consideration of fluid pressure in fast compaction similar to the method proposed by Saunders [152]. Saunders investigated the fluid pressure in unperforated plates where the flow takes place in-plane. In this study the perforated bottom plate allows fluid evacuation at the bottom of the sample additionally to the sides and the flow mainly takes place in the through-thickness direction. The fluid pressure build-up is much smaller in that case because of the shorter flow lengths. However, at very high compaction speeds and elevated loads, which are significantly decreasing the ability of the fluid to flow in a time-scale comparable to the experiment, the pressures might not be completely safe to neglect and this issue should be examined in future work. Besides the flow lengths, the pressure build up also depends on the through-thickness permeability of the textile so that textiles with a lower permeability are more sensitive to such effects. Additionally, it should be investigated if actuating the crosshead during relaxation such as to keep the cavity height constant is feasible. The very accurate actuation required at elevated loads might be beyond the capabilities of the actual testing machines so that actuation error might still remain a burden that cannot be completely eliminated and needs to be dealt with. However, the actuation of submicron-milling machines or atomic-force microscopes is very precise but probably quite expensive. Finally, an analysis of the influence of actuation error on the measurements can be repeated with other models or fields using similar methods.



# Chapter 5: Consolidation model

An increasing attention has been given lately to alternative techniques for the manufacture of Fibre-Reinforced Thermoplastics (FRTP), as cost reductions for the production of structural parts are sought. Thus, novel techniques such as direct-thermoplastic melt impregnation [25], [153], stamp forming of hybrid bicomponent fibres [154] or resin transfer moulding with spacers and high-fluidity thermoplastics [155] have been investigated. Other manufacturing routes generally rely on hybrid systems, meaning that the fibres and thermoplastic are blended at different scales, usually mesoscopically at the ply or microscopically at the tow level.

In hybrid textiles the polymer and the reinforcing fibres are mingled mesoscopically at the textile level, in hybrid side-by-side textiles for example the reinforcing fibre plies and thermoplastic plies are alternatively stacked as shown in Figure 5.1. If flexible thermoplastic plies such as veils are used, the drapeability of the textiles facilitates the production of semi-complex parts. Mingling at the textile level results in lower semi-finished product costs since no microscale homogenization is required but also results in longer impregnation times because of the longer matrix flow length. Nonetheless, Reynolds et al. [10] recently investigated rapid isothermal stamp forming of multilayered textile and thermoplastic veils and proved that this process could produce structural parts within a cycle time of 330 s. Another process suitable for the consolidation of hybrid textiles is two stage press moulding, in which the composite placed into a mould is consolidated in the hot stage of the press before being cooled down under pressure in the cold stage.



Figure 5.1: Picture of a hybrid side-by-side textile based on quasi-unidirectional carbon fibres and polyetherimide veils [156]. The textile stack has a partial and staggered cutaway, unveiling the different layers of the stack.

A robust consolidation model is of great importance in these processes for correct parameter setting without trial and error, to correctly estimate void content resulting from incomplete tow impregnation or even for process optimization. A large body of work dealing with consolidation in composite manufacturing and its related aspects is found in literature, several of them specifically deal with the impregnation of tows in hybrid textiles. In these models Darcy's law [19] for saturated flow in porous media is systematically used to model matrix flow in fibre bundles as detailed in section 2.1. Thereby, permeability is a key parameter, yet very difficult to directly measure for tows. Hardly any method to directly measure tow permeability nor related results were presented

so far [54], [157]. In the literature that parameter is mostly predicted with models, which are heavily influenced by the tow fibre volume fraction. However, permeability models have never been validated at the tow fibre volume fractions which are found in practice as detailed in section 2.3.

A wide variety of consolidation models with different approaches were developed as explained in detail in section 2.7. Thereby, the consensus is that at elevated pressures the change in permeability is rather small [55], [136], [158] as large pressures are required to obtain small changes in tow fibre volume fractions as documented by Gutowski et al. [37] for aligned graphite fibres. The different modelling approaches for the impregnation of tows were mostly developed and validated for a specific type of intermediate material architecture such as film stacking or micro-braided textiles. One could argue that consolidation models should in principle be valid for all the different kinds of hybrid textiles since the consolidation kinetics are very similar, the main phenomena always being the impregnation of fibre tows. Yet, no model was validated for different kinds of hybrid textiles. Hence, a direct comparison of the different consolidation models is overall lacking. Moreover, for hybrid textiles no validation over the entire impregnation process has been yet reported. For this reason, preliminary consolidation experiments aiming at measuring the impregnation degree as a function of the time were conducted and large discrepancies between model predictions and experimental measurements were found.

Entrapped air was suspected to be responsible for these divergences, despite most of the authors assuming that air could freely escape the tow. Others, such as Bernet et al. [34] in their model about the consolidation of commingled yarns, introduced a threshold during impregnation after which the air gets entrapped. Rozant et al. [100] considered that air was trapped in the tows during the whole process in their model about the consolidation of knits. The dissolution of air was however not considered and it is interesting to notice that in their experimental validation the void content decreases continuously with longer consolidation times while the model predicts a constant value as shown in Figure 5.2.

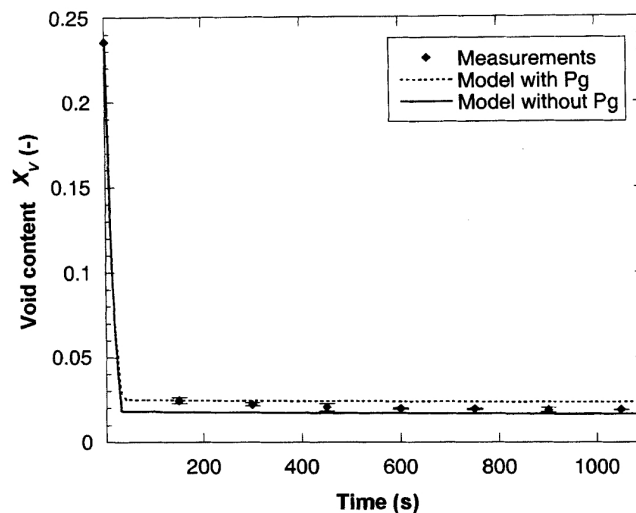


Figure 5.2: Measured void content as a function of the consolidation time along with model predictions with and without taking into account air pressure  $P_g$ . One can see that the measured void content continuously decreases while it remains constant in the model predictions. Reproduced with permission from [100].

Air dissolution and diffusion was deemed necessary to be considered in order to reflect the fact that full impregnation is reached eventually, given enough pressure is applied during consolidation for a sufficient period of time, requiring development of a new consolidation model taking it into account. While the dissolution and diffusion of volatiles has been the subject of a number of studies [95], [159], [160], the models usually consider the formation of bubble in pure liquids [85], [92] and are focused on thermosets as explained more in detail in section 2.4. Despite several studies highlighting the difficulty in obtaining full consolidation in fibrous reinforcements for FRTP [99], [131], only few researchers addressed bubble formation and gas diffusion in fibrous reinforcement. Lundström & Gebart [97] modelled void collapse during resin transfer moulding and experimentally determined a geometric correction factor that accounts for the reduced diffusion in bundles since the fibres are almost impermeable. Several studies addressed the diffusion in porous media and proposed correction factor for diffusion, however most focused on gas diffusion and the effect of more complex geometrical effects on diffusion such as fibre tortuosity is not well understood.[161]–[163]. Therefore, for the processing of thermoplastic composites there is an overall a lack of studies and models when it comes to bubble formation and collapse, air dissolution and diffusion, especially in fibrous reinforcements.

In this chapter, an analytical consolidation model for hybrid textiles is presented. The main novelty lies in the ability of the model to consider air entrapment, dissolution and diffusion. Because voids are almost exclusively located in the unimpregnated region of the tow, void formation and content can also be predicted. Correct prediction of the final void content is relevant in composite production as it is detrimental to mechanical properties [84], [164]. The model presented here is restricted to hybrid textiles with woven reinforcement as impregnation of aligned fibre tows is considered as the main mechanism driving consolidation. Existing diffusion models are applied and extended to the diffusion of dissolved species in fibrous reinforcement by adding a correction diffusion factor which is determined experimentally. The model is experimentally validated for film stacking with two different thermoplastics and at different pressures. The model presented in this study is intended for high-performance hybrid textiles and will be validated and extended to those materials in a second stage. In addition, the validity of the model of Gebart [43] for permeability predictions at very high fibre volume fraction is investigated by directly measuring tow permeability with a customized permeability jig. The influence of air entrapment and dissolution on the consolidation kinetics are evaluated, along with other parameters including permeability and effective diffusion coefficient.

## 5.1 Model approach

### 5.1.1 Process description

At the beginning of the manufacturing process several plies of hybrid textile are stacked in the mould, each at the desired location and with the desired orientation. At this stage the space between the textile and the polymer film forms air channels at the meso scale. The mould is then placed in a heated press until the process temperature is reached before applying pressure for a given amount of time. In the two-stage press process the mould is subsequently moved to the cold stage while in variotherm press moulding the mould is cooled down. In both processes, cooling down is performed under pressure. Demoulding finally allows yield of the consolidated part.

### 5.1.2 Initial conditions

During heating up the thermoplastic melts and air starts to diffuse in it, this goes on until the process temperature is reached. Considering the relatively intimate contact between air and thermoplastic and the resulting short flow lengths, it is assumed that the molten thermoplastic has reached the saturation concentration at atmosphere pressure at the beginning of consolidation. As pressure is applied on the mould consolidation begins: as the meso structure collapses the molten thermoplastic will fill the inter-tow space, thereby the air originally located there gets displaced inside the tows as represented in Figure 5.3. Therefore, dry tows with an amount  $n_\lambda^0$  of entrapped air in moles per unit depth and an inter-tow space filled with molten matrix are considered as initial situation.

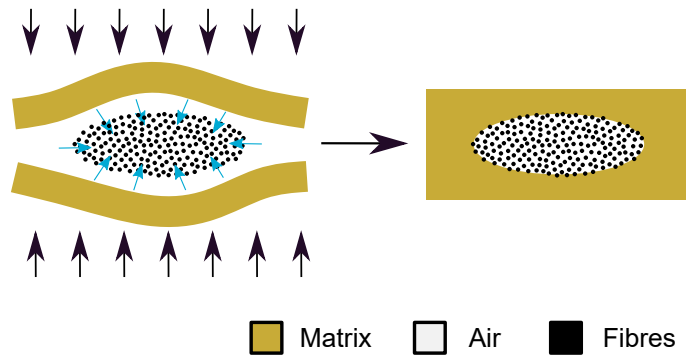


Figure 5.3: Schematic representation of the initial situation on the left. The meso structure starts collapsing as pressure is applied and air is pushed inside the tows, which results in matrix rapidly filling the inter-tow space as shown on the right. The code color for the different phases is kept throughout the article.

The amount of air initially present in the textile is approximated to be the same as the amount of air in a stack of pure, uncompact reinforcing textile. Assuming that the air is equally distributed in the tows,  $n_\lambda^0$  reads, as detailed in Appendix A:

$$n_\lambda^0 = \frac{P_{atm} \cdot A_{tow} \cdot (1 - \nu_{f,0}) \cdot \nu_{f,tow}}{R \cdot T_0 \cdot \nu_{f,0}} \quad (5.1.1)$$



Thereby,  $P_{atm}$  is the atmospheric pressure,  $A_{tow}$  the cross-section of a tow,  $\nu_{f,0}$  the fibre volume fraction of a reinforcing textile stack at rest,  $\nu_{f,tow}$  the fibre volume fraction inside the tows,  $R$  the ideal gas constant and  $T_0$  the initial temperature at the time of entrapment. For tows with elliptical shapes with semi major and minor axes  $l_w$  and  $l_h$  the cross-section area is given as:

$$A_{tow} = \pi \cdot l_h \cdot l_w \quad (5.1.2)$$

### 5.1.3 Impregnation

In the proposed approach it is assumed that the conditions do not vary along the fibre direction. Impregnation of textiles is represented by a two dimensional tow surrounded by a bath of molten thermoplastic as represented in Figure 5.3. The underlying assumptions are that the whole surface of the tows is in contact with the matrix, implying that the tow impregnation behaviour is not influenced by neighbouring tows. In addition, there is no gas transport in fibre direction in the unimpregnated region of the tow. Moreover, it implies that the consolidation dynamics in a single average tow are representative of the behaviour at the macro scale. Such an assumption could be violated for example in a textile with large discrepancies in the dimensions of the tow cross-sections as smaller tows will be impregnated faster than the larger ones.

Further assumptions are that the tows have homogeneous fibre volume fraction and permeability, that the matrix pressure in the immediate surrounding of the tow is homogeneous and that the flow front is sharp. Tow dimensions are assumed constant as possible change of tow geometry with applied pressure and its influence on impregnation are neglected. Furthermore, it is assumed that the gas is trapped only in the unimpregnated region of the tow and not in the matrix.

Darcy's law [19] is applied to describe impregnation of the tow, in which the flow front velocity  $u$  is related to the tow permeability  $K_{tow}$ , the tow fibre volume fraction  $\nu_{f,tow}$ , the fluid viscosity  $\eta$  and the pressure gradient  $\nabla P$  as following:

$$(1 - \nu_{f,tow}) \cdot u = -\frac{K_{tow}}{\eta} \nabla P \quad (5.1.3)$$

No analytical solutions to this equation are known for elliptical shapes which tows typically have. Van West et al. [135] proposed to solve impregnation for a cylinder with equivalent hydraulic radius, which was found to have equal fill time. The radius  $R_{eq}$  of the equivalent circle is given by:

$$R_{eq} = \sqrt{2} \frac{l_w \cdot l_h}{\sqrt{l_w^2 + l_h^2}} \quad (5.1.4)$$

A schematic of a partially impregnated tow and its equivalent geometry is shown in Figure 5.4, where  $r$  is the radial distance to the flow front in the equivalent geometry.

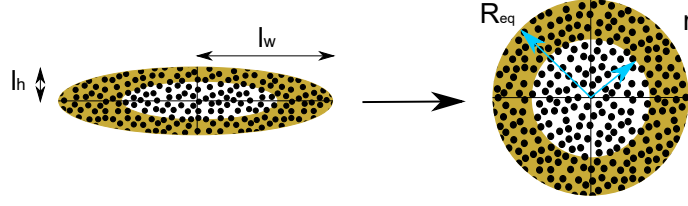


Figure 5.4: Schematical representation of an elliptical tow cross-section on the left and its equivalent cylindrical shape according to Van West [135] on the right.

Darcy's law can be resolved for that equivalent circular geometry, as detailed by Bernet et al. [34], thereby mass is conserved:

$$r \cdot \ln \left( \frac{r}{R_{eq}} \right) \dot{r} = \frac{K_{tow}}{\eta \cdot (1 - \nu_{f,tow})} (P_m + P_c - P_g) \quad (5.1.5)$$

where  $P_m$  is the matrix,  $P_g$  the gas and  $P_c$  the capillary pressure and the term  $(P_m + P_c - P_g)$  will be referred to as the driving pressure. In this article, the capillary pressure is not considered because it is negligible in comparison to the elevated matrix pressures typically occurring during the consolidation of FRTP [34]. The transverse tow permeability  $K_{tow}$  is found analytically with the model of Gebart [43], which reads for an hexagonal arrangement:

$$K_{tow} = \frac{16}{9\pi\sqrt{6}} \left( \sqrt{\frac{\pi}{2\sqrt{3}\nu_{f,tow}}} - 1 \right)^{\frac{5}{2}} r_f^2 \quad (5.1.6)$$

where  $r_f$  is the radius of the fibres. Equation 5.1.5 can be solved numerically as detailed by Bernet and al. [34]. This allows to determine the impregnation degree  $\xi$  which is defined as the ratio of the impregnated tow volume over the total tow volume. Considering the equivalent geometry, it therefore reads:

$$\xi = \frac{R_{eq}^2 - r^2}{R_{eq}^2} \quad (5.1.7)$$

To find the matrix pressure, mechanical equilibrium is applied and the textile stress response  $\sigma_{tex}$  is deducted from the applied pressure  $P_{app}$ :

$$P_m = P_{app} - \sigma_{tex} \quad (5.1.8)$$

A variety of models are available in the literature to describe the stress response of compacted textile stacks [17]. In this article, a quasi-static stress response is adopted because the small strain rates result in little viscoelastic response.

$$\sigma_{tex} = A_{tex} \cdot e^{B_{tex} \cdot \nu_f} \quad (5.1.9)$$

whereas  $\nu_f$  is the fibre volume fraction,  $A_{tex}$  and  $B_{tex}$  are fitting variables and the function was suggested by Robitaille et Gauvin [125]. More elaborate models taking into account viscoelastic effects could be implemented if deemed necessary, for instance the one proposed by Danzi et al. [129].

The fibre volume fraction is a function of the textile areal weight  $M_f^A$ , the matrix mass  $M_m$ , the density of the textile  $\rho_f$  and matrix  $\rho_m$ , the number of layer  $N$ , the tow fibre volume fraction  $\nu_{f,tow}$  and the impregnation degree  $\xi$ . For an homogeneous plate with cavity area  $A_c$  it reads, as detailed in appendix B:

$$\nu_f = \frac{M_f^A}{M_f^A + \frac{M_m \rho_f}{\rho_m N A_c} + M_f^A \frac{(1 - \nu_{f,tow})}{\nu_{f,tow}} (1 - \xi)} \quad (5.1.10)$$

#### 5.1.4 Gas Diffusion and dissolution

The air pressure is determined with the ideal gas law and depends on the number of moles per unit depth  $n_\lambda$ , the volume available for the gas to expand  $V_g$ , the temperature  $T$  and the ideal gas constant  $R$ . In the case of air trapped in a tow, the volume available to the gas depends on the unimpregnated tow volume and its fibre volume fraction. The gas pressure therefore reads:

$$P_g = \frac{n_\lambda \cdot R \cdot T}{V_g} = \frac{n_\lambda \cdot R \cdot T}{A_{tow} \cdot (1 - \nu_{f,tow}) \cdot (1 - \xi)} \quad (5.1.11)$$

where  $V_g$  is the volume occupied by the gas per unit depth. As air is absorbed at the interface and diffused into the molten polymer, the amount of air entrapped per unit depth  $n_\lambda$  changes over time. Therefore,  $n_\lambda$  is obtained based on the initial amount of entrapped air  $n_\lambda^0$  by describing its change over time. This implies that the diffusion of air into the polymer has to be described to express the changes of the gas quantity over time. With a flux of species  $J$  per unit depth the temporal change of entrapped gas reads, considering that in the equivalent geometry the surface available for diffusion is the surface of the cylinder with radius  $r$ :

$$\dot{n}_\lambda = 2 \cdot \pi \cdot r \cdot J \quad (5.1.12)$$

The approximate solution for the diffusion of gas bubbles in liquids proposed by Epstein and Plesset [92] is applied to determine the flux of species. As fibres are assumed impermeable, the dissolved species can only diffuse in the interstitial space between the fibres as represented in Figure 5.5 and diffusion will thus be lower than in pure polymer. Therefore, the diffusion in fibre bundles is described with the diffusion coefficient in pure polymer  $D$  corrected with a correction factor  $G$ . Inserting the Equation of Epstein and Plesset into the previous one yields:

$$\dot{n}_\lambda = -2 \cdot \pi \cdot r \cdot G \cdot D \cdot (C_s - C_\infty) \cdot \left(1 + \frac{1}{\sqrt{\pi D G t}}\right) \quad (5.1.13)$$

where  $C_s$  is the saturation concentration at the bubble interface and  $C_\infty$  the far-field concentration, which is assumed to be the saturation concentration at atmospheric pressure as mentioned earlier. The saturated concentration of a species in a medium is dependent on the pressure  $P$  following Henry's law:

$$C_s = H \cdot P \quad (5.1.14)$$

where  $H$  is Henry's constant, which is specific to each gas/medium system. In this article, the air is simplified as pure nitrogen which makes up the large majority of air composition. However, it is possible to consider an air mix, which would require to calculate the diffusion of each gas separately.

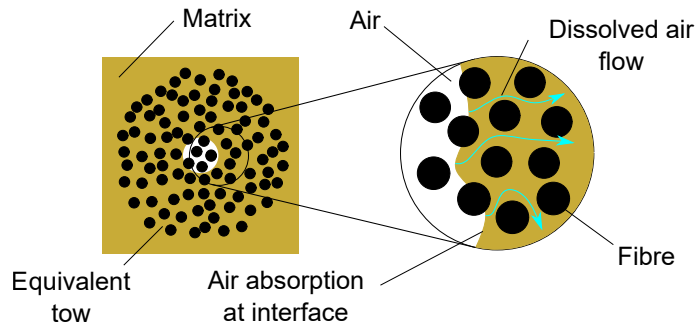


Figure 5.5: Schematical representation of the diffusion in fibre bundles. Air dissolves at the flow front then diffuses outwards through the interstitial space between the fibres.

## 5.2 Materials and material characterization

Glass fibres woven fabric with a quasi-unidirectional (UD) Leno weave fabric architecture, a silane sizing and an areal weight of  $931 \frac{\text{g}}{\text{m}^2}$  provided by Tissa Glasweberei AG was used in this study. This fabric consists of main tows free of crimps held together by smaller tows in both the weave and weft direction that will be referred to as the supporting weave. Figure 5.6 displays a close-up picture of the weave where the main tows and the supporting weave can be distinguished.

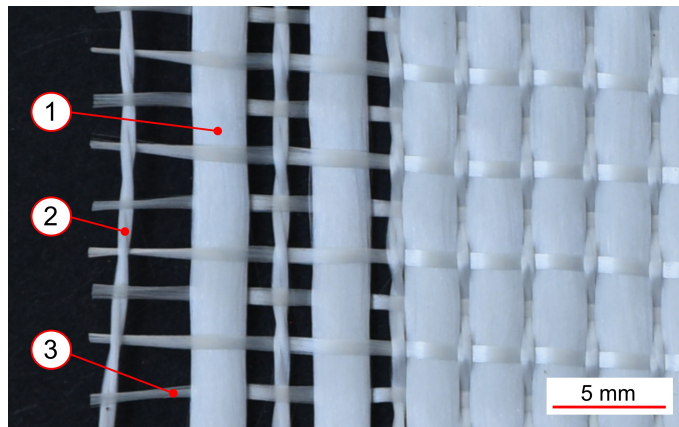


Figure 5.6: Close-up picture of the fabric. The main tow is indicated by 1) and the supporting weave by 2) and 3).

The reinforcing textile stress response was measured with a Zwick Roell Z100 universal testing machine equipped with 135mm perforated steel plates in [17]. The plies were individually coated with the silicone oil Xiameter PMX 200 (Dow Europe GmbH), to obtain a similar lubricating effect as the molten polymer. The fibre volume content at rest  $\nu_{f,0}$  was measured to be 0.414 and a value of 0.03 and 24.2 for the parameters  $A_{tex}$  and  $B_{tex}$  were found. More detailed information about the characterization of the fabric are presented in section 3.

Two thermoplastics were investigated in this study, polypropylene (PP) BJ100HP from Borealis and high density polypropylene (HDPE) Lupolen 5236 HX from LyondellBasell. The technical datasheets specify that the PP has a melting temperature of 165 °C and a density of 906  $\frac{\text{kg}}{\text{m}^3}$  in solid state while these values are respectively 133 °C and 952  $\frac{\text{kg}}{\text{m}^3}$  for the HDPE. The polymers were obtained in the form of granulates and were transformed in 0.15 mm thick foils with a Collin extruder.

The zero-shear viscosity  $\eta_0$  of the molten polymers were measured at 0.1  $\frac{1}{\text{s}}$  with an Anton Paar Physica MCR 300 plate-plate rheometer at 190 °C. The viscosities of PP and HDPE were found to be respectively 495 and 5440 Pa·s. The densities of the molten polymers were measured to be respectively 763 and 786  $\frac{\text{kg}}{\text{m}^3}$  for PP and HDPE at 190 and 160 °C with a MI-2 melt flow indexer. The solubility and diffusion coefficients were taken from the work of Sato et al. [165] at a temperature of 190 and 160 °C for respectively PP and HDPE. Henry's constants  $H$  for the dissolution of nitrogen ( $\text{N}_2$ ) in polypropylene and high-density polyethylene melt of  $3.6 \cdot 10^{-5} \frac{\text{mol}}{\text{Pa} \cdot \text{m}^3}$  for PP and  $4.3 \cdot 10^{-5} \frac{\text{mol}}{\text{Pa} \cdot \text{m}^3}$  for HDPE were used. The nitrogen diffusion coefficients  $D$  of  $5.0 \cdot 10^{-9} \frac{\text{m}^2}{\text{s}}$  for PP at 190 °C and to  $6.0 \cdot 10^{-9} \frac{\text{m}^2}{\text{s}}$  for HDPE at 160 °C were used. Thereby, the influence of the weight fraction of dissolved gas in the polymer described by Sato et al. [165] for very high pressures was neglected.

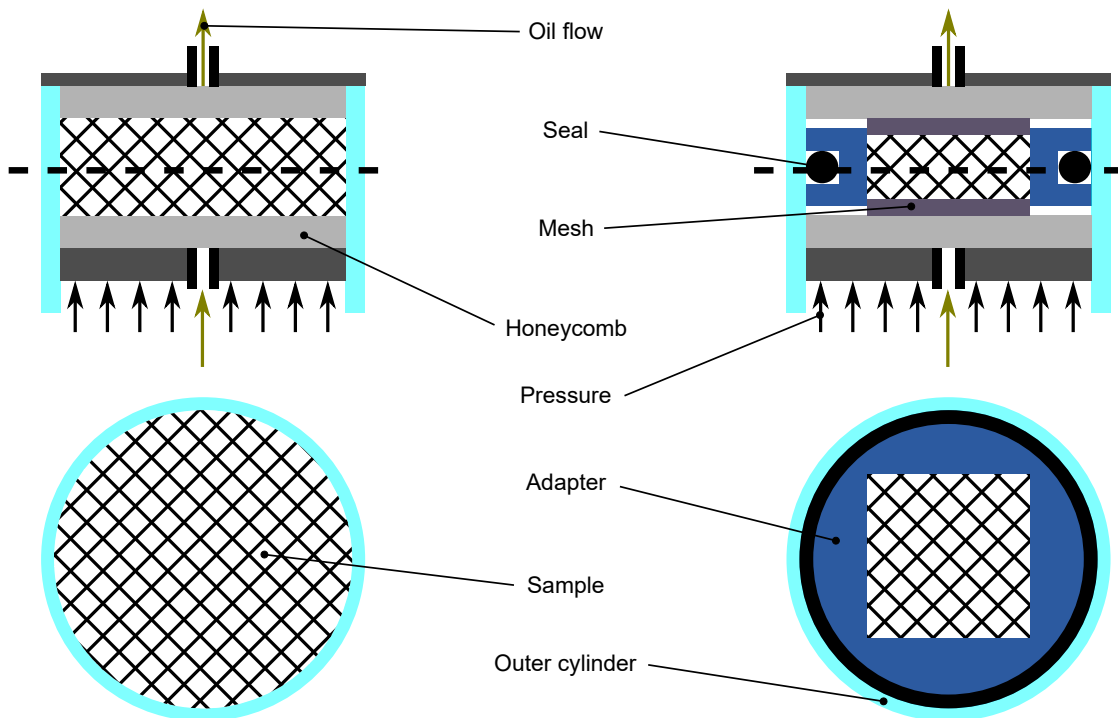


Figure 5.7: Schematic representation of the jig used in this study, as presented by Studer et al. [25] on the left and as modified in this study on the right. The upper half shows a vertical cut of the jig while the bottom half represents a top cut view, whereas the cut is at the level of the dashed line.

### 5.2.1 Tow permeability

Due to the lack of experimental validation at such elevated fibre volume fraction, it was decided to directly measure the tow permeability in order to check the value predicted by the analytical model. The experiment was performed with a through-thickness permeability jig that is schematically represented in Figure 5.7 and was described in detail in other studies [25]. The jig was originally meant for circular samples, which are placed in the cavity between two aluminium honeycombs applying pressure on it. To measure permeability, pressurized oil is let at the one end of the jig and freely flows out at the other end in a recipient that is continuously weighed.

Because manufacturing a circular sample and placing it in the jig without disturbing the loose fibres would be difficult, an adapter was placed inside the cavity to measure permeability on square samples instead. The adapter is a 10 mm thick circular polymethylmethacrylate (PMMA) in the middle of which is a square hole with a side of 50 mm, as shown in Figure 5.8a, where the sample is placed. A sealing on the outside prevents oil from flowing in the interstitial space between the adapter and the jig, which would perturb the measurements. On the top and bottom of the sample are placed 2 mm thick laser cut PMMA meshes with minimal flow resistance. The adapter is meant for samples with a thickness between 6 and 10 mm so that the pressure is transferred on the sample and not to the adapter itself. Figure 5.7 schematically represent the jig as described by Studer [25] on the left and as modified with the adapter placed inside on the right.

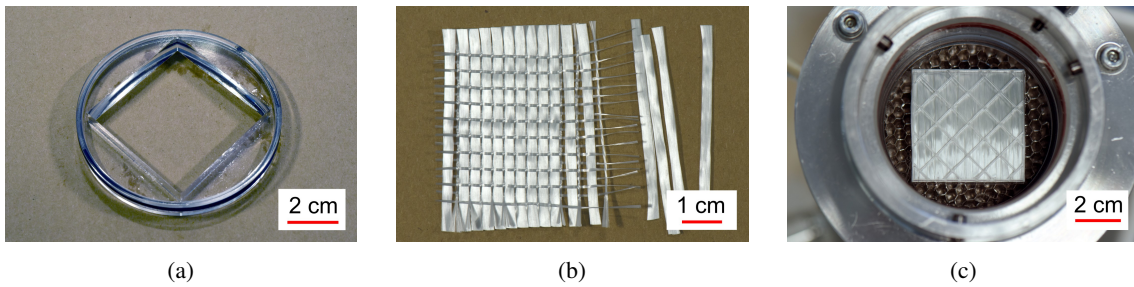


Figure 5.8: Representation of the process for preparing a UD samples. A picture of the adapter is shown in Figure 5.8a, where the square hole for the sample and the seal can be seen. The tows are extracted from the textile cut with a CNC cutting machine as shown in Figure 5.8b. The adapter with the sample is finally placed in the permeability jig as shown in Figure 5.8c. The adapter itself is transparent and cannot be distinguished in the picture, instead the aluminium honeycomb underneath appears. In the middle of the adapter the sample can be seen with the PMMA mesh placed on top of it.

To directly measure the tow permeability a UD fibre stack was created with the tows. Because the rowing spool with which the weave was manufactured was not available, the tows were directly extracted from the fabric. This was done by cutting single plies to rectangles with a length of 50.1 mm in the weave direction with a CNC cutting machine and manually withdrawing the tows as shown in Figure 5.8b. The tows were cut slightly longer than the cavity width to avoid gaps between the sample and the adapter cavity which could disturb the permeability measurement. The amount of tows placed in the cavity was defined such as to obtain a layer with a thickness  $h_{PT}$  that was set to 7 mm. A layer with constant thickness, density  $\rho_f$  and fibre volume fraction  $\nu_{f,tow}$  in the cavity with area  $A_C$  will have a mass  $M_{PT}$  given by:

$$M_{PT} = \rho_f \cdot A_C \cdot h_{PT} \cdot \nu_{f,tow} \quad (5.2.1)$$

The tows were extracted until the target weight  $M_{PT}$  was reached before being carefully and evenly placed in the cavity in an aligned fashion as shown in Figure 5.8c. The pressure applied on the sample soaked in silicon oil was then gradually raised before letting it rest for an hour in order to give time to the tows to rearrange themselves and close possible gaps. The permeability measurement was performed with the silicone oil Xiameter PMX 200 (Dow Europe GmbH) with a viscosity of 0.1 Pa·s, a pressure on the fibres of 1 MPa and an oil pressure of 0.15 MPa. The experiments was performed three times, each time with a virgin sample. Figure 5.7 schematically represents how the jig used in this study was modified to allow direct tow permeability measurement.

The tow permeability was measured to be  $4.3 \cdot 10^{-14} \text{ m}^2$  with a standard deviation of  $1.8 \cdot 10^{-14} \text{ m}^2$ . For comparison, the predicted permeability for a pressure of 1 MPa reads  $6.1 \cdot 10^{-14} \text{ m}^2$ . Figure 5.9 display the predicted permeability as a function of the applied pressure along with the measured permeability. The permeability was predicted according to equation 5.1.6 and the tow fibre volume fraction which depends on the applied pressure as shown in Figure 3.11.

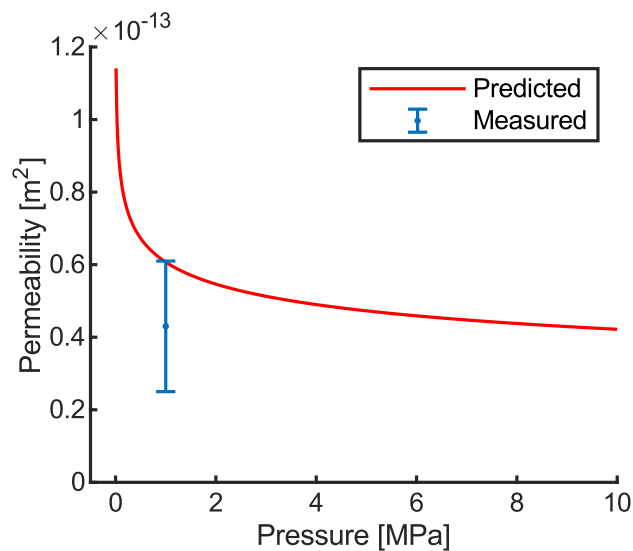


Figure 5.9: Predicted tow permeability as a function of the applied pressure for the textile investigated in this study, along with the measured permeability.

Given the model predictions typically spanning several orders of magnitude depending on the fibre volume fraction and considering the usually reported accuracies of the different models [50], the difference between measured and predicted permeability is well within acceptable bounds. The relatively elevated standard deviation reflects the difficulty to measure materials with such low permeabilities, as tiny gaps or small non uniformity in sample thickness can significantly affect the result. Nonetheless, this result indicates that the analytical model of Gebart can be reasonably applied to predict tow permeability at very elevated fibre volume fractions.

## 5.3 Methods

The experiment consisted of consolidating plates for different periods of time and subsequently measuring their impregnation degree. This allowed to measure the impregnation degree over consolidation time and compare it against model predictions, whereas the diffusion reduction factor  $G$  from equation 5.1.13 was fitted to the measurements. In order to validate the impregnation model, the experiment was then repeated at different pressures and with different materials as summarized in Table 5.1.

Table 5.1: Overview of the experiments including process parameters.

Thermo-plastic	Textile	Number of layers	Press temperature [°C]	Process temperature [°C]	Pressure [MPa]	Press time [min.]
PP	Glass	5	200	190	1.04 / 1.73 / 3.46	0/2/5/15/30/60
HDPE	Glass	5	170	160	1.73 / 3.46 / 6.92	0/2/5/15/30/60

### 5.3.1 Experimental test setup

For the experiments, film stacking was chosen and each textile layer was placed between two 0.15 mm thick thermoplastic foils, such as to target a final fibre volume fraction of 0.55. The textile plies were cut to the dimensions of the mould with a CNC cutting machine while the thermoplastic foils were cut by hand with a cutter and a stencil, in total 5 plies of textile and 10 of foils were required for each plate. While the weight of the textile was calculated based on the areal weight and the area the thermoplastic foils were weighed prior to consolidation.

The plies were then placed into a custom 170x85 mm plate mould, thereby great care was taken to disturb the textile architecture as little as possible. A two-stage 200 kN Vogt hydraulic press was used for the experiments, whereas one stage was heated and the other one water cooled. At the beginning of the experiment the mould containing the plies was placed in the heated press, which temperature was set to 200 °C for polypropylene and 170 °C for polyethylene. Pressure was already applied during heating up to ensure contact with both the top and bottom part of the mould and reduce temperature inhomogeneities, thereby a spacer was inserted to prevent the pressure from translating to the composite.

The mould was let up to heat whilst monitoring the cavity temperature with a thermocouple until five degrees below the process temperature specified in Table 5.1, at which point the spacers were removed and pressure applied to start consolidation. Thermal monitoring revealed that the cavity temperature did not exceed 5 °C above the specified process temperature. These slight thermal variation were neglected and the cavity temperature was assumed constant at the specified process temperature in table 5.1. This implies that other temperature dependent material properties such as viscosity and diffusion coefficient were assumed constant as well. After the given press time was elapsed, the mould was transferred to the cold stage and cooled down under pressure. The transfer lasted up to 30 seconds, during which no pressure was applied onto the mould.



Early heating up trials with several thermal sensors indicated an homogeneous temperature throughout the mould when the consolidation starts. The time required for the mould to reach the melt temperature during the cooling down was measured not to exceed 2 minutes. Since impregnation goes on during cooling down as pressure is applied, the total consolidation time was conservatively defined as the press time plus 1 min. +/- 1 min.

### 5.3.2 Analysis

The consolidated plates were cut transverse to the fibre directions with a Compcut 200 composite circular saw. Microscope analysis of polished samples was found to be difficult because of the tendency of debris material to fill up the voids, which were then hardly distinguishable from matrix. Therefore, the cut surface was then directly photographed in high resolution with a Nikon D810 equipped with a AF-S VR Micro-Nikkor 105 mm 1:2,8G IF-ED objective. The impregnation degree was measured with the software ImageJ by manually selecting and measuring the dry and the whole area of at least 30 tows per sample. The semi-minor and major axes of the tows were also measured with an integrated plug-in of ImageJ automatically fitting ellipses over the selected area. The outer textile layers were not included in the measurements because the cutting process slightly deconsolidated them, the tows close to the edges were also not included to avoid including potential edge effects.

The diffusion reduction factor  $G$  was obtained by minimizing the sum of squares differences between the model predictions and the measured impregnation degrees with an interval halving algorithm based script in MATLAB<sup>®</sup>.

## 5.4 Results

Plates could be successfully produced without deviation from the test plan and the mould remained sealed during the trials as only negligible amounts of polymer flowed in the shear edge clearance. The plates did not show any visible defect and had a final thickness of about 3.8 mm with some slight variation depending on the impregnation degree. A picture of a plate cross-section is shown in Figure 5.10a, which presents homogeneous properties in terms of thickness, tow spacing and impregnation degree. A close-up is displayed in Figure 5.10b, where one can distinguish between the dry and impregnated regions of the tow. A narrow gap is present between the tows in all directions, meaning that the assumption of a tow in a bath of molten thermoplastic as represented in Figure 5.3 on the right is well founded. In addition, no bubbles were observed in the inter-tow region and similar observations can be made in pictures presented in other studies [24], [116], which confirms the assumption that the gas is trapped only in the unimpregnated region of the tow.

The tow dimensions within each plate were found to be rather constant as the standard deviation of the semi-minor and major axis was measured between 3 and 4 %, whereas a significant portion of this value might be induced to measurement inaccuracies since measurements were performed by hand. When comparing the average values of the different plates, variations in the order of 5% are found. The correlation between tow dimensions and pressure or impregnation degree,

which is linked to the degree of compaction, is almost non-existent.

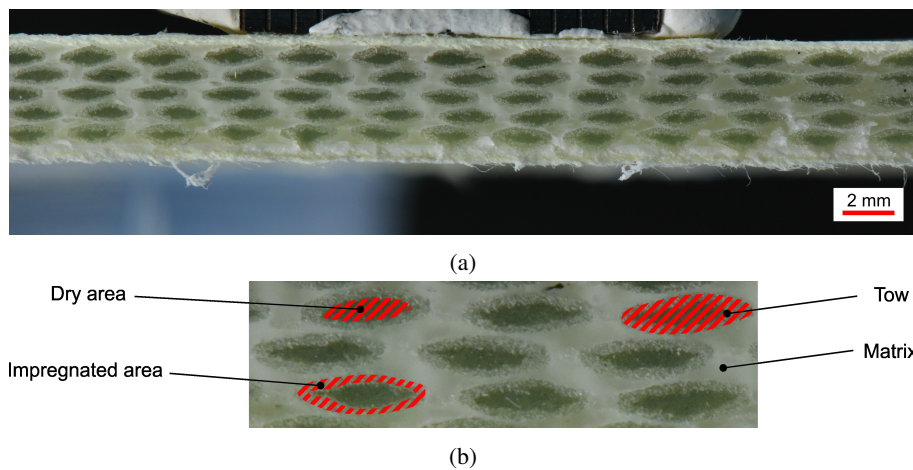


Figure 5.10: 5.10a: Picture of a cross section of the plate with PP matrix consolidated at 1.04 MPa for 5 minutes. 5.10b: Close up of picture 5.10a, where the dry and impregnated zones of the tows can be distinguished.

Figure 5.11 shows the results of the whole set of consolidation experiments. At the very beginning the impregnation degree quickly raises, then a plateau value is reached and impregnation progresses much slower. The impregnation model fits the experimental measurements quite well and is able to explain the observed behaviour for different pressures and materials. At first, impregnation is dominated by matrix flow in the tow, then air pressure builds up and opposes further impregnation, which results in a plateau. At this point, air dissolution and diffusion is necessary for further impregnation and the rate at which this takes place determines the slope of the plateau. In the following, the first stage of impregnation will be referred to as the *pressure difference driven impregnation* while the second stage will be referred to as the *dissolution driven impregnation*. Overall, the model can capture all relevant phenomena and predict consolidation reliably, both during the matrix flow and the diffusion dominated parts.

Figure 5.11a shows an increasing mismatch between predictions and measurements at the beginning of consolidation with increasing pressure. This is attributed to deconsolidation taking place during displacement of the mould to the cold stage, during which no pressure is applied. The matrix pressure vanishes thereby, yet the air trapped in the tow is still pressurized and therefore drives the matrix out. In Figure 5.11 the dashed line is obtained by adding, at the end of the given consolidation time, 30 seconds without matrix pressure at the end to reflect the deconsolidation taking place during displacement of the mould to the cold stage. One can see that while for experiments with HDPE the effect of deconsolidation is limited, for PP however it becomes relevant. This is linked to the higher viscosity of HDPE, which results in slower matrix flow and deconsolidation kinetics in a similar fashion as reported by Wolfrath et al. [138]. One should stress that this calculation represents an absolute conservative estimation of the conservation, because during cooling pressure is applied and the composite at least partially reconsolidates. Nonetheless, this strongly indicates that the observed deviation between predictions and measurements can be imputed to experimental error caused by deconsolidation when transferring the mould from the hot stage to the cold stage.

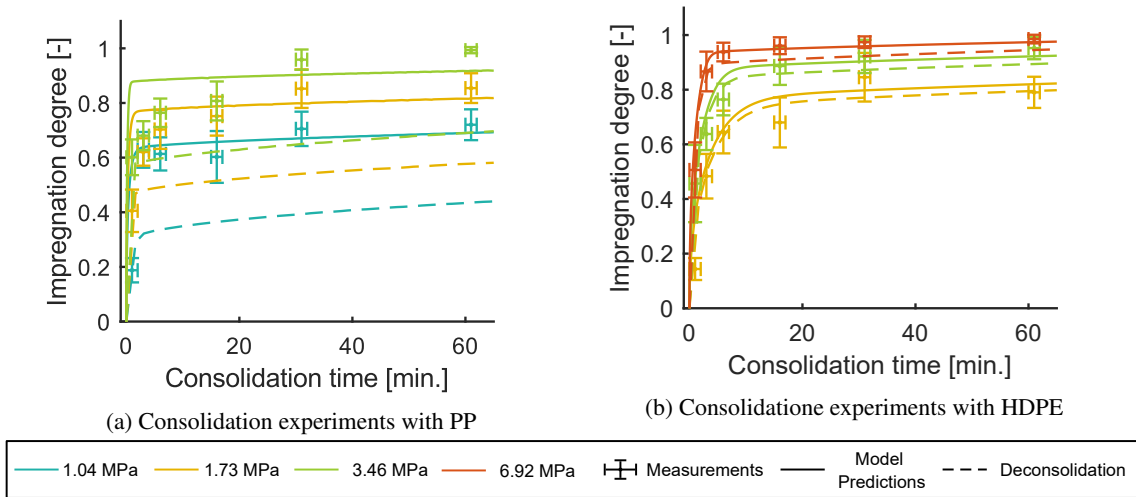


Figure 5.11: Measured and predicted impregnation degree as a function of the consolidation time for PP in Figure 5.11a and HDPE in Figure 5.11b with different consolidation pressures, along with minimal predicted impregnation degree resulting from deconsolidation during mould transfer from the hot to the cold stage.

The diffusion reduction factor  $G$  was fitted to a value of  $2.3 \cdot 10^{-4}$ , thereby the experiments with PP were omitted because of the perturbation caused by deconsolidation and the same value of  $G$  was used for all experiments. The diffusion reduction factor is a purely geometrical effect and is certainly directly influenced by the fibre packing, in this study the change of tow fibre volume fraction with applied pressure is only minimal as reported in Figure 3.11 and was neglected. The low value obtained for the diffusion reduction factor indicates a very strong reduction of diffusion by the highly packed fibres. From the experiments with PP it seems that air diffusion is slightly underpredicted, which is attributed to an imprecise diffusion coefficient definition of the polymers since literature values were employed.

Figure 5.12 shows the measured impregnation degree of the plate with polypropylene consolidated at 1.04 MPa along with the predictions of the consolidation model. In addition, two further predictions are presented: one where it is assumed that only the air originally present in the tows gets entrapped without diffusion and one where air entrapment is neglected. Assuming that only the air originally present in the tow gets entrapped results in a plateau value significantly higher than the measured values, even when assuming no diffusion at all, which strongly hints at a higher amount of entrapped air. If air entrapment is neglected, the proposed model becomes similar to those proposed in the literature so far. Neglecting air entrapment yields, at the beginning, impregnation curves which are very similar to the model proposed in this article. However, the plateau value is not captured. There is a large difference between the different models in terms of time predicted for complete impregnation. This could explain the observations of Groupe et al. [116], who noted a large discrepancy between the time predicted by models available in the literature for complete impregnation and the press times used in practice.

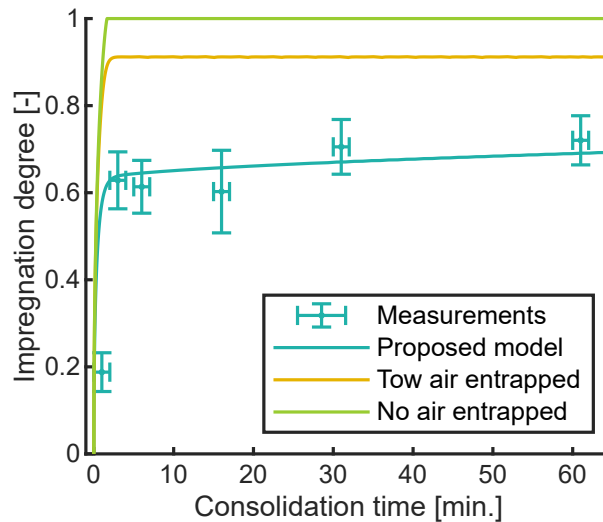


Figure 5.12: Measured impregnation degree as a function of the consolidation time for PP and a pressure of 1.04 MPa, along with the model prediction and the model predictions assuming only tow air entrapped and no air entrapment.

The textile stress response as modelled through Equation 5.1.9 was found to be surprisingly negligible and to take up less than one percent of the applied pressure, even for the lowest consolidation pressure of 1.04 MPa. The fibre volume fraction at the meso scale depends on the impregnation degree as expressed through Equation 5.1.10, which implies that the textile stress response changes during consolidation. Figure 5.13 shows the fibre volume fraction and the textile stress response at different final volume fractions depending on the impregnation degree. This result was obtained with HDPE and a tow fibre volume fraction of 0.75 resulting from an applied pressure of 1 MPa. One can see that very elevated final volume fraction have to be targeted for the portion of applied pressure taken up by the textile to become significant.

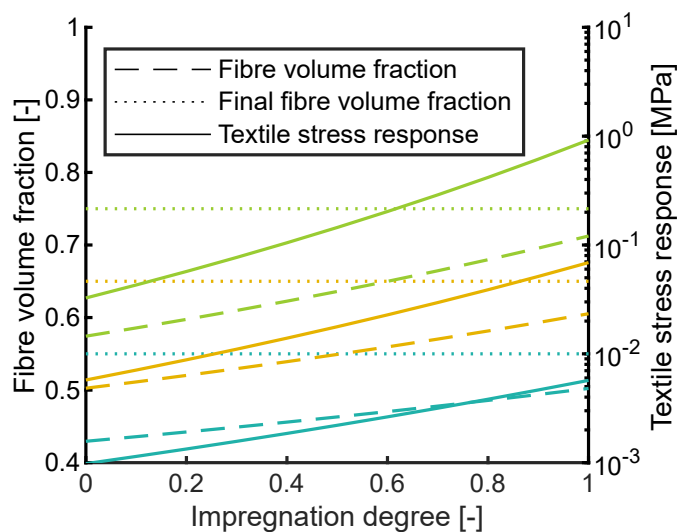


Figure 5.13: Fibre volume fraction and textile stress response as a function of the impregnation degree for a tow fibre volume fraction of 0.75, HDPE matrix and different targeted final volume fractions of 0.55, 0.65 and 0.75. The final fibre volume fractions is more elevated because of the change of density of the matrix resulting from solidification.

Figure 5.14 schematically shows how the compaction state changes during consolidation and helps to understand the results displayed in Figure 5.13. As impregnation goes on matrix will fill in porosities and reduce the volume taken by the composite. Since the amount of textile is confined in a smaller volume, the plies are automatically more compacted and the textile stress response increases. When the composite is cooled down the matrix solidifies and shrinks, which once again cause a reduction of the whole composite volume and thus a higher fibre volume content. This also explains why in Figure 5.13 the fibre volume fraction at full impregnation differs from the final fibre volume fraction in solidified state. These phenomena can also be read from Equation 5.1.10, where both the impregnation degree and the matrix density influences the fibre volume fraction and thus textile stress response following Equation 5.1.9. Now, the densities of the solid and molten matrix differ quite significantly and this explains why plates with elevated final volume fractions in solid state will still have moderate fibre volume fractions and textile stress response during processing in molten state.

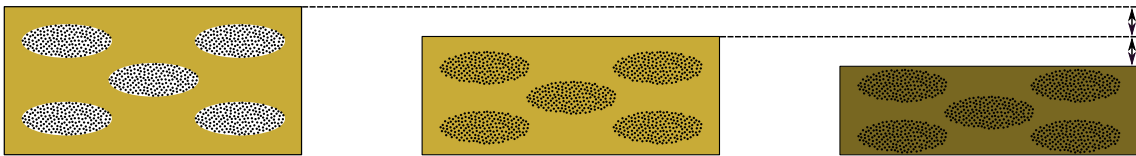


Figure 5.14: Schematical representation of how the compaction state changes during consolidation. The initial state is shown in the left, the fully impregnated state in the middle and the final state after cooling on the right. The light beige shade indicate molten polymer while the darker shade indicates a solidification.

## 5.5 Discussion

Two stages can be differentiated during the impregnation of hybrid textiles, one pressure difference driven matrix flow and the other driven by air dissolution and diffusion. Several assumptions and simplifications were made for the pressure difference driven matrix flow, such as assuming that the whole surface of the tow is in contact with molten polymer, which was found here to be valid. Other simplifications, such as neglecting the change of viscosity with shear rate are commonly made in the literature. Some of these assumptions were addressed and justified, other are thought to have a limited effect on consolidation.

The tow permeability  $K_{tow}$  and the diffusion reduction factor  $G$  are two major sources of uncertainty, both being difficult to predict accurately. Figure 5.15 and 5.16 show respectively the influence on the permeability  $K_{tow}$  and the diffusion factor  $G$  on impregnation with an applied pressure of 1.73 MPa and HDPE matrix. In both cases, the gold line represents the proposed model predictions, the blue line the model prediction with lower variable value and the green line the model prediction with higher variable value. One can see that the tow permeability influences to some extent the pressure difference driven flow and the time at which the transition to the diffusion driven flow takes place. Afterwards however, the different lines can hardly be differentiated from one another. It is not surprising for the diffusion driven flow to be barely influenced by permeability, as it only influences the rate at which pressure equilibrium between matrix and air is achieved but has no direct influences on diffusion itself once that equilibrium is achieved. Therefore, the uncertainty and error bound with the permeability determination has a limited influence

on the overall consolidation behaviour and almost negligible for the consolidation time required for complete impregnation. Regarding the diffusion factor, one can see that the diffusion reduction factor barely affects the pressure difference driven impregnation but influences the dissolution driven impregnation. A higher diffusion reduction factor, which results in a higher effective diffusion coefficient, increases the rate at which dissolution takes place and increases the slope of the impregnation degree curve during the dissolution driven impregnation.

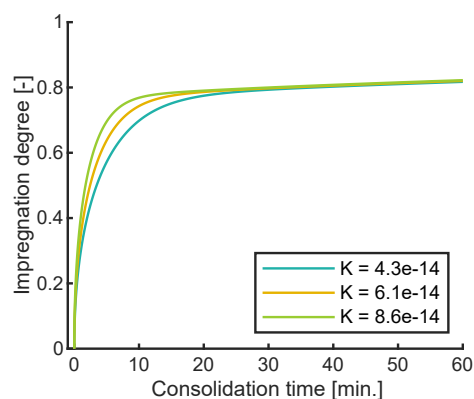


Figure 5.15: Influence of the tow permeability  $K_{tow}$  on the impregnation behaviour according to the proposed model for a pressure of 1.73 MPa and HDPE as matrix.

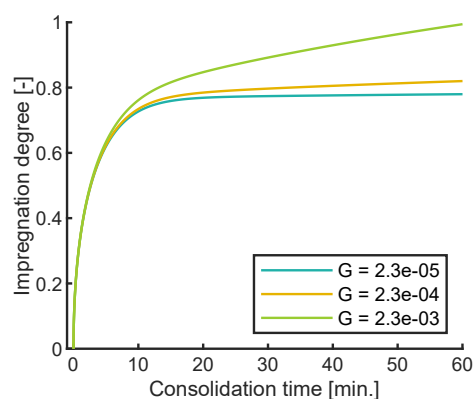


Figure 5.16: Influence of the diffusion reduction factor  $G$  on the impregnation behaviour according to the proposed model for a pressure of 1.73 MPa and HDPE as matrix.

This study presents a methodology to directly measure tow permeability at the highest fibre volume fraction reported, to our best knowledge, so far. The results indicate weak dependence of the tow fibre volume fraction on the applied pressure, however other types of tows such as recycled carbon fibre bundles there might be more compressible and more accurate methods to determine tow fibre volume fractions might be desirable. The results also indicate that the permeability model according to Gebart [43] at very elevated fibre volume fractions is reasonably accurate. It would yet be of interest to enhance the test setup to increase measurement accuracy and decrease scatter in future studies. Considering that tool compliance was found to be a major source of error in permeability measurement [166], it would make sense to use stiffer materials such as steel in the permeability measurement device. Furthermore, building the device in such a way that it can be placed in a universal testing machine during testing would allow to accurately determine at the same time the relation between applied pressure, fibre volume fraction and permeability. In this study, the permeability was only measured at one applied pressure for validation purposes and because of the weak change in fibre volume fraction - and thus permeability - at consolidation pressures above 1 MPa, however in further work with an enhanced measurement device it would be interesting to measure permeability over a larger range of applied pressure.

The air dissolution and diffusion models fit the experimental data well for different polymers and in different conditions, yet some questions marks remains. For instance, the air dissolution and diffusion coefficients in pure polymer should be experimentally measured using for example the equipment described by Sato et al. [167] as for many of them no values were found in the literature nor is the required testing equipment commonplace. It is desirable to have a purely predictive model, meaning that in future work models should be developed to predict the diffusion reduction factor in fibre bundles. This factor is most probably influenced by the fibre volume fraction as

fibres obstruct diffusion, the tow microstructure could also play a role. For instance the tortuosity of the open pores could make the diffusion path longer and hinder diffusion. Investigation of the microstructure as presented for instance by Gomasasca et al. [60] might prove necessary to fully understand the mechanisms at work.

Since the importance of air diffusion has been proven to play a major role in this study, the ability of polymers to dissolve air could become a major selection criterion in the production of hybrid textiles based thermoplastic composites. Instead of focusing heavily on the development of very low viscosity thermoplastics such as the PP used in this study or the polyamide 6 “Evolite HF XS1480” from Solvay [25], [153], their ability to absorb and diffuse air should also be weighed. In addition, the possibility to use existing additives or develop new ones should be considered. Furthermore, as the solubility of gases with low critical temperatures such as nitrogen decrease with increasing temperature [165], this should also be considered when selecting process parameters.

The model presented here assumes that the dimensions of the tow are constant, which was in agreement with experimental observations. Other studies such as the one presented by Kobayashi et al. [136] reported more significant tow flattening during consolidation, but also found that denser fabrics and the presence of several plies inhibited tow flattening. Future studies should quantify both the tow deformation and the influence it has on the accuracy of the consolidation model. The little tow deformation observed in this study is not only attributed to the large tow size, but also to the sizing and the Leno weave architecture that is particularly stable.

The final fibre volume fraction of 0.55 targeted in this study is already quite elevated, yet the assumption of a tow in a molten polymer bath assumption was found to remain valid. The textile stress response was found to amount for less than 1% of the applied stress, even for consolidation at 1.04 MPa, the lowest applied pressure in this study. In future research, one should investigate if the model remains accurate for other textiles and at higher fibre volume fractions. When compared to film stacking which was used in this article for experimental validation, hybrid textiles based on veils for example could have additional air trapped in the polymer layer because of its structure, which is why experimental validation with other architecture of hybrid textile is desirable. At higher fibre volume fractions, the impact of the whole tow surface no longer being in contact with molten polymer, if occurring, should be assessed. As a result of the increasing polymer density during solidification, the fibre volume fraction and thus textile stress response can rise sharply during cooling down, thereby resulting in a decreasing matrix pressure. An insufficient matrix pressure in injection moulding is known to favour void formation as a result of polymer shrinkage [168], in addition lower matrix pressure could potentially result in higher void content as entrapped air bubbles in the matrix will expand or because of the nucleation of absorbed volatiles [85]. Hence, textile stress response during solidification should not be overlooked during composite production.

The experimental results with PP highlight the sensitivity of two-stage press moulding to deconsolidation. If the process allows for a very fast impregnation, then an equally fast deconsolidation is to be expected and even short deconsolidation times can have very significant effects. Rapid isothermal press moulding where heating and cooling is integrated in the mould seems a preferable option for the consolidation textiles as it removes the risk of deconsolidation altogether.

If two stage press moulding is used, swift displacement from to the cold stage is necessary. Alternatively, cooling upon full consolidation is also possible as the whole air is dissolved and cannot drive the matrix out.

The model presented here allows for a comprehensive understanding of the different phenomena taking place during consolidation, and sheds light on new mechanisms. Even though the influence of each parameter can be assessed, it is still unclear at this point what the optimal set of process parameters is. A set of investigations will be conducted in future work to understand if higher pressures result in a faster dissolution of the air in the molten polymer and how does the total impregnation time scales with different parameters such as tow size or temperature. In any cases, applying elevated pressure remain a possible consolidation strategy to reduce void size if not completely eliminating it, yet too elevated pressures can cause fibre damage. Another parameter which should be investigated is the temperature, as increasing it decreases the viscosity and the solubility of nitrogen in polymers (those investigated so far). Therefore, higher temperatures do not necessarily result in faster impregnation times. A strategy could be to vary the temperature such as to have low viscosity during the pressure driven flow and then decrease the temperature to enhance dissolution.

The results presented in this study shows that the time required to obtain a void-free composite with press moulding of hybrid textiles is significantly larger than previously thought. Within industrial applications, the model presented in this study can be used to predict the consolidation time required to obtain acceptable porosity content rather than a void-free composite, in order to keep cycle times within reasonable bounds.

The present model can be very well implemented for consolidation processes in which the temperature is not constant, such as stamp process or for press moulding with variable temperature. In that case, the dependence of viscosity and solubility on temperature needs to be modelled, respectively with an Arrhenius type function [32], [33] and with the function proposed by Sato et al. [165] for instance. This implies that the consolidation model may need coupling with a thermal simulation, should the temperature through the composite not be homogeneous.

Further aspects that should be investigated in future studies include the influence of statistical effects on porosity prediction accuracy. As shown in Figure 5.17, while most of the tows are completely impregnated some still present unimpregnated areas. Towards the end of consolidation it therefore becomes apparent that the consolidation process is not rigorously the same in all tows. Variation in tow dimensions, permeability or amount of entrapped air are possible explanations for these discrepancy. Possibly, understanding and taking these statistical effects into account could help to more accurately model porosity. Otherwise, press moulding under vacuum should be investigated since the time required for total impregnation can be dramatically reduced in the absence of air as shown in Figure 5.12. Feasibility and economically viability studies are required to begin with since applying vacuum is technically challenging, especially at high temperatures.



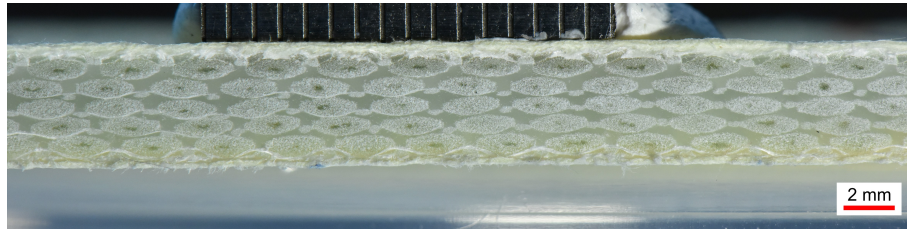


Figure 5.17: Cross section Picture of the plate with HDPE consolidated at 6.92 MPa for 60 minutes. While some tows are completely impregnated, dry areas characterized by a darker shade are visible in other tows.

## 5.6 Summary

In this chapter, we propose and experimentally validate an analytical model for the consolidation of hybrid textiles in which air entrapment and dissolution is considered. Direct tow permeability measurement was carried out to validate, for the first time, the analytical model of Gebart at very high fibre volume fractions and reasonably good agreement was found.

The model was found to be able to reproduce all relevant phenomena and correctly predict the consolidation behaviour for different polymers and at a range of pressures. Entrapped air is shown to have a large influence on the consolidation behaviour and complete dissolution of the air is necessary to fully consolidate the composite, which can take significant amount of time. The model offers new and comprehensive insights about the phenomena taking place during consolidation and enables future process optimization. Some material properties including the solubility and diffusion coefficient which were not taken into account so far are found to largely influence consolidation and should be characterized in future studies.

During consolidation with two-stage press moulding, the short time where no pressure is applied on the mould as it is displaced from the hot to the cold stage is found to be sufficient to induce significant deconsolidation, which has practical consequences for the industry. We recommend using rapid variotherm press moulding instead or at least minimizing the deconsolidation time.

In future work the model will be validated with high performance hybrid textiles and the influence of statistical effects on porosity prediction assessed. The feasibility of rapid variotherm press moulding coupled with vacuum and the achievable cycle times will be investigated.



# Chapter 6: Three-dimensional extension

One of the key advantages of hybrid textiles is their high design flexibility. Many parameters can be easily or locally changed, including the orientation or textile architecture of each layer, the thickness of the thermoplastic ply to influence the fibre volume fraction, and the addition of material in local areas. This allows the composite properties to be tailored for specific applications, making it possible to combine high-performance with geometrical complexity. In addition, using appropriate processes such as rapid isothermal press moulding could also keep the cycle times competitive.

Despite these compelling advantages, the current lack of three-dimensional consolidation model has been a major obstacle to their successful development and implementation. Defects, such as porosities caused by incomplete impregnation or fibre disorientation resulting from in-plane matrix flow, cannot yet be predicted. A three-dimensional consolidation model would not only allow to predict the occurrence of such defects, but also enable design or process optimization in order to produce high-quality, defect-free parts as shown in Figure 6.1.

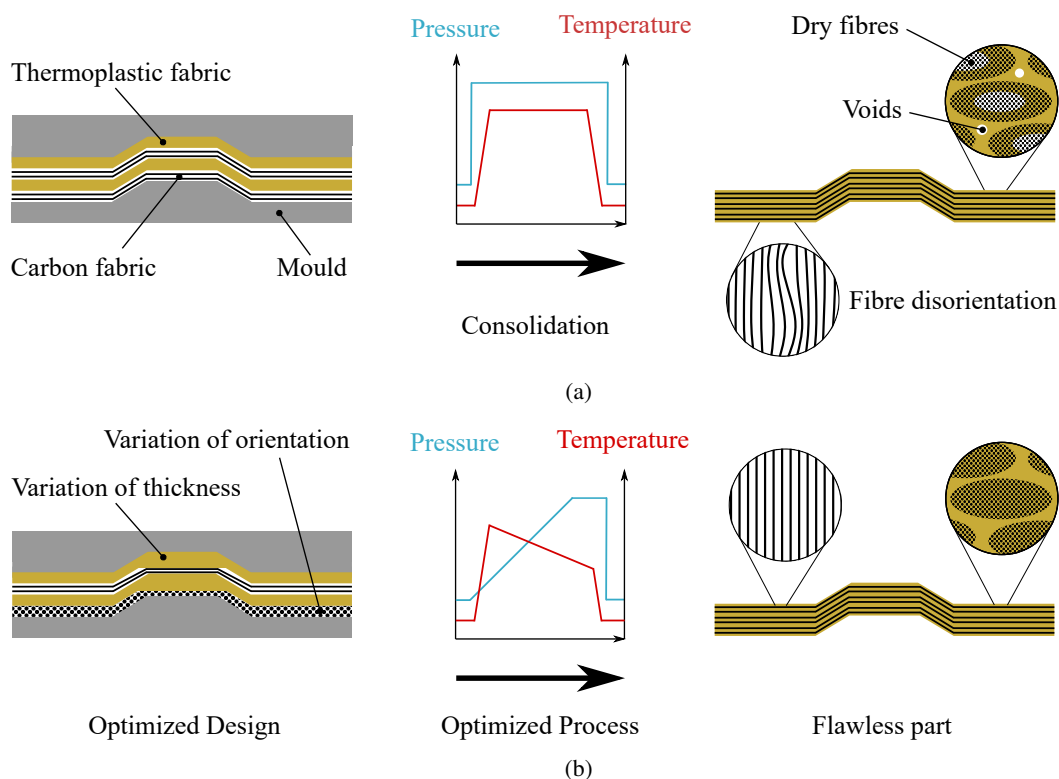


Figure 6.1: a) Representation of state-of-the art consolidation of hybrid textiles. For complex shapes defects such as depicted on the right might occur. The consolidation model presented in this study enables the prediction of such defects. b) Representation of an optimized consolidation process where appropriate selection of the design and process parameters prevents defect formation.

The consolidation of fibre-reinforced composites involves several physical phenomena occurring at the micro, meso and macro level, such as matrix flow, ply compaction, and bubble formation or collapse [12], [13], [37]. All of these phenomena have been extensively studied and are currently well understood [17], [34], [92], [97], [118], [119], [129]. Several models have been proposed for each phenomenon, usually these are valid for specific materials and processes as these heavily influence the underlying effects. This implies that the validity range of a consolidation model will be subjected to the same limitations of the models describing the underlying effects upon which it is built.

Regarding fibre movement for instance, Schuler and Advani [105] found that the fibre-matrix continuum in unidirectional plies behaves as a fluid transversally to the fibres. If the flow field is not homogeneous, fibre-matrix flow can cause fibre disorientation and waviness, which can significantly alter the mechanical properties [169]. Several authors subsequently proposed models for fibre-matrix flow based on the work of Schuler and Advani [107]–[110]. However, the fibre-matrix continuum does not behave as a fluid in fibre direction because the fibres restrict flow in that direction. Therefore, for woven textiles where fibres are oriented in different directions along which they restrict flow, the fibre-continuum cannot be described as a fluid in any direction [105]. Recent investigations by Hautefeuille et al. [111], [112] suggest that for woven textiles there is a threshold in matrix pressure gradient below which percolation regime takes place and above which fibre-matrix flow causing fibre disorientation occurs. Yet, models able to predict fibre disorientation and its extent are still lacking.

Void formation is another material-dependent phenomenon: in thermosets composites volatiles are emitted as a result of curing, which leads to the formation of bubbles. Porosities can also result from incomplete impregnation or from matrix shrinkage upon curing. Different models were proposed to describe bubble formation and collapse in thermosets, and are well established [85], [92], [97]. In thermoplastic composites voids can be created by entrapped air or by crystallisation shrinkage [88], [99], [164], [170].

Developing a three-dimensional consolidation model is challenging, as the different effects influence each other and the volume is not conserved as voids get filled during impregnation. Therefore, simply adding the models for the different phenomena taking place during consolidation is not possible. Developing a full-scale simulation is also difficult due to the multi-scale nature of the process, which represents a formidable computational challenge. Moreover, the complex interactions between textile, matrix and air at both the micro and macro level makes their description difficult. While several authors presented three phase models either for composite processing [171], [172] or earth science [173], [174], these are single scale flow models that cannot consider the impregnation of fibre bundles nor its influence on the matrix pressure. Models that consider dual scale flow [175], [176] on the other hand typically do not consider textile compaction or the change of volume due to impregnation of fibre bundles. Few authors proposed three-dimensional consolidation models that took into account all of these effects. Wysocki et al. attempted to model consolidation with a two-phase continuum framework and entropy inequality [11]–[13], a similar approach was followed by Rouhi et al. [14]–[16]. In both cases, the difficulty to determine the values of variables related to the entropy inequality equation make their implementation challenging in practice.

When it comes to models at the level of a unit cell however, a large body of work is available in the literature. These analytical models can be described as zero-dimensional, in the sense that variations of properties or parameters such as pressure or impregnation degree in any direction cannot be considered. Therefore, potential phenomena arising during consolidation and especially for complex shapes, such as in-plane and through-thickness material flow, are typically missing. Moreover, the change of volume due to impregnation and the resulting textile deformation and compaction is usually disregarded in available consolidation models. Most of the consolidation models at the level of a unit cell presented so far focus on modelling matrix flow in fibre bundles to predict impregnation degree and porosity [55], [100], [116], [134]–[136]. Jespersen et al. [24] a proposed one-dimensional consolidation model in the through-thickness direction that can account for matrix flow based on the work of Michaud et al. [118], [119], [177], [178] and Sommer and Mortensen [137], which model the impregnation of a compressible fibre mat.

Most of the authors assumed that air could freely escape the tow. Others, such as Bernet et al. [34] in their model about the consolidation of commingled yarns, introduced a threshold during impregnation after which the air gets entrapped. Rozant et al. [100] considered that air was trapped in the tows during the whole process in their model about the consolidation of knits, but did not consider dissolution. Several studies highlighted the difficulty in obtaining full consolidation in fibrous reinforcement due to internal voids [99], [131]. The experimental validation of consolidation models presented by many authors show poor accuracy in predicting the voids of fully consolidated composites. Yet, correct prediction of the final void content is relevant in composite production as it is detrimental to mechanical properties [84], [164].

In chapter 5 a model for the consolidation of hybrid textiles in which air entrapment and dissolution within the tow is considered was proposed and validated. The approach proved to be able to accurately predict porosity content, even in fully consolidated composites with low void content. Yet, the model complexity remains zero-dimensional and a three-dimensional extension is desirable in order to simulate the consolidation of complex-shaped parts.

In this chapter, the consolidation model recently proposed in chapter 5 is extended and implemented three-dimensionally in a way suitable for finite-element implementation and experimentally verified. The model considers a free form plate with changing thickness and constant through-thickness properties, and neglects any textile deformation. Since draping usually takes place before consolidation, the consolidation model presented here could be used in combination with existing models such as the ones presented in [179]–[181].

The consolidation model can predict parameters such as fibre volume and porosity content locally in a three-dimensional manner and takes into account in-plane matrix flow, as opposed to most of the current models for the consolidation of hybrid textiles. Additionally, the novel homogenization approach allows to consider change of volume as a result of in-plane matrix flow and impregnation. Compared to existing three-dimensional models, the model has the advantages that parameters can be easily identified through material characterization. The proposed consolidation model can identify areas with elevated matrix pressure gradients that are prone to defect formation. The study demonstrates that matrix pressure and impregnation degree in three-dimensional parts are non-uniform and that pressure gradients can cause fibre disorientation, leading to defects whose magnitude is proportional to the maximum matrix pressure gradient during consolidation.

## 6.1 Approach

In order to derive the constitutive equations for the three-dimensional consolidation of thermoplastic composites, a homogenization method based on a unit cell approach and a consolidation model were adopted. While the consolidation model proposed by Werlen et al. [18] was selected for this study, the methodology presented here is intended to be more general and applicable to other models as well. This homogenization method avoids the need for numerically expensive full-scale simulations at both the macro and micro level. Instead, finite element analysis is performed only on the homogenized medium at the macro level. Despite this simplification, the state of the homogenized medium remains well described by a set of descriptors, such as the impregnation degree or the fibre volume fraction.

During consolidation, the medium at hand is a three-phase mixture constituted of the liquid matrix, the solid fibres and air. At the beginning of consolidation the tows are dry and surrounded by completely molten polymer which fills the inter-tow space. In the tows, an initial quantity  $n_0$  of air is entrapped. The initial conditions and assumptions regarding consolidation are the same as in the consolidation model of Werlen et al. [18], where these are stated in greater detail.

A free form plate with non-uniform thickness and constant through-thickness properties, such as the part shown in Figure 6.2, is considered. It is assumed that the tows are incompressible, and that there is no fibre disorientation during consolidation, while shearing of the textile plies is neglected. While the model is strictly speaking not valid for consolidation with fibre disorientation, the effect is local so that it is safe to assume that the effects on the consolidation at part level can be neglected. In addition, the three-phase mixture is assumed to be deformable only in the normal direction to the textile plane orientation. In a standard press moulding process the mould is closed only in one direction, perpendicular to the textile, which is neither extended nor compressed in the in-plane direction.

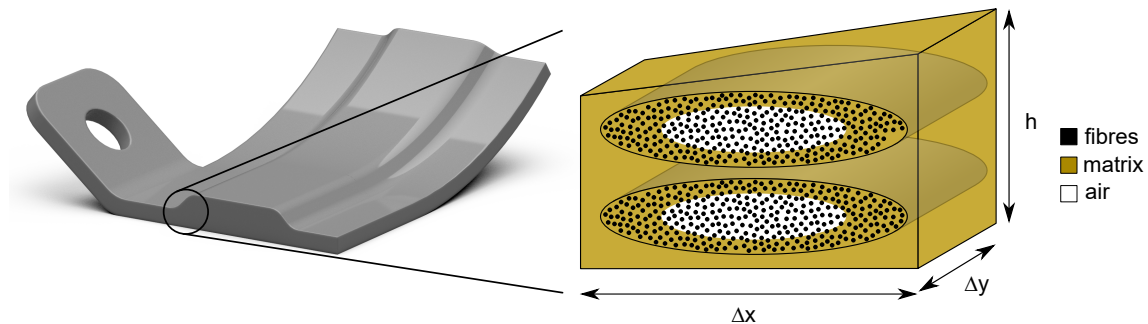


Figure 6.2: Example of a free form plate with non-uniform thickness and constant through-thickness properties, which corresponds to the geometrical complexity addressed by the model in this study. The part is discretized into unit cells that have a trapezoidal shape as represented on the right, which contain a three phase mixture consisting of air, fibres and matrix. The inter-tow space is completely filled with molten polymer, while the intra-tow space is occupied by matrix and air.

A unit cell is considered here, which will be used to derive the equations for the homogenized medium. The unit cell is obtained by discretizing the free form plate in both in-plane directions to obtain trapezoids containing the three-phase mixture with a number of portions of tow as shown in Figure 6.2. The trapezoid has a width  $\Delta x$ , a depth  $\Delta y$  and an height  $h$  spanning the whole local thickness of the plate since the plate is not discretized through-thickness. Since

the unit cell is a trapezoid,  $h$  depends linearly on  $x$  and  $y$  in order to be able to capture variations in thickness. The unit cell is constructed around the reinforcing textile, and the  $z$  direction of either the unit or homogenized medium is always normal to the local plane formed by the textile. The unit cell has fixed width  $\Delta x$  and depth  $\Delta y$  while the four edge heights can vary according to the aforementioned assumptions. In-plane matrix flow is allowed across the boundaries to reflect in-plane matrix flow resulting from pressure gradient. However no fibre crosses the boundaries as the unit cell is centred around it.

## 6.2 Constitutive equations

### 6.2.1 Medium descriptors

The consolidation model is written based on volume fractions formulation since a continuum formulation is sought. The fibre volume fraction  $\nu_f$  is defined as the ratio of the volume of a given entity over the total volume. While the matrix, gas and meso fibre volume fractions  $\nu_m$ ,  $\nu_g$  and  $\nu_f$  are defined over the unit cell volume, the tow fibre volume fraction  $\nu_{f,tow}$  is defined over the tow volume as expressed through Equation 6.2.1. Thereby, the unit cell volume  $V$ , density  $\rho$  and mass  $M$  are related through Equation 6.2.2:

$$\nu_m = \frac{V_m}{V} \quad \nu_g = \frac{V_g}{V} \quad \nu_f = \frac{V_f}{V} \quad \nu_{f,tow} = \frac{V_f}{V_{tow}} \quad (6.2.1)$$

$$M_m = \rho_m V_m \quad M_f = \rho_f V_f \quad (6.2.2)$$

where the subscripts  $f$ ,  $m$  and  $g$  indicates that the property is related to respectively fibre, matrix, or gas, and  $V_{tow}$  is the space occupied the tows, which includes the interstitial space between the fibres. The different volumes such as  $V_{tow}$  and  $V_g$ , refer to the sum of the volume of all the portions of tows inside the unit cell and not a single particular tow. The sum of the volumes of the different phases add up to the total volume and it therefore holds, by inserting Equation 6.2.1:

$$V_m + V_f + V_g = V \quad \nu_m + \nu_f + \nu_g = 1 \quad (6.2.3)$$

The tow impregnation degree is defined as the volume of impregnated tow  $V_{tow,impr.}$  divided by the volume occupied by the tow  $V_{tow}$ :

$$\xi = \frac{V_{tow,impr.}}{V_{tow}} \quad (6.2.4)$$

It is assumed that voids consist solely of the space between the fibres of the unimpregnated tow, where air is entrapped. Therefore, porosity and gas volume fraction are equivalent and one can establish a relation for  $V_g$  and describe  $\nu_g$  by inserting Equation 6.2.4 and 6.2.1 as following:

$$\begin{aligned} V_g &= (V_{tow} - V_{tow,impr.})(1 - \nu_{f,tow}) \\ \nu_g &= \nu_f(1 - \xi) \frac{(1 - \nu_{f,tow})}{\nu_{f,tow}} \end{aligned} \quad (6.2.5)$$

## 6.2.2 Constitutive equations

Mass conservation is applied to the unit cell, shown in Figure 6.2, to derive equations for the continuum. Considering that the fibres remain in the unit cell and have constant density, one can write, using Equation 6.2.2:

$$\frac{\partial M_f}{\partial t} = 0 \quad \frac{\partial \rho_f}{\partial t} = 0 \quad \frac{\partial V_f}{\partial t} = 0 \quad (6.2.6)$$

For the mass conservation of matrix the flux needs to be taken into account, with constant matrix density  $\rho_m$  and with Equation 6.2.2 it holds:

$$\frac{\partial M_m}{\partial t} = \frac{\partial V_m \rho_m}{\partial t} = \rho_m \frac{\partial V_m}{\partial t} \quad (6.2.7)$$

Equations 6.2.1, 6.2.3, 6.2.5 and 6.2.6 can be combined to yield, as detailed in appendix C:

$$\frac{\partial \nu_f}{\partial t} = -\frac{\nu_f}{V} \frac{\partial V_m}{\partial t} + \nu_f^2 \frac{1 - \nu_{f,tow}}{\nu_{f,tow}} \frac{\partial \xi}{\partial t} \quad (6.2.8)$$

$$\frac{\partial \nu_g}{\partial t} = (\nu_g - 1) \left( \nu_f \frac{1 - \nu_{f,tow}}{\nu_{f,tow}} \frac{\partial \xi}{\partial t} \right) - \frac{\nu_g}{V} \frac{\partial V_m}{\partial t} \quad (6.2.9)$$

To resolve the temporal change of matrix volume, which is directly linked to the in-plane matrix flow, Darcy's law [19] is applied and the unit cell and discretized as detailed in appendix D. Inserting the result back in the equations yields:

$$\begin{aligned} \frac{\partial \nu_f}{\partial t} = & \nu_f^2 \frac{1 - \nu_{f,tow}}{\nu_{f,tow}} \frac{\partial \xi}{\partial t} \\ & - \frac{\nu_f}{\eta} \left( \vec{\nabla} K \vec{\nabla} P_m + \frac{\vec{\nabla} h^T K \vec{\nabla} P_m}{h} \right) \end{aligned} \quad (6.2.10)$$

$$\begin{aligned} \frac{\partial \nu_g}{\partial t} = & (\nu_g - 1) \left( \nu_f \frac{1 - \nu_{f,\mu}}{\nu_{f,\mu}} \frac{\partial \xi}{\partial t} \right) \\ & - \frac{\nu_g}{\eta} \left( \vec{\nabla} K \vec{\nabla} P_m + \frac{\vec{\nabla} h^T K \vec{\nabla} P_m}{h} \right) \end{aligned} \quad (6.2.11)$$

whereas  $K$  is a second order diagonal tensor with permeability  $K_x$  and  $K_y$  in x and y direction, which depends on the fibre volume fraction [36], [37], [43].

$$K = \begin{pmatrix} K_x & 0 \\ 0 & K_y \end{pmatrix} \quad (6.2.12)$$

## 6.2.3 Consolidation model

In the following, the consolidation model proposed in chapter 5 is implemented to resolve the temporal change of impregnation degree  $\frac{\partial \xi}{\partial t}$ . This model describes the impregnation of an elliptical tow with semi major and minor axis  $l_w$  and  $l_h$  by considering an equivalent round tow with radius  $R_{eqv}$ , radius to the flow front  $r$  as shown in Figure 6.3, and similar impregnation kinetics. Because of the assumptions of homogeneous variables in the through-thickness direction, all



the tows inside an unit cell and their impregnation kinetics are identical, therefore considerations about a single tow can be extended to the whole unit cell. For instance, the tow impregnation degree can be related to the equivalent radius:

$$\xi = \frac{R_{eq}^2 - r^2}{R_{eq}^2} \quad (6.2.13)$$

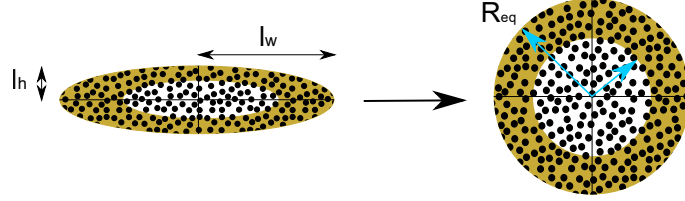


Figure 6.3: Schematic representation of the equivalent geometry. Reproduced with permission from [18].

In the consolidation model proposed in chapter 5, the flow front behaviour is described by resolving Equation 6.2.14. Expressing  $\frac{\partial \xi}{\partial t}$  on the basis of Equation 6.2.13 and combining it with Equation 6.2.14 allows to obtain Equation 6.2.15, as detailed in appendix E:

$$r \cdot \ln \left( \frac{r}{R_{eq}} \right) \frac{\partial r}{\partial t} = \frac{K_{tow}(P_m + P_c - P_g)}{\eta(1 - \nu_{f,tow})} \quad (6.2.14)$$

$$\frac{\partial \xi}{\partial t} = \frac{-2K_{tow}(P_m + P_c - P_g)}{R_{eq}^2 \eta (1 - \nu_{f,tow}) \ln(\sqrt{1 - \xi})} \quad (6.2.15)$$

In this equation  $K_{tow}$  is the tow permeability and  $P_m$ ,  $P_c$  and  $P_g$  are respectively the matrix, capillary and gas pressure. All the assumptions, considerations and equations of the consolidation model, including those to obtain  $P_m$  and  $P_g$  are described in detail in chapter 5. The capillary pressure  $P_c$  is still considered small in comparison with the elevated matrix pressure and neglected. The tow fibre volume fraction is assumed to remain constant here as it was found in other articles to have a weak dependence on applied pressure [18], [37].

The tow permeability  $K_{tow}$  is largely influenced by the tow fibre volume fraction, which depends on the applied pressure. Therefore, one can model the tow permeability as a function of the applied pressure despite the assumption of a constant tow fibre volume fraction. By describing  $K_{tow}$  as a function of the applied pressure through the function  $A_{tow} \cdot \log(P_{app}) + B_{tow}$  and inserting it into the model of Gebart [43] for the permeability of unidirectional reinforcements one obtains Equation 6.2.16, where  $R_f$  is the fibre radius. More detailed informations are provided in chapter 5.

$$K_{tow} = \frac{16}{9\pi\sqrt{6}} R_f^2 \cdot \left( \sqrt{\frac{\pi}{2\sqrt{3}(A_{tow} \cdot \log(P_{app}) + B_{tow})}} - 1 \right)^{\frac{5}{2}} \quad (6.2.16)$$

The gas pressure of the entrapped gas is obtained on the basis of the ideal gas law in Equation 6.2.17, thereby the initial amount of entrapped gas  $n_\lambda^0$  is given by Equation 6.2.18 and the variation of the amount of entrapped gas  $n_\lambda$  is described through Equation 6.2.19.

$$P_g = \frac{n_\lambda \cdot R \cdot T}{A_{tow} \cdot (1 - \nu_{f,tow}) \cdot (1 - \xi)} \quad (6.2.17)$$

$$n_\lambda^0 = \frac{P_{atm} \cdot A_{tow} \cdot (1 - \nu_{f,0} \cdot \nu_{f,tow})}{R \cdot T_0 \cdot \nu_{f,0}} \quad (6.2.18)$$

$$\dot{n}_\lambda = -2 \cdot \pi \cdot r \cdot G \cdot D \cdot (C_s - C_\infty) \cdot \left(1 + \frac{1}{\sqrt{\pi \cdot D \cdot G \cdot t}}\right) \quad (6.2.19)$$

where  $A_{tow}$  is the cross-sectional area of the tow,  $R$  the ideal gas constant,  $T$  the temperature,  $n_\lambda^0$  the initial amount of entrapped gas per unit depth in each tow,  $P_{atm}$  the atmospheric pressure,  $\nu_{f,0}$  the fibre volume fraction of the textile stack at rest,  $T_0$  the temperature at the beginning of consolidation,  $D$  the diffusion of air in molten polymer,  $G$  the correction factor for diffusion in fibrous medium,  $C_s$  the saturation concentration at the air-polymer interface and  $C_\infty$  the saturation concentration at atmospheric pressure. These three Equations are taken from chapter 5, where they are described in greater detail.

#### 6.2.4 Boundary conditions

For the boundary conditions an infinitely stiff guided mould is considered with an exact control system such that the cavity height or applied pressure perfectly corresponds to the prescribed one. This implies that the change of cavity height  $h_{cav}$  is the same everywhere in the mould and the closing speed  $v_{close}$  is defined as:

$$v_{close} = \frac{\partial h_{cav}}{\partial t} \quad (6.2.20)$$

The closure rate of the mould will translate to the composite and act as a boundary condition, but only if both are in contact. Therefore, the local rate  $v$  at which the composite thickness  $h$  changes reads:

$$v = \frac{\partial h}{\partial t} = \begin{cases} v_{close} & h = h_{cav} \\ 0 & h < h_{cav} \end{cases} \quad (6.2.21)$$

The composite thickness  $h$  and cavity height  $h_{cav}$  are schematically represented in Figure 6.4a. The local change of composite thickness is related to in-plane matrix flow and impregnation, which results in the composite taking up less space as the volume occupied by the gas phase is reduced. In the unit cell, whose width  $\Delta x$  and depth  $\Delta y$  are constant, simple geometrical considerations allow to relate the change of volume and thickness as following:

$$V = \Delta x \cdot \Delta y \cdot h \quad \frac{\partial V}{\partial t} = \Delta x \cdot \Delta y \cdot \frac{\partial h}{\partial t} \quad (6.2.22)$$

Combining these equations as described in appendix F transforms Equation 6.2.21 into:

$$\frac{v}{h} = \frac{\vec{\nabla} K \vec{\nabla} P_m}{\eta} + \frac{(\vec{\nabla} h)^T K \vec{\nabla} P_m}{h \cdot \eta} - \nu_f \frac{1 - \nu_{f,tow}}{\nu_{f,tow}} \frac{\partial \xi}{\partial t} \quad (6.2.23)$$

Within industrial manufacture mostly an applied force  $F_{app}$  is prescribed to the press and acts as boundary condition. Equation 6.2.23 always holds true with the aforementioned assumptions, therefore the closing speed which will require the prescribed amount of applied force is sought:

$$\begin{aligned} v_{close} \mid \iint (P_m + P_c - P_g) dx dy \\ = \iint P_{app} dx dy = F_{app} \end{aligned} \quad (6.2.24)$$

Thereby, the mechanical equilibrium between applied pressure  $P_{app}$ , matrix pressure  $P_m$  and textile stress response  $\sigma_{tex}$  as described in chapter 5 applies:

$$P_m = P_{app} - \sigma_{tex} \quad (6.2.25)$$

Here, no direct formulation to solve Equation 6.2.24 is proposed. Instead, iterative optimization methods are used to find the value of  $v_{close}$  satisfying the boundary condition.

### 6.2.5 Initial conditions

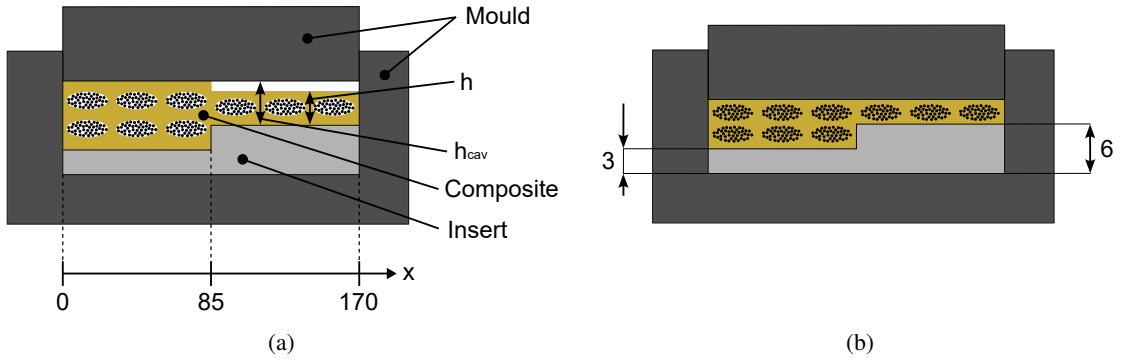


Figure 6.4: Schematic representation of the mould containing an insert to produce a plate with changing thickness with dimensions in mm. Figure 6.4a and Figure 6.4b represents respectively the unconsolidated and fully impregnated state. In Figure 6.4a the meso structure of the hybrid textile already collapsed and matrix completely fills the inter-tow space, as per the assumptions of the consolidation model. Because the void volume per unit area is larger in the thicker part of the mould, at the beginning of consolidation only the thick part is in contact with the mould. The tows are here shown schematically and the scale is not respected, as in the case study and in the experiments there are more layers of the glass textile fabric.

It is considered that the local amount of fibres and matrix are known, and that at the beginning of consolidation the tows are completely dry. The mould is manufactured to match the geometry of the fully consolidated plate, neglecting any in-plane matrix flow. The local height of the composite can be formulated with Equations 6.2.26, as detailed in appendix G:

$$h = \frac{N \cdot M_m^A}{\rho_m} + \frac{N \cdot M_f^A}{\rho_f} \left( 1 + (1 - \xi) \cdot \frac{1 - \nu_{f,tow}}{\nu_{f,tow}} \right) \quad (6.2.26)$$

where  $M_m^A$  and  $M_f^A$  are the local areal weight in a single layer of respectively the matrix and the fibres,  $N$  is the number of hybrid textile layers, and an impregnation degree  $\xi$  of 0 and 1 is inserted to obtain respectively the initial and final local plate thickness  $h_{start}$  and  $h_{end}$ . The initial fibre, matrix and volume fraction  $\nu_f^{start}$ ,  $\nu_m^{start}$  and  $\nu_g^{start}$  at the beginning of impregnation read, as described in appendix G and assuming an impregnation degree  $\xi$  of 0 at the beginning of consolidation:

$$\begin{aligned}\nu_f^{start} &= \frac{N \cdot M_f^A}{\rho_f \cdot h_{start}} \\ \nu_m^{start} &= \frac{N \cdot M_m^A}{\rho_m \cdot h_{start}} \\ \nu_g^{start} &= \frac{N \cdot M_f^A}{\rho_f \cdot h_{start}} \frac{1 - \nu_{f,tow}}{\nu_{f,tow}}\end{aligned}\quad (6.2.27)$$

### 6.3 Materials and material characterization

In this study, a quasi-unidirectional (UD) Leno glass fibre woven fabric with an areal weight of  $931 \frac{\text{g}}{\text{m}^2}$  provided by Tissa Glasweberei AG and polypropylene (PP) BJ100HP from Borealis in the form of 0.15 thick foils were used. The material properties used for the simulation are summarized in Table 6.1, with values taken from chapter 3 and 5. The areal weight of a matrix ply was measured by weighting polymer foils of known dimensions with a precision scale. The in-plane textile permeability transverse to fibre direction  $K_{xx}$  was measured with a custom setup. For the measurements the textile was cut to dimension with a CNC cutter machine, then placed in a cavity with adjustable height which is defined with spacers. Judicious selection of both the number of textile layers and cavity height allows to tailor the fibre volume fraction. During the measurement, a pressurized vessel let silicone oil flow in-plane through the textile which was then collected in a recipient whose weight was continuously measured. Several pressure sensors placed throughout the cavity allowed to measure the pressure and infer the pressure gradient. Finally, the permeability can be measured from the mass flow, density, pressure gradient, cavity height and width as detailed elsewhere [69]. Permeability was measured at fibre volume fractions of 0.37 and 0.49 with three repeats and a virgin sample for each new measurement, then the permeability in function of the fibre volume fraction was fitted to the following function, based on the modified Carman-Kozeny equation proposed by Gutowski et al. [36], [37]:

$$K = K_c \cdot \frac{\sqrt{\frac{\nu_f^{max}}{\nu_f} - 1}^3}{\frac{\nu_f^{max}}{\nu_f} + 1}\quad (6.3.1)$$

Table 6.1: List of the variables that were used in this study and corresponding values.

Variable	Description	Value	Unit
$A_{tex}$	First fitted constant for textile stress response	0.03	$\frac{\text{N}}{\text{m}^2}$
$A_{tow}$	Tow cross-sectional surface area	$1.14 \cdot 10^{-6}$	$\text{m}^2$
$A_{tow}^{\nu f}$	First fitted constant for tow fibre volume fraction	$8.23 \cdot 10^{-3}$	-
$B_{tex}$	Second fitted constant for textile stress response	24.2	-
$B_{tow}^{\nu f}$	Second fitted constant for tow fibre volume fraction	0.6244	-
$D$	Diffusion coefficient	$5 \cdot 10^{-9}$	$\frac{\text{m}^2}{\text{s}}$
$F_{app}$	Applied force	14.45	kN
$G$	Diffusion correction factor	$2.3 \cdot 10^{-4}$	-
$H$	Henry's constant	$3.6 \cdot 10^{-5}$	$\frac{\text{mol}}{\text{Pa} \cdot \text{m}^3}$
$K_c$	Fitted constant for in-plane textile permeability	$1.3 \cdot 10^{-9}$	$\frac{\text{m}^2}{\text{s}}$
$K_x$	In-plane textile permeability	$5 \cdot 10^{-11}$	$\text{m}^2$
$M_f^A$	Areal weight of a textile ply	0.931	$\frac{\text{kg}}{\text{m}^2}$
$M_m^A$	Areal weight of a matrix ply	0.287	$\frac{\text{kg}}{\text{m}^2}$
$N_1$	Number of plies in the thin part of the plate	4	-
$N_2$	Number of plies in the thick part of the plate	8	-
$R_{eq}$	Equivalent radius	$4.47 \cdot 10^{-4}$	m
$R_f$	Fibre radius	9	$\mu\text{m}$
$T$	Processing temperature	463.15	K
$\eta$	Molten polymer viscosity	495	$\text{Pa} \cdot \text{s}$
$\nu_{f,0}$	Textile fibre volume fraction at rest	0.4378	-
$\nu_{f,max}^{hex}$	Maximal hexagonal packing	$\frac{\pi}{2\sqrt{3}}$	-
$\nu_{f,tow}$	Tow fibre volume fraction	0.75	-
$\rho_m$	Density of molten polymer	763	$\frac{\text{kg}}{\text{m}^3}$
$\rho_f$	Density of the textile	2524	$\frac{\text{kg}}{\text{m}^3}$

## 6.4 Case study

A case study was conducted to numerically validate the model and examine phenomena on geometries that are more complex than a flat plate. Specifically, a flat plate with a stepwise thickness change was selected, whereas four plies of hybrid textile were placed in the thinner part of the plate and twice as many plies in the thicker part. It was considered that the part was pressed in a mould designed to match the thickness of the fully consolidated plate in its molten state, which was respectively 3 and 6 mm. In this study, the desired mould geometry was obtained by placing an insert in a custom 170x85 mm mould originally meant to produce flat plates, as represented in Figure 6.4. In the following, the coordinate system defined in Figure 6.4 is used when describing the position along the plate. Accordingly, the thick part of the plate is located between 0 to 85 mm.

To simulate the consolidation process, the set of equations was implemented in the PDE module of COMSOL Multiphysics® 5.4. The problem was reduced to a 2D problem since the consolidation is homogeneous along the plate width. The set of equations was implemented on a 1D domain only, as the change of thickness (second dimension) was implicitly defined in the set of equations. The closing speed in function of time was optimized to satisfy the boundary condition expressed in Equation 6.2.24. A mean applied pressure of 1 MPa was selected as the boundary condition, which corresponds to an applied force of 14.5 kN, and consolidation is simulated for 10 min.

The results indicated that none of the variables were homogeneous, confirming that unit cell models are not sufficient for complex shapes. Figure 6.5 shows the value distribution of several variables along the plate after a consolidation time of 60 s. The most significant changes in variable values occurred in the middle of the plate where the thickness changes. The thicker part of the plate was subjected to a higher pressure, which led to a more elevated impregnation degree, which resulted in a lower void volume fraction and somewhat higher fibre volume fraction in agreement with Equations 6.2.5 and 6.2.10.

The evolution of the mean values of the impregnation degree  $\xi$ , the fibre volume content  $\nu_f$  and the porosity  $\nu_g$  as a function of time is shown in Figure 6.6. The impregnation degree rapidly increased at the beginning of consolidation, after which the curve flattened out. The model also predicted a fast closure speed of  $1.1 \cdot 10^{-4} \frac{m}{s}$  at the beginning of consolidation, which then sharply decreases to  $5.5 \cdot 10^{-9} \frac{m}{s}$  after 10 minutes. This behaviour is explained by the dependence of the mould closure speed on the impregnation degree expressed in Equation 6.2.23. The mean matrix pressure was equal to the applied pressure defined as the boundary condition due to mechanical equilibrium, since the textile stress response was predicted to be negligible. All of these observations correspond to an expected behaviour, very similar to the results described by Werlen et al. [18] for the 0D case of a homogeneous flat plate.

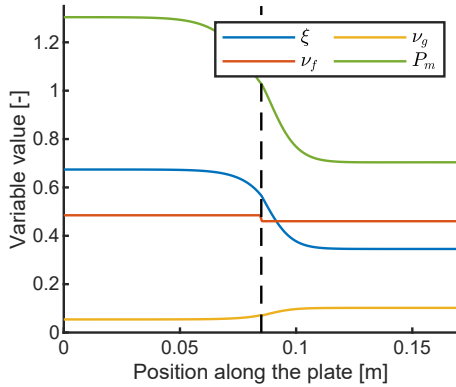


Figure 6.5: Model prediction on the impregnation degree  $\xi$ , fibre volume fraction  $\nu_f$ , void volume fraction  $\nu_g$  in function of the position in the mould after 60s. of consolidation under 1 MPa of applied pressure. The dotted line indicates the location of the thickness change.

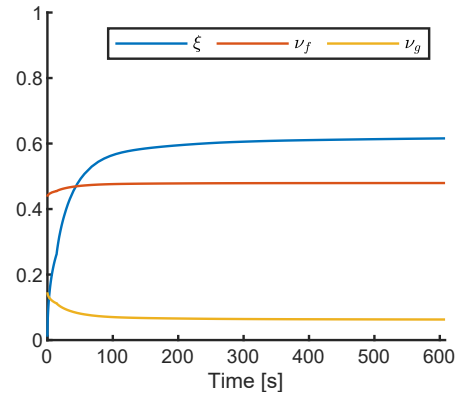


Figure 6.6: Model prediction on the mean impregnation degree  $\xi$ , fibre volume fraction  $\nu_f$ , gas volume fraction  $\nu_g$  for an applied pressure of 1 MPa in function of the consolidation time  $t$ .

Figure 6.9 presents the evolution of the pressure distribution in the plate as a function of time. The composite thickness change is dependent on the impregnation degree and proportional to the number of textile layers, as expressed through equation 6.2.26. Because the change of thickness resulting from impregnation is greater in the thicker part of the step plate, and because the mould fits the fully impregnated plate, at beginning of consolidation only the thicker part of the step plate will be in contact with the mould and under pressure.

A considerable matrix pressure gradient arises in the middle of the plate, as a result of this pressure distribution imbalance. This significant pressure gradient creates an in-plane flow, which can cause fibre disorientation if the tows are dragged along. With progressing impregnation the thickness decreases because voids gets filled as represented in Figure 6.7. Hence, at some point

the thinner part of the plate also comes in contact with the mould and pressure starts to build up there. In Figure 6.9, this can be observed after 12 s. Overall, the pressure gradient results in an in-plane flow which counteracts the pressure imbalance, as a result the maximal pressure gradient decreases over time as shown in Figure 6.8. Simulation performed with other boundary conditions show that the initial maximum pressure gradient is proportional to the closure speed and applied pressure.

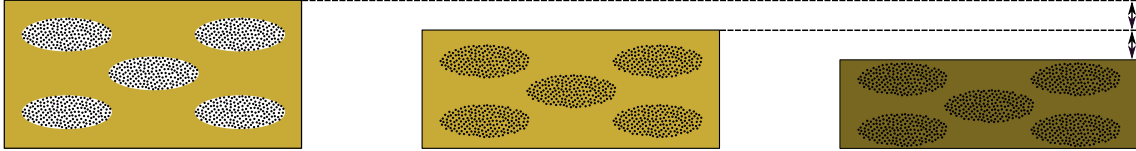


Figure 6.7: Schematic representation of the change of thickness during consolidation. The initial state is shown in the left, the fully impregnated state in the middle and the final state after cooling on the right. The light beige shade indicate molten polymer while the darker shade indicates a solidification.

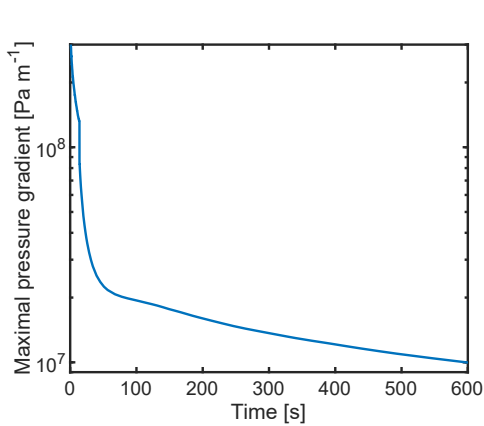


Figure 6.8: Predicted maximal pressure gradient in function of the time for a consolidation pressure of 1 MPa, which is always located at 85 mm in the middle of the plate where thickness changes.

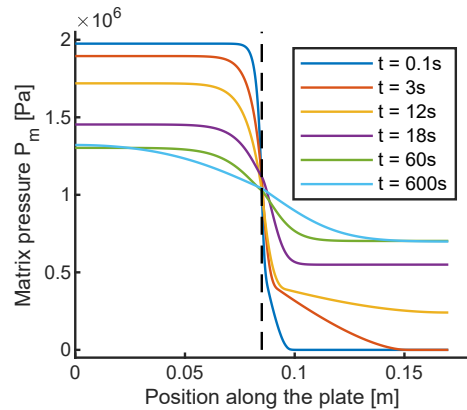


Figure 6.9: Predicted matrix pressure  $P_m$  distribution in the mould in function of the consolidation time  $t$ . The dotted line indicates the location of the thickness change.

## 6.5 Experimental verification

Step plates were pressed at different pressures, then possible defects were measured and quantified. As the validation of impregnation was already carried out in chapter 5, the focus of the experimental verification was laid on effects taking place only in complex geometries. The following points, ensuing from the case study, were sought to be demonstrated:

1. In complex geometries in-plane matrix pressure and flow arise and can potentially create defect by altering the textile architecture and disorienting the fibres.

2. During the consolidation of step plates, the highest matrix pressure gradient takes place where the thickness changes, in the middle of the plate. Therefore, this is where fibre disorientation should arise.
3. The maximal pressure gradient is proportional to the applied force, therefore higher applied pressures should result in larger defects.

For the experiments, textile plies were cut to the dimensions of the mould with a CNC cutting machine while the thermoplastic foils were cut by hand with a cutter and a stencil. The plies were then placed into the custom plate mould equipped with the insert and temperature sensor, thereby great care was taken not to disturb the textile architecture, which was ensured by visual inspection. The mould containing the plies was placed in a press heated to 200 °C with a spacer to avoid applying pressure during heating up, which was then removed when the composite reached processing temperature. This ensured the consolidation process to be identical and comparable to the simulation. The mould was then placed in a cold press and cooled down under the same pressure. Plates were produced with the following pressures, which were kept constant during consolidation: 0.07/0.14/0.5/1/3.5 MPa. The consolidation experiments were performed with two different presses, because a single one could not have covered the whole range of pressures. At low consolidation pressures up to 0.5 MPa, an APV Meyer press was used while at higher pressures experiments were performed with a two-stage Vogt press.

A visual inspection revealed fibre disorientation in some of the produced plates. In the plate consolidated at the lowest pressure, hardly any defect could be observed. However, irregularities were then more pronounced with increasing consolidation pressure. The biggest defects were located in the middle of the plate where the thickness changes, in addition zones where the textile is either stretched or compressed could be observed. This is illustrated in Figure 6.10, where a close-up of the plates produced at the lowest and highest pressure is shown.

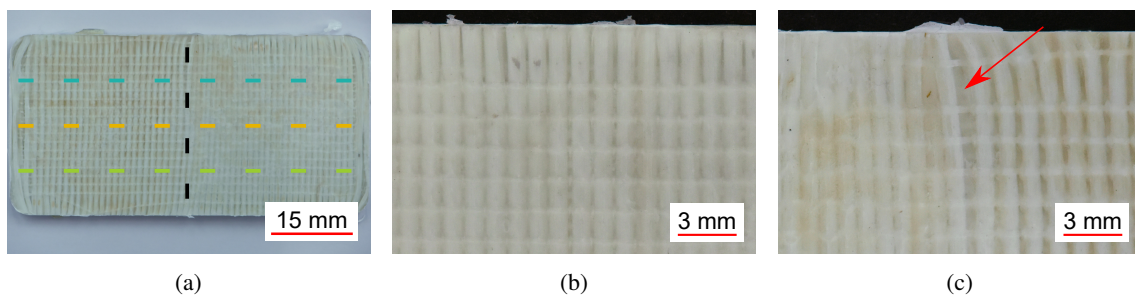


Figure 6.10: Picture of the backside of the plate pressed at 3.5 MPa in Figure 6.10a, whereas the vertical dashed line indicates the location of the step change and the defects were measured along the three horizontal dashed lines. Close up pictures of the backside, in the region of the thickness change, of the plates produced with a consolidation pressure of 0.07 MPa in Figure 6.10b and 3.5 MPa in Figure 6.10c. The defect is indicated in Figure 6.10c with a red arrow while almost undisturbed textile geometry can be observed in Figure 6.10b. Additional Pictures can be seen in appendix H.

The plates were then analysed and the defects measured. The deviation from average tow spacing was selected as a method to quantify the defects, because in an ideal plate all the tows of the textile would be perfectly straight and equidistant. To this end, the face of the plate without step was photographed in high resolution with a Nikon D810 camera, together with a scale for reference. The position of the tows were manually measured with the software ImageJ by pinpointing



the left and right edge of each tow along a virtual line parallel to the plate in the x direction. The position of each tow was then inferred as the mean value of the two points, subsequently the distance between two tows  $d$  and the average distance between the tows  $\bar{d}$  were measured. The deviation from mean spacing  $\Delta d$  is defined in Equation 6.5.1:

$$\Delta d = d - \bar{d} \quad (6.5.1)$$

The measurements were repeated along three different lines separating the plate in equidistant parts. The defect size  $\widetilde{\Delta d}$  was finally measured as the seven-point mean moving average of the defects, to reduce the noise in the single measurement points and identify trends. In all the plates produced, the largest measured defects were located in the middle of the plate where the thickness changes as expected, confirming that the largest pressure gradients arise at this location. Exemplary results for the plates produced with a consolidation pressure of 0.07 and 3.5 MPa are shown in Figure 6.11a and 6.11b. Thereby, the defects were measured along three different lines as mentioned earlier and as represented in Figure 6.10a.

Measuring the defects of the plate produced at the lowest pressure in Figure 6.11a confirms that the plate is nearly defect free and indicates a measurement precision of  $1 \cdot 10^{-4}$  m, therefore it cannot be excluded that the very small measured defect size are measurement inaccuracies. The single defect points are in the range of  $0 \pm 2 \cdot 10^{-4}$  m, which indicates the measurement accuracy of single points. The defect size along the plate confirms that applying a moving average helps to reduce noise, as its value remains very close to zero.

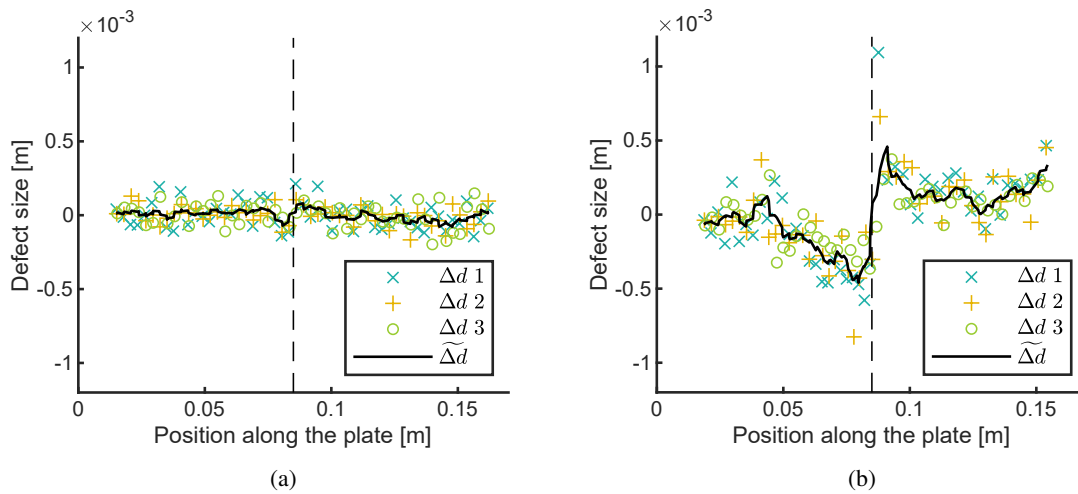


Figure 6.11: Measured defects of the plates pressed at 0.07 MPa in Figure 6.11a and 3.5 MPa in Figure 6.11b.  $\Delta d$  is the deviation between tow spacing and mean tow spacing, measured along three different lines.  $\widetilde{\Delta d}$  is the moving average of the single measurement points, which is defined in this study as the defect size. The dotted lines indicates the thickness change in the middle of the plate.

Figure 6.11b is very different and illustrates the presence of fibre displacement. The largest defects are located in the middle of the plate, and the zones where the average defects are positive and negative indicates respectively stretching and compression, in line with the observations made with the naked eye. The moving average of the defects along single measurement lines are very close to each other, which is expected as all parameters should remain constant along fibre direction.

Figure 6.12 shows the maximal measured defect size in function of the consolidation pressure. Since larger defects are caused by higher pressure gradient, these observations are therefore in line with the model which predicted maximal matrix pressure gradients proportional to the consolidation pressure. In addition, the largest defects systematically occur as predicted where the plate thickness change, demonstrating the ability of the model to capture the relevant phenomena during consolidation. One can see in Figure 6.12 that for the virtually defect-free plate pressed at 0.7 bar the defect size is below the detection threshold, while in the plate pressed at 1.4 bar the measured defect is already significant. This indicates a defect formation threshold at a consolidation pressure around 1 bar, which corresponds to  $45 \text{ MPa m}^{-1}$ , the maximal pressure gradient in Figure 6.8.

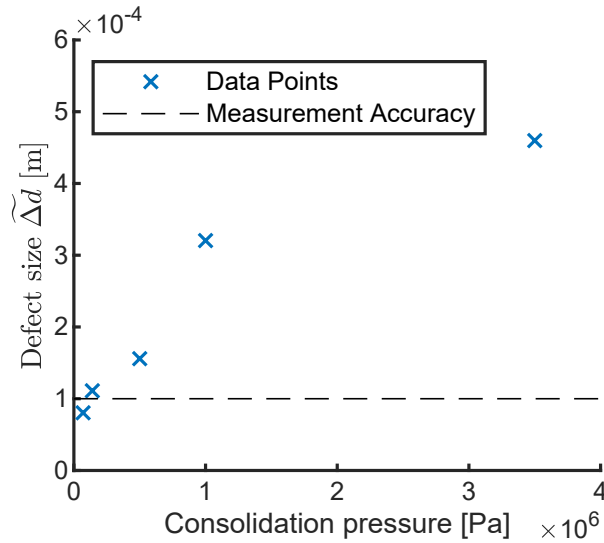


Figure 6.12: Measured maximal defects in step plates produced at different consolidation pressures. The defect size in function of the pressure gradient follow similar trends, since consolidation pressure and pressure gradient are proportional.

## 6.6 Discussion

The model developed in this study can predict consolidation of free form plates with changing thickness and constant through-thickness properties. The model was implemented in 2D in order to perform experimental verification. Complex phenomena arising in three-dimensional geometries could be successfully identified and explained. To our best knowledge, fibre disorientation resulting from thickness change during press moulding of hybrid textiles has not been documented so far. This work is an intermediate step towards a fully three-dimensional consolidation model, in which the assumption of constant through-thickness properties will be overcome. The 2D implementation in FEM is intended to demonstrate the feasibility and meaningfulness of the approach and for verification purposes. Full FEM implementation of the consolidation model in three-dimension is foreseen as future step, for which it is thought that a dedicated solver is necessary. Since most of the parameters such as impregnation degree are not homogeneous throughout complex parts, the proposed consolidation model can be used in the design phase al-

ready to identify critical areas and optimize both design and process.

During consolidation trials on step plates, lower pressures were found to result in smaller defects, however within industrial production this is not a reasonable solution to produce a defect-free part as it also results in significantly larger cycle times. Another solution to minimize defect size would be for example to change the textile orientation. The textile architecture most probably has an influence too, which is however unclear at the moment. It would be useful to develop, in future research, a model predicting the defect size in function of the textile architecture and pressure gradient. Hautefeuille et al. [111] reported a threshold for fibre disorientation for in-plane flow, which depends on the viscosity and flow rate. In this study, consolidating step plates below 1 bar of pressure resulted in defect-free parts and it was found that the threshold of matrix pressure gradient above which fibre disorientation takes place is  $45 \text{ MPa m}^{-1}$ .

Since the pressure gradient is predicted to be maximum at the beginning and then rapidly decrease, another possibility to reduce defect size that should be investigated is to apply first very low pressure and then to gradually increase it. This way of doing could allow to strike a balance between defect minimization and cycle time in order to keep the process relevant for the industry. One last possibility would be to optimize the geometry, for example by smoothing the transition between zones with different thicknesses with ply drop-off.

Since the model can predict a set of properties at each location throughout the part such as porosity and fibre volume fraction, it could be used during the design phase for optimization purposes. In this study, the hybrid textile properties were homogeneous in the plate. Yet, the model can be used on complex shaped with different textiles, textile orientations and areal weights at different locations in the part.

In this study, the model complexity was limited by the assumption that the composite properties are constant through-thickness. In future work, the model will be fully extended to three dimensions, so that inhomogeneous hybrid textile layups and through-thickness effects can be considered. Through-thickness effects can arise if there is an imbalance of textile stress response for example, as described for example in Studer et al. [25] or Michaud et al. [118], [119].

In future work, it is planned to validate the model with the high-performance hybrid textile shown in Figure 7.2e and to measure a set of parameters such as matrix pressure and porosity throughout the part to compare it against model predictions. After fully implementing the model in three dimensions, it should also be validated for more complex geometries and lay-up. It is thought that a dedicated solver is necessary to implement the model fully numerically in three dimensions, in addition further boundary conditions should be implemented. While in this study it was assumed that the mould is rigid, in reality steel is elastic and this should be embedded in the simulation, as this is relevant for high pressure consolidation.

In order to be able to simulate the whole consolidation process, it would be furthermore necessary to implement a thermal simulation in the model and include matrix phase transitions. During a variothermal press cycle and especially for thick parts, the temperature is not homogeneously distributed throughout the part. Since several parameters such as viscosity and solubility of gases in molten polymer have a very strong dependence on temperature, accurately modelling it is of prime importance. Implementing the matrix phase transition such as vitrification and crystallisation would allow to properly predict the fibre volume content in solidified state, which differs

from the molten state since the matrix density and thus total volume are different as pictured in Figure 6.7. During cooling down, solidification could also result in pressure gradient and defect formation and this should be investigated in future studies.

The consolidation model proposed in this study allows to determine a variety of parameters in complex shaped composites, and can be used to identifying porosities or zones with potential fibre disorientation during the design phase already. The information about fibre volume fraction and porosity provided by the model could be used as a basis to determine the mechanical properties. Therefore, all the necessary variables to enable optimization of complex-shaped composites are available.

## 6.7 Summary

In this chapter, a three-dimensional consolidation model for hybrid textile is proposed and experimentally verified. By adopting a homogenisation method, the multi-scale nature of the problem can be bypassed and computational power requirements significantly reduced when compared to a full scale simulation. The model is based on the consolidation model proposed in chapter 5, however the method is applicable to other consolidation models as well. The consolidation model can predict the properties of the part at each location through a set of characteristic parameters such as fibre volume fraction, impregnation degree and porosity.

The model successfully predicted the emergence of matrix pressure gradients in three-dimensional geometries, which can lead to fibre disorientation. Experimental verification confirmed the model predictions, and new mechanisms for the emergence of matrix pressure gradients and defect formation resulting from thickness differences in the mold were unveiled and explained.

Current model limitations are the assumptions that the properties are assumed constant through-thickness, however this issue will be addressed in future work. Phase change for the matrix will be introduced, so that consolidation can be predicted in full three-dimensional complexity over the whole production cycle. This will allow to verify model predictions on local characteristic parameters. Finally, the consolidation model presented in this study enables design and process optimization, which shall be investigated in future work.

## Chapter 7: Summary and outlook

Developing a three-dimensional consolidation model is paramount to enable the breakthrough of press moulding of hybrid textiles in the industry, as it can predict a set of properties locally as well as possible defects such as porosity and fibre disorientation. It also enables optimization of both process and design, paving the way for high quality composite part production.

The objectives of this Thesis were to develop a three-dimensional consolidation model for the press moulding of hybrid textiles that is suitable for FEM analysis. In this work, a thorough analysis of the state-of-the-art was performed to understand well the capacities and limitations of the different models addressing topics relevant for consolidation. Then, an analytical model for the stress response of textiles was experimentally validated, thereby a numerical approach was proposed to determine the model parameters. A novel consolidation model considering air entrapment and dissolution was then developed and experimentally validated, as these effects were usually disregarded so far yet found to significantly influence impregnation. Finally, the model was extended and implemented in a way suitable for finite-element implementation and experimentally verified with the consolidation of a free form plate with changing thickness and constant through-thickness properties, which is representative of geometries found in press moulding.

The three branches Maxwell Wiechert model with strain dependent stiffness and strain-rate dependent relaxation time validated in this work was thought to be well suited for a consolidation model because of its ability to accurately describe the viscoelastic stress response of textiles at different strain rates and degree of compaction. Yet, the textile stress response was found to be almost negligible during compaction, because the matrix phase change results in lower fibre volume fraction during processing when compared to the solidified state, thereby decreasing the textile stress response. Therefore, simply describing the quasi-static stress response was found to be largely sufficient and viscoelastic effects were finally not implemented in the consolidation model. However, the proposed numerical approach and the findings related to the influence of strain deviation during material characterization remain valuable for other process and fields.

The consolidation model considering air entrapment and dissolution proposed in this thesis not only demonstrated the relevance of these effects, but was able to accurately predict remaining porosity as a result of entrapped air. This is very important for defect prediction, but also unveils new mechanisms taking place during impregnation and provides for a better understanding. These findings imply that fast impregnation times could be achieved if the air was evacuated, by the mean of vacuum for example, making press processes attractive for the industry.

A three-phase unit cell approach that is able to take into account volume change as a result of matrix flow and impregnation was adopted to extend the consolidation model in three dimensions, furthermore homogenizing it allows to reduce computation time. This novel approach allowed to achieve the objectives of this thesis and model the consolidation of three-dimensional parts. The mechanisms leading to the emergence of matrix pressure gradients and fibre disorientation, which were not known so far, could be identified, explained and experimentally verified.

While a method to model the three-dimensional consolidation of hybrid textiles was successfully presented and implemented, significant work is still necessary until each of the novel topics addressed in this thesis is fully understood and validated. Still following the same method, the consolidation model can be further enhanced in order to overcome current limitation in future work, and progresses remains to be done in the FEM implementation, which will probably require the development of a dedicated solver.

Regarding the consolidation model, validation is desirable with other materials and necessary with hybrid textiles. Additional research about air entrapment and diffusion in fibrous media could allow to refine the model, while characterization of the solubility and diffusion factors of polymers is necessary since it is still almost completely lacking. While direct tow permeability measurement was performed to validate the permeability model of Gebart at very high fibre volume fractions, it is desirable to enhance the setup in order to obtain more accurate measurements since permeability is a major source of uncertainty. By making the measurement device more stiff, using steel for instance, and by accurately measuring the cavity height, with a linear variable displacement transducer for example, both the fibre volume fraction and the permeability at different pressures would be measured at once.

Based on the results of this study, the economical and technical feasibility of press moulding under vacuum, rapid variothermal press moulding or a combination of both should be investigated. Different strategies can be followed depending on the part complexity and cost constraints, for example infrared heating coupled to automated draping and demoulding would be suitable for simple parts with lower costs while manual hand lay-up can be applied for more complex and costly parts. To simulate the whole process, it is necessary to implement matrix phase transition in the model and couple it to thermal simulation.

When it comes to the three-dimensional extension of the consolidation model, it would be useful to develop in future research a model able to predict the extent of fibre disorientation in function of relevant material parameters and matrix pressure gradients. Furthermore, the through-thickness homogeneity assumption should be overcome. While it is rather straightforward to implement through-thickness matrix flow with the current approach, dealing with volume change as a result of matrix flow and impregnation might be more complicated. The following approach is proposed, as illustrated in Figure 7.1:

- Solve consolidation for a given timestep
- Calculate the change of volume in each mesh element
- Determine the new center of each mesh element:
  - Start with the layer fully in contact with the mould
  - Determine, layer by layer, the center of each mesh element based on the location of the element underneath and the thickness of the elements
  - Thereby, the center of mesh elements can only move in the direction normal to the local layer orientation (following the assumption that the textile do not undergo any deformation).
  - Reconstruct the mesh and make sure that mass is conserved.
  - Update mould closure such that it is in contact with the composite.

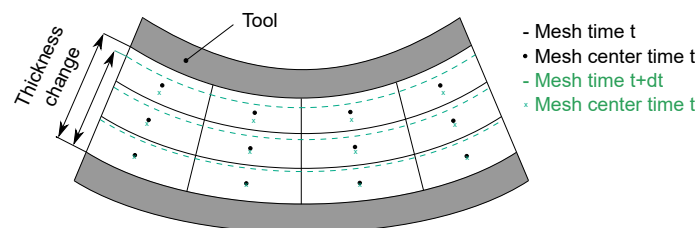


Figure 7.1: Representation of the proposed remeshing method for each timestep, to take into account the change of thickness as a result of impregnation.

Thereby, a dedicated solver might be required to implement the adaptive meshing and address the difficulties that a change of volume and medium properties bring. While the current proposition focuses on FEM solving, the suitability of other methods such as Material Point Method (MPM) solving shall be investigated.

The current implementation, which was mostly meant for demonstration purposes, adopted a boundary condition based on an infinitely stiff tool which could not be solved directly. In future work, the mould could be modelled to introduce a flexible layer while the composite is assumed rigid over a small time-step. This would allow to model the redistribution of pressure on the composite, enabling to solve consolidation over a time-step directly.

Within the ConThP project, it is planned as next step to validate consolidation with high-performance hybrid textiles, which are represented in Figure 7.2 along with the different stages of the production. Polyetherimide (PEI) was obtained in the form of granulates shown in Figure 7.2a, which was then melt-spun in a spool pictured in Figure 7.2b and turned into a textile as shown in Figure 7.2c. Alternatively stacking the PEI textile with a tailor-made quasi-UD carbon layer represented in Figure 7.2d finally yields the side-by-side hybrid textile shown in Figure 7.2e. By building a custom tool for a semi complex part with integrated pressure sensors, it is intended to validate the three dimensional consolidation model and demonstrate the possibilities of press moulding hybrid textiles. This will be performed by our project partners at the Faserinstitut Bremen (FIBRE).

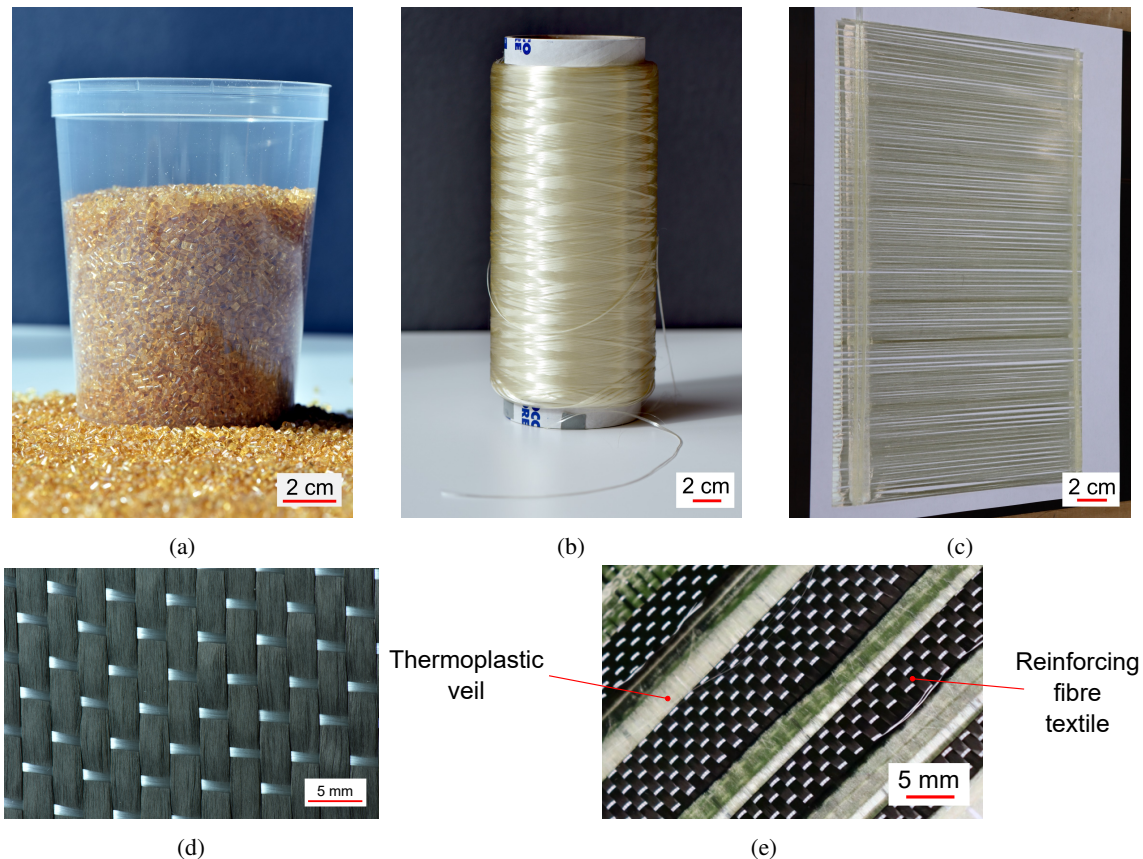


Figure 7.2: Picture of the hybrid side-by-side textile intended for validation purposes in Figure 7.2e along with the different stages of the production. The textile stack has a partial and staggered cutaway, unveiling the different layers of the stack. Reproduced with permission from [156]. Figure 7.2a shows the PEI granulate as received, which was then melt spun in a rowing spool shown in Figure 7.2b. Figure 7.2c shows a picture of a single layer of flexible thermoplastic ply, which was obtained by filament winding and local welding. The quasi-UD carbon textile is shown in Figure 7.2d.

Finally, the possibility to optimize design and process on the basis of the consolidation model should be experimentally demonstrated in order to attain the vision presented in this work. Hopefully, this thesis will enable the production of high-end complex shaped parts, the breakthrough of press-moulded hybrid textiles, and overall contribute to bring better, more cost-effective and sustainable products to the market.



# Appendix

## A Initial amount of entrapped air

To determine the amount of air trapped in each tow per unit depth, a stack of textile at rest as represented in Figure 7.3 with volume  $V$  and depth  $d$  is considered. The volume occupied by the tows, by a single tow and by the fibres are denoted respectively  $V_{tow}$ ,  $V_{tow}^{single}$  and  $V_f$ . The volume occupied by the tows includes everything inside the tow boundaries, meaning both the fibres and the space between them.

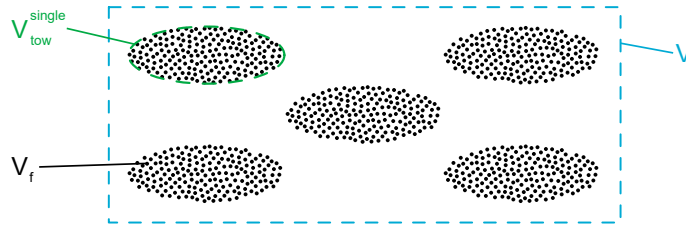


Figure 7.3: Schematic representation different volumes at the meso level of a stack of textile: the volume occupied by the fibres  $V_f$ , the volume occupied by a single tow  $V_{tow}^{single}$  and the total volume  $V$ . The volume  $V_{tow}$  is not indicated but would be the sum of the volumes occupied by the single tows  $V_{tow}^{single}$ .

To begin with, the fibre volume fraction at rest  $\nu_{f,0}$  and the tow volume fractions  $\nu_{f,tow}$  are defined as:

$$\nu_{f,0} = \frac{V_f}{V} \quad (\text{A.1})$$

$$\nu_{f,tow} = \frac{V_f}{V_{tow}} \quad (\text{A.2})$$

The volume occupied by the gas phase  $V_g$  is directly found by subtracting the volume occupied by the fibres from the total volume. Inserting the definition of the fibre volume fraction one finds:

$$V_g = V - V_f = (1 - \nu_{f,0}) \cdot V \quad (\text{A.3})$$

Assuming that the air is equally distributed, the amount of air  $V_{g,tow}$  that will be pushed inside each tow is found by dividing the volume occupied by the gas phase in a given control volume with the number of tows  $n_{tow}$  present in that control volume:

$$V_{g,tow} = \frac{V_g}{n_{tow}} \quad (\text{A.4})$$

This variable is found by relating the volume occupied by the tows to the volume occupied by a single tow, which is the product of its cross-section  $A_{tow}$  and its depth.

$$n_{tow} = \frac{V_{tow}}{V_{tow}^{single}} = \frac{V_{tow}}{A_{tow} \cdot d} \quad (\text{A.5})$$

The ideal gas law is applied to determine the amount of air entrapped per tow and unit depth  $n_{\lambda}^0$ . Considering that the volume occupied by the air  $V_{g,tow}$  that will be pushed in each tow is initially at atmospheric pressure  $P_{atm}$  and temperature  $T_0$ , it is given as:

$$n_{\lambda}^0 = \frac{P_{atm} \cdot V_{g,tow}}{R \cdot T_0 \cdot d} \quad (\text{A.6})$$

Finally, inserting all these together yields:

$$n_{\lambda}^0 = \frac{P_{atm} \cdot (1 - \nu_{f,0}) \cdot \nu_{f,tow} \cdot A_{tow}}{R \cdot T_0 \cdot \nu_{f,0}} \quad (\text{A.7})$$

## B Fibre volume fraction

The fibre volume fraction is defined as:

$$\nu_f = \frac{V_f}{V_f + V_m + V_g} \quad (\text{B.1})$$

where  $V_f$ ,  $V_m$  and  $V_g$  are the volume occupied respectively by the fibre, matrix and gas as represented in Figure 7.4.

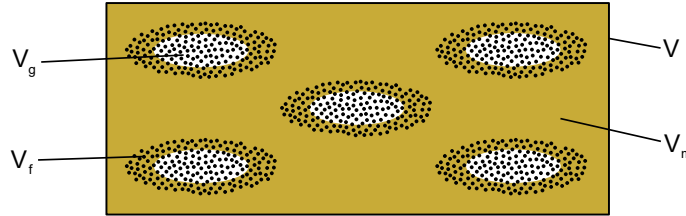


Figure 7.4: Schematical representation of the volume occupied by the different phases during consolidation: the volume occupied by the fibres  $V_f$ , the volume occupied by the air  $V_g$ , the volume occupied by the matrix  $V_m$  and the total volume  $V$ .

The volume occupied by the fibres in a tow can be determined on the basis of their weight  $M_f$  and their density through Equation B.2, similar considerations apply to the matrix and Equation B.3 relates the matrix volume to its mass  $M_m$  and density.

$$V_f = \frac{M_f}{\rho_f} \quad (\text{B.2})$$

$$V_m = \frac{M_m}{\rho_m} \quad (\text{B.3})$$

The volume occupied by the tows  $V_{tow}$  consists of the volume occupied by the fibres in the main tows  $V_{f,tow}$  and the space between the fibres. The gas volume  $V_g$  is equal to the space between the fibres in the volume of the unimpregnated region of the tow, which is directly related

to the impregnation degree. Hence, the volume occupied by the gas can be described with Equation B.4 assuming that the impregnation degree is homogeneous in the composite. Putting Equations B.2, B.3, B.4 and A.2 into Equation B.1 yields Equation B.5:

$$V_g = V_{tow} \cdot (1 - \nu_{f,tow}) \cdot (1 - \xi) \quad (\text{B.4})$$

$$\nu_f = \frac{\frac{M_f}{\rho_f}}{\frac{M_f}{\rho_f} + \frac{M_m}{\rho_m} + \frac{M_f}{\rho_f} \cdot \frac{(1 - \nu_{f,tow})}{\nu_{f,tow}} \cdot (1 - \xi)} \quad (\text{B.5})$$

For  $N$  layers and a cavity area  $A_c$  the total fibre mass  $M_f$  is found with Equation B.6 :

$$M_f = N \cdot A_c \cdot M_f^A \quad (\text{B.6})$$

Inserting this Equation back into Equation B.5 finally yields:

$$\nu_f = \frac{M_f^A}{M_f^A + \frac{M_m \rho_f}{\rho_m N A_c} + M_f^A \frac{(1 - \nu_{f,tow})}{\nu_{f,tow}} (1 - \xi)} \quad (\text{B.7})$$

## C Derivation of fibre volume fractions

The fibre and gas volume fraction temporal change reads, based on equation 6.2.1 and 6.2.6:

$$\begin{aligned} \frac{\partial \nu_f}{\partial t} &= \frac{\partial V_f}{\partial t} \frac{1}{V} \\ &= -V_f \frac{1}{V^2} \frac{\partial V}{\partial t} \end{aligned} \quad (\text{C.1})$$

$$\begin{aligned} \frac{\partial \nu_g}{\partial t} &= \frac{\partial V_g}{\partial t} \frac{1}{V} \\ &= \frac{1}{V} \frac{\partial V_g}{\partial t} - V_g \frac{1}{V^2} \frac{\partial V}{\partial t} \end{aligned} \quad (\text{C.2})$$

The temporal volume change reads, using equation 6.2.3 and 6.2.6:

$$\frac{\partial V}{\partial t} = \frac{\partial V_f}{\partial t} + \frac{\partial V_m}{\partial t} + \frac{\partial V_g}{\partial t} = \frac{\partial V_m}{\partial t} + \frac{\partial V_g}{\partial t} \quad (\text{C.3})$$

The variation of the gas volume over time can be described on the basis of Equation 6.2.5 by inserting Equation 6.2.1, 6.2.4 and 6.2.6, and neglecting changes in tow fibre volume fraction

$\nu_{f,tow}$  since the tow is assumed incompressible:

$$\begin{aligned}
 \frac{\partial V_g}{\partial t} &= \frac{\partial}{\partial t} (V_{tow} - V_{tow,impr.}) (1 - \nu_{f,tow}) \\
 &= \frac{\partial}{\partial t} (V_{tow} - \xi V_{tow}) (1 - \nu_{f,tow}) \\
 &= \frac{\partial}{\partial t} \left( (1 - \xi) \frac{V_f}{\nu_{f,tow}} \right) (1 - \nu_{f,tow}) \\
 &= V_f \frac{1 - \nu_{f,tow}}{\nu_{f,tow}} \frac{\partial}{\partial t} (1 - \xi) \\
 &= -V_f \frac{1 - \nu_{f,tow}}{\nu_{f,tow}} \frac{\partial \xi}{\partial t}
 \end{aligned} \tag{C.4}$$

Inserting this result into the previous equation yields:

$$\frac{\partial V}{\partial t} = \frac{\partial V_m}{\partial t} - V_f \frac{1 - \nu_{f,tow}}{\nu_{f,tow}} \frac{\partial \xi}{\partial t} \tag{C.5}$$

Inserting it back into Equation C.1 together with equation 6.2.1 yields:

$$\begin{aligned}
 \frac{\partial \nu_f}{\partial t} &= -V_f \frac{1}{V^2} \frac{\partial V}{\partial t} \\
 &= -\frac{\nu_f}{V} \frac{\partial V_m}{\partial t} + \nu_f^2 \frac{1 - \nu_{f,tow}}{\nu_{f,tow}} \frac{\partial \xi}{\partial t}
 \end{aligned} \tag{C.6}$$

For the gas volume fraction inserting Equations C.5, C.4 and 6.2.1 into Equation C.2 yields:

$$\begin{aligned}
 \frac{\partial \nu_g}{\partial t} &= \frac{1}{V} \frac{\partial V_g}{\partial t} - \frac{\nu_g}{V} \left[ \frac{\partial V_m}{\partial t} + \frac{\partial V_g}{\partial t} \right] \\
 &= (\nu_g - 1) \left( \nu_f \frac{1 - \nu_{f,tow}}{\nu_{f,tow}} \frac{\partial \xi}{\partial t} \right) - \frac{\nu_g}{V} \frac{\partial V_m}{\partial t}
 \end{aligned} \tag{C.7}$$

## D Matrix volume change

We consider the infinitesimal trapezoid as shown in Figure 7.5 with dimensions  $\Delta x$ ,  $\Delta y$  in the x and y direction, height  $h(x, y)$  linearly depending on x and y in the z direction and volume  $V$ . In the following, the height of the corners are referred to as  $h_1$ ,  $h_2$ ,  $h_3$  and  $h_4$ , the mid side heights in function of either x or y as  $h_{12}(x)$ ,  $h_{13}(y)$ ,  $h_{34}(x)$  and  $h_{24}(y)$ , their average value  $\bar{h}_{ij}$  and the average height of the trapezoid  $\bar{h}$ .

To resolve the temporal change of matrix volume Darcy's law [19] is applied to the four sides of the trapezoid, no matrix flowing through either the top or bottom surface since the through-

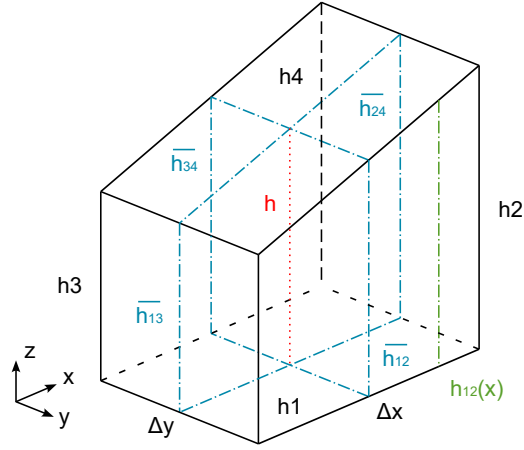


Figure 7.5: Representation of the trapezoid unit cell.

thickness parameters, including matrix pressure, are assumed constant:

$$\begin{aligned}
 \frac{1}{V} \frac{\partial V_m}{\partial t} = \frac{1}{V} & \left[ \int_y^{y+\Delta y} \int_z^{z+h_{13}(y)} -\frac{K_x}{\eta} \frac{\partial P_m}{\partial x} dz dy \right. \\
 & - \int_y^{y+\Delta y} \int_z^{z+h_{24}(y)} -\frac{K_x}{\eta} \frac{\partial P_m}{\partial x} dz dy \\
 & + \int_x^{x+\Delta x} \int_z^{z+h_{34}(x)} -\frac{K_y}{\eta} \frac{\partial P_m}{\partial y} dz dx \\
 & \left. - \int_x^{x+\Delta x} \int_z^{z+h_{12}(x)} -\frac{K_y}{\eta} \frac{\partial P_m}{\partial y} dz dx \right] \quad (D.1)
 \end{aligned}$$

For the continuum formulation we let  $\Delta x$  and  $\Delta y$  tend to zero, which implies that  $K_x$ ,  $K_y$ ,  $\eta$ ,  $\frac{\partial P}{\partial x}$  and  $\frac{\partial P}{\partial y}$  can be considered constant in the volume and taken out of the integral. This leaves only a surface integral which is straightforward to solve, therefore the previous equation becomes:

$$\begin{aligned}
 \frac{1}{V} \frac{\partial V_m}{\partial t} = \frac{1}{V} & \left[ \frac{K_x \Delta \bar{h}_{24} \Delta y}{\eta} \frac{\partial P_m(x + \Delta x)}{\partial x} \right. \\
 & - \frac{K_x \bar{h}_{13} \Delta y}{\eta} \frac{\partial P_m(x)}{\partial x} \\
 & + \frac{K_y \bar{h}_{12} \Delta y}{\eta} \frac{\partial P_m(y + \Delta y)}{\partial y} \\
 & \left. - \frac{K_y \bar{h}_{34} \Delta y}{\eta} \frac{\partial P_m(y)}{\partial y} \right] \quad (D.2)
 \end{aligned}$$

Simple geometry considerations allows to write  $V$  as:

$$V = \Delta x \cdot \Delta y \cdot h \quad (D.3)$$

In addition, the change of average height in x and y direction  $\Delta \bar{h}_x$  and  $\Delta \bar{h}_y$  are expressed through Equation D.4 and inserting it back yields Equation D.5:

$$\bar{h}_{24} = \bar{h}_{13} + \Delta \bar{h}_x \quad \bar{h}_{12} = \bar{h}_{34} + \Delta \bar{h}_y \quad (D.4)$$

$$\begin{aligned}
 \frac{1}{V} \frac{\partial V_m}{\partial t} &= \left[ \frac{K_x h_{13}^-}{\eta \Delta x h} \left( \frac{\partial P_m(x + \Delta x)}{\partial x} - \frac{\partial P_m(x)}{\partial x} \right) \right. \\
 &+ \frac{K_x \Delta \bar{h}_x}{\eta \Delta x h} \frac{\partial P_m(x + \Delta x)}{\partial x} \\
 &+ \frac{K_y h_{34}^-}{\eta \Delta y h} \left( \frac{\partial P_m(y + \Delta y)}{\partial y} - \frac{\partial P_m(y)}{\partial y} \right) \\
 &\left. + \frac{K_y \Delta \bar{h}_y}{\eta \Delta y \cdot h} \frac{\partial P_m(y + \Delta y)}{\partial y} \right]
 \end{aligned} \tag{D.5}$$

As  $\Delta x$  and  $\Delta y$  tend to zero  $h_{13}^-$  and  $h_{34}^-$  tend towards  $h$  and we can express the equations, based on the definition of a derivative, as:

$$\begin{aligned}
 \frac{1}{V} \frac{\partial V_m}{\partial t} &= \left[ \frac{K_x}{\eta} \frac{\partial^2 P_m}{\partial x^2} + \frac{K_x}{\eta \bar{h}} \frac{\partial h}{\partial x} \frac{\partial P_m}{\partial x} \right. \\
 &+ \left. \frac{K_y}{\eta} \frac{\partial^2 P_m}{\partial y^2} + \frac{K_y}{\eta \bar{h}} \frac{\partial h}{\partial y} \frac{\partial P_m}{\partial y} \right] \\
 &= \frac{\vec{\nabla} K \vec{\nabla} P_m}{\eta} + \frac{\vec{\nabla} h^T K \vec{\nabla} P_m}{h \eta}
 \end{aligned} \tag{D.6}$$

## E Derivative of impregnation degree

In Equation E.1, the derivative of  $\xi$  is expressed by inserting Equation 6.2.13 and developing the expression considering that  $R_{eq}$  is constant. Then, Equation 6.2.14 is inserted to replace the term  $r \frac{\partial r}{\partial t}$  and finally  $\frac{r}{R_{eq}}$  is expressed in terms of impregnation degree using Equation 6.2.13.

$$\begin{aligned}
 \frac{\partial \xi}{\partial t} &= \frac{\partial}{\partial t} \frac{R_{eq}^2 - r^2}{R_{eq}^2} \\
 &= \frac{-2}{R_{eq}^2} r \frac{\partial r}{\partial t} \\
 &= \frac{-2}{R_{eq}^2} \frac{K_\mu (P_m + P_c - P_g)}{\eta (1 - \nu_{f,tow})} \frac{1}{\ln \left( \frac{r}{R_{eq}} \right)} \\
 &= \frac{-2 K_\mu (P_m + P_c - P_g)}{R_{eq}^2 \eta (1 - \nu_{f,tow}) \ln(\sqrt{\xi - 1})}
 \end{aligned} \tag{E.1}$$

## F Derivative of thickness

The temporal change of height reads, combining Equation 6.2.22, C.5 and based on the volume definition of the trapezoidal unit cell, as:

$$\begin{aligned}
 \frac{\partial h}{\partial t} &= \frac{1}{\Delta x \cdot \Delta y} \frac{\partial V}{\partial t} = \frac{h}{V} \frac{\partial V}{\partial t} \\
 &= \frac{h}{V} \left[ \frac{\partial V_m}{\partial t} - V_f \frac{1 - \nu_{f,tow}}{\nu_{f,tow}} \frac{\partial \xi}{\partial t} \right]
 \end{aligned} \tag{F.1}$$

inserting equations 6.2.21, 6.2.1 and D.6 yields:

$$\begin{aligned} \frac{v}{h} &= \frac{1}{V} \left[ \frac{\partial V_m}{\partial t} - V_f \frac{1 - \nu_{f,tow}}{\nu_{f,tow}} \frac{\partial \xi}{\partial t} \right] \\ &= \frac{\vec{\nabla} K \vec{\nabla} P_m}{\eta} + \frac{(\vec{\nabla} h)^T K \vec{\nabla} P_m}{h \cdot \eta} - \nu_f \frac{1 - \nu_{f,tow}}{\nu_{f,tow}} \frac{\partial \xi}{\partial t} \end{aligned} \quad (\text{F.2})$$

## G Initial conditions

To describe the height of the composite, Equation 6.2.22 is first combined with Equation 6.2.3, then Equation 6.2.2 and 6.2.5 are inserted. The final equation is obtained by inserting the areal weight  $M_m^A$  and  $M_f^A$  of the fibres and matrix in a ply and the local number of plies  $N$ :

$$\begin{aligned} h &= \frac{V}{\Delta x \cdot \Delta y} = \frac{V_m}{\Delta x \cdot \Delta y} + \frac{V_f}{\Delta x \cdot \Delta y} + \frac{V_g}{\Delta x \cdot \Delta y} \\ &= \frac{M_m}{\Delta x \cdot \Delta y \cdot \rho_m} + \frac{M_f}{\Delta x \cdot \Delta y \cdot \rho_f} \\ &\quad + \frac{M_f}{\Delta x \cdot \Delta y \cdot \rho_f} (1 - \xi) \frac{1 - \nu_{f,tow}}{\nu_{f,tow}} \\ &= \frac{N \cdot M_m^A}{\rho_m} + \frac{N \cdot M_f^A}{\rho_f} \left( 1 + (1 - \xi) \cdot \frac{1 - \nu_{f,tow}}{\nu_{f,tow}} \right) \end{aligned} \quad (\text{G.1})$$

The volume fractions of the matrix, fibre and gas are obtained on the basis of Equation 6.2.1, the phase volumes are then expressed in function of areal weight in a similar fashion to Equation G.1:

$$\begin{aligned} \nu_f &= \frac{V_f}{V} = \frac{M_f}{\rho_f \cdot h \cdot \Delta x \cdot \Delta y} = \frac{N \cdot M_f^A}{\rho_f \cdot h} \\ \nu_m &= \frac{V_m}{V} = \frac{M_m}{\rho_m \cdot h \cdot \Delta x \cdot \Delta y} = \frac{N \cdot M_m^A}{\rho_m \cdot h} \\ \nu_g &= \frac{V_g}{V} = \frac{N \cdot M_f^A}{\rho_f \cdot h} \cdot (1 - \xi) \cdot \frac{1 - \nu_{f,tow}}{\nu_{f,tow}} \end{aligned} \quad (\text{G.2})$$

## H Additional Pictures

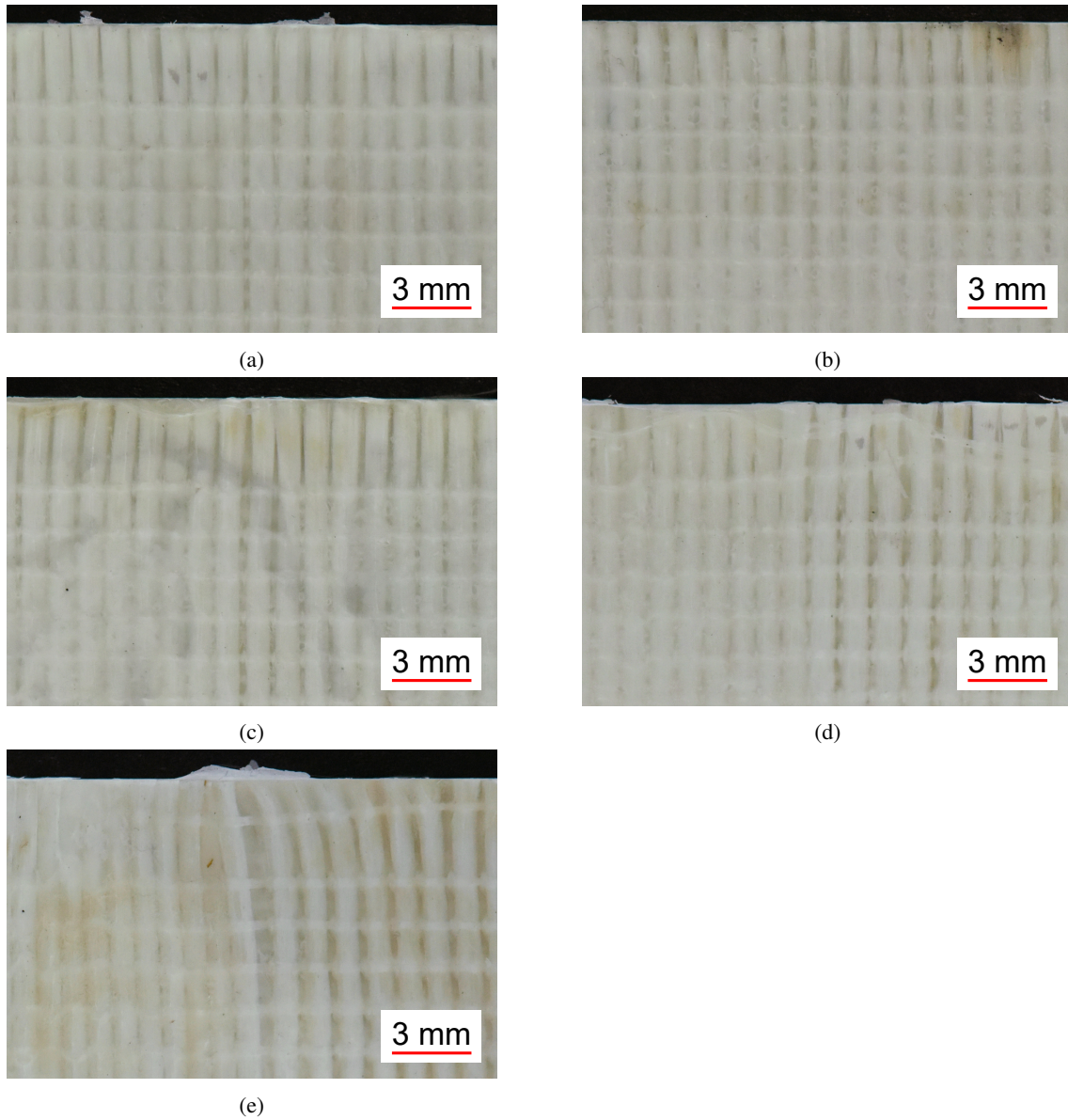


Figure 7.6: Close up pictures of the backside, in the region of the thickness change, of the plates pressed at 0.07, 0.14, 0.5, 1 and 3.5 MPa in Figures 7.6a to 7.6e.



# Bibliography

- [1] M. P. Bendsoe and O. Sigmund, *Structural Optimization: Theory, Methods and Applications*. Springer, 2004.
- [2] <https://engineeringproductdesign.com>. Date of access: 26.08.2022.
- [3] D. Gay, S. V. Hoa, and S. W. Tsai, *Composite Materials: Design and Applications*, 2nd ed. CRC Press, 2002.
- [4] A. E. Albanesi, I. Peralta, F. Bre, B. A. Storti, and V. D. Fachinotti, “An optimization method based on the evolutionary and topology approaches to reduce the mass of composite wind turbine blades,” *Structural and Multidisciplinary Optimization*, vol. 62, no. 2, pp. 619–643, 2020.
- [5] J.-P. Pascault, H. Sauterau, J. Verdu, and R. J. Williams, *Thermosetting polymers*. Taylor and Francis, 2002.
- [6] M. Biron, *Thermoplastics and Thermoplastic Composites*, 2nd ed. William Andrew, 2013.
- [7] R. Bernatas, S. Dagneou, A. Despax-Ferrerres, and A. Barasinski, “Recycling of fiber reinforced composites with a focus on thermoplastic composites,” *Cleaner Engineering and Technology*, vol. 5, p. 100 272, 2021.
- [8] CompositesWorld, *Clean sky 2 thermoplastic composite demonstrator advances toward full assembly*. [www.compositesworld.com](http://www.compositesworld.com). Date of access: 22.04 .2022.
- [9] CompositesWorld, *Zebra project launched to develop first 100% recyclable wind turbine blades*, [www.compositesworld.com](http://www.compositesworld.com). Date of access: 22.04 .2022.
- [10] N. Reynolds, S. Awang-Ngah, G. Williams, and D. J. Hughes, “Direct Processing of Structural Thermoplastic Composites Using Rapid Isothermal Stamp Forming,” *Applied Composite Materials*, vol. 27, no. 1-2, pp. 107–115, 2020, ISSN: 15734897.
- [11] M. Wysocki, R. Larsson, and S. Toll, “Hydrostatic consolidation of commingled fibre composites,” *Composites Science and Technology*, vol. 65, no. 10, pp. 1507–1519, 2005, ISSN: 02663538.
- [12] M. Wysocki, S. Toll, and R. Larsson, “Press forming of commingled yarn based composites: The preform contribution,” *Composites Science and Technology*, vol. 67, pp. 515–524, 2007, ISSN: 02663538.
- [13] M. Wysocki, R. Larsson, and S. Toll, “Modelling the consolidation of partially impregnated prepregs,” in *ICCM17*, 2009.

- [14] M. S. Rouhi, M. Wysocki, and R. Larsson, "Modeling of coupled dual-scale flow-deformation processes in composites manufacturing," *Composites Part A: Applied Science and Manufacturing*, vol. 46, pp. 108–116, 2013.
- [15] M. S. Rouhi, "Poromechanical Modeling of Composites Manufacturing," Doctoral Thesis, Chalmers University of Technology, 2015.
- [16] M. S. Rouhi, M. Wysocki, and R. Larsson, "Simulation of 3D Rtm Process Using Solid Shell Element," in *14th International Conference on Flow Processes in Composite Materials*, Sweden, 2018.
- [17] V. Werlen, C. Rytka, and V. Michaud, "A numerical approach to characterize the viscoelastic behaviour of fibre beds and to evaluate the influence of strain deviations on viscoelastic parameter extraction," *Composites Part A: Applied Science and Manufacturing*, vol. 143, no. October 2020, p. 106 315, 2021, ISSN: 1359835X.
- [18] V. Werlen, R. Vocke, C. Brauner, C. Dransfeld, V. Michaud, and C. Rytka, "A model for the consolidation of hybrid textiles considering air entrapment, dissolution and diffusion," *Composites Part A: Applied Science and Manufacturing*, vol. 166, no. December 2022, p. 107 413, 2023, ISSN: 1359835X.
- [19] H. Darcy, *Les fontaines publiques de la ville de Dijon*. Paris: Dalmont, 1856.
- [20] L. A. Richards, "Capillary conduction of liquids through porous mediums," *Physics*, vol. 1, no. 5, pp. 318–333, 1931.
- [21] M. A. Celia and E. T. Bouloutas, "A General Mass-Conservative Numerical Solution for the Unsaturated Flow Equation," *Water Resources Research*, vol. 26, no. 1, 1990.
- [22] M. T. van Genuchten, "Closed-Form Equation for Predicting the Hydraulic Conductivity of Unsaturated Soils.," *Soil Science Society of America Journal*, vol. 44, no. 5, pp. 892–898, 1980.
- [23] F. Klunker, "Aspekte zur Modellierung und Simulation des Vacuum Assisted Resin Infusion," Dissertation, Technischen Universität Clausthal, 2008, p. 224.
- [24] S. T. Jespersen, M. D. Wakeman, V. Michaud, D. Cramer, and J.-A. E. Manson, "Film stacking impregnation model for a novel net shape thermoplastic composite preforming process," *Composites Science and Technology*, vol. 68, pp. 1822–1830, 2008.
- [25] J. Studer, C. Dransfeld, J. C. Cano, *et al.*, "Effect of fabric architecture, compaction and permeability on through thickness thermoplastic melt impregnation," *Composites Part A: Applied Science and Manufacturing*, vol. 122, 2019.
- [26] V. Michaud, "A Review of Non-saturated Resin Flow in Liquid Composite Moulding processes," *Transport in Porous Media*, vol. 115, no. 3, pp. 581–601, 2016.
- [27] J. Wolfrath, V. Michaud, A. Modaressi, and J.-A. E. Manson, "Unsaturated flow in compressible fibre preforms," *Composites Part A: Applied Science and Manufacturing*, vol. 37, pp. 881–889, 2006.
- [28] T. Osswald and N. Rudolph, *Polymer Rheology*. 2013.

- [29] T. G. Mezger, *The Rheology Handbook: For users of rotational and oscillatory rheometers*, 2nd ed. Vincentz Network, 2006.
- [30] M. M. Cross, "Rheology of non-Newtonian fluids: A new flow equation for pseudoplastic systems," *Journal of Colloid Science*, vol. 20, no. 5, pp. 417–437, 1965.
- [31] P. J. Carreau, "Rheological Equations From Molecular Network Theories.," *Trans Soc Rheol*, vol. 16, no. 1, pp. 99–127, 1972.
- [32] S. Arrhenius, "Über die Reaktionsgeschwindigkeit bei der Inversion von Rohrzucker durch Säuren," *Zeitschrift für Physikalische Chemie*, vol. 4U, no. 1, pp. 226–248, 1889.
- [33] S. R. Logan, "The origin and status of the Arrhenius Equation," *Journal of Chemical Education*, vol. 59, no. 4, 1982.
- [34] N. Bernet, V. Michaud, P. E. Bourban, and J.-A. E. Manson, "An Impregnation model for the consolidation of Thermoplastic composites Made from Commingled Yarns," *Journal of Composite Materials*, vol. 33, no. 8, pp. 751–772, 1999.
- [35] J. W. Seo and W. il Lee, "A Model of the Resin Impregnation in Thermoplastic Composites," *Journal of Composite Materials*, vol. 25, no. 9, pp. 1127–1142, 1991, ISSN: 1530793X.
- [36] P. C. Carman, "Fluid flow through granular beds," *Process Safety and Environmental Protection: Transactions of the Institution of Chemical Engineers, Part B*, vol. 75, pp. 32–48, 1997.
- [37] T. G. Gutowski, Z. Cai, S. Bauer, D. Boucher, J. Kingery, and S. Wineman, "Consolidation Experiments for Laminate Composites," *Journal of Composite Materials*, vol. 21, pp. 650–669, 1987.
- [38] J. Happel, "Viscous flow relative to arrays of cylinders," *AIChE Journal*, vol. 5, no. 2, pp. 174–177, 1959, ISSN: 15475905.
- [39] J. E. Drummond and M. I. Tahir, "Laminar viscous flow through regular arrays of parallel solid cylinders," *International Journal of Multiphase Flow*, pp. 515–540, 1984.
- [40] E. M. Sparrow and A. L. Loeffler, "Longitudinal laminar flow between cylinders arranged in regular array," *AIChE Journal*, vol. 5, no. 3, pp. 325–330, 1959, ISSN: 15475905.
- [41] S. Kuwabara, "The forces experienced by randomly distributed parallel circular cylinders," *Journal of the physical society of Japan*, vol. 14, no. 4, p. 1959, 1959.
- [42] A. S. Sangani and A. Acrivos, "Slow flow past periodic arrays of cylinders with application to heat transfer," *International Journal of Multiphase Flow*, vol. 8, no. 3, pp. 193–206, 1982.
- [43] B. Gebart, "Permeability of Unidirectional Reinforcements for RTM," *Journal of Composite Materials*, vol. 26, no. 8, pp. 1100–1133, 1992.
- [44] H. Hasimoto, "On the periodic fundamental solutions of the Stokes equations and their application to viscous flow past a cubic array of spheres," *Journal of Fluid Mechanics*, vol. 5, no. 2, pp. 317–328, 1959, ISSN: 14697645.

- [45] C. P. Yu and T. T. Soong, "Random Cell Model for Pressure Drop Prediction in Fibrous Filters.," *American Society of Mechanical Engineers (Paper)*, no. 75 -APM-G, pp. 301–304, 1975, ISSN: 04021215.
- [46] L. Spielman and S. L. Goren, "Model for Predicting Pressure Drop and Filtration Efficiency in Fibrous Media," *Environmental Science and Technology*, vol. 2, no. 4, pp. 279–287, 1968, ISSN: 15205851.
- [47] M. V. Brusckhe and S. G. Advani, "Flow of generalized Newtonian fluids across a periodic array of cylinders," *Journal of Rheology*, vol. 37, no. 3, pp. 479–498, 1993.
- [48] N. Epstein and J. H. Masliyah, "Creeping flow through clusters of spheroids and elliptical cylinders," *The Chemical Engineering Journal*, vol. 3, no. C, pp. 169–175, 1972, ISSN: 03009467.
- [49] D. Merhi, V. Michaud, L. Kämpfer, P. Vuilliomenet, and J. A. Manson, "Transverse permeability of chopped fibre bundle beds," *Composites Part A: Applied Science and Manufacturing*, vol. 38, no. 3, pp. 739–746, 2007.
- [50] G. W. Jackson and D. F. James, "The permeability of fibrous porous media," *The Canadian Journal of Chemical Engineering*, vol. 64, no. 3, pp. 364–374, 1986, ISSN: 1939019X.
- [51] M. A. Ali, R. Umer, K. A. Khan, S. Bickerton, and W. J. Cantwell, "Non-destructive evaluation of through-thickness permeability in 3D woven fabrics for composite fan blade applications," *Aerospace Science and Technology*, vol. 82-83, pp. 520–533, 2018.
- [52] A. Endruweit, F. Gommer, and A. C. Long, "Stochastic analysis of fibre volume fraction and permeability in fibre bundles with random filament arrangement," *Composites Part A: Applied Science and Manufacturing*, vol. 49, pp. 109–118, 2013.
- [53] R. Gennaro, M. Christmann, A. Greco, G. Rieber, P. Mitschang, and A. Maffezzoli, "Experimental Measurement of Transversal Micro- and Macro Permeability During Compression Molding of PP/Glass Composites," *Polymer Composites*, vol. 35, no. 1, 2013.
- [54] M. G. Godbole, R. Purandare, R. Harshe, *et al.*, "Influence of filament distribution on transverse tow permeability: Model predictions and experimental validation," *Composites Part A: Applied Science and Manufacturing*, vol. 118, no. June 2018, pp. 150–161, 2019.
- [55] R. Phillips, D. A. Akyüz, and J.-A. E. Manson, "Prediction of the consolidation of woven fibre-reinforced thermoplastic composites. Part I. Isothermal case," *Composites - Part A: Applied Science and Manufacturing*, pp. 395–402, 1998.
- [56] M. Bodaghi, A. Vanaerschot, S. V. Lomov, and N. C. Correia, "Composites : Part A On the stochastic variations of intra-tow permeability induced by internal geometry variability in a 2 / 2 twill carbon fabric," *Composites Part A*, vol. 101, pp. 444–458, 2017.
- [57] F. Gommer, A. Endruweit, and A. C. Long, "Quantification of micro-scale variability in fibre bundles," *Composites Part A: Applied Science and Manufacturing*, vol. 87, pp. 131–137, 2016.
- [58] F. Gommer, A. Endruweit, and A. C. Long, "Analysis of filament arrangements and generation of statistically equivalent composite micro-structures," *Composites Science and Technology*, vol. 99, pp. 45–51, 2014.

- [59] G. Bechtold and L. Ye, "Influence of fibre distribution on the transverse flow permeability in fibre bundles," *Composites Science and Technology*, vol. 63, pp. 2069–2079, 2003.
- [60] S. Gomasasca, D. M. J. Peeters, B. Atli-veltin, and C. Dransfeld, "Characterising microstructural organisation in unidirectional composites," *Composites Science and Technology*, vol. 215, no. September, 2021.
- [61] Z. Cai and A. L. Berdichevsky, "Numerical simulation on the permeability variations of a fiber assembly," *Polymer Composites*, vol. 14, no. 6, pp. 529–539, 1993.
- [62] T. S. Lundström and B. R. Gebart, "Effect of Perturbation of Fibre Architecture on Permeability Inside Fibre Tows," *Journal of Composite Materials*, vol. 29, no. 4, pp. 424–443, 1995, ISSN: 1530793X.
- [63] X. Chen and T. D. Papathanasiou, "The transverse permeability of disordered fiber arrays: A statistical correlation in terms of the mean nearest interfiber spacing," *Transport in Porous Media*, vol. 71, no. 2, pp. 233–251, 2008.
- [64] A. S. Sangani and C. Yao, "Transport processes in random arrays of cylinders. II. Viscous flow," *Physics of Fluids*, vol. 31, no. 9, pp. 2435–2444, 1988, ISSN: 0031-9171.
- [65] X. Chen and T. D. Papathanasiou, "Micro-scale modeling of axial flow through unidirectional disordered fiber arrays," *Composites Science and Technology*, vol. 67, no. 7-8, pp. 1286–1293, 2007.
- [66] T. J. Vaughan and C. T. McCarthy, "A combined experimental-numerical approach for generating statistically equivalent fibre distributions for high strength laminated composite materials," *Composites Science and Technology*, vol. 70, no. 2, pp. 291–297, 2010.
- [67] F. Gommer, K. C. Wedgwood, and L. P. Brown, "Stochastic reconstruction of filament paths in fibre bundles based on two-dimensional input data," *Composites Part A: Applied Science and Manufacturing*, vol. 76, pp. 262–271, 2015.
- [68] M. W. Czabaj, M. L. Riccio, and W. W. Whitacre, "Numerical reconstruction of graphite/epoxy composite microstructure based on sub-micron resolution X-ray computed tomography," *Composites Science and Technology*, vol. 105, pp. 174–182, 2014.
- [69] R. Arbter, J. M. Beraud, C. Binetruy, *et al.*, "Experimental determination of the permeability of textiles: A benchmark exercise," *Composites Part A: Applied Science and Manufacturing*, vol. 42, pp. 1157–1168, 2011.
- [70] D. May, A. Aktas, and A. Yong, "International Benchmark Exercises on Textile Permeability and Compressibility Characterization," in *ECCM18*, Athens, Greece, 2018, pp. 24–28.
- [71] M. A. Kabachi, M. Danzi, S. Arreguin, and P. Ermanni, "Experimental study on the influence of cyclic compaction on the fiber-bed permeability, quasi-static and dynamic compaction responses," *Composites Part A: Applied Science and Manufacturing*, vol. 125, no. April, 2019.
- [72] M. Yun, H. Sas, P. Simacek, and S. G. Advani, "Characterization of 3D fabric permeability with skew terms," *Composites Part A: Applied Science and Manufacturing*, vol. 97, pp. 51–59, 2017.

- [73] M. Nordlund, T. Lundstöm, V. Frishfelds, and A. Jakovics, “Permeability network model for non-crimp fabrics,” *Composites - Part A: Applied Science and Manufacturing*, vol. 37, no. 6, pp. 826–835, 2006.
- [74] Z. R. Chen, L. Ye, and M. Lu, “Permeability predictions for woven fabric preforms,” *Journal of Composite Materials*, vol. 44, no. 13, pp. 1569–1586, 2010.
- [75] E. B. Belov, S. V. Lomov, I. Verpoest, *et al.*, “Modelling of permeability of textile reinforcements: Lattice Boltzmann method,” *Composites Science and Technology*, vol. 64, no. 7-8, pp. 1069–1080, 2004.
- [76] S. V. Lomov, I. Verpoest, B. Verleye, B. Laine, and F. Boust, “WiseTex-based models of permeability of textiles,” in *The 8th International Conference on Flow Processes in Composite Materials, FPCM-8*, Douai, 2006.
- [77] C. C. Wong and A. C. Long, “Modelling variation of textile fabric permeability at mesoscopic scale,” *Plastics, Rubber and Composites*, vol. 35, no. 3, pp. 101–111, 2006, ISSN: 14658011.
- [78] B. Verleye, R. Croce, M. Griebel, *et al.*, “Permeability of textile reinforcements: Simulation, influence of shear and validation,” *Composites Science and Technology*, vol. 68, no. 13, pp. 2804–2810, 2008, ISSN: 02663538.
- [79] L. He, S. Yan, Y. Li, P. Wen, X. Xie, and W. Liu, “Simulation of stochastic flow considering mesoscale permeability variability during the resin transfer molding process,” *Polymer Composites*, vol. 41, no. 5, pp. 1701–1710, 2020, ISSN: 15480569.
- [80] I. Verpoest and S. V. Lomov, “Virtual textile composites software WiseTex: Integration with micro-mechanical, permeability and structural analysis,” *Composites Science and Technology*, vol. 65, pp. 2563–2574, 2005.
- [81] E. E. Swery, R. Meier, S. V. Lomov, K. Drechsler, and P. Kelly, “Predicting permeability based on flow simulations and textile modelling techniques: Comparison with experimental values and verification of FlowTex solver using Ansys CFX,” *Journal of Composite Materials*, vol. 50, no. 5, pp. 601–615, 2016.
- [82] I. Straumit, C. Hahn, E. Winterstein, B. Plank, S. V. Lomov, and M. Wevers, “Computation of permeability of a non-crimp carbon textile reinforcement based on X-ray computed tomography images,” *Composites Part A: Applied Science and Manufacturing*, vol. 81, pp. 289–295, 2016.
- [83] M. Karaki, R. Younes, F. Trochu, and P. Lafon, “Progress in experimental and theoretical evaluation methods for textile permeability,” *Journal of Composites Science*, vol. 3, no. 3, 2019, ISSN: 2504477X.
- [84] C. Dong, “Effects of Process-Induced Voids on the Properties of Fibre Reinforced Composites,” *Journal of Materials Science and Technology*, vol. 32, no. 7, 2016.
- [85] J. R. Wood and M. G. Bader, “Void control for polymer-matrix composites (1): Theoretical and experimental methods for determining the growth and collapse of gas bubbles,” *Composites Manufacturing*, vol. 5, no. 3, pp. 139–147, 1994.

- [86] S. G. Advani and K. T. Hsiao, *Manufacturing techniques for polymer matrix composites (PMCs)*. Woodhead Publishing, 2012.
- [87] A. Arafath, G. Fernlund, and A. Poursartip, “Gas transport in prepregs: model and permeability experiments,” in *ICCM17*, 2009.
- [88] D. Zhang, “Void Consolidation of Thermoplastic Composites via Non-Autoclave Processing,” Dissertation, University of Delaware, 2017.
- [89] C. Schneeberger, N. Aegerter, and P. Ermanni, “An impregnation-free value chain for large thermoplastic matrix composites,” in *SAMPE Europe Conference*, Baden, Switzerland, 2021.
- [90] W. Henry, “Experiments on the quantity of gases absorbed by water, at different temperatures, and under different pressures,” *Phil. Trans. R. Soc.*, vol. 93, 1803.
- [91] A. Fick, “Ueber Diffusion,” *annalen der physik*, vol. 170, no. 1, 1855.
- [92] P. S. Epstein and M. S. Plesset, “On the stability of gas bubbles in liquid-gas solutions,” *The Journal of Chemical Physics*, vol. 18, no. 11, pp. 1505–1509, 1950, ISSN: 00219606.
- [93] J. C. Jaeger and H. S. Carslaw, “Heat Flow in the Region bounded Internally by a Circular Cylinder,” *Proceedings of the Royal Society of Edinburgh*, 1942.
- [94] W. R. Phillips and P. J. Mahon, “On approximations to a class of Jaeger integrals,” *Proceedings of the Royal Society A: Mathematical, Physical and Engineering Sciences*, vol. 467, no. 2136, pp. 3570–3589, 2011, ISSN: 14712946.
- [95] J. Crank, *The Mathematics of Diffusion*, 2nd ed. Oxford: Clarendon Press, 1975, vol. 79.
- [96] J. S. Leclerc and E. Ruiz, “Porosity reduction using optimized flow velocity in Resin Transfer Molding,” *Composites Part A*, vol. 39, no. 12, pp. 1859–1868, 2008, ISSN: 1359-835X.
- [97] T. S. Lundström, “Measurement of void collapse during resin transfer moulding,” *Composites Part A: Applied Science and Manufacturing*, vol. 28, no. 3, pp. 201–214, 1997, ISSN: 1359835X.
- [98] Y. Leterrier and C. G’Sell, “Formation and elimination of voids during the processing of thermoplastic of matrix composites,” *Polymer Composites*, vol. 15, no. 2, pp. 101–105, 1994, ISSN: 15480569.
- [99] D. Zhang, D. Heider, and J. W. Gillespie, “Void reduction of high-performance thermoplastic composites via oven vacuum bag processing,” *Journal of Composite Materials*, vol. 51, no. 30, pp. 4219–4230, 2017, ISSN: 1530793X.
- [100] O. Rozant, V. Michaud, P. E. Bourban, and J.-A. E. Manson, “A Model for the Consolidation of Warp-Knitted Reinforced Laminates,” *Polymer Composites*, vol. 22, no. 3, 2001.
- [101] M. R. Piggott, “The effect of fibre waviness on the mechanical properties of unidirectional fibre composites: A review,” *Composites Science and Technology*, vol. 53, no. 2, pp. 201–205, 1995, ISSN: 02663538.

- [102] P. Kulkarni, K. D. Mali, and S. Singh, "An overview of the formation of fibre waviness and its effect on the mechanical performance of fibre reinforced polymer composites," *Composites Part A: Applied Science and Manufacturing*, vol. 137, no. June, p. 106013, 2020, ISSN: 1359835X.
- [103] R. Balasubramanyam, R. S. Jones, and A. B. Wheeler, "Modelling transverse flows of reinforced thermoplastic materials," *Composites*, vol. 20, no. 1, pp. 33–37, 1989.
- [104] F. N. Cogswell, "The experience of thermoplastic structural composites during processing," *Composites Manufacturing*, vol. 2, no. 3-4, pp. 208–216, 1991.
- [105] S. Schuler and S. G. Advani, "Transverse squeeze flow of concentrated aligned fibers in viscous fluids," *Journal of Non-Newtonian Fluid Mechanics*, vol. 65, pp. 47–74, 1996.
- [106] J. P. Belnoue, O. J. Nixon-Pearson, D. S. Ivanov, and S. R. Hallett, "A novel hyper-viscoelastic model for consolidation of toughened prepregs under processing conditions," *Mechanics of Materials*, vol. 97, pp. 118–134, 2016.
- [107] C. Ghnatios, E. Abisset-Chavanne, C. Binetruy, F. Chinesta, and S. G. Advani, "3D modeling of squeeze flow of multiaxial laminates," *Journal of Non-Newtonian Fluid Mechanics*, vol. 234, pp. 188–200, 2016.
- [108] G. Sorba, C. Binetruy, A. Leygue, and S. Comas-Cardona, "Squeeze flow in heterogeneous unidirectional discontinuous viscous prepreg laminates: Experimental measurement and 3D modeling," *Composites Part A: Applied Science and Manufacturing*, vol. 103, pp. 196–207, 2017, ISSN: 1359835X.
- [109] C. Servais, A. Luciani, and J.-A. E. Manson, "Squeeze flow of concentrated long fibre suspensions: experiments and model," *Journal of Non-Newtonian Fluid Mechanics*, vol. 104, pp. 165–184, 2002.
- [110] G. P. Picher-Martel, A. Levy, and P. Hubert, "Compression moulding of Carbon/PEEK Randomly-Oriented Strands composites: A 2D Finite Element model to predict the squeeze flow behaviour," *Composites Part A: Applied Science and Manufacturing*, vol. 81, pp. 69–77, 2016.
- [111] A. Hautefeuille, S. Comas-Cardona, and C. Binetruy, "Mechanical signature and full-field measurement of flow-induced large in-plane deformation of fibrous reinforcements in composite processing," *Composites Part A: Applied Science and Manufacturing*, vol. 118, no. May 2018, pp. 213–222, 2019.
- [112] A. Hautefeuille, S. Comas-Cardona, and C. Binetruy, "Consolidation and compression of deformable impregnated fibrous reinforcements: Experimental study and modeling of flow-induced deformations," *Composites Part A: Applied Science and Manufacturing*, vol. 131, 2020.
- [113] M. Bodaghi, P. Simacek, S. G. Advani, and N. C. Correia, "A model for fibre washout during high injection pressure resin transfer moulding," *Journal of Reinforced Plastics and Composites*, vol. 37, no. 13, pp. 865–876, 2018.



- [114] M. Bodaghi, P. Simacek, N. Correia, and S. G. Advani, "Experimental parametric study of flow-induced fiber washout during high-injection-pressure resin transfer molding," *Polymer Composites*, vol. 41, no. 3, pp. 1053–1065, 2020.
- [115] K. Terzaghi, R. B. Peck, and G. Mesri, *Soil mechanics in engineering practice*. John Wiley & Sons, 1996.
- [116] W. J. Grouve and R. Akkerman, "Consolidation process model for film stacking glass/PPS laminates," *Plastics, Rubber and Composites*, vol. 39, no. 3-5, pp. 208–215, 2010, ISSN: 14658011.
- [117] J. Merotte, P. Simacek, and S. G. Advani, "Resin flow analysis with fiber preform deformation in through thickness direction during Compression Resin Transfer Molding," *Composites Part A: Applied Science and Manufacturing*, vol. 41, pp. 881–887, 2010.
- [118] V. Michaud and J.-A. E. Manson, "Impregnation of compressible fiber mats with a thermoplastic resin. Part I: Theory," *Journal of Composite Materials*, vol. 35, no. 13, 2001.
- [119] V. Michaud, R. Törnqvist, and J.-A. E. Manson, "Impregnation of compressible fiber mats with a thermoplastic resin. Part II: Experiments," *Journal of Composite Materials*, vol. 35, no. 13, 2001.
- [120] J. Park and M. K. Kang, "A numerical simulation of the resin film infusion process," *Composite Structures*, vol. 60, no. 4, pp. 431–437, 2003.
- [121] C. H. Park and A. Saouab, "Analytical modeling of composite molding by resin infusion with flexible tooling: VARI and RFI processes," *Journal of Composite Materials*, vol. 43, no. 18, pp. 1877–1900, 2009, ISSN: 1530793X.
- [122] S. Bickerton, M. J. Buntain, and A. A. Somashekar, "The viscoelastic compression behavior of liquid composite molding preforms," *Composites Part A: Applied Science and Manufacturing*, vol. 34, no. 5, pp. 431–444, 2003.
- [123] C. M. Van Wyk, "Note on the Compressibility of Wool," *Journal of the Textile Institute Transactions*, 1946.
- [124] S. Toll, "Packing Mechanics of Fiber Reinforcements," *Polymer Engineering and Science*, vol. 38, no. 8, pp. 1337–1350, 1998.
- [125] F. Robitaille and R. Gauvin, "Compaction of textile reinforcements for composites manufacturing. I: Review of experimental results," *Polymer Composites*, vol. 19, no. 2, pp. 198–216, 1998.
- [126] Y. R. Kim, S. P. McCarthy, and J. P. Fanucci, "Compressibility and Relaxation of Fiber Reinforcements During Composite Processing," *Polymer Composites*, vol. 12, no. 1, pp. 13–19, 1991.
- [127] L. Vangheluwe and P. Kiekens, "Modelling relaxation behaviour of yarns part I: Extended, nonlinear maxwell model," *Journal of the Textile Institute*, vol. 87, no. 2, pp. 296–304, 1996.

- [128] A. A. Somashekar, S. Bickerton, and D. Bhattacharyya, "Modelling the viscoelastic stress relaxation of glass fibre reinforcements under constant compaction strain during composites manufacturing," *Composites Part A: Applied Science and Manufacturing*, vol. 43, no. 7, pp. 1044–1052, 2012.
- [129] M. Danzi, C. Schneeberger, and P. Ermanni, "A model for the time-dependent compaction response of woven fiber textiles," *Composites Part A: Applied Science and Manufacturing*, vol. 105, pp. 180–188, 2018.
- [130] P. A. Kelly, "A viscoelastic model for the compaction of fibrous materials," *Journal of the Textile Institute*, vol. 102, no. 8, pp. 689–699, 2011.
- [131] M. Hou, L. Ye, H. J. Lee, and Y. W. Mai, "Manufacture of a carbon-fabric-reinforced polyetherimide (CF/PEI) composite material," *Composites Science and Technology*, vol. 58, no. 2, pp. 181–190, 1998, ISSN: 02663538.
- [132] L. Ye, K. Friedrich, and J. Kästel, "Consolidation of GF/PP commingled yarn composites," *Applied Composite Materials*, vol. 1, pp. 415–429, 1995, ISSN: 15734897.
- [133] L. Ye, K. Friedrich, J. Kästel, and Y.-W. Mai, "Consolidation of unidirectional CF/PEEK composites from commingled yarn prepreg," *Composites Science and Technology*, vol. 54, pp. 349–358, 1995, ISSN: 02663538.
- [134] V. Klinkmüller, M. K. Um, M. Steffens, K. Friedrich, and B. S. Kim, "A new model for impregnation mechanisms in different GF/PP commingled yarns," *Applied Composite Materials*, vol. 1, pp. 351–371, 1995.
- [135] B. P. Van West, R. B. Pipes, and S. G. Advani, "The consolidation of commingled thermoplastic fabrics," *Polymer Composites*, vol. 12, pp. 417–427, 1991.
- [136] S. Kobayashi, T. Tsukada, and T. Morimoto, "Resin impregnation behavior in carbon fiber reinforced polyamide 6 composite: Effects of yarn thickness, fabric lamination and sizing agent," *Composites Part A: Applied Science and Manufacturing*, vol. 101, pp. 283–289, 2017, ISSN: 1359835X.
- [137] J. L. Sommer and A. Mortensen, "Forced unidirectional infiltration of deformable porous media," *Journal of Fluid Mechanics*, vol. 311, pp. 193–217, 1996.
- [138] J. Wolfrath, V. Michaud, and J.-A. E. Manson, "Deconsolidation in glass mat thermoplastic composites: Analysis of the mechanisms," *Composites Part A: Applied Science and Manufacturing*, vol. 36, pp. 1608–1616, 2005.
- [139] J. Wolfrath, V. Michaud, and J.-A. E. Manson, "Deconsolidation in glass mat thermoplastics: Influence of the initial fibre/matrix configuration," *Composites Science and Technology*, vol. 65, pp. 1601–1608, 2005.
- [140] J. Studer, C. Dransfeld, and B. Fiedler, "Direct thermoplastic melt impregnation of carbon fibre fabrics by injection moulding," in *ECCM17*, Munich, Germany, 2016.
- [141] J. Kay, "Gas Transport and Void Evolution in Composite Prepregs," Ph.D. dissertation, University of British Columbia, 2017.

- [142] P. Bhat, J. Merotte, P. Simacek, and S. G. Advani, "Process analysis of compression resin transfer molding," *Composites Part A: Applied Science and Manufacturing*, vol. 40, no. 4, pp. 431–441, 2009.
- [143] B. Bachmann, K. Masania, and C. Dransfeld, "Simulation of the compression resin transfer moulding process for high volume manufacturing," in *TexComp-11*, Leuven, 2013.
- [144] T. A. Cender, P. Simacek, and S. G. Advani, "Resin film impregnation in fabric prepregs with dual length scale permeability," *Composites Part A: Applied Science and Manufacturing*, vol. 53, pp. 118–128, 2013.
- [145] V. Werlen, C. Rytka, S. Wegmann, *et al.*, "Novel tooling for direct melt impregnation of textile with variotherm injection moulding: Methodology and proof of concept," *Journal of Composite Materials*, vol. 56, no. 28, pp. 4245–4257, 2022.
- [146] C. Servais, V. Michaud, and J.-A. E. Manson, "The packing stress of impregnated fiber mats," *Polymer Composites*, vol. 22, no. 2, pp. 298–311, 2001.
- [147] K. Wei, D. Liang, M. Mei, X. Yang, and L. Chen, "A viscoelastic model of compression and relaxation behaviors in preforming process for carbon fiber fabrics with binder," *Composites Part B: Engineering*, vol. 158, pp. 1–9, 2019.
- [148] A. X. H. Yong, A. Aktas, D. May, *et al.*, "Experimental characterisation of textile compaction response: a benchmark exercise," *submitted to: Composites - Part A: Applied Science and Manufacturing*, 2020.
- [149] P. Sousa, S. V. Lomov, and J. Ivens, "Methodology of dry and wet compressibility measurement," *Composites Part A: Applied Science and Manufacturing*, vol. 128, no. August 2019, p. 105 672, 2020.
- [150] G. Papanicolaou and S. Zaoutsos, "Viscoelastic constitutive modeling of creep and stress relaxation in polymers and polymer matrix composites," in *Creep and Fatigue in Polymer Matrix Composites*, second, Woodhead Publishing, 2019.
- [151] K. Murty, *Linear Programming*. John Wiley & Sons, 1983.
- [152] R. Saunders, C. Lekakou, and M. G. Bader, "Compression in the processing of polymer composites 2. Modelling of the viscoelastic compression of resin-impregnated fibre networks," *Composite Science and Technology*, vol. 59, pp. 1483–1494, 1999.
- [153] V. Werlen, C. Rytka, S. Wegmann, *et al.*, "Novel tooling for direct melt impregnation of textile with variothermal injection moulding: methodology and proof of concept," *submitted to: Journal of Composite Materials*, 2022.
- [154] C. Schneeberger, J. C. Wong, and P. Ermanni, "Hybrid bicomponent fibres for thermoplastic composite preforms," *Composites Part A: Applied Science and Manufacturing*, vol. 103, pp. 69–73, 2017, ISSN: 1359835X.
- [155] C. Gomez, D. Salvatori, B. Caglar, R. Trigueira, G. Orange, and V. Michaud, "Resin Transfer molding of High-Fluidity Polyamide-6 with modified Glass-Fabric preforms," *Composites Part A: Applied Science and Manufacturing*, vol. 147, 2021, ISSN: 1359835X.

- [156] V. Werlen, R. Vocke, P. Schwanemann, *et al.*, “Consolidation of hybrid textiles for aerospace applications,” in *20th European Conference on Composite Materials ECCM20*, Lausanne, Switzerland, 2022.
- [157] M. A. F. Zarandi, S. Arroyo, and K. M. Pillai, “Longitudinal and transverse flows in fiber tows: Evaluation of theoretical permeability models through numerical predictions and experimental measurements,” *Composites Part A: Applied Science and Manufacturing*, vol. 119, no. November 2018, pp. 73–87, 2019, ISSN: 1359835X.
- [158] S. Kobayashi and T. Morimoto, “Experimental and numerical characterization of resin impregnation behavior in textile composites fabricated with micro-braiding technique,” *Mechanical Engineering Journal*, vol. 1, no. 4, SMM0031–SMM0031, 2014.
- [159] J. Crank, *Diffusion in Polymers*. Academic Press, 1968.
- [160] L. Zingraff, V. Michaud, P. E. Bourban, and J. A. Månson, “Resin transfer moulding of anionically polymerised polyamide 12,” *Composites Part A: Applied Science and Manufacturing*, vol. 36, no. 12, 2005.
- [161] W. Szmyt, C. Guerra, and I. Utke, “Diffusion of dilute gas in arrays of randomly distributed, vertically aligned, high-aspect-ratio cylinders,” *Beilstein Journal of Nanotechnology*, vol. 8, no. 1, pp. 64–73, 2017, ISSN: 21904286.
- [162] W. Szmyt, C. Dransfeld, I. Utke, and C. Guerra-nu, “Solving the inverse Knudsen problem : Gas diffusion in random fibrous media,” *Journal of Membrane Science*, vol. 620, no. April 2020, 2021.
- [163] F. Transvalidou and S. V. Sotirchos, “Effective Diffusion Coefficients in Square Arrays of Filament Bundles,” *AIChE Journal*, vol. 42, no. 9, pp. 2426–2438, 1996.
- [164] D. Saenz-castillo, M. I. Martín, S. Calvo, F. Rodriguez-lence, and A. Güemes, “Effect of processing parameters and void content on mechanical properties and NDI of thermoplastic composites,” *Composites Part A*, vol. 121, no. March, pp. 308–320, 2019, ISSN: 1359-835X.
- [165] Y. Sato, K. Fujiwara, T. Takikawa, Sumarno, S. Takishima, and H. Masuoka, “Solubilities and diffusion coefficients of carbon dioxide and nitrogen in polypropylene, high-density polyethylene, and polystyrene under high pressures and temperatures,” *Fluid Phase Equilibria*, vol. 162, no. 1-2, pp. 261–276, 1999, ISSN: 03783812.
- [166] D. May, A. Aktas, S. G. Advani, *et al.*, “In-plane permeability characterization of engineering textiles based on radial flow experiments: A benchmark exercise,” *Composites Part A: Applied Science and Manufacturing*, vol. 121, no. October 2018, pp. 100–114, 2019, ISSN: 1359835X.
- [167] Y. Sato, M. Yurugi, K. Fujiwara, S. Takishima, and H. Masuoka, “Solubilities of carbon dioxide and nitrogen in polystyrene under high temperature and pressure,” *Fluid Phase Equilibria*, vol. 125, no. I 996, pp. 129–138, 1996.
- [168] C. A. Harper, *Handbook of Plastic Processes*, C. A. Harper, Ed. New Jersey: John Wiley & Sons, 2006.

- [169] H. J. Chun, J. Y. Shin, and I. M. Daniel, "Effects of material and geometric nonlinearities on the tensile and compressive behavior of composite materials with fiber waviness," *Composites Science and Technology*, vol. 61, no. 1, pp. 125–134, 2001.
- [170] A. Vaxman, M. Narkis, A. Siegmann, and S. Kenig, "Void formation in short-fiber thermoplastic composites," *Polymer Composites*, vol. 10, no. 6, pp. 449–453, 1989, ISSN: 15480569.
- [171] S. A. Niaki, A. Forghani, R. Vaziri, and A. Poursartip, "A two-phase integrated flow-stress process model for composites with application to highly compressible phases," *Mechanics of Materials*, vol. 109, pp. 51–66, 2017, ISSN: 01676636.
- [172] S. A. Niaki, A. Forghani, R. Vaziri, and A. Poursartip, "A three-phase integrated flow-stress model for processing of composites," *Mechanics of Materials*, vol. 117, no. March 2017, pp. 152–164, 2018, ISSN: 01676636.
- [173] A. R. Khoei and T. Mohammadnejad, "Numerical modeling of multiphase fluid flow in deforming porous media: A comparison between two- and three-phase models for seismic analysis of earth and rockfill dams," *Computers and Geotechnics*, vol. 38, no. 2, pp. 142–166, 2011, ISSN: 0266352X.
- [174] F. Nagel and G. Meschke, "An elasto-plastic three phase model for partially saturated soil for the finite element simulation of compressed air support in tunnelling," *International Journal for Numerical and Analytical Methods in Geomechanics*, vol. 34, 2009.
- [175] N. Kuentzer, P. Simacek, S. G. Advani, and S. Walsh, "Correlation of void distribution to VARTM manufacturing techniques," *Composites Part A: Applied Science and Manufacturing*, vol. 38, no. 3, pp. 802–813, 2007.
- [176] H. Tan and K. M. Pillai, "Multiscale modeling of unsaturated flow in dual-scale fiber preforms of liquid composite molding I: Isothermal flows," *Composites Part A: Applied Science and Manufacturing*, vol. 43, no. 1, pp. 1–13, 2012.
- [177] V. Michaud and A. Mortensen, "Infiltration processing of fibre reinforced composites: governing phenomena," *Composites Part A: Applied Science and Manufacturing*, vol. 32, pp. 981–996, 2001.
- [178] V. Michaud, J. L. Sommer, and A. Mortensen, "Infiltration of fibrous preforms by a pure metal: Part V. Influence of preform compressibility," *Metallurgical and Materials Transactions A: Physical Metallurgy and Materials Science*, vol. 30, no. 2, pp. 471–482, 1999.
- [179] A. K. Pickett, G. Creech, and P. D. Luca, "Simplified and advanced simulation methods for prediction of fabric draping methods for prediction of fabric draping," *Revue Européenne des Éléments Finis*, vol. 14, pp. 677–691, 2005.
- [180] B. Chen and M. Govindaraj, "A Physically Based Model of Fabric Drape Using Flexible Shell Theory," *Textile Research Journal*, vol. 65, no. 6, pp. 324–330, 1995.
- [181] D. E. Breen, D. H. House, and M. J. Wozny, "A Particle-Based Model for Simulating the Draping Behavior of Woven Cloth," *Textile Research Journal*, vol. 64, no. 11, pp. 663–685, 1994.

- [182] V. K. Kothari and A. Das, "Compressional behaviour of nonwoven geotextiles," *Geotextiles and Geomembranes*, vol. 11, no. 3, pp. 235–253, 1992, ISSN: 02661144.
- [183] A. Geoffre, Y. Wielhorski, N. Moulin, J. Bruchon, S. Drapier, and P.-j. Liotier, "Influence of intra-yarn flows on whole 3D woven fabric numerical permeability: from Stokes to Stokes-Darcy simulations," *International Journal of Multiphase Flow*, vol. 129, 2020.
- [184] D. Salvatori, B. Caglar, and V. Michaud, "3D spacers enhance flow kinetics in resin transfer molding with woven fabrics," *Composites Part A*, vol. 119, no. January, 2019.
- [185] A. Maazouz, K. Lamnawar, and M. Dkier, "Chemorheological study and in-situ monitoring of PA6 anionic-ring polymerization for RTM processing control," *Composites Part A*, 2018, ISSN: 1359-835X.
- [186] A. C. Long, *Design and manufacture of textile composites*. CRC Press, 2005.
- [187] H. Gu, "Research on the impregnation behaviour of the micro-braided thermoplastic matrix," *Materials and Design*, vol. 25, pp. 167–170, 2004, ISSN: 02641275.
- [188] P. Ouagne, T. Ouahbi, C. H. Park, J. Bréard, and A. Saouab, "Continuous measurement of fiber reinforcement permeability in the thickness direction: Experimental technique and validation," *Composites Part B: Engineering*, vol. 45, no. 1, pp. 609–618, 2013.
- [189] H. M. El-Dessouky, B. Liu, M. N. Saleh, and R. J. Scaife, "Co-woven carbon and nylon fibres for manufacturing thermoplastic composite plaques," in *2nd CIRP Conference on Composite Material Parts Manufacturing*, Elsevier B.V., 2019.
- [190] H. Brunig, R. Beyreuther, R. Vogel, and B. Tandler, "Melt spinning of fine and ultra-fine PEEK-filaments," *Journal of Materials Science*, vol. 38, pp. 2149–2153, 2003.
- [191] B. Caglar, G. Broggi, M. A. Ali, L. Orgéas, and V. Michaud, "Deep learning accelerated prediction of the permeability of fibrous microstructures," *Composites Part A: Applied Science and Manufacturing*, vol. 158, no. February, 2022.
- [192] H. Lessard, G. Lebrun, A. Benkaddour, and X. T. Pham, "Influence of process parameters on the thermostamping of a [0/90]<sub>12</sub> carbon/polyether ether ketone laminate," *Composites Part A: Applied Science and Manufacturing*, vol. 70, pp. 59–68, 2015, ISSN: 1359835X.
- [193] M. A. Ali, R. Umer, K. A. Khan, and W. J. Cantwell, "Application of X-ray computed tomography for the virtual permeability prediction of fiber reinforcements for liquid composite molding processes: A review," *Composites Science and Technology*, vol. 184, p. 107 828, 2019.
- [194] A. Ward, "The viscosity of pure liquids," *Transactions of the Faraday Society*, vol. 33, pp. 88–97, 1937.
- [195] A. Ayadi, M. Deleglise-Lagardere, C. H. Park, and P. Krawczak, "Analysis of Impregnation Mechanism of Weft-Knitted Commingled Yarn Composites by Staged Consolidation and Laboratory X-Ray Computed Tomography," *Frontiers in Materials*, vol. 6, 2019.
- [196] N. Bernet, M. D. Wakeman, P. E. Bourban, and J.-A. E. Manson, "An integrated cost and consolidation model for commingled yarn based composites," *Composites - Part A: Applied Science and Manufacturing*, vol. 33, pp. 495–506, 2002.

- [197] J. P. Belnoue, T. Mesogitis, O. J. Nixon-Pearson, *et al.*, “Understanding and predicting defect formation in automated fibre placement pre-preg laminates,” *Composites Part A: Applied Science and Manufacturing*, vol. 102, pp. 196–206, 2017.
- [198] J. J. Gangloff, P. Simacek, S. Sinha, and S. G. Advani, “A process model for the compaction and saturation of partially impregnated thermoset prepreg tapes,” *Composites Part A: Applied Science and Manufacturing*, vol. 64, pp. 234–244, 2014, ISSN: 1359835X.
- [199] A. Danezis, D. Williams, M. Edwards, and A. A. Skordos, “Heat transfer modelling of flashlamp heating for automated tape placement of thermoplastic composites,” *Composites Part A*, vol. 145, no. March, p. 106 381, 2021.
- [200] A. Koponen, D. Kandhai, E. Hellén, *et al.*, “Permeability of three-dimensional random fiber webs,” *Physical Review Letters*, vol. 80, no. 4, pp. 716–719, 1998, ISSN: 10797114.
- [201] B. Barari, P. Simacek, S. Yarlagadda, R. M. Crane, and S. G. Advani, “Prediction of process-induced void formation in anisotropic Fiber-reinforced autoclave composite parts,” *International Journal of Material Forming*, vol. 13, no. 1, pp. 143–158, 2020.
- [202] E. Guzman-Maldonado, N. Hamila, P. Boisse, and J. Bikard, “Thermomechanical analysis, modelling and simulation of the forming of pre-impregnated thermoplastics composites,” *Composites Part A: Applied Science and Manufacturing*, vol. 78, pp. 211–222, 2015, ISSN: 1359835X.
- [203] S. C. Garcea, Y. Wang, and P. J. Withers, “X-ray computed tomography of polymer composites,” *Composites Science and Technology*, vol. 156, pp. 305–319, 2018, ISSN: 02663538.
- [204] M. S. Rouhi, M. Wysocki, and R. Larsson, “Experimental assessment of dual-scale resin flow-deformation in composites processing,” *Composites Part A: Applied Science and Manufacturing*, vol. 76, pp. 215–223, 2015.
- [205] S. Beland, *High Performance Thermoplastic Resins and Their Composites*. Noyes Data Corporation, 1990.
- [206] D. Dorr, F. Henning, and L. Karger, “Nonlinear hyperviscoelastic modelling of intraply deformation behaviour in finite element forming simulation of continuously fibre-reinforced thermoplastics,” *Composites Part A: Applied Science and Manufacturing*, vol. 109, pp. 585–596, 2018.
- [207] Z. Xiao, X. Liu, L. T. Harper, A. Endruweit, and N. A. Warrior, “Modelling the permeability of random discontinuous carbon fibre preforms,” *Journal of Composite Materials*, vol. 54, no. 20, pp. 2739–2751, 2020, ISSN: 1530793X.
- [208] P. De Luca, P. Lefébure, and A. K. Pickett, “Numerical and experimental investigation of some press forming parameters of two fibre reinforced thermoplastics: APC2-AS4 and PEI-CETEX,” *Composites Part A: Applied Science and Manufacturing*, vol. 29, pp. 101–110, 1998.
- [209] R. Helmus, T. Centea, P. Hubert, and R. Hinterhölzl, “Out-of-autoclave prepreg consolidation: Coupled air evacuation and prepreg impregnation modeling,” *Journal of Composite Materials*, vol. 50, no. 10, pp. 1403–1413, 2016, ISSN: 1530793X.

- [210] C. Dransfeld, K. Masania, E. Kramer, M. Siegfried, and S. Klauser, “Fast impregnation of complex shapes for the manufacturing of high performance composites and its associated tooling,” in *11th International Conference Flow Processing in Composite Materials*, Auckland, New Zealand, 2012.
- [211] S. Schuler and S. G. Advani, “Flow Instabilities during the Squeeze Flow of Multiaxial Laminates,” *Journal of Composite Materials*, vol. 31, no. 21, pp. 2146–2160, 1997.
- [212] M. Abounaim, O. Diestel, G. Hoffmann, and C. Cherif, “High performance thermoplastic composite from flat knitted multi-layer textile preform using hybrid yarn,” *Composites Science and Technology*, vol. 71, pp. 511–519, 2011.
- [213] H. S. Carslaw and J. C. Jaeger, *Conduction of Heat in Solids*, 2nd ed., C. Press, Ed. 1959.
- [214] T. Guglhör, “Experimentelle und modellhafte Betrachtung des Konsolidierungsprozesses von carbonfaserverstärktem Polyamid-6,” Ph.D. dissertation, Augsburg University, 2017.
- [215] A. Nabovati, E. W. Llewellyn, and A. C. Sousa, “A general model for the permeability of fibrous porous media based on fluid flow simulations using the lattice Boltzmann method,” *Composites Part A: Applied Science and Manufacturing*, vol. 40, no. 6-7, pp. 860–869, 2009.
- [216] S. Sriramula and M. K. Chryssanthopoulos, “Quantification of uncertainty modelling in stochastic analysis of FRP composites,” *Composites Part A: Applied Science and Manufacturing*, vol. 40, no. 11, pp. 1673–1684, 2009.
- [217] B. Yenilmez, B. Caglar, and E. M. Sozer, “Viscoelastic modeling of fiber preform compaction in vacuum infusion process,” *Journal of Composite Materials*, vol. 51, no. 30, pp. 4189–4203, 2017, ISSN: 1530793X.
- [218] N. Ray, A. Rupp, R. Schulz, and P. Knabner, “Old and New Approaches Predicting the Diffusion in Porous Media,” *Transport in Porous Media*, vol. 124, no. 3, pp. 803–824, 2018, ISSN: 15731634.
- [219] K. Senthil, A. Arockiarajan, R. Palaninathan, B. Santhosh, and K. M. Usha, “Defects in composite structures: Its effects and prediction methods - A comprehensive review,” *Composite Structures*, vol. 106, pp. 139–149, 2013, ISSN: 02638223.
- [220] H. E. Bersee and A. Beukers, “Consolidation of Thermoplastic Composites,” *Journal of Thermoplastic Composite Materials*, vol. 16, pp. 433–455, 2003.
- [221] A. Endruweit and A. C. Long, “A model for the in-plane permeability of triaxially braided reinforcements,” *Composites - Part A: Applied Science and Manufacturing*, vol. 42, no. 2, pp. 165–172, 2011.
- [222] N. Bernet, V. Michaud, P. E. Bourban, and J.-A. E. Manson, “Commingled yarn composites for rapid processing of complex shapes,” *Composites Part A: Applied Science and Manufacturing*, vol. 32, no. 11, pp. 1613–1626, 2001.
- [223] M. Szarski and S. Chauhan, “Composite temperature profile and tooling optimization via Deep Reinforcement Learning,” *Composites Part A: Applied Science and Manufacturing*, vol. 142, no. November 2020, p. 106 235, 2021.



- [224] R. Larsson, M. Wysocki, and S. Toll, "Process-modeling of composites using two-phase porous media theory," *European Journal of Mechanics, A/Solids*, vol. 23, pp. 15–36, 2004, ISSN: 09977538.
- [225] N. Prasad and R. Wanhill, *Aerospace Materials and Material Technologies, Volume 1: Aerospace Material Technologies*. 2017, vol. 1, p. 586.
- [226] P. L. Durrill and R. G. Griskey, "Diffusion and solution of gases into thermally softened or molten polymers: Part II. Relation of diffusivities and solubilities with temperature pressure and structural characteristics," *AIChE Journal*, vol. 15, no. 1, pp. 106–110, 1969.
- [227] F. Lisa, D. A. Olivier, F. Jean-Charles, and S. Fabrice, "Effect of poly(ether ether ketone) degradation on commingled fabrics consolidation," *Composites Part A: Applied Science and Manufacturing*, vol. 149, no. May, p. 106482, 2021, ISSN: 1359835X.
- [228] D. Liu, J. Ding, X. Fan, X. Lin, and Y. Zhu, "Non-isothermal forming of glass fiber/polypropylene commingled yarn fabric composites," *Materials and Design*, vol. 57, pp. 608–615, 2014.
- [229] T. S. Lundström and B. R. Gebart, "Influence from process parameters on void formation in resin transfer molding," *Polymer Composites*, vol. 15, no. 1, pp. 25–33, 1994, ISSN: 15480569.
- [230] F. Loix, P. Badel, L. Orgéas, C. Geindreau, and P. Boisse, "Woven fabric permeability: From textile deformation to fluid flow mesoscale simulations," *Composites Science and Technology*, vol. 68, no. 7-8, pp. 1624–1630, 2008, ISSN: 02663538.
- [231] P. Boisse, J. Colmars, N. Hamila, N. Naouar, and Q. Steer, "Bending and wrinkling of composite fiber preforms and prepregs. A review and new developments in the draping simulations," *Composites Part B: Engineering*, vol. 141, pp. 234–249, 2018.
- [232] C. Binetruy and B. Hilaire, "Tow Impregnation Model and Void Formation Mechanisms during RTM," *Journal of Composite Materials*, vol. 32, no. 3, 1998.
- [233] R. A. Greenkorn, *Flow Phenomena in Porous Media*, first. CRC Press, 1983.
- [234] P. Knabner and L. Angermann, *Numerik partieller Differentialgleichungen: eine anwendungsorientierte Einführung*. Springer-Verlag, 2013.
- [235] M. Koerdt, P. Schiebel, O. Focke, and H. Axel S., "Hybrid Textiles – the Other Way of Forming High-Performance Thermoplastic Composites for Primary Structure," in *ECCM17*, Munich, Germany, 2016, ISBN: 9783000533877.
- [236] B. Gourichon, C. Binetruy, and P. Krawczak, "Experimental investigation of high fiber tow count fabric unsaturation during RTM," *Composites Science and Technology*, vol. 66, no. 7-8, pp. 976–982, 2006.
- [237] H. M. El-Dessouky, M. N. Saleh, M. Gautam, G. Han, R. J. Scaife, and P. Potluri, "Tailored fibre placement of commingled carbon-thermoplastic fibres for notch-insensitive composites," *Composite Structures*, vol. 214, pp. 348–358, 2019, ISSN: 02638223.

- [238] T. Dopler, A. Modaressi, and V. Michaud, "Simulation of metal-matrix composite isothermal infiltration processing," *Metallurgical and Materials Transactions B: Process Metallurgy and Materials Processing Science*, vol. 31, pp. 225–234, 2000.
- [239] S. Roychowdhury and S. G. Advani, "An experimental investigation of consolidation in thermoplastic filament winding," *Composites Manufacturing*, vol. 2, no. 2, pp. 97–104, 1991, ISSN: 09567143.
- [240] C. J. Tranter, "Heat conduction in the region bounded internally by an elliptical cylinder and an analogous problem in atmospheric diffusion," *Quarterly Journal of Mechanics and Applied Mathematics*, vol. 4, no. 4, pp. 461–465, 1951, ISSN: 00335614.
- [241] Y. Gong, X. Peng, Y. Yao, and Z. Guo, "An anisotropic hyperelastic constitutive model for thermoplastic woven composite prepregs," *Composites Science and Technology*, vol. 128, pp. 17–24, 2016.
- [242] J. Merotte, P. Simacek, and S. G. Advani, "Flow analysis during compression of partially impregnated fiber preform under controlled force," *Composites Science and Technology*, vol. 70, pp. 725–733, 2010.
- [243] A. Levy and P. Hubert, "Interstrand void content evolution in compression moulding of randomly oriented strands (ROS) of thermoplastic composites," *Composites Part A: Applied Science and Manufacturing*, vol. 70, pp. 121–131, 2015, ISSN: 1359835X.
- [244] A. Endruweit, S. Gehrig, and P. Ermanni, "Mechanisms of Hydrodynamically Induced In-plane Deformation of Reinforcement Textiles in Resin Injection Processes," *Journal of Composite Materials*, vol. 37, no. 18, pp. 1675–1692, 2003.
- [245] A. Tamayol and M. Bahrami, "Transverse permeability of fibrous porous media," *Physical Review E - Statistical, Nonlinear, and Soft Matter Physics*, vol. 83, no. 4, pp. 1–9, 2011, ISSN: 15393755.
- [246] M. E. Foley and J. W. Gillespie, "Modeling the effect of fiber diameter and fiber bundle count on tow impregnation during liquid molding processes," *Journal of Composite Materials*, vol. 39, no. 12, pp. 1045–1065, 2005.
- [247] P. E. Bourban, N. Bernet, J.-E. Zanetto, and J.-A. E. Manson, "Material phenomena controlling rapid processing of thermoplastic composites," *Composites Part A: Applied Science and Manufacturing*, vol. 32, pp. 1045–1057, 2001.
- [248] Z. M. Huang, "Simulation of the mechanical properties of fibrous composites by the bridging micromechanics model," *Composites Part A: Applied Science and Manufacturing*, vol. 32, no. 2, pp. 143–172, 2001, ISSN: 1359835X.
- [249] M. Roux, N. Eguemann, C. Dransfeld, F. Thiebaud, and D. Perreux, "Thermoplastic carbon fibre-reinforced polymer recycling with electrodynamical fragmentation: From cradle to cradle," *Journal of Thermoplastic Composite Materials*, vol. 30, no. 3, 2017, ISSN: 15307980.

- [250] O. J. Nixon-Pearson, J. P. Belnoue, D. S. Ivanov, K. D. Potter, and S. R. Hallett, "An experimental investigation of the consolidation behaviour of uncured prepregs under processing conditions," *Journal of Composite Materials*, vol. 51, pp. 1911–1924, 2016, ISSN: 1530793X.
- [251] J. C. Jaeger, "Conduction of Heat in an Infinite Region Bounded Internally By A Circular Cylinder of a Perfect Conductor," *Australian Journal of Physics*, 1956.
- [252] A. Keller, C. Dransfeld, and K. Masania, "Flow and heat transfer during compression resin transfer moulding of highly reactive epoxies," *Composites Part B*, vol. 153, no. May, 2018, ISSN: 1359-8368.
- [253] T. S. Lundström, V. Frishfelds, and A. Jakovics, "A statistical approach to permeability of clustered fibre reinforcements," *Journal of Composite Materials*, vol. 38, no. 13, pp. 1137–1149, 2004.
- [254] J. R. Weitzenböck, R. A. Sheno, and P. A. Wilson, "Radial flow permeability measurement. Part A: theory," *Composites Part A: Applied Science and Manufacturing*, vol. 30, no. 6, pp. 781–796, 1999.
- [255] M. K. Um, "A Study on Permeability of Unidirectional Fiber Beds," *Journal of Reinforced Plastics and Composites*, vol. 16, no. 17, pp. 1575–1590, 1997.
- [256] S. Wegmann, C. Rytka, M. Diaz-rodenas, *et al.*, "A life cycle analysis of novel lightweight composite processes : Reducing the environmental footprint of automotive structures," *Journal of Cleaner Production*, vol. 330, 2022.
- [257] D. Bublitz, D. Colin, and K. Drechsler, "Implementation of a viscoelastic material model to predict the compaction response of dry carbon fiber preforms," *Composites Part A: Applied Science and Manufacturing*, vol. 153, no. November 2021, p. 106718, 2022.
- [258] D. S. Clague, B. D. Kandhai, R. Zhang, and P. M. Slood, "Hydraulic permeability of (un)bounded fibrous media using the lattice Boltzmann method," *Physical Review E - Statistical Physics, Plasmas, Fluids, and Related Interdisciplinary Topics*, vol. 61, no. 1, pp. 616–625, 2000.
- [259] E. Syerko, C. Binetruy, S. Comas-Cardona, and A. Leygue, "A numerical approach to design dual-scale porosity composite reinforcements with enhanced permeability," *Materials and Design*, vol. 131, 2017.
- [260] N. Vernet, E. Ruiz, S. Advani, *et al.*, "Experimental determination of the permeability of engineering textiles: Benchmark II," *Composites Part A: Applied Science and Manufacturing*, vol. 61, pp. 172–184, 2014, ISSN: 1359835X.
- [261] S. Boztepe, P. Šimáček, K. Labastie, *et al.*, "Effect of the initial resin distribution in partially impregnated thermoplastic prepregs on consolidation," *Composites Science and Technology*, vol. 225, no. August 2021, 2022.
- [262] J. A. Barnes and F. N. Cogswell, "Transverse flow processes in continuous fibre-reinforced thermoplastic composites," *Composites*, vol. 20, no. 1, pp. 38–42, 1989.

- [263] R. A. Witik, J. Payet, V. Michaud, C. Ludwig, and J.-a. E. Månson, "Assessing the life cycle costs and environmental performance of lightweight materials in automobile applications," *Composites Part A*, vol. 42, no. 11, 2011, ISSN: 1359-835X.
- [264] A. Endruweit, A. C. Long, F. Robitaille, and C. D. Rudd, "Influence of stochastic fibre angle variations on the permeability of bi-directional textile fabrics," *Composites Part A: Applied Science and Manufacturing*, vol. 37, no. 1, pp. 122–132, 2006, ISSN: 1359835X.
- [265] S. Ranganathan, S. G. Advani, and Lamontia, "A Non-Isothermal Process Model for Consolidation and Void Reduction during In-Situ Tow Placement of Thermoplastic Composites," *Journal of Composite Materials*, vol. 29, no. 8, pp. 1040–1062, 1995, ISSN: 1530793x.
- [266] S. Roychowdhury, J. W. Gillepsie Jr, and S. G. Advani, "Volatile-Induced Void Formation in Materials : I . Modeling and Parametric Studies," *Journal of Composite Materials*, vol. 35, no. 04, pp. 340–366, 2001.
- [267] I. Gnaba, P. Wang, D. Soulat, F. Omrani, M. Ferreira, and P. Vroman, "Investigation about the Effect of Manufacturing Parameters on the Mechanical Behaviour of Natural Fibre Nonwovens Reinforced Thermoplastic Composites," *Materials*, vol. 12, 2019.
- [268] W. Wu and W. Li, "A novel material for simulation on compaction behavior of glass fiber non-crimp fabric," *Composite Structures*, vol. 219, pp. 8–16, 2019, ISSN: 02638223.
- [269] H. Xiong, N. Hamila, and P. Boisse, "Consolidation Modeling during Thermoforming of Thermoplastic Composite Prepregs," *Materials*, vol. 12, 2019.
- [270] M. S. Rouhi and M. Wysocki, "3D simulation of transversely isotropic laminated composites in RTM using poromechanics," *Materials Science: Advanced Composite Materials*, vol. 2, no. 4, pp. 1–9, 2018.
- [271] A. J. Thompson, B. El Said, D. S. Ivanov, J. P. Belnoue, and S. R. Hallett, "High fidelity modelling of the compression behaviour of 2D woven fabrics," *International Journal of Solids and Structures*, vol. 154, pp. 104–113, 2018.
- [272] A. Tamayol and M. Bahrami, "Analytical determination of viscous permeability of fibrous porous media," *International Journal of Heat and Mass Transfer*, vol. 52, no. 9-10, pp. 2407–2414, 2009, ISSN: 00179310.
- [273] M. Bonnet, *Kunststofftechnik*. Springer Vieweg Wiesbaden, 2014.
- [274] Q. T. Nguyen, E. Vidal-Salle, P. Boisse, *et al.*, "Mesoscopic scale analyses of textile composite reinforcement compaction," *Composites Part B: Engineering*, vol. 611-612, pp. 356–362, 2013, ISSN: 10139826.
- [275] F. Henning, L. Kärger, D. Dörr, F. J. Schirmaier, J. Seuffert, and A. Bernath, "Fast processing and continuous simulation of automotive structural composite components," *Composites Science and Technology*, vol. 171, no. September 2017, pp. 261–279, 2019, ISSN: 02663538.
- [276] G. A. Carnaby and N. Pan, "Theory of the Compression Hysteresis of Fibrous Assemblies," *Textile Research Journal*, vol. 59, no. 5, pp. 275–284, 1989.

## BIBLIOGRAPHY

---

- [277] P. Ouagne and J. Bréard, “Continuous transverse permeability of fibrous media,” *Composites Part A: Applied Science and Manufacturing*, vol. 41, no. 1, pp. 22–28, 2010.
- [278] Tepex dynalite glass/pa6 technical datasheet. Edition 2020-10-23, LANXESS Deutschland GmbH.



# List of symbols

Symbol	Parameter	Unit
$A_{arrh}$	First constant in Arrhenius's equation	[Pa · s]
$A_{geb}$	First constant in Gebart's equation	[-]
$A_c$	Cavity area	[m <sup>2</sup> ]
$A_{\dagger}$	First constant in Cross's equation	[-]
$A_{\diamond}$	First constant in Carreau's equation	[-]
$A_{\rho^m}$	First fitting constant for molten density	[ $\frac{kg}{m^3 \cdot K}$ ]
$A_{tex}$	First fitting constant for quasi-static stress response	[Pa]
$A_{tow}$	Tow cross-sectional surface area	[m <sup>2</sup> ]
$A_{tow}^{\nu f}$	First fitting constant for tow fibre volume fraction	[]
$A_{\tau}$	First fitting constant for relaxation time	[s]
$B_{arrh}$	Second constant in Arrhenius's equation	[-]
$B_{geb}$	Second constant in Gebart's equation	[-]
$B_{\dagger}$	Second constant in Cross's equation	[-]
$B_{\diamond}$	Second constant Carreau's equation	[-]
$B_{\rho^m}$	Second fitting constant for molten density	[ $\frac{kg}{m^3}$ ]
$B_{tex}$	Second fitting constant for quasi-static stress response	[-]
$B_{tow}^{\nu f}$	Second fitting constant for tow fibre volume fraction	[]
$B_{\tau}$	Second fitting constant for relaxation time	[-]
$c$	Moisture capacity	[ $\frac{m \cdot s^3}{kg}$ ]
$C$	Concentration	[ $\frac{mol}{m^3}$ ]
$C_s$	Saturation concentration	[ $\frac{mol}{m^3}$ ]
$C_{\infty}$	Far-field concentration	[ $\frac{mol}{m^3}$ ]
$d$	Depth of control volume	[m]
$D$	Diffusion coefficient	[ $\frac{m^2}{s}$ ]
$E$	Young's modulus	[Pa]
$Error$	Total relative modelling error	[-]
$Error_E$	Total relative elastic error	[-]
$Error_{VE}$	Total relative viscoelastic error	[-]
$h_{cav}$	Cavity height	[m]
$h_{cav,0}$	Initial cavity height	[m]
$H$	Henry's constant	[ $\frac{mol}{m^3 \cdot Pa}$ ]
$J$	Flux of diluted species	[ $\frac{mol}{m^4}$ ]
$k_r$	Relative permeability	[-]

Symbol	Parameter	Unit
$K$	Permeability	[m <sup>2</sup> ]
$K_x$	Permeability in x direction	[m <sup>2</sup> ]
$K_y$	Permeability in y direction	[m <sup>2</sup> ]
$K_{tow}$	Tow permeability	[m <sup>2</sup> ]
$K_{//}$	Permeability in fibre direction	[m <sup>2</sup> ]
$K_{\perp}$	Permeability transverse to fibre direction	[m <sup>2</sup> ]
$l_h$	Semi-minor axis	[m]
$l_w$	Semi-major axis	[m]
$M^A$	Areal weight	[ $\frac{kg}{m^2}$ ]
$M_f$	Textile mass	[kg]
$M_f^A$	Areal weight of textile ply	[ $\frac{kg}{m^2}$ ]
$M_m$	Matrix mass	[kg]
$M_m^A$	Areal weight of matrix ply	[ $\frac{kg}{m^2}$ ]
$N$	Number of plies	[-]
$n_{tow}$	Number of tows in control volume	[-]
$n_{\lambda}$	Amount of air entrapped per tow and unit depth	[ $\frac{mol}{m}$ ]
$n_{\lambda}$	Initial amount of air entrapped per tow and unit depth	[ $\frac{mol}{m}$ ]
$P$	Pressure	[Pa]
$P_{app}$	Applied pressure	[Pa]
$P_{atm}$	Atmospheric pressure	[Pa]
$P_c$	Capillary pressure	[Pa]
$P_g$	Gas pressure	[Pa]
$P_{dp}$	Driving pressure	[Pa]
$P_m$	Matrix pressure	[Pa]
$q$	Volumetric flux	[ $\frac{m}{s}$ ]
$r$	Radius to the flow front	[m]
$r_f$	Fibre radius	[m]
$S$	Saturation	[-]
$R^2$	Coefficient of determination	[-]
$R_{eqv}$	Equivalent radius	[m]
$t$	Time	[s]
$T$	Temperature	[K]
$T_g$	Glass transition temperature	[K]
$T_m$	Melting temperature	[K]
$v$	Flow front speed	[ $\frac{m}{s}$ ]
$V$	Volume / unit cell volume	[m <sup>3</sup> ]
$V_f$	Volume occupied by the fibres	[m <sup>3</sup> ]
$V_g$	Volume occupied by the gas	[m <sup>3</sup> ]
$V_{g,tow}$	Volume occupied by the gas in each tow	[m <sup>3</sup> ]
$V_l$	Volume occupied by the liquid	[m <sup>3</sup> ]
$V_m$	Volume occupied by the matrix	[m <sup>3</sup> ]



List of symbols

---

<b>Symbol</b>	<b>Parameter</b>	<b>Unit</b>
$V_{tow}$	Volume occupied by the tows	[m <sup>3</sup> ]
$V_{tow}^{single}$	Volume occupied by the tows	[m <sup>3</sup> ]
$\alpha$	Tunable parameter for the model of Klunker	[-]
$\dot{\gamma}$	Shear rate	[ $\frac{1}{s}$ ]
$\epsilon$	Strain	[-]
$\eta$	Dynamic viscosity	[Pa · s]
$\eta_0$	Zero-shear viscosity	[Pa · s]
$\nu_f$	Fibre volume fraction	[-]
$\nu_{f,tow}$	Tow fibre volume fraction	[-]
$\nu_{f,max}$	Maximum packing density	[-]
$\nu_{f0}$	Fibre volume fraction in uncompact state	[-]
$\nu_m$	Matrix volume fraction	[-]
$\nu_v$	Void volume fraction	[-]
$\epsilon$	Impregnation degree	[-]
$\rho$	Density	[ $\frac{kg}{m^3}$ ]
$\rho_f$	Fibre density	[ $\frac{kg}{m^3}$ ]
$\rho_m^m$	Molten matrix density	[ $\frac{kg}{m^3}$ ]
$\rho_m^s$	Solid-state matrix density	[ $\frac{kg}{m^3}$ ]
$\sigma$	Stress	[Pa]
$\sigma_{meas.}$	Measured fibre bed stress response	[Pa]
$\sigma_{model}$	Modelled fibre bed stress response	[Pa]
$\sigma_{tex}$	Textile stress response	[Pa]
$\sigma_{meas.}^{max}$	Maximum measured fibre bed stress response	[Pa]
$\sigma_{E,meas.}^{max}$	Maximum measured elastic fibre bed stress response	[Pa]
$\sigma_{VE,meas.}^{max}$	Maximum measured viscoelastic fibre bed stress response	[Pa]
$\sigma_{model}^{max}$	Maximum modelled fibre bed stress response	[Pa]
$\sigma_{E,model}^{max}$	Maximum modelled elastic fibre bed stress response	[Pa]
$\sigma_{VE,model}^{max}$	Maximum modelled viscoelastic fibre bed stress response	[Pa]
$\tau$	Relaxation time	[s]
$\phi$	Porosity	[-]



# Publications

- Werlen V, Rytka C, Michaud V. A numerical approach to characterize the viscoelastic behaviour of fibre beds and to evaluate the influence of strain deviations on viscoelastic parameter extraction. *Compos Part A Appl Sci Manuf.* 2021;143(October 2020):106315.
- Werlen V, Vocke R, Schwanemann P, Michaud V, Brauner C, Dransfeld C, et al. Consolidation of hybrid textiles for aerospace applications. In: 20th European Conference on Composite Materials ECCM20. Lausanne, Switzerland; 2022.
- Werlen V, Rytka C, Wegmann S, Philipp H, Khalaf Y, Michaud V, et al. Novel tooling for direct melt impregnation of textile with variotherm injection moulding: Methodology and proof of concept. *J Compos Mater.* 2022;56(28):4245–57.
- Wegmann S, Rytka C, Diaz-rodenas M, Werlen V, Schneeberger C, Ermanni P, et al. A life cycle analysis of novel lightweight composite processes : Reducing the environmental footprint of automotive structures. *J Clean Prod.* 2022;330.
- Werlen V, Vocke R, Brauner C, Dransfeld C, Michaud V, Rytka C. A model for the consolidation of hybrid textiles considering air entrapment, dissolution and diffusion. *Compos Part A Appl Sci Manuf.* 2023;166(December 2022):107413.
- Werlen V, Rytka C., Dransfeld C, Brauner C, Michaud V. A multi scale consolidation model for press moulding of hybrid textiles into complex geometries. Submitted to *Polymer Engineering and Science*.
- Yong A. & al. 2nd International Permeability and Compressibility Benchmark Exercise. To be submitted.





# Vincent Werlen

MSc ETH ME

Date of Birth: 24.01.1994  
Nationality: Swiss

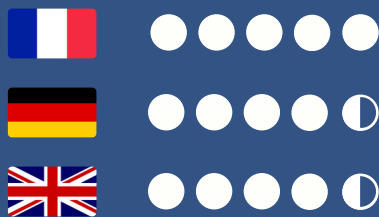
## PROFILE

Self-driven, goal-oriented mechanical engineer in the field of fibre-reinforced composites with a focus on the consolidation, modelling and simulation of thermoplastic composites.

## CONTACT

✉ vinc.werlen@gmail.com  
📍 Bachmattstrasse 15  
CH-5210 Windisch  
☎ +41 78 786 98 29

## LANGUAGES



## HOBBIES



## WORK EXPERIENCE

**Research Associate** 03.2022 - 07.2023

FHNW, Windisch (AG)

Collaboration in an Innosuisse Research Project for the prototype manufacturing of carbon fibre-reinforced tapes for lifting applications.

**Mechanical Engineer** 05.2018 - 07.2019

SCHMID Group GmbH, Lengnau (AG)

Construction of assemblies in CAD (SolidWorks and Autodesk Inventor), including development, layout, evaluation and technical drawing.

**Intern** 09.2016 - 11.2016

RUAG Luftfahrt, Emmen (LU)

Creation of a detailed FE model in Hypermesh and fatigue analysis of a finding.

## EDUCATION

**PhD in Advanced Manufacturing** 08.2019 - 07.2023

Swiss Federal Institute of Technology Lausanne

Development and implementation of a three dimensional consolidation model to simulate the press process of complex-shaped fibre-reinforced thermoplastic composites. Workplace FHNW in Windisch (AG).

**MSc in Mechanical Engineering** 09.2015 - 10.2017

Swiss Federal Institute of Technology Zurich

With a focus on the following topics: fibre-reinforced composites, FE analysis, optimization, fatigue.

**BSc in Mechanical Engineering** 09.2012 - 08.2015

Swiss Federal Institute of Technology Zurich

## SKILLS

- Accountable
- Flexible
- Organized
- Self-reliant
- Critical thinking

## SOFTWARE

- Data Analysis (Matlab, Python, MS Excel)
- FEM Simulation (Siemens NX, Comsol Multiphysics)
- CAD (SolidWorks, Siemens NX, Autodesk Inventor)
- Machine Learning (Python)

## REFERENCES

- **Pr. Dr. Véronique Michaud, Associate Professor**  
Swiss Federal Institute of Technology Lausanne  
email: veronique.michaud@epfl.ch
- **Pr. Dr. Christian Rytka, Group Leader**  
FHNW Group of Polymer Engineering  
email: christian.rytka@fhnw.ch